Dissertation zur Erlangung des Doktorgrades

der Fakultät für Chemie und Pharmazie

der Ludwig-Maximilians-Universität München

Structural and biochemical characterization of BusR and c-di-AMP specific phosphodiesterases

Adrian Maurice Bandera

aus

Stuttgart, Deutschland

2021

Erklärung

Diese Dissertation wurde im Sinne von §7 der Promotionsordnung vom 28. November 2011 von Herrn PD Dr. Gregor Witte betreut.

Eidesstattliche Versicherung

Diese Dissertation wurde eigenständig und ohne unerlaubte Hilfe erarbeitet.

München, 23.9.2021

…….

Adrian Maurice Bandera

Dissertation eingereicht am	23.9.2021
1. Gutachter	PD Dr. Gregor Witte
2. Gutachter	Prof. Dr. Roland Beckmann
Mündliche Prüfung am	15.11.2021

This thesis has been prepared from Mai 2017 to September 2021 in the laboratory of Professor Dr. Karl-Peter Hopfner at the Gene Center of the Ludwig-Maximilians-University Munich.

This is a cumulative thesis based on following publications:

Bandera, A. M.; Bartho J.; Lammens K.; Drexler D.; Kleinschwärzer J.; Hopfner K. P.; Witte G. BusR Senses Bipartite DNA Binding Motifs by a Unique Molecular Ruler Architecture. *Nucleic Acids Research*, **2021**, *49* (17), 10166–10177

Drexler, D.; Müller, M.; Rojas-Cordova, C. A.; Bandera, A. M.; Witte, G. Structural and Biophysical Analysis of the Soluble DHH/DHHA1-Type Phosphodiesterase TM1595 from Thermotoga maritima. *Structure* **2017**, *25* (12), 1887-1897.e4.

Latoscha A.; Drexler D.; Al-Bassam M. M.; Bandera A. M.; Kaever V.; Findlay K. C.; Witte G.; Tschowri N. C-di-AMP hydrolysis by the phosphodiesterase AtaC promotes differentiation of multicellular bacteria. *PNAS* **2020**, *117* (35), 7392-7400.

Table of Contents

1 Summary

In order to react to changing environmental conditions, bacteria use second messenger molecules, which transduce an external or internal signal to initiate appropriate intracellular responses. Cyclic-di-AMP is a nucleotide second messenger that has aroused great interest among the scientific community in recent years. Cyclic-di-AMP is widely found in gram-positive bacteria, especially firmicutes and actinobacteria. The second messenger has been linked to cell wall homeostasis, biofilm formation, virulence, DNA integrity, sporulation, osmolyte and potassium homeostasis. In contrast to other second messengers, c-di-AMP is essential under standard conditions in many organisms it naturally occurs in. Among them are many human pathogens like *Staphylococcus aureus, Listeria monocytogenes* or *Streptococcus pneumoniae.* This makes c-di-AMP an interesting target for therapeutic approaches.

In recent years it has become evident that c-di-AMP has a central role in osmoregulation. It controls both activity and expression levels of a multitude of potassium and osmolyte transporters. Its levels within the cell correlate with the availability of potassium, and mutants deprived of c-di-AMP are highly susceptible to varying osmolarity. In *S. agalactia* the gene for the carnitine-betaine osmolyte importer BusA is under the control of the c-di-AMP sensitive transcription factor BusR.

For a better understanding of c-di-AMP regulated osmoregulation, especially with regard to the underlying molecular mechanisms, a thorough biochemical and structural investigation of *S. agalactiae* BusR was conducted and its c-di-AMP dependent activation and gene repression mechanisms were investigated. The binding specificity of BusR to c-di-AMP has been elucidated by isothermal titration calorimetry. A full-length crystal structure shows that BusR has a novel tetrameric “two parallel, two antiparallel head-to-tail” arrangement with a central tetrameric coiled-coil motif. Additional high-resolution crystal structures of the ligand binding domain, accompanied by biochemical data, reveal an autoinhibited state that is dissolved upon c-di-AMP binding. A mutant was described that circumvents the control of c-di-AMP and leads to constant activation of BusR. Cryo-electron microscopy structures of the transcription factor in complex with both the ligand and the physiological DNA substrate show how BusR recognizes bipartite binding motifs using a molecular ruler like architecture, novel for its GntR transcription factor family.

Apart from c-di-AMP signaling, also c-di-AMP homeostasis is of scientific interest. C-di-AMP is synthesized by diadenylate cyclase domain containing cyclases and degraded by phosphodiesterases. The phosphodiesterases can be subdivided into the DHH, the HD and the AtaC type of phosphodiesterases. Part of this work is the contribution to the structural and biochemical characterization of the DHH-type PDE from *T. maritima*, as well as the novel phosphodiesterase AtaC from *Streptomyces venezuelae* that advance our understanding of c-di-AMP degradation.

2 Introduction

Living cells are confronted with continuously changing environmental conditions. Fluctuations in temperature, pH and osmolarity or different nutritional sources have to be perceived and adequately responded to in order to ensure fitness and survival of the organism. After a primary signal has been perceived, nucleotide second messengers transduce the signal and initiate an adequate cellular response on multiple levels, which can include gene expression, enzymatic activity, interaction stability and cellular dynamics of proteins.

2.1 Bacterial nucleotide second messenger

Nucleotide second messengers occur in all kingdoms of life but this work focuses on bacterial nucleotide second messengers (Figure 1). They are involved in central pathways and decisively dictate bacterial behavior [1]. The field of nucleotide second messengers is now little more than half a century old and originates from the discovery of cyclic 3',5' adenosine monophosphate (cAMP) in liver cells by Sutherland et al. in 1957 [2]. Earl Sutherland and his elucidation of "the mechanism of the action of hormones" was later honored with the Nobel Prize in Physiology or Medicine in 1971. In 1963, cAMP was demonstrated to be present and physiological relevant in prokaryotes, as well [3]. Since then, the list of bacterial nucleotide second messengers is continuously growing. Structurally they all share purine derived nucleotides and can form mononucleotides, cyclic nucleotides or cyclic dinucleotides. Apart from cAMP important bacterial nucleotide second messengers include cyclic 3',5'-guanosine monophosphate (cGMP), cyclic di-3',5'-adenosine monophosphate (c-di-AMP), cyclic di-3',5'-guanosine monophosphate (c-di-GMP), cyclic 3',3'-AMP-GMP (3',3'-cGAMP), and guanosine penta- and tetraphosphate ((p)ppGpp) [1].

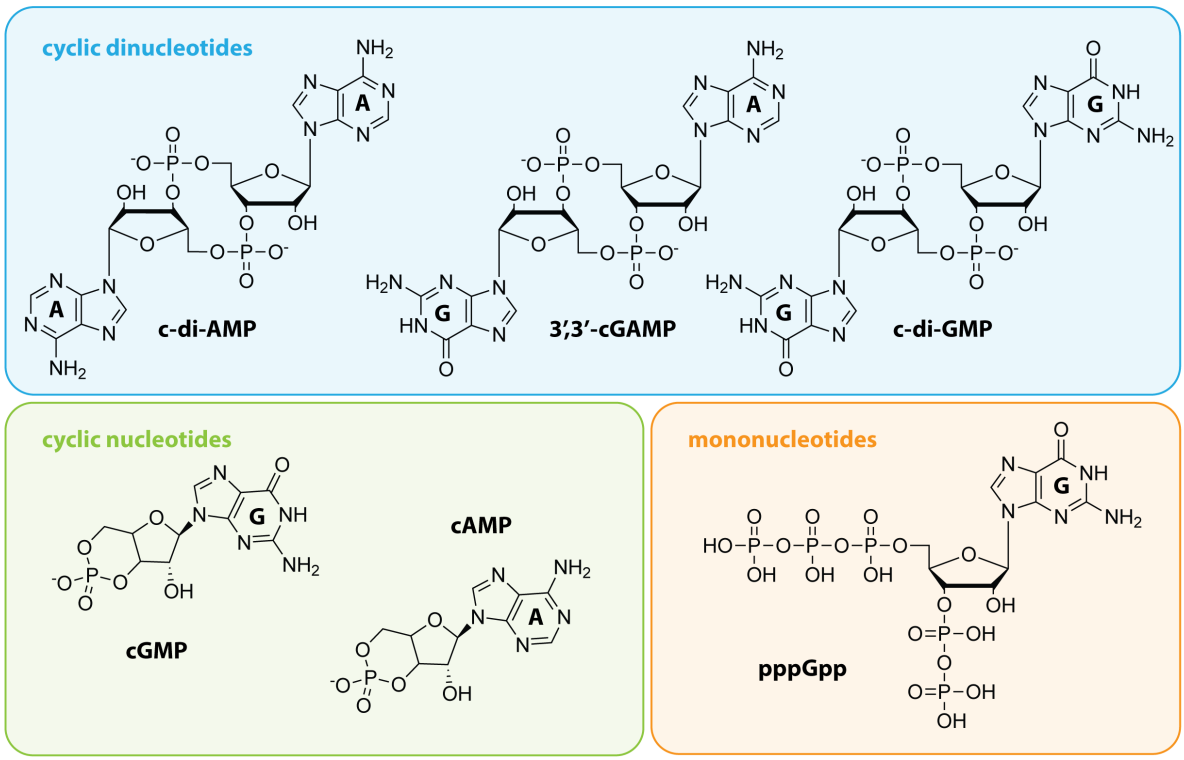

Figure 1. Bacterial nucleotide second messenger. Overview of physiological relevant bacterial nucleotide second messengers classified according to their composition.

2.1.1 cAMP

Since its discovery a lot of functions and underlying mechanisms of cyclic 3',5'-AMP signaling have been characterized in detail. cAMP levels are regulated by the adenylate cyclase CyaA and the cAMP phosphodiesterase CpdA [4, 5].

cAMP is a central regulator in carbon catabolite repression. In presence of preferable carbon sources as for example glucose opposed to lactose, cAMP directs the cell to first metabolize glucose. In absence of glucose, phosphorylated glucose specific enzyme IIA ($EIIA^{Glc}$) activates CyaA that leads to an increase in cAMP levels. cAMP binds to the cAMP response receptor (CRP) and this complex then induces basal gene expression of a broad range of metabolic genes including the *lac* operon. The presence of a preferred sugar like glucose, in contrast, leads to the dephosphorylation of $EIIA^{Glc}$. Dephosphorylated $EIIA^{Glc}$ inhibits transporters responsible for the uptake of secondary carbon sources and inhibits translation of genes of secondary carbon sources via the cAMP-CRP complex [6].

While its role in catabolite repression is well understood in *E.* coli, the effects that cAMP exerts on the cell vary depending on the organism. In many pathogens cAMP is a master regulator of virulence. For instance, cAMP-CRP in *Yersinia enterocolitica* activates type III secretion systems, necessary for infection of eukaryotic host cells [7]. Besides the expression of type III secretion systems, in *pseudomonas Aeruginosa* cAMP further orchestrates virulence by regulating motility and toxin

production [8]. The cholera toxin is expressed upon cAMP signaling. Within the host cell the toxin upregulates the endogenous adenylate cyclase to upregulate the host's cAMP levels that suppresses the innate immune functions [9].

2.1.2 (p)ppGpp

When confronted by severe nutrient starvation, bacteria respond rigorously and activate the stringent response to ensure survival. The stringent response allows the cells to shut down non-essential pathways, stop growth and channel the available resources into urgent pathways like amino acid synthesis. The responses are diverse and dependent on the original signal but utilize a common set of messengers, the alarmones guanosine penta- and tetraphosphate ((p)ppGpp) and the more recently discovered guanosine 5'-monophosphate-3'-diphosphate (pGpp) [10, 11]. The research field opened up in 1969 when (p)ppGpp was first discovered in *E. coli* by Cashel and Gallant [12]. (p)ppGpp levels are maintained by the protein family of the RelA/SpoT homologs (RSH). RSH enzymes are bifunctional as they contain a synthetase domain and a hydrolase domain next to additional regulatory domains. Monofunctional proteins exist that either lack one of the enzymatic domains or carry a degenerate version [13]. These proteins integrate the different stress signals and direct the cellular response via (p)ppGpp levels. A very well understood example of (p)ppGpp regulation and signaling can be illustrated upon amino acid starvation in *E. coli*. Under amino acid shortage the fraction of deacetylated- over aminoacyl-tRNA increases. RelA loads deacetylated tRNA into the A-site of a ribosome, which triggers its (p)ppGpp synthetase activity [14]. (p)ppGpp then binds to two different sites on the RNA polymerase (RNAP) and alters global transcription levels [15, 16]. For *E. coli* it was demonstrated that 1224 genes were altered in their expression levels only 10 minutes after induction of (p)ppGpp by RelA [17]. (p)ppGpp further reshapes the cell by influencing nucleotide synthesis, DNA replication, rRNA transcription, ribosome maturation, translation, lipid metabolism, virulence, biofilm formation and antibiotic resistance [18].

2.1.3 c-di-GMP

c-di-GMP is the first **c**yclic-**di**-**n**ucleotide (CDN) to be discovered and was first described in 1987 by Benziman et al. as an allosteric activator of the cellulose synthase from *Gluconacetobacter xylinus* [19, 20] (Figure 1). C-di-GMP is nearly ubiquitous among bacteria and is most prominently involved in biofilm formation, virulence and cell cycle regulation among others [21]. The level of c-di-GMP promotes the switch between mobile and sessile lifestyle. High levels of c-di-GMP generally lead to biofilm formation while low levels promote dispersal [22]. This is achieved by c-di-GMP interacting with a broad range of RNAs and proteins on the transcriptional, translational and post-translational level. C-di-GMP reduces flagellar expression and activity to reduce motility while promoting

adherence through type IV pili [23-25]. Furthermore, production of extracellular matrix components like cellulose or the secretion of the alternative exopolysaccharide poly-β-1,6-*N*-acetylglucosamine is induced by c-di-GMP [19, 26].

Besides its role as lifestyle switch, c-di-GMP is a major determinant of virulence as it steers an infection between an acute and a chronic progression. Biofilm formation and adherence are already important virulence factors as they prevent easy disposal by the host and increase antibiotic resistance [27]. Toxin production in *clostridium difficile* has been shown to be negatively regulated by c-di-GMP [28]. While c-di-GMP is often recognized as pathogen associated pattern by the host cells immune system, it has also been shown to weaken the immune response by inactivating siderocalin, which exhibits antibacterial activity by restricting accessibility of iron [29]. The fact that c-di-GMP is a central mediator of virulence makes c-di-GMP signaling a possible antimicrobial target [30].

The high diversity of c-di-GMP related signaling results in a need for precise finetuning of both global as well as local c-di-GMP levels. For synthesis of c-di-GMP bacteria use a large family of diguanylate cyclases that contain a catalytic GGDEF domain and phosphodiesterases with either an EAL or HD-GYP domain for degradation of the messenger [31]. These proteins are often found to be combined in a bifunctional assembly with either both, synthetase as well as phosphodiesterase being potentially active or one being degenerated and serving as regulatory domain [32]. They are also commonly accompanied by addition of regulatory domains [33]. This allows for various primary signals like nitric oxide, metals, light, nutrient availability and many more to be sensed and integrated to distinct levels of c-di-GMP that trigger the specific and diverse responses outlined above [22].

2.2 c-di-AMP

The presence of cyclic-di-AMP may be considered as a natural continuation after the discovery of cAMP and c-di-GMP. Yet, c-di-AMP remained elusive for another 20 years since the discovery of c-di-GMP. In 2008 Witte *et al.* solved the crystal structure of the **D**NA **i**ntegrity **s**canning protein **A** (DisA) from *Thermotoga maritima*. An extra density in the electron density map was observed that could convincingly be identified by mass spectrometry and biochemical assays to be 3'-5'-cyclic-di-AMP [34]. The Gründling lab achieved groundbreaking results by conducting a *Staphylococcus aureus* genome wide open reading frame screen, revealing many novel c-di-AMP binding proteins [35]. This started a new chapter in cyclic-dinucleotide research and c-di-AMP signaling has become a rapidly growing field. Since then, several directed or unbiased searches in various organisms have revealed an increasing number of interaction partners [36-39]. In only a single decade, significant advances were made. C-di-AMP is synthesized by a family of diadenylate cyclase (DAC) domain containing proteins and phosphodiesterases of different types, including DhhP, GdpP, PgpH and AtaC [40-43] (chapter 2.2.1). C-di-AMP is most commonly found in firmicutes, actinobacteria and other gram-positive bacteria but

also in gram-negative bacteria like cyanobacteria or even archaea [34, 36, 44, 45]. The messenger is involved in cell wall synthesis, biofilm formation, virulence, antibiotic resistance, potassium and osmolyte homeostasis, osmoregulation, DNA integrity, sporulation and carbon metabolism [34, 39, 42, 44, 46, 47] (Figure 2, chapter 2.2.2). In order to regulate the cellular processes, c-di-AMP interacts with a diverse set of proteins and riboswitches (chapter 2.2.4). For most organisms that produce c-di-AMP, the messenger has been shown to be conditional essential. Under standard laboratory conditions both high and low levels are toxic [37, 48-51]. For this reason, c-di-AMP has been termed an “essential poison” [52]. The fact that many organisms possessing a c-di-AMP pathway are human pathogens like *S. aureus* or *L. monocytogenes*, has increased interest in the c-di-AMP pathways as potential antimicrobial targets [53].

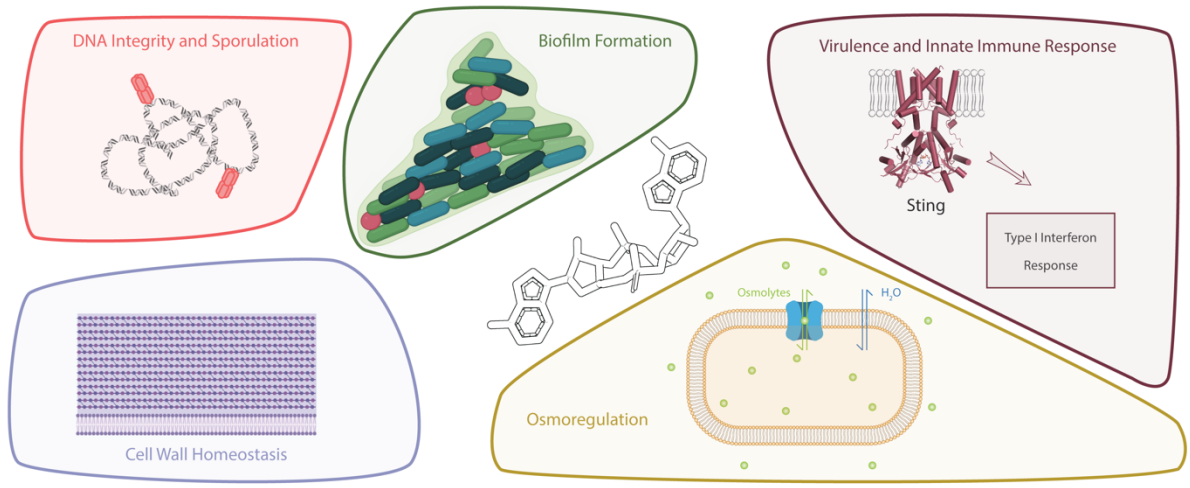

Figure 2. Overview of important cellular processes that are regulated by c-di-AMP.

2.2.1 C-di-AMP homeostasis

The level of c-di-AMP in the cell is primarily determined by three factors, comprising synthesis, degradation and export of the second messenger (Figure 3). All rates for these factors can be adjusted on multiple levels including transcription, translation or protein activity. In this chapter these processes that govern c-di-AMP homeostasis will be dissected and the different proteins involved introduced.

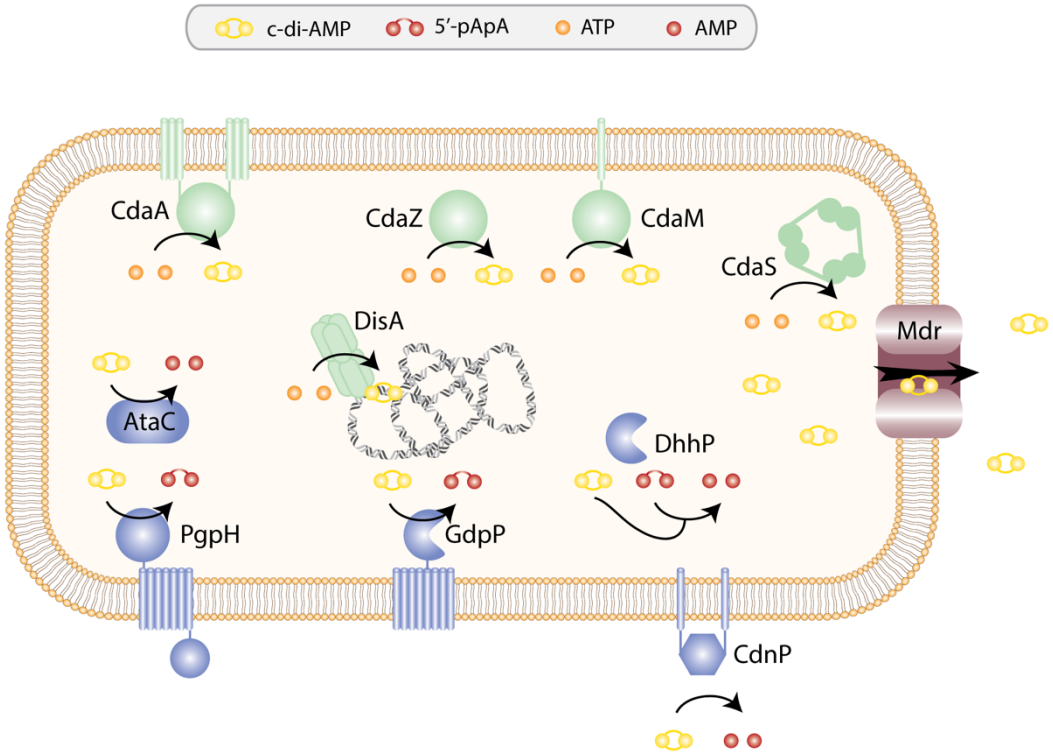

Figure 3. Schematic overview of the synthesis, degradation and export pathways that determine c-di-AMP homeostasis within the cell. C-di-AMP is synthesized from two molecules of ATP by DAC domain containing proteins (green) and degraded by phosphodiesterases of different types (blue). Multidrug export systems (red) also lower the c-di-AMP concentration in the cell. Proteins are neither drawn to scale nor realistic features and do not necessarily occur simultaneously in every organism.

2.2.1.1 Synthesis

All known cyclases that produce c-di-AMP share a conserved DAC domain that converts two molecules of ATP to c-di-AMP. Yet, the paralogous cyclases specialize on different functions based on their auxiliary domains accompanying and regulating the DAC domain. So far, five different cyclases have been experimentally determined, CdaA, DisA, CdaS, CdaM and CdaZ [54].

CdaA

Cyclic **d**i-**A**MP synthase **A** (CdaA or DacA in *S. aureus*) is the most ubiquitous cyclase and in many organisms, including *S. aureus*, *L. monocytogenes* and *Streptococcus pneumoniae*, the only cyclase found. CdaA is membrane bound via three helices at the N-terminus and linked by coiled-coils to its C-terminal DAC domain [52]. Crystal structure have been solved for the cytosolic part from *S. aureus* as well as *L. monocytogenes* [55, 56]. The DAC domain needs Mn^{2+} for highest catalytic activity but accepts Co^{2+}, as well [57]. The DAC domain forms a dimer and higher transient oligomeric assemblies are proposed to be important for catalytic activity in *S. aureus* [56]. CdaA shares an operon with the CdaA regulatory protein (CdaR) and the phosphoglucosamine mutase (GlmM). CdaR is membrane

anchored and its soluble C-terminus protrudes into the extracytoplasmic space [58]. CdaR interacts with the membrane domain of CdaA to negatively regulate its cyclase activity in *L. monocytogenes* and *S. aureus* [59, 60]. While the primary signal for CdaR is still unknown, a minor role in osmoadaptation of *L. monocytogenes* could be assigned to it [58]. CdaA is further regulated by GlmM in *Bacillus subtilis, S. aureus*, *Lactococcus lactis* and *L. monocytogenes* [52, 56, 58, 60]. CdaA and GlmM form a dimer of dimers according to small-angle X-ray scattering (SAXS) data, where GlmM blocks the active site of CdaA [56]. Simultaneous binding of CdaR and GlmM to CdaA is not mutually exclusive [52]. GlmM is an important enzyme in the biosynthesis pathway for peptidoglycan and therefore a potential link of c-di-AMP signaling to cell wall homeostasis [52] (chapter 2.2.2.1). Expression of *cdaA* is upregulated upon increasing availability of potassium ions, which forms a regulatory link between potassium homeostasis and c-di-AMP signaling [61] (chapter 2.2.2.7).

DisA

DisA was the first DAC domain protein to be described and the availability of several crystal structures from different organisms and different reaction intermediates allow for a good understanding of its reaction mechanism [34, 62] (Figure 4). DisA is present mostly in spore forming firmicutes or actinobacteria. Depending on the organism, DisA can function as the primary DAC protein or be accompanied by other cyclases as found in *B. subtilis* [54]. Unlike CdaA, DisA is a cytosolic protein that co-localizes with the nucleoid [63]. DisA has an N-terminal DAC domain, a linker region and a C-terminal helix-hairpin-helix (HhH) domain. In solution DisA forms a dumbbell-shaped octameric assembly with the DAC domains forming the inner core and a quartet of HhH domains facing outwards on either side. Two opposing DAC domains form an active center with two conserved RHR and DGA motifs [34]. For adenylate activity magnesium or manganese ions are needed. The β- and γ-phosphates of the bound ATP moieties are coordinated by the metal ion and the RHR motif. The DGA is involved in the coordination of the metal and the correct positioning of the ribose for a nucleophilic attack from the 3'-hydroxygroup on the α-phosphate [62]. The constitutively active diadenylate cyclase activity is inhibited upon binding to branched nucleic acids [34]. This turns DisA into a central link between c-di-AMP signaling and DNA maintenance, which will be further discussed in chapter 2.2.2.4.

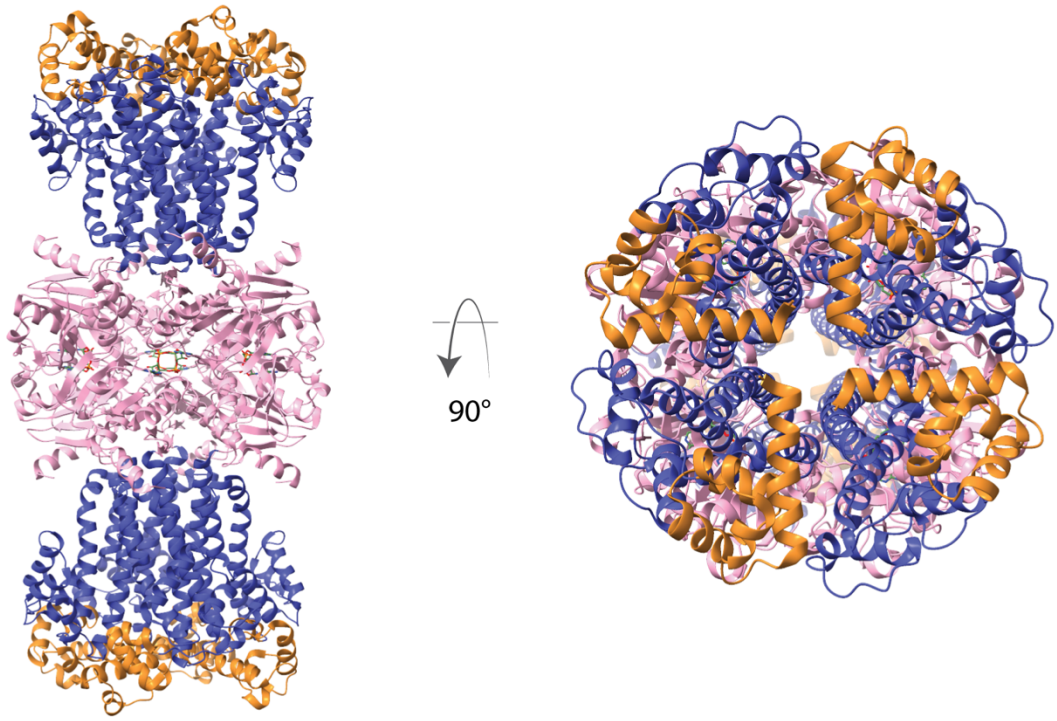

Figure 4. X-ray crystal structure of *T. maritima* DisA (pdb id: 3C1Y). (left) front view of the DisA octamer. The central DAC domain (pink) contains the active site with co-purified c-di-AMP (green) bound. Tetrameric linker regions (blue) on either side of the DAC domain connect the distal helix-hairpin-helix domain (orange). (right) Topview along the longitudinal axis of DisA.

CdaS

The **c**-**d**i-**A**MP synthase **S** (CdaS) differs from CdaA and DisA as it does not suffice as the primary DAC, due to not being constitutively expressed. Instead, CdaS is only expressed during sporulation [64]. The gene therefore always occurs alongside CdaA or DisA. CdaS is mostly limited to the *Bacillus* genus, where it acts as a specific diadenylate cyclase necessary during germination of the spores [50]. CdaS has a C-terminal conserved DAC domain coupled to two α-helices. The DAC domain forms enzymatically active dimers. The full protein is postulated to form hexamers with autoinhibited DAC activity due to active site displacement in absence of a yet to be determined stimulus [65].

CdaM

The c-di-AMP synthase of *Mycoplasma* (CdaM) is found in the genus of *Mycoplasma.* Its diadenylate cyclase activity has been experimentally proven and the gene is essential in *Mycoplasma pneumoniae*. The DAC domain is linked to a N-terminal helix that likely anchors the protein to the membrane, but further experimental data is missing [66]. Future studies will have to further shed light on the regulation of CdaM.

CdaZ

CdaZ comprises an N-terminal pyruvate kinase like domain and a C-terminal DAC domain. CdaZ is special as it is found in archaea. For *Methanocaldococcus jannaschii* CdaZ diadenylate cyclase activity has been detected when expressed in *E.* coli [67]. In *Haloferax volcanii cdaZ* (*dacZ*) is essential and resulting c-di-AMP levels have been experimentally determined *in vivo* [45]. These findings extend c-di-AMP signaling to the domain of archaea.

2.2.1.2 Degradation

When the primary stimulus for c-di-AMP signaling stops, the signal response has to be downregulated as well. In order to do so, c-di-AMP levels have to be regulated at basal concentration. The cell can utilize two basic mechanisms. The second messenger can either be degraded or exported out of the cell by export systems.

C-di-AMP is degraded by different types of phosphodiesterases (PDEs), including the major DHH and HD-type families. They comprise both membrane and soluble PDEs and will be introduced in the following chapter. All PDEs share in common a strict dependency on metal ions. While a lot of structural and biochemical data is available that explains the catalytic reaction, the regulation of the PDEs is still vague [68].

DHH-type phosphodiesterases

The family of DHH-type PDEs is named after its conserved amino acid motif in the active site (Asp-His-His). The catalytic domain is formed by the DHH domain and a smaller DHHA1 domain that contains an additional conserved GGGH motif. The DHH-type PDEs can further be divided into the membrane bound GdpP-type and the soluble DhhP-type [68].

The first c-di-AMP specific PDE that has been described was the GGDEF domain protein containing phosphodiesterase (GdpP, formerly YybT) from *B. subtilis* [41]. GdpP is widespread among organisms that utilize c-di-AMP including *S. pneumoniae, Listeria monocytogenes* and *Staphylococcus aureus* [44, 51, 69]. It requires Mn^{2+} or Co^{2+} for cleavage of c-di-AMP and produces exclusively the linear degradation intermediate product 5'-pApA. In addition to the C-terminal catalytic DHH/DHHA1 domain, GdpP contains two N-terminal membrane helices, a PAS domain and a degenerate GGDEF domain [41]. The PAS domain is expected to exert regulatory control over GdpP activity. For *B. subtilis* and *Geobacillus thermodenitrificans* heme binding has been observed, which enable the PAS domain to sense nitric oxide [70, 71]. The PAS domain forms antiparallel dimers in solution according to an NMR structure of the PAS domain from *G. thermodenitrificans* [71]. Less is known about the GGDEF domain. GGDEF domains often have diguanylate cyclase activity but can also be degenerated and function as ligand binding and regulatory domain [32, 72]. The GGDEF domain in the GdpP is

degenerated. Instead of cyclase activity, ATPase activity was observed in *B. subtilis* [70]. However, its physiological role remains elusive.

The soluble DhhPs contain no regulatory domains in addition to the catalytic DHH-DHHA1 domain. It is not known whether or how they are regulated. The observed substrate specificity varies depending on the organism. DhhPs from *S. aureus* and *T. maritima* and *S. pneumoniae* have a strong preference for 5'-pApA over c-di-AMP and thereby carry out the second step in c-di-AMP degradation [69, 73, 74]. In contrast, DhhPs from *Borrelia burgdorferi, Mycobacterium tuberculosis* or *Mycobacterium pneumoniae* degrade c-di-AMP directly to AMP [66, 75]. Structural information is available for *T. maritima* and *M. tuberculosis* PDEs [40, 74] (Figure 5). The catalysis is well understood based on detailed structural data. Two metal ions are coordinated by the DHH motif and activate a water molecule for subsequent nucleophilic attack on the phosphate bond [40, 74]. The structures share high similarity with the crystal structure of the *S. aureus* GdpP DHH/DHHA1 domain [76]. The authors of the latter study explore the different substrate specificity exhibited by DhhP and GdpP-type PDEs. They divide the active site into G, C and R with the latter being needed for hydrolysis of 5'-pApA. In contrast to *M. tuberculosis* DhhP, the R site in *S. aureus* GdpP DHH/DHHA1 is too small to accommodate 5'-pApA [76].

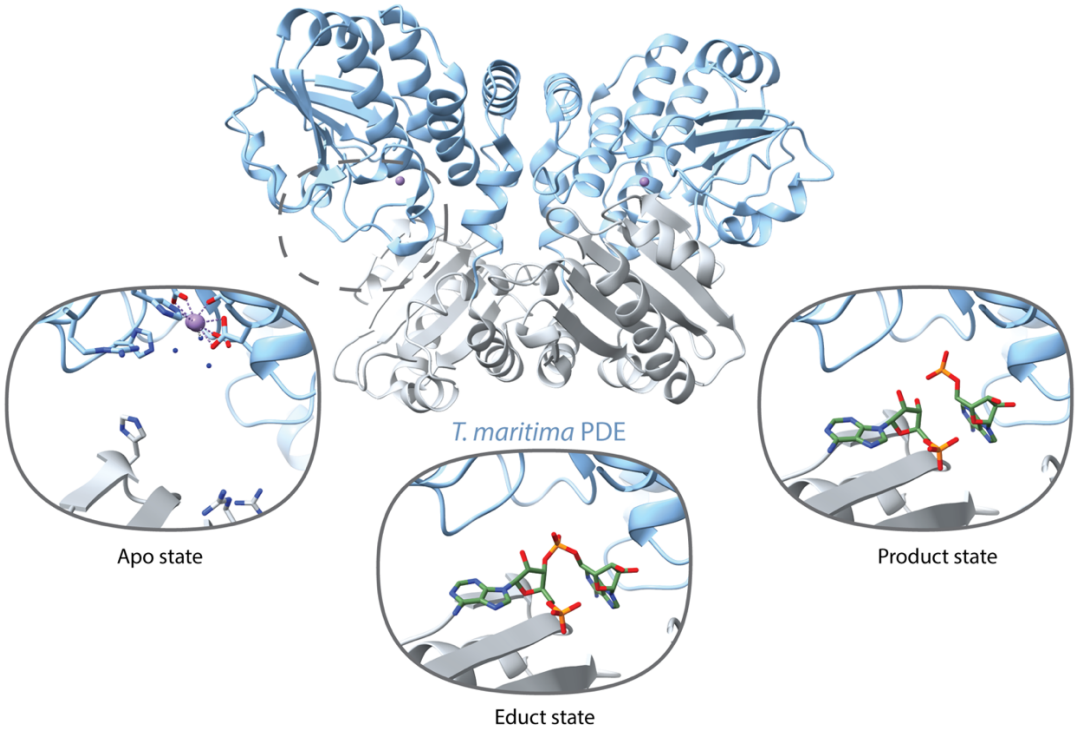

Figure 5. Crystal structures of *T. maritima* TmPDE. (Main) The DHH (blue) and DHHA1 (grey) domain form the typical butterfly like shape observed for all DHH-DHHA1 domains. Manganese ions are depicted as purple spheres. (Magnifying glass) close-up on one of the active sites (dashed line) in wt apo state (pdb id: 5O25), educt (pdb id: 5O70) and product state (pdb id: 5O4Z) of the inactive mutant. Water molecules coordinated by manganese ions are depicted as blue spheres.

HD-type Phosphodiesterases

Apart from the DHH-type PDEs a second ubiquitously family called PgpH has been discovered to catalyze the degradation of c-di-AMP. PgpH was first discovered in *L. monocytogenes* but is widely distributed in firmicutes and can also be found in many cyanobacteria, bacteroidetes, fusobacteria, and δ-proteobacteria [42]. Like GdpP, PgpH can significantly influence c-di-AMP levels *in vivo* [52]. PgpH contains a C-terminal cytosolic HD domain, seven transmembrane helices and an N-terminal extracellular domain. The HD domain from *L. monocytogenes* PgpH has been crystallized. It utilizes a very similar reaction mechanism as observed for DhhP family PDEs. Two Mn^{2+} ions are coordinated by histidine and aspartate residues and activate a water for a nucleophilic attack on the phosphate group [42]. The extracellular domain has not been characterized, yet, but is believed to sense an extracellular signal and mediate HD activity accordingly [68]. The fact that the mechanism of c-di-AMP hydrolysis is so similar and the tertiary assembly is strikingly different, suggests that both PDEs integrate different signals into c-di-AMP homeostasis and are relevant at different environmental conditions. Indeed, for *L. monocytogenes* GdpP is more active in host cells while PgpH dominates in broth culture [42].

AtaC

Numerous actinobacteria use c-di-AMP but lack both HD and DHH-type PDEs. This led to the discovery of a new class of PDEs, called **A**ctinobacterial PDE **ta**rgeting **c**-di-AMP (AtaC). While originally discovered in *Streptomyces venezuelae*, AtaC is further present in human pathogens like *S. pneumoniae* or *M. tuberculosis*. AtaC is a monomeric protein that specifically cleaves c-di-AMP to AMP in a Mn^{2+} dependent manner, likely similar to the mechanism observed for GdpP and PgpH [43].

CdnP

The **c**yclic **d**inucleotide **p**hosphodiesterase (CdnP) from *S. agalactiae* is a specialized PDE involved in dampening the host immune response. CdnP is a membrane anchored ectonucleotidase with c-di-AMP specific phosphodiesterase activity. It contains an N-terminal signal peptide for secretion, a metallophosphatase domain, a nucleotidase domain and a C-terminal LPxTG motif for cell wall anchoring including an additional transmembrane domain. A conserved NHE motif in the active site and Mn^{2+} ions are essential for PDE activity. The soluble part of the protein forms a monomer in solution. *In vivo,* CdnP hydrolyzes extracellular c-di-AMP, which stimulates the innate immune response from the host cell via STING binding (chapter 2.2.2.3). Thus, the degradation of c-di-AMP evades STING activation and increases viability in the host environment [77].

2.2.1.3 Export

As a phosphodiesterase independent mechanism of reducing the amount of c-di-AMP in a cell, the second messenger can be exported out of the cell. *L. monocytogenes* uses several c-di-AMP unspecific

multi**d**rug **r**esistance efflux pumps (MDRs) of the MFS superfamily, including MdrM, MdrT, MdrA and MdrC [78]. Similar, *L. lactis* mutants with elevated levels of c-di-AMP due to a knock-out mutation in the *gdpP* gene can bypass the detrimental amounts of c-di-AMP by acquiring activating mutations in an MDR of the EmrB family [79]. Export of c-di-AMP allows for a fast reduction of potentially toxic levels of c-di-AMP upon rapid changing environmental conditions, but it also puts a pathogen at risk of being detected by the hosts immune system [68, 78] (chapter 2.2.2.3).

2.2.2 c-di-AMP signaling

Once synthesized c-di-AMP targets a plethora of cellular targets, including transporters, channels, transcription factors, riboswitches and enzymes to steer the cellular behavior in the physiological context of cell wall synthesis, biofilm formation, virulence, antibiotic resistance, potassium and osmolyte homeostasis, osmoregulation, DNA integrity, sporulation and carbon metabolism [34, 39, 42, 44, 46, 47]. In the following chapter these signaling pathways and the factors involved will be introduced in greater detail.

2.2.2.1 Cell wall homeostasis

One of the first observations made in regard to c-di-AMP dependent phenotypes concern defects in cell wall homeostasis. Lipoteichoic acid (LTA) is a crucial component of the cell wall in *S. aureus*. LTA deficiency can be rescued upon acquisition of mutations in the *gdpP* gene that results in elevated c-di-AMP levels. This strain compensated for the lack of LTA by an elevated amount of cross-linked peptidoglycan [44]. In agreement with its postulated role in cell wall homeostasis, several observations were made that alterations in c-di-AMP levels result in susceptibility to peptidoglycan synthesis targeting antibiotics. *B. subtilis* and *L. monocytogenes* with elevated c-di-AMP levels are more resistant to cefuroxime while depletion of c-di-AMP leads to susceptibility to cefuroxime, ampicillin or penicillin [51, 80]. In *Streptomyces venezuelae* and *Streptomyces coelicolor* a direct link between c-di-AMP and cell wall homeostasis is established. The gene **r**esuscitation-**p**romoting **f**actor **A** (*rpfA)* is under transcriptional control of a c-di-AMP dependent YdaO-like riboswitch. RpfA is a muralytic enzyme involved in cell wall remodeling during resuscitation [81]. An intricate and still not fully understood link between c-di-AMP and cell wall homeostasis has been observed in the regulation of c-di-AMP levels by GlmM (see above). GlmM is involved in the biosynthesis pathway for peptidoglycan and inhibits cdaA cyclase activity upon a yet undiscovered stimulus [56, 60]. In order to generate the substrate for GlmM, which is D-glucosamine 6-phosphate, glutamine is converted to glutamate. Therefore, the regulation of c-di-AMP levels by GlmM could also be a link to glutamate homeostasis instead (2.2.2.7). In their opinion paper Commichau *et al.* argue that the observed cell

wall related phenotypes may be indirect. Instead, the well-established role of c-di-AMP in osmolyte homeostasis and the consequences that uncontrolled osmolyte uptake has on the cell wall, could explain the cell wall related phenotypes in bacteria excluding actinobacteria [82]. Furthermore, high c-di-AMP disturbs muropeptide synthesis in *L. monocytogenes* partially by impairing D-Ala:D-Ala ligase activity by depriving it of potassium [83]. D-Ala:D-Ala ligase is involved in the peptidoglycan pathway.

2.2.2.2 Biofilm formation

Biofilm formation is a process of primary importance for numerous bacteria and is considered the prevalent form of bacterial life in nature. Bacterial biofilms are complex multi-species communities solidified in a polymeric matrix, with intensive exchange of metabolites and signals between cells. Adhesion and biofilm formation provides protection against starvation, dehydration, anti-microbial agents and mechanical assaults for its inhabitants [84]. C-di-GMP is the main signal transducer influencing the cell wide decision between sessile or motile lifestyle (chapter 2.1.3), but for some organisms c-di-AMP has been shown to have a direct or indirect impact on biofilm formation, as well. In *Streptococcus mutans* deletion of the gene for the GdpP homolog *pdeA* leads to higher levels of c-di-AMP and biofilm formation. C-di-AMP binds to **c**-di-**A**mp **b**inding **p**rotein **A** (CabPA), likely to its RCK_C domain [85] (chapter 2.2.4.1). CabPA interacts with VicR, the signal response factor of the two-component system VicKR, that modulates expression of *gtfB* [85, 86] (Figure 6). GtfB is a glucan producing enzyme, critical for biofilm formation. Deletion of *cabPA* or *gtfB* rescued the *pdeA* phenotype. This suggests a direct link of c-di-AMP to biofilm formation in *S. mutans* via the CabPA/VicR/GtfB signaling pathway [85]. In *Streptococcus suis* high levels of c-di-AMP lead to increased biofilm formation, as well [46]. C-di-AMP plays an important role in the symbiosis of *B. subtilis* and *Arabidopsis thaliana* that requires adhesion of *B. subtilis* to the plant roots. Alterations of c-di-AMP levels affect biofilm morphology via the *tapA* operon that is important for structural integrity of the biofilm. *B. subtilis* strains with reduced levels of c-di-AMP were severely impaired in their ability to colonize *A. thaliana* plant roots [87]. As c-di-AMP induces potassium export and potassium leakage induces biofilm formation in *B. subtilis*, the role of c-di-AMP in biofilm formation could be indirect in *B. subtilis*. In contrast to the given examples, not an increase but a decrease in c-di-AMP levels has been shown to promote biofilm formation in *S. aureus* [88]. The drop of c-di-AMP leads to reduced expression of the **a**ccessory **g**ene **r**egulator operon (*agr*). *Agr* negatively regulates biofilm formation amongst others by inhibiting the release of extracellular DNA (eDNA), which is important for biofilm formation in *S. aureus* [88, 89].

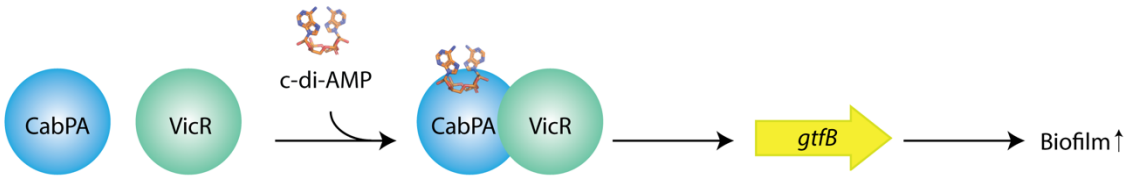

Figure 6. C-di-AMP dependent upregulation of Biofilm formation by CabPA. C-di-AMP binds to CabPA. CabPA-c-di-AMP interacts with VicR that is part of a two-component system that upregulates *gtfB* expression. GtfB is a major glucan producing enzyme important for biofilm formation [85].

2.2.2.3 Virulence and the Innate Immune System

Biofilm formation is an important virulence factor of pathogens as it grants protection against the hostile environment encountered in the host. Apart from its role in biofilm formation (chapter 2.2.2.2), c-di-AMP is further involved in virulence of many human pathogens, including *L. monocytogenes, S. pneumoniae*, *S. pyogenes, B. anthracis* and *M. tuberculosis* [42, 69, 90, 91]. In *S. pyogenes* expression of SpeB, a major virulence factor, depends on c-di-AMP. Strains with high or low levels of c-di-AMP by mutation of DacA or Pde2, a DhhP-type phosphodiesterase, show diminished virulence in a mouse model [90]. The deadly disease Anthrax is caused by the anthrax toxin secreted by *B. anthracis*. Strains with elevated c-di-AMP levels caused by *PgpH* and *GdpP* deletion express less toxins and S-layer components, which are further important for virulence. These strains were further substantially limited in their ability to infect mice [91]. Similar studies were conducted with *L. monocytogenes, M. tuberculosis* and *S. pneumoniae.* Deletion of the c-di-AMP degradation pathways lead to reduced virulence in mouse models that cannot solely account to the growth defects observed for these strains [42, 69]. This is partially due to the innate immune system that recognizes c-di-AMP secreted or released by intracellular pathogens as conserved pathogen-associated molecular pattern (PAMP). One receptor for c-di-AMP is the stimulator of interferon genes (STING). STING is an adaptor protein in the cGAS-STING pathway that binds the eukaryotic 2'-3'-cGAMP, produced by cGAS upon recognition of DNA in the cytoplasm, to then induce a type I interferon response. But STING can also bind c-di-AMP and elicit an immune response [92]. A strain of the intracellular pathogen *L. monocytogenes* with increased export of c-di-AMP due to the overexpression of the **m**ulti**d**rug **r**esistance (MDR) transporter causes an increased STING dependent immune response in mice, while deletion of all MDRs severely hampers a protective response [93]. Sensing CDNs directly is considered to be an early evolutional ability of STING and that it has since become central in the innate immune response to DNA [94]. The **e**ndoplasmic **r**eticulum **ad**aptor **p**rotein (ERAdP) is a more specialized sensor for c-di-AMP with much higher affinity and specificity than STING. Mice that lack ERAdP in myeloid cells are more vulnerable to *L. monocytogenes* and have reduced cytokine levels [95]. C-di-AMP is further sensed by the

oxidoreductase RECON (**re**ductase **co**ntrolling **N**F-kB). In hepatocytes binding of bacterial CDNs leads to inactivation of RECON and thereby to NF-kB activation independent of STING [96].

2.2.2.4 Sporulation and DNA integrity

Sporulation and DNA integrity were one of the earliest discoveries of c-di-AMP signaling. In absence of DNA damage, the c-di-AMP cyclase DisA is constitutively active. Upon recognition of damage in form of branched nucleic acids, cyclase activity subsides [34]. This is in accordance with the observation that DisA scans along the DNA and upon recognition of a holiday junction (HJ) c-di-AMP levels drop significantly [47, 63]. The control of DNA integrity has further been linked to sporulation as *B. subtilis* DisA arrests spore formation upon DNA damage in a c-di-AMP dependent manner by affecting gene expression of various sporulation genes [47, 97, 98]. The *Bacillus* genus utilizes a second diadenylate cyclase CdaS (see above). Deletion of cdaS delays germination in *B. subtilis* [65]. In *Streptomyces venezuelae* the resuscitation-promotion factor RpfA is under negative transcriptional control of c-di-AMP and is important in germination initiation [81].

2.2.2.5 Crosstalk between c-di-AMP and stringent response

C-di-AMP has repeatedly been described to interconnect with the ppGpp stringent response. The phosphodiesterase GdpP from *B. subtilis* and *S. aureus* is competitively inhibited by ppGpp with an IC_{50} of 234 µM and a Ki of 130 µM, respectively [41, 49]. Furthermore, PgpH from *L. monocytogenes* is inhibited by ppGpp, likely by an allosteric mechanism [42].

In return, in *S. aureus* under stress conditions high levels of c-di-AMP result in an increase in (p)ppGpp levels in an RSH dependent manner and in a similar transcriptional profile as observed for the stringent response [49]. In *L. monocytogenes* c-di-AMP is essential in rich media not due to dysregulation of potassium uptake but due to a toxic accumulation of (p)ppGpp and uptake of osmolyte active oligopeptides [99, 100]. The discovery of the involvement of CbpB (DarB in *B. subtilis*) led to valuable insights into the cross-talk of c-di-AMP and (p)ppGpp. In *L. monocytogenes* CbpB directly activates RelA and leads to (p)ppGpp accumulation independent of the ribosome or starvation (Figure 7). (p)ppGpp inhibits both c-di-AMP specific PDEs in *L. monocytogenes*, which increases the c-di-AMP levels. C-di-AMP binds to the CBS domain of CbpB and deactivates CbpB in respect to RelA activation. Therefore, CbpB closes a homeostatic regulatory circuit between c-di-AMP and (p)ppGpp. The molecular mechanism of the c-di-AMP dependent inhibition is not clear, yet [101]. The regulation of CbpB dependent activation of RelA by c-di-AMP has been confirmed in *B. subtilis* [102]. CbpB is absent from *S. aureus* and the exact mediator between c-di-AMP and ppGpp synthesis in this organism is a highly anticipated finding in the field.

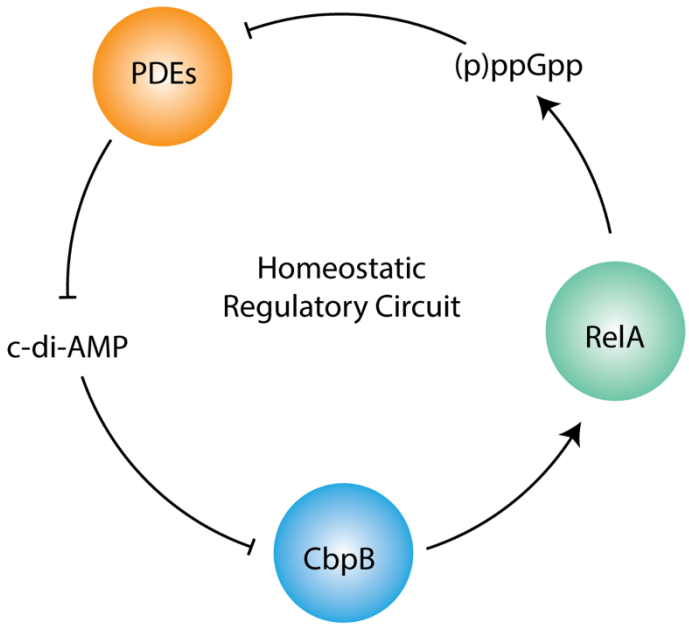

Figure 7. c-di-AMP and (p)ppGpp homeostasis in *L. monocytogenes*. CbpB activates RelA in a ribosome independent manner, leading to an increase in (p)ppGpp. In *L. monocytogenes* (p)ppGpp inhibits all c-di-AMP specific PDEs, which results in an increase in c-di-AMP. C-di-AMP binds to the CBS domain of CbpB and prevents CbpB from activating RelA, which will result in lower levels of (p)ppGpp. The PDEs are not inhibited anymore and c-di-AMP levels drop, closing the homeostatic regulatory circuit between c-di-AMP and (p)ppGpp [101].

2.2.2.6 Additional c-di-AMP controlled pathways

The pathways of c-di-AMP signaling are by far not comprehensively understood. While many observed phenotypes and findings could already be related to each other under general themes like osmoregulation or cell wall formation, other findings of c-di-AMP seem to be specific to certain organisms or environmental niches.

In *L. monocytogenes*, *Enterococcus faecalis* and *L. lactis* c-di-AMP allosterically inhibits the activity of the pyruvate carboxylase (PC), which catalyzes the formation of oxaloacetate from pyruvate [39, 103]. Depletion of c-di-AMP alters metabolic activity in *L. monocytogenes.* The citrate cycle in *L. monocytogenes* is truncated, as it lacks the α-ketoglutarate dehydrogenase, and PC is required for downstream metabolites like glutamate, which represents a possible link between c-di-AMP and glutamate homeostasis in *L. monocytogenes* [39]. In *L. lactis* the level of aspartate is primarily affected by PC activity in response to different c-di-AMP levels [103].

In *Mycobacterium smegmatis* the cyclic-**d**i-**A**MP **r**eceptor **r**egulator (DarR), a TetR-like transcription factor has been characterized. C-di-AMP binding to DarR increases the affinity of DarR to its target DNA sequence. DarR has been implicated in regulation of genes involved in fatty acid metabolism and cold shock response [104]. But further confirmation is needed and so far, no *in vivo* data is available on the direct regulation of c-di-AMP on these genes.

In the cyanobacterium *Synechococcus elongatus* c-di-AMP has a crucial role in night time survival as shown by an unbiased high-throughput genetic interaction screen. In absence of c-di-AMP *S. elongatus* encounters increased oxidative stress [36].

The P_{II}-like **s**ignal **t**ransduction protein **A** (PstA, also DarA) was one of the first c-di-AMP binding targets to be discovered in a screen conducted in *S. aureus* [35]. Yet, after nearly a decade later, no binding partners are known and its function within the cell remains obscure. For the first time a recent study identified a phenotype of a Δ*darA* mutant. A *B. subtilis* strain lacking c-di-AMP was only able to grow in presence of complex medium containing potassium and glutamate if darA was deleted and additional mutations in potassium uptake systems were acquired, indicating that DarA is involved in potassium regulation [105].

The list of c-di-AMP binding partners is increasing rapidly. New interaction partners will likely reveal new roles of c-di-AMP or help explain the interdependence of the already observed phenotypes due to common central roles of c-di-AMP. Studies on c-di-AMP in different organisms will be crucial to fully dissect the manifold pathways of c-di-AMP regulation.

2.2.2.7 Potassium and Osmolyte Homeostasis

As a consequence of possessing a semipermeable membrane, changes in the osmolarity of the environment pose an immediate threat to living cells. High osmolarity of the environment leads to water efflux and cell shrinkage while osmotic downshift can rapidly lead to swelling and rupture of the cell. Apart from the necessity of controlling the osmolarity to avoid cell death by rupture, bacterial cells use osmotic pressure to upkeep the cell turgor that is critical for growth and cell division [106]. Bacteria have developed intriguing and diverse mechanisms to adapt to different levels of salt. Seemingly straight forward is the “salt in” approach. Ions are taken up to the same or nearly the same level as the surroundings in order to achieve equilibrium. However, the resulting high ionic strength severely compromises protein stability, impairs protein-DNA interaction and translation. While halophilic bacteria specialize on a protein design that can cope with the elevated ionic strength, other bacteria only temporarily allow for ion uptake, especially potassium, as a first response and acute remedy to the threat. In a second step, compatible solutes are either newly synthesized or taken up from the environment. Compatible solutes comprise molecules like proline, betaine or carnitine that are highly soluble, lack a net charge, and do not directly interfere with cellular processes even at high concentrations. This way, compatible solutes allow for osmotic equilibration at lower cytoplasmic ionic strength. This two-step adaptation illustrates how closely potassium and osmolyte uptake are correlated [107].

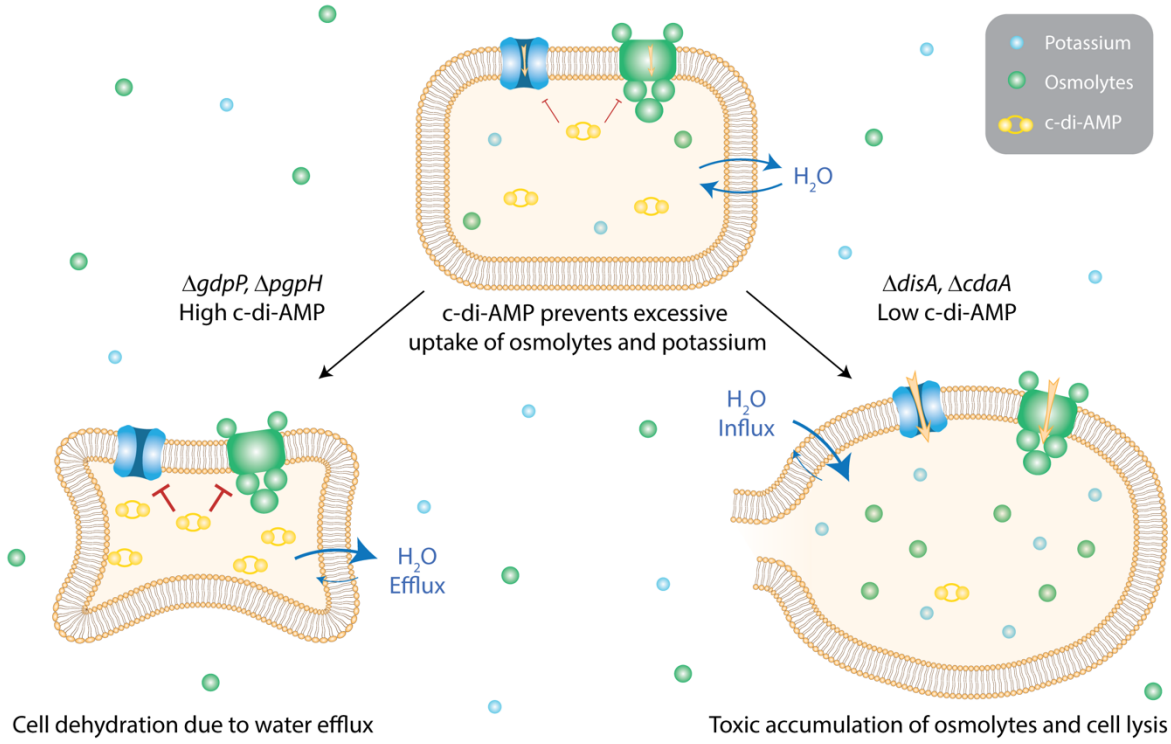

Figure 8. Osmoregulation and c-di-AMP phenotypes. In order to adapt to changing osmolarity the cell among others modulates osmolyte and potassium uptake and export via potassium (blue) and osmolyte transporters (green). C-di-AMP inhibits uptake of potassium and osmolytes on multiple levels. Low c-di-AMP strains caused by deletion of the cyclases or overexpression of the PDEs result in accumulation of osmolytes and potassium and lead to larger cells or cell lysis. High levels of c-di-AMP caused by deletion of the PDEs or overexpression of the cyclases lead to dehydration (Adapted from [82]).

In recent years, a central role in osmolyte regulation has been assigned to c-di-AMP. Recent studies support a central role of c-di-AMP in the homeostasis of osmolyte active potassium and glutamate in several organisms, including *S. aureus*, *L. monocytogenes*, *B. subtilis* and *S. agalactiae*. C-di-AMP binds to a wide variety of transporters, enzymes, transcription factors, signaling proteins and riboswitches to adequately regulate levels of potassium, glutamate and osmolytes, often in response to rapidly changing environmental conditions that would otherwise prove detrimental or fatal to the cell (Figure 8). C-di-AMP free strains of *B. subtilis* are only viable in absence of potassium or glutamate [61, 105]. *S. aureus* strains that are free of c-di-AMP can only grow at minimal concentrations of osmolytes and amino acids which can be turned into osmolytes [108].

Many organisms do not rely on just a single uptake system for potassium, but use a range of low and high affinity transporters to ensure uptake at different potassium levels (Figure 9). The transporters are structurally diverse, as well as their mode of regulation by c-di-AMP. Some are directly inactivated or activated by c-di-AMP binding, others are regulated on the transcriptional level either via a riboswitch or transcription factor. Furthermore, not all organism that use c-di-AMP for osmolyte

homeostasis have the same transporter under control of the signaling molecule. While the pathways and mechanisms differ significantly between distinct organisms, the general mode of c-di-AMP signaling seems conserved. Lack of c-di-AMP leads to excessive accumulation of potassium and osmolytes and subsequent osmotic lysis, whereas high levels of c-di-AMP inhibit uptake thereof resulting in dehydration [82]. While the pathways that lead to osmoregulation by c-di-AMP are being delineated at continuous speed, the mechanisms that primarily sense the osmotic state of the cell and feed into the c-di-AMP levels remain obscure. In *B. subtilis* and *L. lactis* c-di-AMP levels correlate with the intracellular potassium concentration. Knock-out experiments in *S. pneumoniae* show that c-di-AMP levels are modulated by the c-di-AMP effector protein (CabP) that regulates the potassium transporter TrkH [109]. But it remains unclear how c-di-AMP homeostasis is affected in detail.
In the following part of this chapter a selection of different potassium and osmolyte transporters that have experimentally been shown to be regulated by c-di-AMP will be described in more detail.

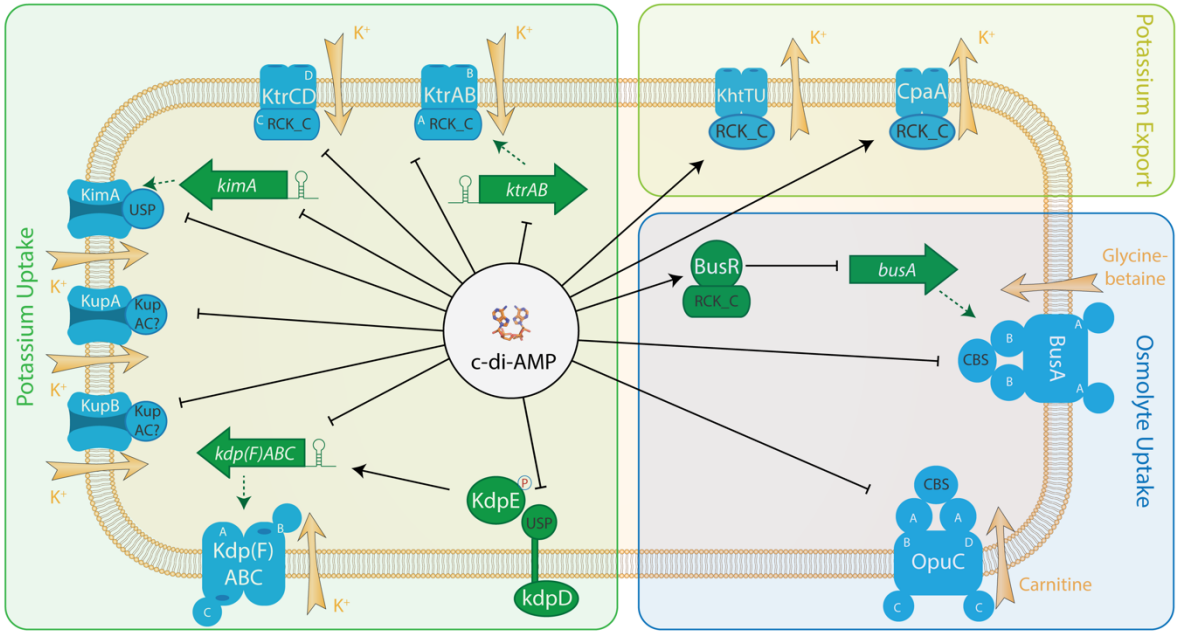

Figure 9. Components involved in c-di-AMP dependent osmolyte and potassium homeostasis. C-di-AMP negatively regulates potassium and osmolyte uptake on the transcriptional level (green), as well as the post-translational level (blue). Transcriptional control by a riboswitch is displayed as green hairpin loop. C-di-AMP binding domains are named in black. Proteins are depicted schematically to account for structural feature but are not drawn to scale.

KtrAB - KtrCD - TrkH

KtrAB belongs to the Trk/Ktr/HKT family of ion transporters and in *B. subtilis* it allows for growth down to micromolar potassium concentrations in the environment [61]. The availability of structural data makes KtrAB particularly well understood (Figure 10). KtrB forms a dimer embedded in the membrane. The pores are formed by four pairs of transmembrane helices by a single KtrB monomer. The pore is

further lined by a selectivity filter and a central intramembrane loop blocks excessive ion flow [110]. KtrA consists of an RCK_C and an RCK_N domain and forms an octamer in solution. In complex with KtrB it acts as a gating ring that modulates KtrB activity by accepting multiple small nucleotide input signals [110]. ADP induces a state of low basal activity while ATP upregulates ion flow [111]. The RCK_C domain binds c-di-AMP as was shown by differential radial capillary action of ligand assay (DRaCALA) and binding of c-di-AMP inhibits potassium uptake [35, 112]. For KtrCD, which is a paralogue of KtrAB, it has been shown that binding of c-di-AMP to KtrC stabilizes its octameric fold [113]. A study with CabP and TrkH, paralogues of KtrA and KtrB respectively, indicates that c-di-AMP disrupts the interaction between CabP and TrkH [114]. While the crystal structures of the c-di-AMP bound KtrA RCK_C are available, a full length KtrA structure in presence of c-di-AMP has not yet been reported [115].

KtrAB is also regulated on the transcriptional level in *B. subtilis* and *B. thuringiensis*. The riboswitch *ktrAB* (formerly *ydaO*) located in the 5' untranslated region of the corresponding gene senses c-di-AMP in the picomolar to lower nanomolar range. Binding of c-di-AMP triggers transcription termination and hence, reduced expression of KtrAB and potassium uptake [116].

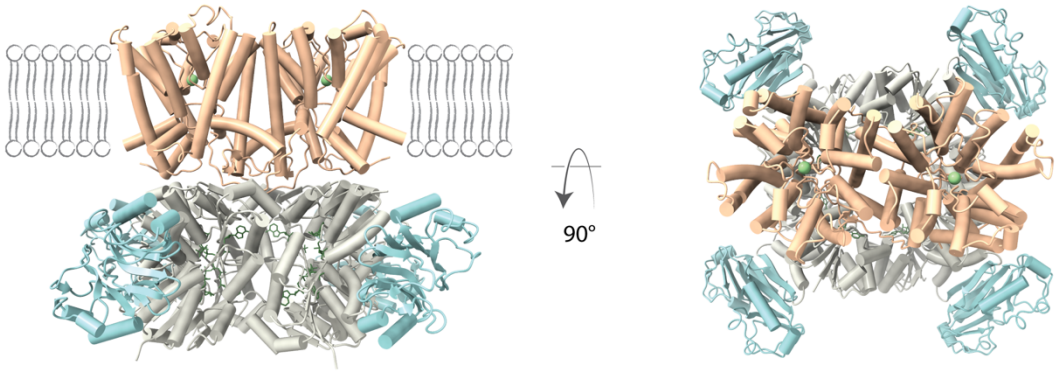

Figure 10. Crystal structure of ATP bound KtrAB (pdb id: 4J7C) in a modeled membrane part. The dimeric transmembrane component KtrB (beige) needs the octameric ring-shaped KtrA for full activity. KtrA regulates KtrB activity by binding ADP or ATP (green) at the RCK_N domain (grey), while binding of c-di-AMP to the RCK_C domain (cyan) inhibits transport of potassium (light green sphere).

KimA - KupA - KupB

The K^+ importer A (KimA) is a high affinity potassium importer that belongs to the K^+ uptake (KUP) family. KimA consist of an N-terminal transmembrane domain and a C-terminal cytoplasmic domain. An inward-occluded conformation of KimA has been solved by Cryo-EM (Figure 11). KimA forms a homodimer with a large cytoplasmic tunnel, tightly sealed from the outside by a gate. It is postulated that KimA transitions from an outward-open to an inward-open state, thereby transporting a potassium ion along a proton gradient [117].

Similar to KtrAB, c-di-AMP regulates KimA both on the protein as well as on the transcriptional level. The Expression of *B. subtilis* KimA is under the control of a c-di-AMP sensitive riboswitch *kimA* (formerly YdaO) [61]. Only at low potassium concentrations c-di-AMP levels are low enough to allow for KimA expression. KimA from *B. subtilis* or *L. monocytogenes* also binds c-di-AMP directly via its USP-like domain and is inhibited upon c-di-AMP as demonstrated by DRaCALA assay and by co-expression with CdaA in a heterologous system deprived of its native potassium importers [99, 118, 119]. KupA and KupB share considerable similarity with KimA except for the USP-like domain. In *L. lactis* KupA and KupB are the only potassium uptake system that have so far been linked to c-di-AMP signaling. Mutations in KupB led to restoration of osmolyte tolerance of high c-di-AMP *L. lactis* ΔgdpP strains [79]. KupA and KupB import activity is reduced at increasing c-di-AMP levels [120]. In absence of structural data, it is not known where exactly c-di-AMP binds to. It has been proposed that the C-terminal domain of KupA and KupB is another yet uncharacterized general c-di-AMP binding domain referred to as KupAC [119].

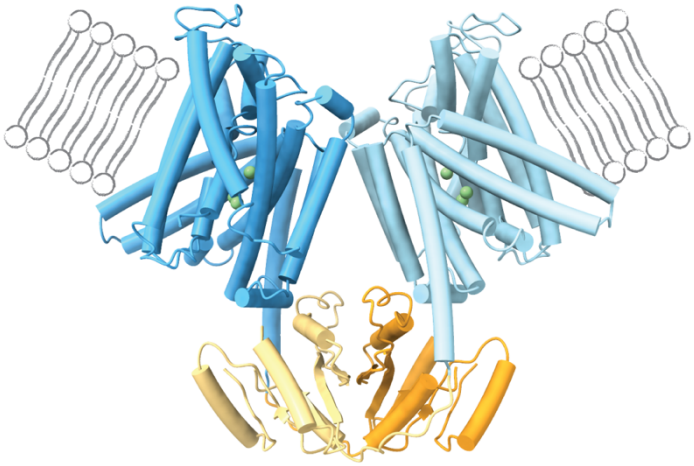

Figure 11. Cryo-EM structure of *B. subtilis* apo KimA (pdb id: 6S3K) with modeled membrane part. KimA forms a homodimer (light colors vs dark colors), with each protomer consisting of the N-terminal transmembrane part (blue) and a cytoplasmic C-terminal USP-like domain (orange), that is swapped in respect to the second protomer. [117].

KdpFABC

The potassium uptake system kdp is composed of the P-type ATPase high affinity potassium transporter KdpFABC and the regulatory two-component system KdpDE. In firmicutes the Kdp system has evolved to be regulated by c-di-AMP on several levels. As was shown for other high affinity potassium transporters, transcription of *kdpFABC* is under the control of a c-di-AMP sensitive riboswitch in *B. thuringiensis* [121]. In *S. aureus* and *C. difficile* c-di-AMP binds to the USP domain of KdpD [112, 122]. KdpD is a histidine kinase that autophosphorylates upon appropriate stimulus but is inhibited by c-di-AMP. The phosphate is transferred to the response regulator KdpE, which binds to the *kdpFABC* operon and activates transcription [68, 122]. Both pathways translate elevated c-di-AMP levels into repression of potassium uptake.

CpaA

CpaA was first discovered in an *S. aureus* wide screen for c-di-AMP binding proteins. It has an N-terminal transmembrane domain to which cytosolic RCK_N and RCK_C domains are linked. Binding of c-di-AMP was confirmed for the RCK_C domain, for which a crystal structure has been solved as well [35, 123]. CpaA is a cation / proton antiporter that exports sodium and potassium and is stimulated by c-di-AMP [123]. These results were confirmed for a homolog from *B. subtilis* [118]. Besides its engagement in potassium uptake this expands c-di-AMP signaling further to include potassium export as well.

khtTU

Similar to CpaA khtTU is a K^+/H^+ antiporter. It consists of KhtU, the transmembrane domain, and KhtT a cytoplasmic protein with a c-di-AMP binding RCK_C domain [118]. The complex of KhtTU is inactive and cannot export potassium ions [124]. Upon binding of c-di-AMP to the RCK_C domain the transport activity increases, likely by weakening the interaction of KhtT and KhtU [125].

OpuC

The osmoprotectant uptake system C (OpuC) belongs to the Opu family of compatible solute ABC transporters. In comparison to other members of the family, OpuC accepts a broader spectrum of substrates and has high affinity for carnitine. It consists of four subcomponents. OpuCB and OpuCD form the transmembrane channel while OpuCC is an extracellular domain for substrate binding. OpuCA is an intracellular ABC protein that couples substrate translocation to ATP hydrolysis. It further contains a cystathionine beta synthase (CBS) domain. For *B. subtilis*, *S. aureus*, *Enterococcus faecalis* and *L.* monocytogenes the CBS domain of OpuCA has been shown to bind c-di-AMP. Binding of c-di-AMP to the CBS domain inhibits osmolyte uptake [118, 126, 127].

2.2.3 BusA & BusR

The **b**etaine **u**ptake **s**ystem A (BusA, also OpuA) is a type I ABC importer for glycine-betaine [128]. The *busA* operon is composed of two genes that code for BusAA and BusAB. BusAA (OpuAA) is an ABC protein that drives osmolyte uptake in an ATP dependent fashion. Apart from the nucleotide-binding domain (NBD) responsible for ATP binding, it further consists of two CBS domains that bind c-di-AMP in *L. lactis* BusA. Two molecules of ATP are needed per transport cycle [129]. In BusAB the transmembrane protein and the extracellular substrate binding domain (SBD) are covalently coupled. This assembly is found in *Clostridiaceae*, *Listeriaceae*, *Streptococcaceae* and *Staphylococceae* [130]. More commonly, including organisms like *B. subtilis* the operon architecture includes three genes and *busAB* is split into *opuAB* and *opuAC* that are translated into the membrane protein and substrate binding domain, respectively [131]. BusA activity is stimulated by an increase in the cytoplasmic ionic

strength and elevated fractions of anionic lipids in the membrane [132]. Mg^{2+} ions are 4-5-fold as effective in stimulating transport activity of BusA compared to monovalent ions [133]. A structure of BusA embedded in nanodiscs has been solved by cryo-EM [134]. BusA forms a dimer of dimers with two entities of BusAA and of BusAB. The transmembrane domain is embraced by structurally important scaffold-like helixes (Figure 12). In the resting state, the transmembrane domain opens to the cytoplasmic side. In the substrate-SBD complex and ATP bound state but before hydrolysis has occurred, the NBDs are dimerized and the transmembrane helices face outward. In this occluded state, the affinity of the SBD for glycine-betaine is reduced upon docking to the transporter, and the substrate is released into a hydrophobic cavity within the transmembrane domain without translocating to the cytoplasm [134]. Hydrolysis of ATP by the NBD returns the membrane helices to the inward-facing conformation and releases the SBD for a second cycle [128, 134].

The ionic strength is sensed by a positively charged helix-turn-helix motif within BusAA that interacts with the negatively charged lipid head groups and inhibits transport. Binding of c-di-AMP abolishes transport independent of the ionic strength [134]. In presence of c-di-AMP, the CBS domains dimerizes which in turn prevents the NBDs from dimerizing. This results in an inward-facing transporter even in presence of an outside docked SBD and hence does not allow for translocation of the substrate. It is thought that BusA is stimulated by high ionic strength as a primary signal of hypertonicity and that c-di-AMP acts as “off switch” to prevent excessive uptake of osmolytes [134]. Considering that binding or direct regulation of BusA by c-di-AMP has not been confirmed for *B. subtilis* BusA even though it contains a CBS domain, and suppressor screens with high c-di-AMP strains have not yet been reported to result in BusA mutants, it remains to be investigated how conserved the regulation of BusA by c-di-AMP is. A suppressor screen in *B. subtilis* with a c-di-AMP free strain resulted in a point mutation in OpuA close to its gating region that could potentially affect its activity [135].

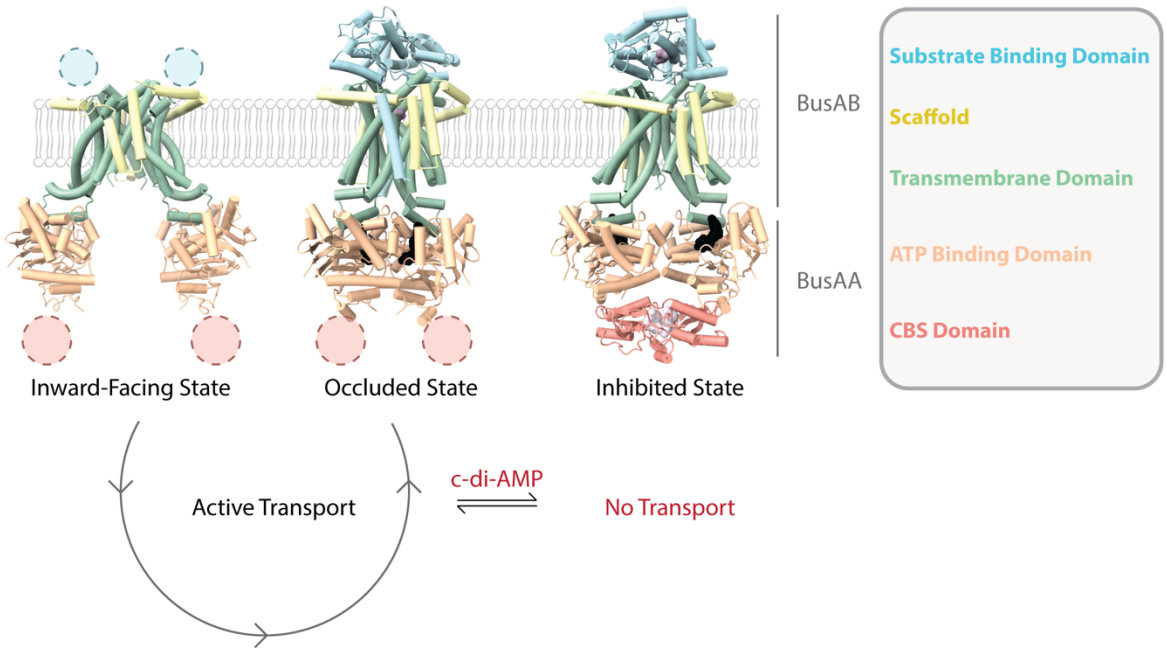

Figure 12. Cryo-EM structures of BusA from *L. lactis* in different transport cycle states with modeled membrane parts. (middle) In the occluded state the substrate binding domains (blue) are docked to the transmembrane domain (green). ATP (grey) bound to the ATP binding domain (orange) of BusAA is not hydrolyzed because of a Q190A Walker B mutation. The CBS domain responsible for c-di-AMP binding is not resolved (dashed circle) (pdb id: 7AHD). (left) Hydrolysis of ATP converts the transporter into the inward-facing state, which releases the substrate into the cytoplasm (pdb id: 7AHC). (right) Binding of c-di-AMP (purple) to the CBS domain arrests BusA in an inhibited state and thereby prevents further substrate translocation (pdb id: 7AHH).

Apart from its regulation by c-di-AMP on the protein level, *busA* is further regulated on the transcriptional level via its c-di-AMP sensitive transcriptional repressor BusR, which is the focus of this work. It is the first c-di-AMP dependent transcription factor involved in osmolyte homeostasis described to date. *BusR* is mostly found in *Streptococcus, Enterococcus, Lactococcus* and *Clostridium.* Not all organisms that have a copy of *busA* also contain *busR.* In *Bacillus infantis, opuA* is under the control of the MarR family transcriptional repressor OpuAR [136]. BusR is assigned to the GntR family of transcription factors due to its N-terminal winged helix-turn-helix (wHTH) domain. A predicted coiled-coil region separates the DNA binding domain from the C-terminal RCK_C domain (Figure 13). BusR was originally found in a thorough genetic screen with a strain of *E. coli* that carried the *busA* promotor ($busA_p$) coupled to the lacZ gene tested against different genomic fragments from *L. lactis*. In *L. lactis* the gene *busR* is located immediately upstream of *busA*. BusR binds to the -35 to -10 region of $busA_p$ and represses transcription of the entire operon [137]. Even in presence of BusR, the RNA polymerase can bind to $busA_p$ in a transcription deficient ternary complex. High ionic strength releases BusR from the ternary complex [138] (Figure 13C). *L. lactis busA* promotor activity is moderately enhanced upon ionic strength up to a 2-fold level in a BusR dependent manner [79].

BusR specifically binds c-di-AMP [48, 79] (Figure 13A). Expression of BusA and subsequently glycine-betaine levels are modulated by BusR and c-di-AMP [48, 79]. In a high c-di-AMP strain of *L. lactis* glycine-betaine levels were 10-fold reduced in a BusR dependent manner compared to the wildtype [79]. Very similar to *L.* lactis, also in *Streptococcus agalactiae* repression of *busA* was shown to be under the control of BusR in a c-di-AMP dependent manner, even though *busA* and *busR* are separated by 655 kb within the genome. The BusR-BusA pathway is responsible for the conditional essentiality of c-di-AMP in presence of osmolytes in *S. agalactiae*. In *S. agalactiae* two binding sites of BusR have been identified in the promotor region of *busA* [48] (Figure 13B). An ortholog of BusR (OpuR) has been described in *C. difficile* that binds c-di-AMP and represses the transcription of *opuCA*. Deletion of *OpuR* is more resistant to hyperosmotic stress but also to bile salts [112].

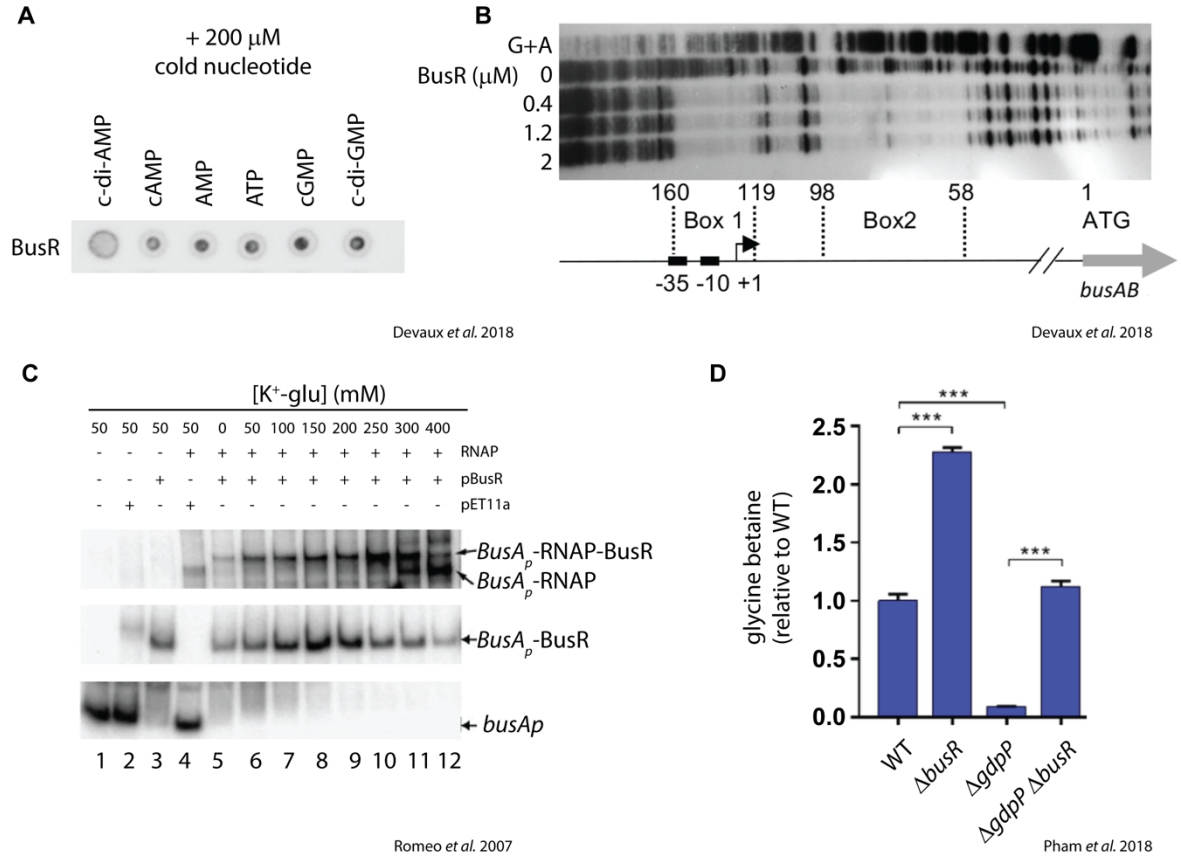

Figure 13. The c-di-AMP sensitive transcriptional repressor BusR. (A) competition DRaCALA with BusR bound to radioactive c-di-AMP against similar cold nucleotides. Binding of c-di-AMP to BusR is specific as it can only be displaced by cold c-di-AMP [79]. (B) DNA-Footprint experiment. *S. agalactiae* BusR binds to two large sites in the promotor region of *busA* [48]. (C) BusR binds $BusA_p$ simultaneously with RNAP. Ionic strength releases BusR from the ternary complex [138]. (D) Intracellular glycine-betaine levels are reduced in a BusR and c-di-AMP dependent manner in *L. lactis* [79].

At the start of this work, the pathway of BusR regulation was already understood to a great extent. However, little was known of the mechanism of c-di-AMP induced transcriptional repression on a

molecular level. While crystal structures of both, the wHTH and RCK_C from paralogous proteins with close similarity were available, no structure of the overall assembly, not to mention the different states of ligand induced repression, had been solved. In this work BusR has been biochemically and structurally characterized in detail, which makes BusR the currently best understood c-di-AMP controlled transcription factor.

2.2.4 The c-di-AMP binding domains

Although the discovery of c-di-AMP dates back only 13 years, the list of interacting proteins and available structures thereof has reached a considerable number. This allows for a dissection of different binding modes that c-di-AMP assumes in contact with different proteins and sometimes even the same protein. Both c-di-AMP and c-di-AMP binding proteins display a striking versatility in possible interaction formats. In the following chapter distinct conformations and binding modes of c-di-AMP shall be highlighted from a structural perspective on the basis of common c-di-AMP binding domains and unique binding partners. This list confines itself to signaling proteins and omits cyclases and phosphodiesterase, which shall not implicate that they are any less of interest from a structural perspective.

2.2.4.1 RCK_C

The C-terminal regulator of K^+ conductance domain (also TrkA_C) is found both in prokaryotes as well as eukaryotes. Its name derives from the fact that the domain often serves as regulatory domain for potassium transporters, and channels (KtrA, KtrC, CpaA, KhtT) but it is also found in BusR (RCK_C pfam accession nr.: PF02080) [35, 48, 79, 118]. High resolution crystal structures of the domain are available of apo and unbound states from different organisms and proteins [110, 115, 123, 125, 139]. The RCK_C domain consists of four to five anti-parallel beta sheets with up to two alpha-helices on top. RCK_C domains in complex with c-di-AMP are always dimers while the apo protein can be monomeric [115, 123]. C-di-AMP binds in a cleft in the dimer interface. The residues involved in c-di-AMP coordination vary significantly, but in all known structures c-di-AMP always adopts a highly similar U-type conformation (Figure 14). For instance, the RMSD of c-di-AMP in *S. aureus* RCK_C domain of KtrA (RCK_C_{KtrA}, pdb id: 4XTT) compared to RCK_C_{CpaA} (pdb id: 5F29) is only 0.4 Å. The U-type conformation of c-di-AMP is the so far most often observed conformation and can also be found in DisA or the eukaryotic adaptor protein STING [34, 140]. The molecular mechanism by which c-di-AMP binding elicits attenuated protein activity has not been entirely resolved. For *S. aureus* KtrA RCK_C it has been shown that binding of c-di-AMP leads to contraction and stabilization of the dimer which likely leads to allosteric inhibition of KtrAB [115].

In RCK_C_{CpaA}, Phe, Leu and Ile residues form a hydrophobic pocket that can very well accommodate c-di-AMP. Coordination of the adenine bases (ade1 and ade2) involves hydrogen bonds to the main chain and an CH-π interaction with the neighboring leu160. The phosphate groups are each coordinated by hydrogen bonds to arg161 and the main chain. A water molecule is collectively coordinated by his184, the phosphate group and N7 of ade1 and positioned above ade2 for lone pair-π interaction with the delocalized electrons of the adenine base. The RCK_C_{CpaA} has a K_D of 9 µM for c-di-AMP. The binding pocket is perfectly C2 symmetrical [123] (pdb id: 5F29).

The RCK_C of KtrA (RCK_C_{KtrA}) follows the same principles, while the overall domain and the single amino acids involved in coordination vary significantly. The hydrophobic pocket is lined by several isoleucine residues and a proline and is more enclosed than in RCK_C_{CpaA}. The 2'-hydroxy group of the ribose forms hydrogen bonds to the main chain and an aspartate sidechain. Only one phosphate group is coordinated by arg169, while arg169 from the second protomer stacks between the adenine bases and forms a cation-π interaction with the bases. In addition, the arginine coordinates a single water molecule that forms lone pair-π interactions with one of the adenine bases. The adenine bases are further coordinated by hydrogen bonds to the main chain but also by a CH-π interaction to ile162. Compared to RCK_C_{CpaA} the affinity of RCK_C_{KtrA} is more than two orders of magnitude higher with a K_D of 43 nM [115].

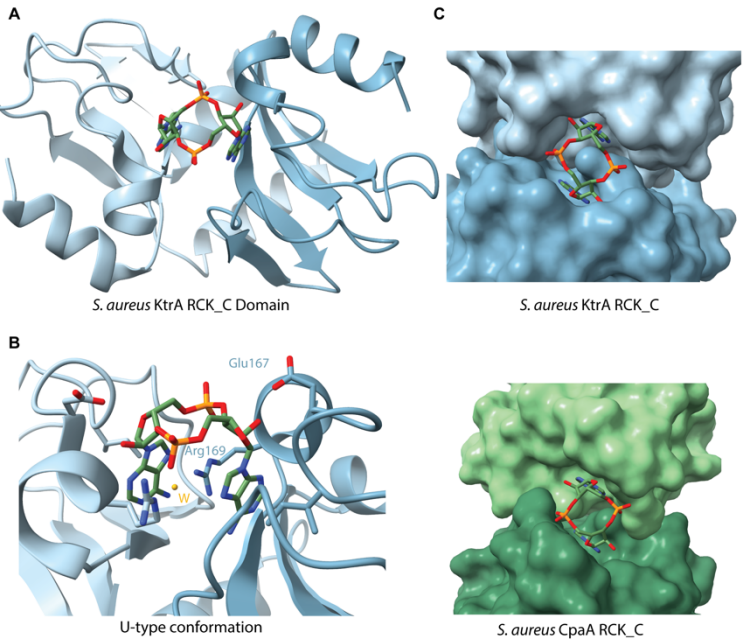

Figure 14. Crystal structure of the dimeric RCK_C domain. (A) *S. aureus* KtrA RCK_C domain in complex with c-di-AMP. C-di-AMP binds canonically in the dimer interface of the RCK_C domain. (B) close up on the coordination of c-di-AMP. Arg169 coordinates a water (W, yellow) that contributes a lone pair-π interactions with one of the adenine bases. (C) Surface representation of *S. aureus* KtrA RCK_C and *S. aureus* CpaA RCK_C.

2.2.4.2 CBS

The cystathionine beta synthase domain is common to all kingdoms of life and acts as a regulatory switch to modulate protein activity of a wide variety of proteins. The secondary structure of the CBS motif follows the secondary structure scheme β1-α1- β2- β3-α2. Two of these CBS domains that are often covalently linked, dimerize to form a Bateman module [141]. These Bateman modules can further dimerize to form a disklike assembly, also referred to as CBS module [142]. The CBS module is a sensor of adenine moieties, including AMP, ADP, ATP, NAD, 5'-deoxy-5'-methylthioadenosine and more recently c-di-AMP [126, 127, 141].

The CBS domain has first been described to bind c-di-AMP by the Woodward and Gründling groups in 2016. Both groups simultaneously investigated the CBS domain of OpuC from *L. Monocytogenes* and *S. aureus*, respectively. To date, a total of four structures of a CBS in complex with c-di-AMP have been deposited in the protein data bank, the CBS of *L. monocytogenes* and *B. subtilis* CbpB, *L. monocytogenes* OpuCA and *L. lactis* OpuAA [101, 126, 134]. All four structures form disklike CBS modules. Intriguingly, c-di-AMP displays uncommon conformational flexibility (Figure 15). In the structure of CBS module of *L. monocytogenes* OpuCA (CBS_{OpuCA}), c-di-AMP adopts a O-type conformation that can also be found in the structure of the pyruvate carboxylase PycA from *l. monocytogenes* [39]. In *l. lactis* CBS_{OpuAA} c-di-AMP adopts a V-type conformation, with both adenine bases facing the same direction [134]. in *L. monocytogenes* CbpB two copies of c-di-AMP are bound upside-down in the U-type conformation on either side of the disk [101]. The c-di-AMP moieties are in a slightly tilted, upside-down position with the phosphate groups and one adenine base (ade1) buried in the pocket and the other adenine base (ade2) reaching away. This is in contrast to the RCK_C domain. Of particular prominence is a stacking interaction with a tyrosine and a highly asymmetric binding mode in presence of a highly symmetric conformation by c-di-AMP. Tyr45 is positioned in between the bases in perfect geometry for parallel displaced π-π stacking with ade1. Only ade1, but not Ade2, is specifically coordinated by multiple hydrogen bonds with the main chain and a CH-π interaction of Ile128. The asymmetric binding of the adenine bases is continued for the binding of the phosphate and the ribose. The ribose of ade2 forms a hydrogen bond to Arg131 while the 5' connected phosphate group is coordinated by ser46. The ribose of ade1 is flanked by the aromatic ring of phe115 and forms a hydrogen bond to the main chain while its phosphate group lies in a positive patch and its 3'-phosphoester bond is coordinated by a strong hydrogen bond to Arg131 [101].

Opposed to *L. monocytogenes* CBS_{CbpB}, the coordination of c-di-AMP in CBS_{OpuCA} is perfectly symmetrical. The binding pocket for c-di-AMP is large and elongated due to the stretched-out O-type conformation of c-di-AMP. It reaches from the interface of one Bateman module to the interface of the second Bateman module. The adenine base is again coordinated by Tyr342 but the geometry does

not allow for ideal π-π stacking. On the other side of the base a CH-π interaction is formed to Val280 that is essential for c-di-AMP binding. Unique to this structure is the coordination of the phosphates. A hydrogen bond is formed to the main chain peptide bond that is at the N-terminal end of an α-helix. It is likely that the phosphate is further coordinated by the dipole of the α-helix [126].

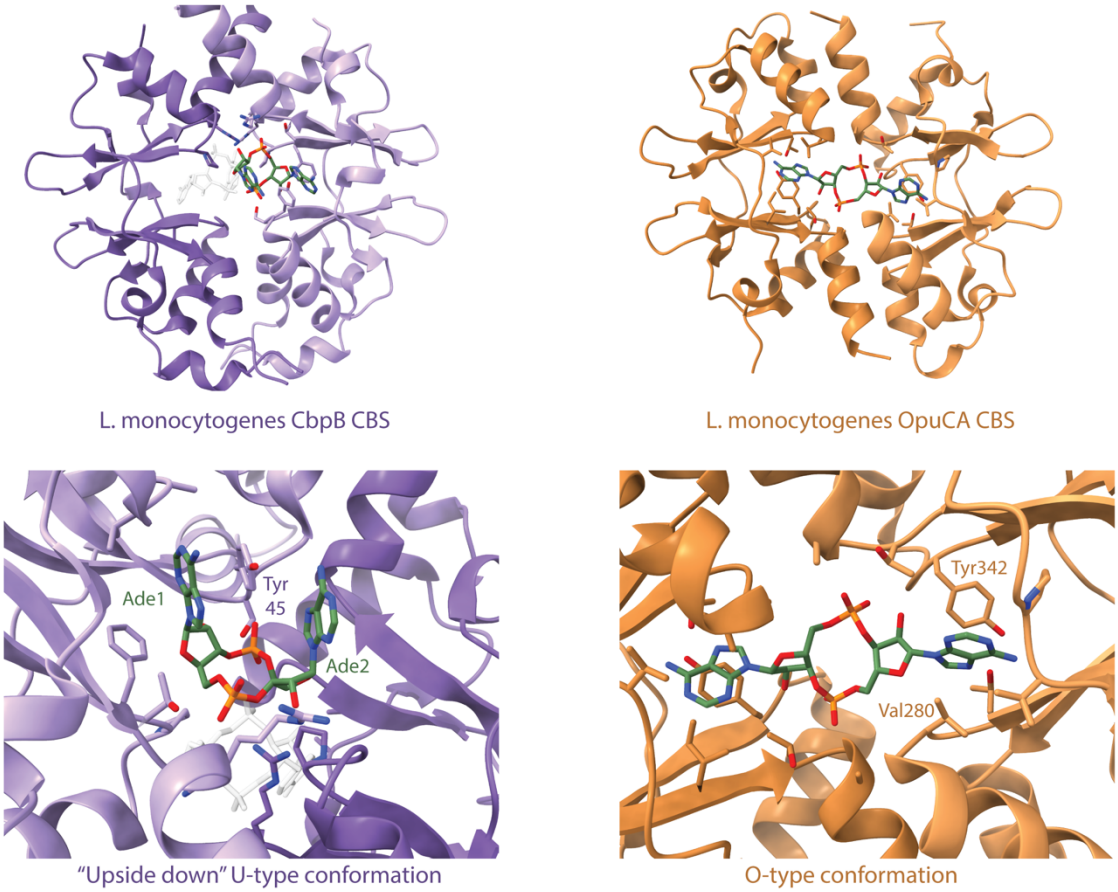

Figure 15. Crystal structures of c-di-AMP bound CBS domains. The coordination of c-di-AMP by CbpB CBS from *L. monocytogenes* (pdb id: 6XNV) is strikingly different from OpuCA from *L. monocytogenes* (pdb id: 5KS7).

2.2.4.3 USP

The family of the universal stress protein (USP) is widespread among bacteria, archaea and eukaryotes and expression of many members is enhanced upon stress. Many USPs have been shown to bind adenine moieties like ATP, ADP, AMP, cAMP or c-di-AMP [122, 143, 144]. C-di-AMP binding USP-like domains have been discovered in *S. aureus* KdpD, which is part of the two-component system KdpDE, and in *B. subtilis* KimA, a high affinity potassium transporter [118, 122]. Structures have been solved for both USP-like domains, however, only for *S. aureus* KdpD a structure with bound c-di-AMP is available [117, 145] (for KimA see chapter 2.2.2.7) (Figure 16). In *S. aureus* KdpD a single monomeric USP domain coordinates c-di-AMP in contrast to the dimeric CBS and RCK_C domains. The adenine

base that is deeper buried within the protein domain resides in a hydrophobic pocket made up of Val, Ile, Leu and Tyr residues. Hydrogen bonds are only formed to the main chain. The outer adenine base is sandwiched by Tyr281 and the β1-α1 loop [145]. It is not clear how c-di-AMP binding to the USP domain affects the activity of either KdpD or KimA. It is interesting that a comparable residue to Tyr281 is missing in the USP domain of KimA, but could be contributed by the membrane domain by Arg337 instead, in a similar fashion as observed for PstA (see below).

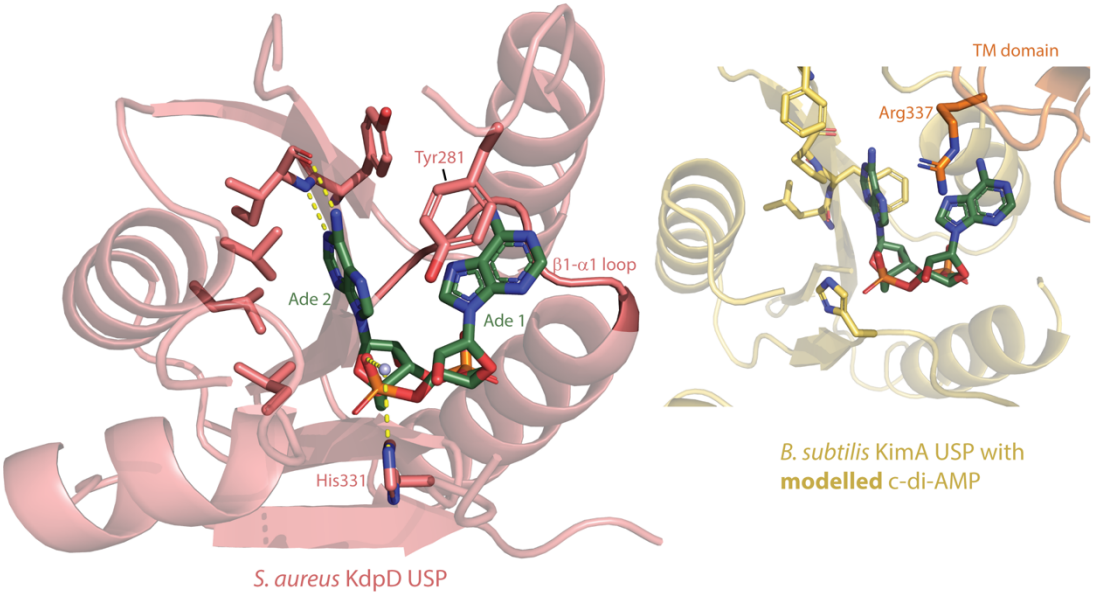

Figure 16. USP domain. (left) Crystal structure of *S. aureus* KdpD USP domain with c-di-AMP bound (pdb id: 7JI4). (right) Cryo-EM structure of the putative c-di-AMP pocket of *B. subtilis* KimA with modelled c-di-AMP according to KdpD (pdb id: 6S3K). The USP domain is colored in yellow while the transmembrane (TM) domain is colored in orange.

2.2.4.4 YdaO Riboswitch

In c-di-AMP signaling, riboswitches play a strikingly more significant role in control of gene expression than transcription factors do according to the number of currently known targets. The *ydaO* riboswitch is widespread in bacteria and can be found in the firmicutes *Bacillus* and *Clostridium* but also in the actinobacteria *S. coelicolor* or *M. tuberculosis* [146]. *YdaO* and *ydaO*-like riboswitches reside in the 5' untranslated region of the mRNA and have been characterized as c-di-AMP responsive modules in the operons of *B. subtilis ktrAB* and *kimA*, of *B. thuringiensis kdpFABC* and *S. coelicolor rpfA* [61, 81, 116, 121]. *YdaO* binds c-di-AMP with pico- to nanomolar affinity and high specificity which then leads to transcriptional repression of the controlled gene [81, 116]. Crystal structures of the *YdaO* riboswitch are available from *B. subtilis*, *Thermoanaerobacter tengcongenesis, Thermoanaerobacter pseudethanolicus* and *Thermovirga lienii* and share high similarity [147-149]. The riboswitch forms a pseudo symmetrical fold with its second half folding back on the first in a head-to-tail arrangement.

Two three-helix junctions each form an equivalent binding site for a c-di-AMP molecule. In the *B. subtilis* YdaO riboswitch, c-di-AMP adopts a V-type confirmation very similar to what has been observed for when bound to OpuAA CBS. In contrast, the adenine bases face opposing directions forming a symmetrical conformation not present in OpuAA. Both c-di-AMP molecules are intensively coordinated on the Hoogsteen edge, the Watson & Crick edge as well as the ribose edge. Each adenine base further forms π- π stacking interactions with unpaired adenosines. The 2'OH groups of both riboses as well as the phosphate groups are coordinated by hydrogen bonds. Upon binding of c-di-AMP the riboswitch adopts a more compact form, according to SAXS experiments [148]. The thorough coordination results in the high affinity and specificity unmatched by other known c-di-AMP binders.

2.2.4.5 PstA

PstA was intensively studied from a structural point of view, with crystal structures available from *L. monocytogenes, S. aureus* and *B. subtilis* [150-153]. PstA forms a homotrimer with three c-di-AMP binding sites in each monomer-monomer interface (Figure 17). The binding site is structurally distinct from RKC_C and CBS domains but the coordination of c-di-AMP shares similarity to the USP domain. In PstA from *S. aureus* c-di-AMP adopts an asymmetrical V-type conformation with both adenine bases buried in narrow but distinct pockets. The wide gap of the V-type conformation allows for a peptide chain to run through. Unique for PstA is that Arg26 from this chain and a Phe36 from the neighboring protomer sandwich Ade1 in a tight embrace, forming cation-π and parallel displaced π-π interactions, respectively. This leads to stabilization of the T-loop, a common loop in P_{II}-like proteins, that phe36 is part of. In PstA the T-loop and B-loop are inverted in length compared to canonical P_{II} proteins. Ade2 is coordinated differently via a T-shape π-π interaction by Phe99 and multiple hydrogen bonds to the main chain that give specificity for c-di-AMP. It is speculated that binding of c-di-AMP leads to a rearrangement of the B-loop, a region of low complexity that has not been dissolved in any crystal structure. This could then interfere with complex formation with an until now unknown binding partner [153].

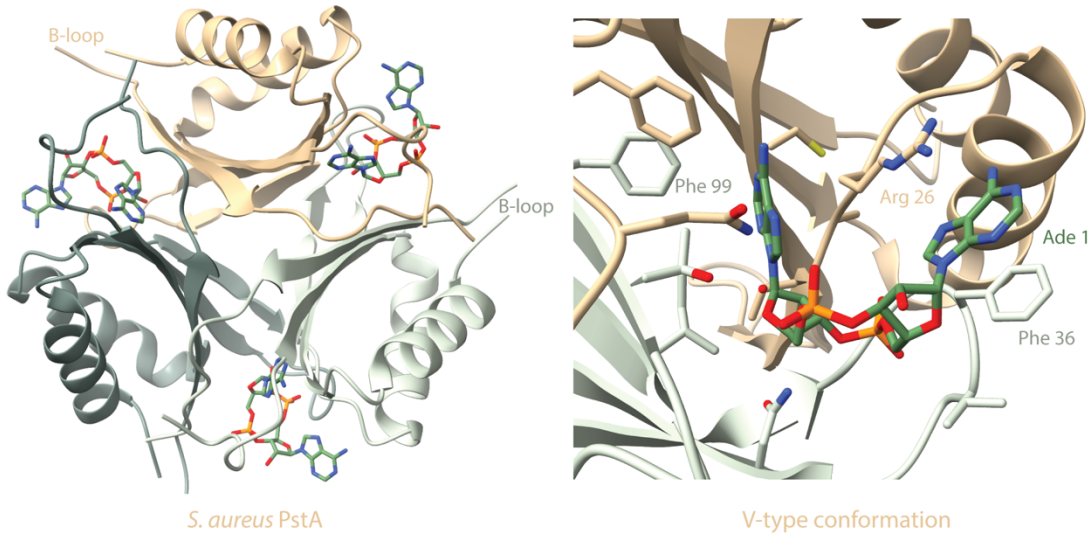

Figure 17. Crystal structure of PstA from *S. aureus* (pdb id: 4WK1). Three molecules of c-di-AMP are coordinated each in a monomer-monomer interface of PstA in a unique binding mode.

2.3 Transcription factors

Transcription of genes and subsequent translation to proteins is an expensive undertaking of a cell in terms of energy and resources. In order to stay competitive, cells have to adequately adjust gene expression to the current needs. Transcription factors arguably assume a pivotal role in regulation of gene transcription. They act DNA specific and can both up- and downregulate transcription as activators or repressors, respectively. Typically, activators bind upstream of the -35 region while repressors bind in between the -35 and -10 region or downstream. In prokaryotes, most transcription factors contain an additional ligand binding domain and are regulated by small molecules like metabolites, second messengers or toxins [154]. These molecules can activate the transcription factor (increase affinity for DNA), as in case for cAMP and CRP, or deactivate it, as can be observed for the lac repressor and allolactose [155, 156]. Other transcription factors are part of a two-component system and are activated by a histidine kinase. Transcription factors can act both locally, regulating a single gene, or globally, reshaping large parts of the cellular gene expression profile, as known from CRP. A single gene can further be under control of a single transcription factor or integrate multiple signaling pathways [154].

Transcriptional activators utilize diverse mechanisms for activation and will only briefly be introduced. Activation is a complex process, but often revolves around the recruitment of the RNAP to the promotor. For example, CRP can activate transcription by interacting upstream with the C-terminal domain of the α-subunit of the RNAP to promote RNAP binding to the promotor [157]. Activation can further occur indirectly by reshaping the promotor site so it can be recognized by the RNAP, as has been shown for BmrR and which will be introduced in greater detail [158] (see below). However,

activation mechanism can become increasingly complex with an increasing number of involved components. For example, activation can occur indirectly by activating a second activator or releasing the RNAP of repression by a repressor [159].

Transcriptional repression by a transcription factor can vary in its mechanism (Figure 18). A repressor can turn off gene expression by steric hindrance, preventing the RNA polymerase from binding to the promoter sequence or from transitioning into elongation. Binding of the RNAP can further be prevented by distortion of the promoter or looping of the DNA. In a different approach, repressors can bind upstream of the -35 region, as is rather typical for activators, and interact with the α-subunit of the polymerase to lock it in place. Furthermore, repressors can compete with activators for their binding site, depriving the polymerase of its activation [159]. In the following chapter, several transcription factors, both activators and repressors, will be highlighted that are related to BusR for different reasons, either sequence homology, functional or structural similarity and will also be discussed (4.1.3).

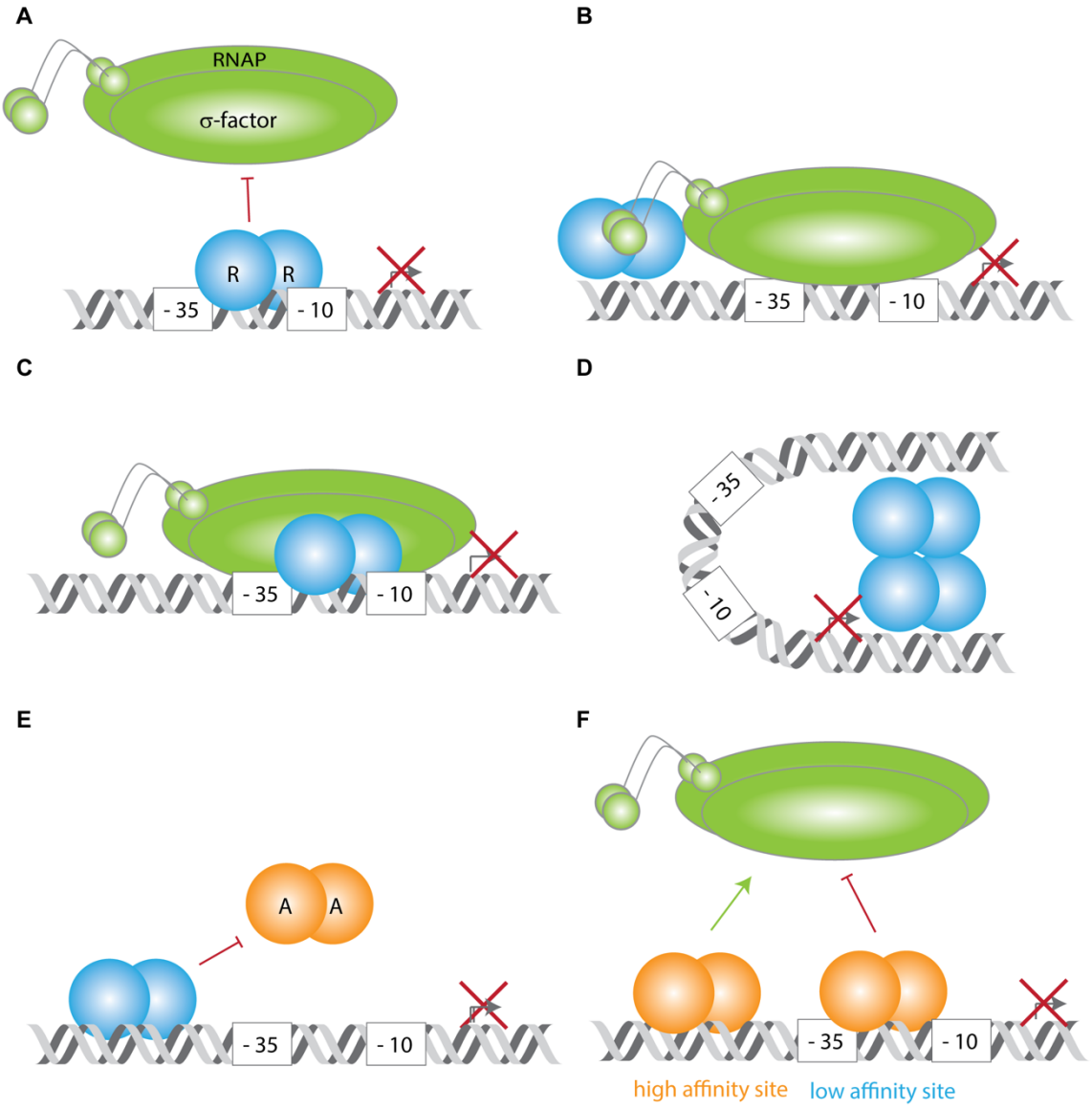

Figure 18. Graphical Overview of different mechanisms by transcriptional repressors. The RNA polymerase (green) is simplified depicted with the β and β' subunit as large oval sphere, the sigma factor as slightly smaller oval sphere and the α subunits drawn as small dumbbells. (A) The repressor (blue, R) binds in between the -10 and -35 region and sterically hinders RNAP (green) from binding to the promoter. (B) The repressor binds upstream and interacts with the α subunits of RNAP and prevents transcription initiation. (C) The repressor binds in between the -10 and -35 region and prevents transcription initiation. (D) The repressor introduces DNA looping that makes the promotor inaccessible for RNAP. (E) The repressor binds upstream and sterically hinders an activator (orange, A) from binding. (F) An activator turns into a repressor at high concentration by binding to a second low affinity site where it sterically hinders RNAP from binding (Adapted from [159]).

2.3.1 The GntR family

The focus of this work, the transcription factor BusR, belongs to the large and diverse GntR family of prokaryotic transcription factors. The family was first described by Haydon and Guest in 1991 and has since been recognized to be one of the most abundant family of transcription factors [160]. The family shares a common N-terminal winged-helix-turn-helix (wHTH) motif that shares high similarity secondary structure [161]. This domain is paired with diverse C-terminal effector binding domains, upon which the family is subdivided into subfamilies [162]. Prominent subfamilies include FadR, HutC, MocR, YtrA, AraR, PlmA and DevA [163-169]. According to Pfam database the GntR family comprises approx. 90,000 members of 154 different domain combinations and is distributed most prominently among actinobacteria, firmicutes and proteobacteria (Pfam accession number: PF00392) [170]. GntR family transcription factors can act both as repressors or as activators and regulate a large spectrum of biological processes as their diverse effector domain allows for integration of very different stimuli. Furthermore, despite the simplicity of the wHTH motif the quaternary assembly in complex with its target DNA and the mode of regulation do not follow a general trend [162]. Instead, the modular architecture of the GntR family results in striking versatility as shall be demonstrated in the following examples.

2.3.1.1 FadR

With nearly half of all sequences in Pfam database belonging to this subfamily, FadR forms the largest subfamily and has been intensively studied. One characteristic feature of this group is the all-helical C-terminal effector domain, consisting of 6 to 7 α-helices. Members of FadR are commonly involved in the oxidation of substrates in amino acid metabolism [171]. The family's eponym member FadR from *E. coli* is also the best understood member [162]. FadR binds acyl coenzyme A (acyl-CoA) and regulates both catabolic as well as anabolic genes of fatty acid pathways. This implies that FadR acts both as activator and as repressor [172, 173]. FadR forms a dimer in solution that is able to bind its DNA substrate. Binding of acyl-CoA to the C-terminus leads to derepression and dislodges FadR from its DNA substrate. Binding of the ligand induces rotational movement of the 30 Å separated DNA binding domain by 13°. This results in a widening of the wHTH motifs and release of the DNA [164].

2.3.1.2 VanR / Atu1419

The VanR subgroup is a subclass of the FadR subfamily. They are classified upon the number of their C-terminal alpha helices of which VanR has one less than FadR. A majority of members have a conserved metal binding site [162]. Atu1419 from *agrobacterium fabrum*, a recently characterized member of the VanR subgroup, is a N5,N10-methylenetetrahydrofolate dependent transcriptional

repressor involved in the hydroxycinnamic acids catabolic pathway. Unusual for GntR family transcription factor, Atu1419 forms a stable tetramer (Figure 19). Atu1419 connects two distant short 10 bp long palindromic binding sites by looping the DNA. All four wHTH motifs interact equally with the DNA. The authors of this study suggest that binding of the effector N5,N10-methylenetetrahydrofolate leads to constrained flexibility of the wHTH motifs by a stronger interaction with the effector domain that reduces Atu1419's affinity for DNA and releases repression of the target genes [174].

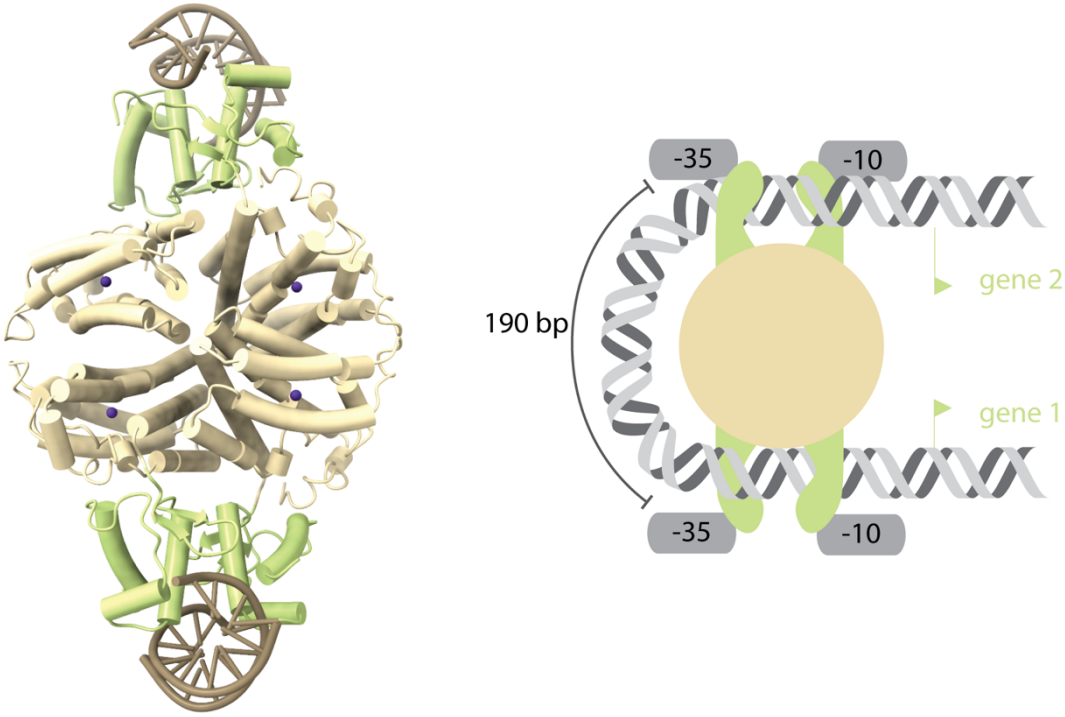

Figure 19. Crystal structure of Atu1419 (pdb id: 6ZA3). Atu1419 belongs to the VanR subgroup of the GntR family and is a tetramer in solution. Binding of Atu1419 to its target DNA via the wHTH domains (green) causes DNA looping. Zn ions are depicted as purple spheres within the effector binding domain (beige).

2.3.1.3 HutC / NagR

HutC forms the second largest subfamily of the GntR transcription factors and members are often involved in sensing the nutritional status, growth and antibiotic production [162, 171, 175]. The effector domain resembles a degenerate chorismite lyase domain and is required for dimerization. NagR (also YvoA) is a structurally well characterized transcriptional repressor of the HutC family and regulates genes involved in N-acetylglucosamine utilization. In the DNA bound state, the DNA binding domains are only loosely held in position by the effector domain via a linking loop. In presence of glucosamine-6-phosphate or N-acetylglucosamine-6-phosphate, the DNA binding domains are displaced by nearly 70 Å (Figure 20). The loosely connecting loop in the DNA bound state forms a

stable beta sheet in the effector bound state, arresting the DNA binding domains and preventing picomolar affinity for the target DNA. The ligand does not abolish binding completely but only fine tunes the affinity of NagR for its DNA substrate [163].

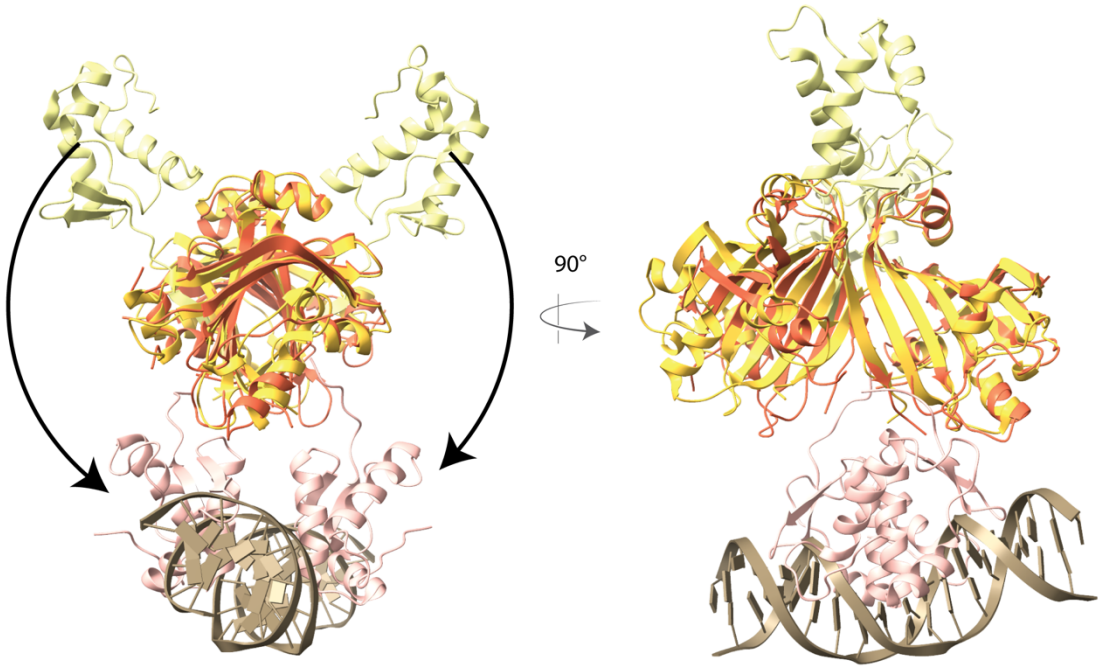

Figure 20. Crystal structure of N-acetylglucosamine-6-phosphate-NagR (pdb id: 4U0W, yellow) and DNA bound NagR (pdb id: 4WWC, red). The wHTH domain (light yellow, light red) relocates by 70 Å upon binding to DNA in the ligand free state.

2.3.1.4 YtrA / CGL2947

The smallest subfamily of GntR transcription factors in terms of molecular size is YtrA. Members feature a very short C-terminal effector domain that consists of two α-helices, that is still capable of ligand binding and dimerization [171] (Figure 21). The α-helices position the wHTH motif in exactly the right distance that corresponds to the distance between the major grooves of the inverted binding motifs. For CGL2947 from *Corynebacterium glutamicum* a crystal structure with and without 2-methyl-2,4-pentanediol (MPD) was solved. While MPD is not the physiological substrate, its binding to the connecting α-helices results in an expanded conformation with enlarged distance between the recognition helices of the wHTH motif, which is postulated to be the basis of regulation of DNA binding affinity [166].

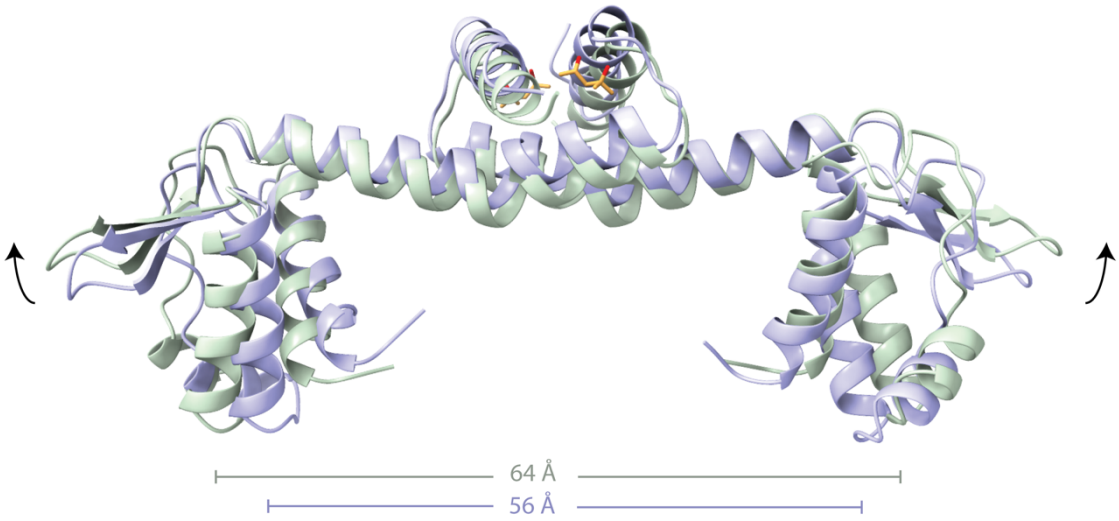

Figure 21. Crystal structure of YtrA from *Corynebacterium glutamicum.* The apo state (purple, pdb id: 2EK5) adopts an expanded conformation upon binding of MBP (green, pdb id: 2DU9).

2.3.2 The MerR family

The MerR family is a group of transcriptional activators that are defined by a common N-terminal wHTH motif of the MerR-type, a conserved coiled-coil region and an interchangeable C-terminal effector domain [176]. Members are widely distributed among bacteria, especially in actinobacteria and proteobacteria (Pfam accession number: PF00376). Transcription factors of the MerR family generally bind to a large region in between the -35 and -10 sequence of a promoter. The distance in between these promotor elements is not optimal and often too long. Binding of the transcription factor induce transcription by distorting the non-optimal promoter in order for the RNA polymerase to be able to initiate transcription. The MerR family can be classified into metal sensing and multidrug binding transcription factors. The range of metals sensed by MerR-like transcription factors include, zinc, mercury, copper, cadmium and cobalt [176]. The family's eponym member MerR also acts as repressor in absence of its inducer Hg^{2+} [177]. Metal binding occurs at the hinge between the wHTH and the coiled-coil motif. Metal coordination leads to a helix-to-loop transition accompanied by significant wHTH rearrangement [178].

2.3.2.1 BmrR

BmrR is a well-studied member of the second group of the MerR family of non-metal binders. BmrR is a sensor for toxic compounds and activates the transcription of the *bmr* gene encoding a multi drug exporter [179]. The range of effectors that the C-terminal multidrug-binding domain accepts are broad and comprise lipophilic cationic compounds that are also substrates of Bmr [180]. The flexibility of BmrR in regard to its ligands stems from a rigid binding pocket that uses a platform of aromatic

residues for unspecific hydrophobic interactions and acidic residues to select for cations within the effector [181]. For BmrR a wealth of structural data is available including apo state, several effector-induced states, DNA bound state and DNA bound state in complex with the RNA polymerase [158, 181-184]. In contrast to MerR the C-terminal effector domain is significantly larger. Effector binding allows BmrR to bind its target DNA (Figure 22). Thereby the coiled-coils reveal conformational plasticity through a flexible central joint [182]. Upon binding of BmrR to the -35 and -10 promoter element, the DNA is bent by approx. 50° away from the protein and base-pair breaking and base sliding occurs [183]. This allows the RNA polymerase to recognize the otherwise non-optimal promotor side and to bind from the opposite side in a cooperative manner without any protein-protein contacts with BmrR itself [158].

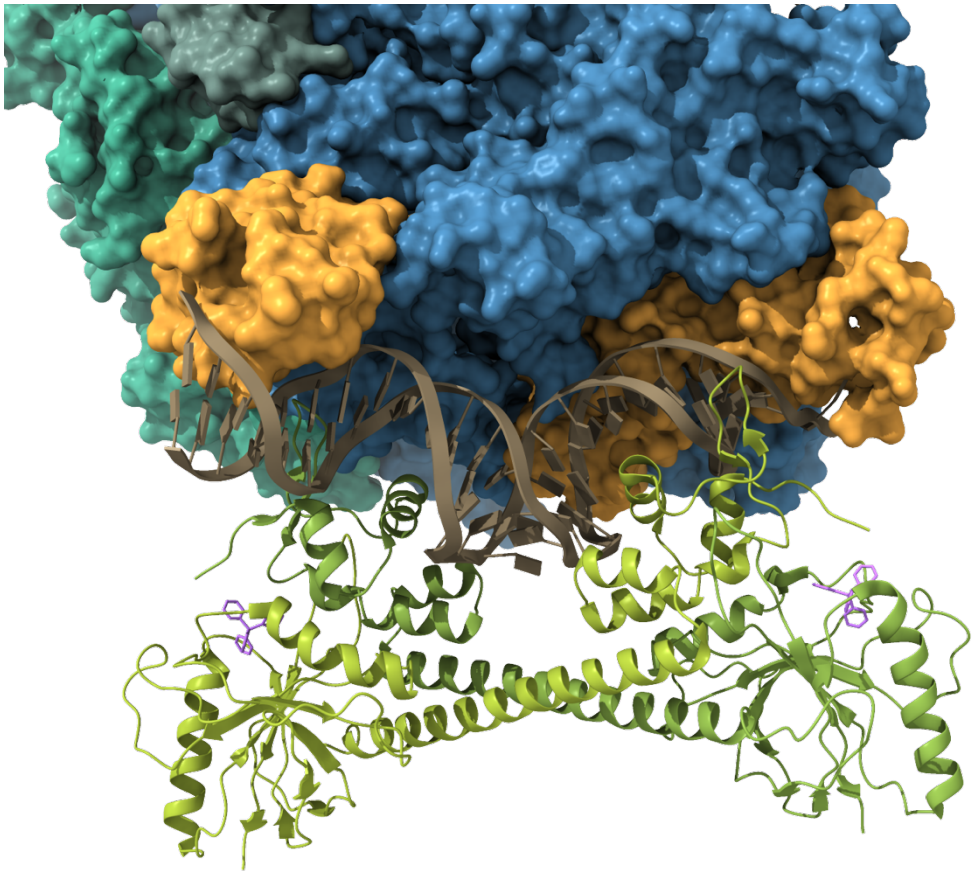

Figure 22. cryo-EM structure of BmrR in complex with its target DNA and RNA polymerase (pdb id: 7CKQ). Binding of BmrR (green) to the promotor bends the DNA and facilitates RNA polymerase binding (σ-subunit: yellow, β- and β'-subunits: blue, ω-subunit: dark turquoise, α-subunits: light turquoise). The activating ligand tetraphenylphosphonium (pink) is bound to the effector binding domain of BmrR.

2.3.2.2 BrlR

BrlR is a transcriptional activator that confers resistance to several antibiotics by regulating genes that code for multi drug efflux pumps [185, 186]. BrlR contains an N-terminal wHTH DNA binding domain of the MerR-type and intermediate coiled-coil motif and a C-terminal GyrI-like domain similar to BmrR [187]. Both c-di-GMP as well as pyocyanin are known ligands [187, 188]. A crystal structure of *Pseudomonas aeruginosa* BrlR is available in apo and ligand bound states [187]. In contrast to BmrR, BrlR is a tetramer in solution and forms a dimer of dimers (Figure 23). Each dimer consists of a head-to-tail arrangement with the central dimeric coiled-coils as dimerization interface. Both dimeric coiled-coils from the separate dimers unite at the tips of the motifs and via the attached globular domains. Monomers from two different pairs interact with each other in a head-to-tail arrangement [187]. C-di-GMP binds to two different binding sites. One is located at the wHTH close to the GyrI interface and the other in the wHTH-coiled-coil transition region. Interestingly the second binding site does not discriminate between c-di-GMP and c-di-AMP. Upon binding of c-di-GMP the coiled-coils bend accompanied by rigid body movement of the globular domains. This brings the wHTH of a single dimer closer together by 1.2 Å, which likely facilitates DNA binding. Only a GyrI-pyocyanin crystal structure is available but not a full-length structure in conjunction with the ligand. pyocyanin binds to the GyrI domain close to the wHTH and is thought to reposition the wHTH in a DNA binding active state, as well. Both ligands activate BrlR in an additive manner [187]. No structural or stochiometric Data is available on the DNA bound complex.

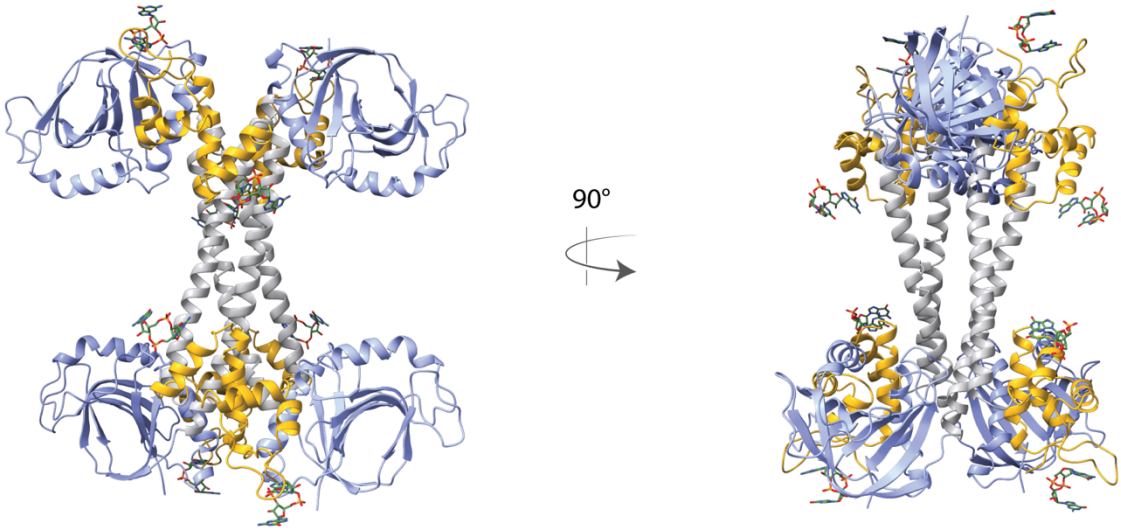

Figure 23. Crystal structure of BrlR from *P. aeruginosa* (pdb id: 5XBT). The c-di-GMP responsive transcriptional activator forms a tetramer with a head-to-tail arrangement. The wHTH (gold) and the GyrI-like domain (purple) are positioned on either side of the central coiled-coil motif (grey). BrlR contains two c-di-GMP (green) binding sites.

3 Publications - Summary

3.1 BusR Senses Bipartite DNA Binding Motifs by a Unique Molecular Ruler Architecture

Bandera, A. M.; Bartho J.; Lammens K.; Drexler D.; Kleinschwärzer J.; Hopfner K. P.; Witte G. BusR Senses Bipartite DNA Binding Motifs by a Unique Molecular Ruler Architecture. *Nucleic Acids Research*, **2021**, *49* (17), 10166–10177

DOI: https://doi.org/10.1093/nar/gkab736

URL: https://academic.oup.com/nar/advance-article/doi/10.1093/nar/gkab736/6357733

Summary

Osmolyte uptake by the glycine-betaine transporter BusA is under the transcriptional control of the transcription factor BusR. It is further known that repression by BusR depends on the bacterial nucleotide second messenger c-di-AMP. Yet, very little is known on the molecular mechanisms that underlie this pathway. In this publication the BusR was investigated on a structural and biochemical level. A 2.8 Å resolution crystal structure of apo BusR reveals a novel tetrameric assembly unobserved before in the GntR family of transcription factors. Furthermore, A 4.5 Å resolution structure of DNA bound full length BusR reveals large conformational changes upon c-di-AMP induced DNA binding. The central coiled-coil motif defines the distance of the DNA binding domains and thus acts as a molecular ruler to recognize a DNA sequence of inverted repeats with a 22bp spacer in between. High resolution crystal structures of the RCK_C domains in apo and c-di-AMP bound states in combination with full length apo and DNA bound states and biochemical data using electrophoretic mobility shift assays allow a good understanding of the regulation mechanism. BusR is under autoinhibitory control of its RCK_C domain. Binding of c-di-AMP to the RCK_C domain triggers activation of BusR by dissolving the intramolecular RCK_C – wHTH interface. This releases autoinhibition and allows subsequent DNA binding and transcriptional repression of *busA*.

Author contribution

The Author of this work established the purification protocol for *S. agalactiae* BusR. He crystallized the published constructs and solved the structures. Furthermore, sample preparation, sample measurement and data processing surrounding cryo-EM was conducted by the author. He designed and conducted ITC, RALS and SAXS experiments to characterize BusR *in vitro*. He established EMSA assays for analyzing the DNA binding behavior of BusR. Lastly, he wrote the manuscript with the help of the co-authors.

3.2 Structural and Biophysical Analysis of the Soluble DHH/DHHA1-Type Phosphodiesterase TM1595 from *Thermotoga maritima*

Drexler, D.*; Müller, M.*; Rojas-Cordova, C. A.; Bandera, A. M.; Witte, G. Structural and Biophysical Analysis of the Soluble DHH/DHHA1-Type Phosphodiesterase TM1595 from Thermotoga maritima. *Structure* **2017**, *25* (12), 1887-1897.e4.

* contributed equally

DOI: https://doi.org/10.1016/j.str.2017.10.001

URL: https://www.sciencedirect.com/science/article/pii/S0969212617303295

Summary

In this publication the degradation mechanism of c-di-AMP by the DhhP type phosphodiesterase TmPDE was investigated. The soluble PDE from *T. maritima* was biochemically and structurally investigated. The combination of affinity assays, using SPR and ITC, as well as activity assays allowed to dissect the substrate specificity of TmPDE. The linear degradation products 5'-pApA, as well as 5'-pApG and 5'-pGpG were identified to be the physiological substrates, while degradation of c-di-AMP was detected at significantly lower levels. A putative nanoRNAse activity of TmPDE could be excluded. These findings are supported by an intensive structural characterization of TmPDE by multiple crystal structures of the intermediate reaction states that allow to fully delineate the reaction mechanism. The structural data was further supported by biophysical characterization of TmPDE in solution, using RALS and SAXS. Based on the provided data a two-step mechanism for the degradation of c-di-AMP was proposed.

Author contribution

The Author of this work purified different constructs of *B. subtilis* GdpP for activity assays using an ion exchange chromatography method. The author further prepared figures for this manuscript and contributed to the text.

3.3 c-di-AMP hydrolysis by the phosphodiesterase AtaC promotes differentiation of multicellular bacteria

Latoscha A.*; Drexler D.*; Al-Bassam M. M.; Bandera A. M.; Kaever V.; Findlay K. C.; Witte G.; Tschowri N. C-di-AMP hydrolysis by the phosphodiesterase AtaC promotes differentiation of multicellular bacteria. PNAS **2020,** *117* (13) 7392-7400

* contributed equally

DOI: https://doi.org/10.1073/pnas.1917080117
URL: https://www.pnas.org/content/117/13/7392

Summary

This publication describes the new c-di-AMP specific phosphodiesterase AtaC from *Streptomyces venezuelae,* a new c-di-AMP binding protein CpeA and how c-di-AMP affects the transition from filaments to spores in actinobacteria.

In actinobacteria, neither DHH-DHHA1- nor PgpH-type PDEs are present. Instead, AtaC was discovered as a c-di-AMP specific phosphodiesterase in *S. venezuelae*, which represents a beforehand missing link in the c-di-AMP homeostasis of this phylum. This was shown by affinity as well as activity assays using isothermal titration calorimetry, DRaCALA and ion exchange chromatography assays. Despite a missing crystal structure, a model was proposed based on small angle X-ray scattering and size exclusion chromatography coupled right angle light scattering data as well as sequence homology to the known structure of the phosphonoacetate hydrolase from *Sinorhizobium meliloti*. Inactivation of AtaC *in vivo* leads to elevated c-di-AMP levels and delays development of aerial hyphae to fully sporulated hyphae. Furthermore, it was shown that a low c-di-AMP strain displays high susceptibility to elevated levels ionic stress, indicating that c-di-AMP regulates osmoregulation also in actinobacteria. CpeA, an RCK_C domain containing protein, was identified as a specific-di-AMP binder. C-di-AMP binding is weak as shown by surface plasmon resonance (SPR) and nano differential scanning fluorimetry (nanoDSF) but in a physiological relevant range and specific as shown by DRaCALA assays.

Author contributions

The author of this thesis purified CpeA and conducted affinity assays for c-di-AMP and comparable nucleotides using nanoDSF and SPR. He further conducted SEC-RALS and SAXS measurements with CpeA.

4 Discussion

4.1 c-di-AMP signaling

Research on c-di-AMP and the elucidation of the signaling pathways has become an intensively growing field of research. The role of c-di-AMP as a major regulator of osmoregulation represents a milestone in clarifying its physiological importance. But while a large number of components of the signaling network have been uncovered rapidly, the knowledge on molecular mechanisms that underly regulation by c-di-AMP lacks behind. Therefore, this work explores the details of c-di-AMP dependent transcriptional control by BusR from a structural and biochemical perspective. RCK_C domains, the domain responsible for c-di-AMP binding in BusR, are widespread among proteins involved in c-di-AMP signaling pathways concerning osmoregulation (chapter 2.2.4.1). Yet, structural data of this domain so far lacked important states, like apo and ligand bound states of the same protein. This makes it difficult to dissect the allosteric mechanism on a molecular scale and leaves open important questions. Here, our determination of multiple key intermediate structures of BusR is able to provide new insights. This work explains how binding of c-di-AMP primes BusR for DNA binding, how DNA substrate specificity is achieved and furthermore discusses possible models how transcriptional repression is ultimately achieved. In the following chapter these insights into BusR will be contrasted with other RCK_C domain containing proteins and structurally related transcription factors. Based on this, models will be discussed how binding of BusR ultimately causes transcriptional repression. Furthermore, the impact of ionic strength, which was described to be the trigger for BusR signaling before the discovery of c-di-AMP, will be examined on the basis of the new structural data.

4.1.1 Coordination of c-di-AMP by the RCK_C domain.

RCK_C domains that bind c-di-AMP have been structurally characterized in four different proteins. They comprise the transcription factor BusR, the KtrAB potassium uptake system, the KhtTU and the CpaA K^+/H^+ antiporters [115, 123, 125, 189]. In all RCK_C domains, c-di-AMP is bound in the cleft of the RCK_C dimer interface. The 3D structures of the single monomers of the RCK_C domains from *S. aureus* CpaA with c-di-AMP, *B. subtilis* KtrA without c-di-AMP, *S. aureus* KtrA with c-di-AMP and BusR with and without c-di-AMP superimpose with an RMSD below 1.5 Å, indicating their almost identical fold (Figure 24A). The RCK_C domain appears very rigid with almost no main chain deviation. It was shown that ligand binding induces no significant changes within a single monomer. Instead, it is the orientation of the RCK_C monomers in respect to each other that underlies changes upon c-di-AMP binding [115, 189].

A significant deviation in the main chain is observed only for an enlarged loop in CpaA in residues 161-169. In CpaA these residues are not involved in c-di-AMP coordination, which results in an open and

exposed c-di-AMP binding pocket [123]. In contrast, in the RCK_C domains of *S. aureus* KtrA, *S. agalactiae* BusR and *B. subtilis* KhtT this loop tightly encloses the binding pocket and coordinates c-di-AMP (Arg110 in *B. subtilis* KhtT, Arg169 in *S. aureus* KtrA and Trp159 in *S. agalactiae* BusR) via main and side chain contacts. This difference is reflected in a significant lower affinity of *S. aureus* CpaA towards c-di-AMP (RCK_C_{SaKtrA}: K_D = 43 nM, RCK_$C_{SgaBusR}$: K_D = 112 nM, RCK_C_{BsKhtT}: K_D = 43 nM, RCK_C_{SaCpaA}: K_D = 9 µM) [115, 125, 189].

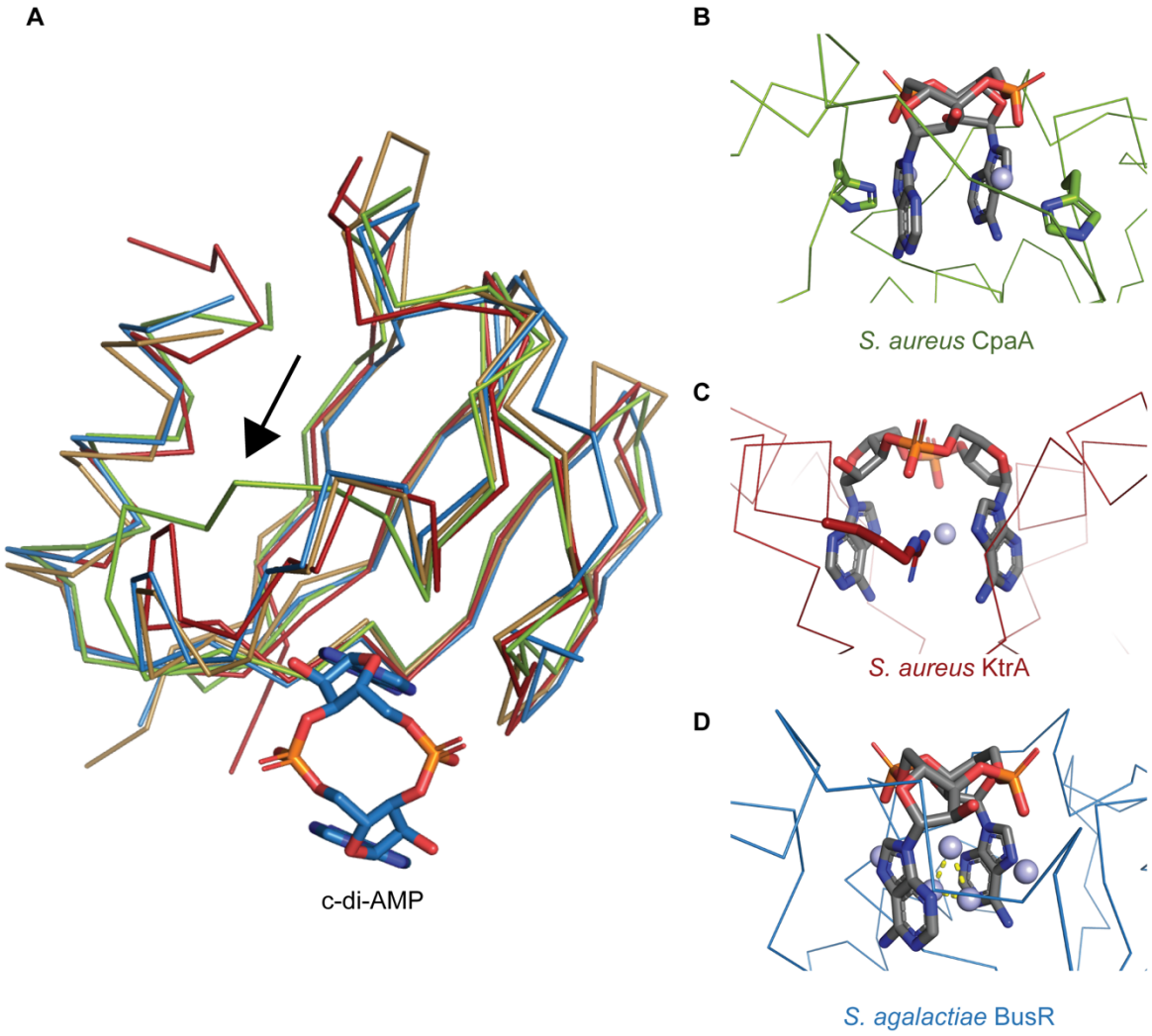

Figure 24. Comparison of c-di-AMP binding RCK_C domains. (A) Superposition of the single monomers of RCK_C domains from *S. aureus* CpaA (green, pdb id: 5F29), *S. aureus* KtrA (red, pdb id: 4XTT), *S. agalactiae* BusR with c-di-AMP (blue, pdb id: 7B5U) and *B. subtilis* KtrA without c-di-AMP (brown, pdb id: 4J91). The second monomers of all proteins are hidden. An enlarged loop in CpaA is marked with a black arrow. (B-D) In all RCK_C domains, a water molecule (light blue spheres) is coordinated by a lone pair-π interaction to the adenine base. This water molecule is coordinated in different ways. In CpaA (B) and KtrA (C) it is coordinated by a histidine and an arginine respectively. In BusR (D), a highly coordinated network of water molecules substitutes the sidechain contacts (distances marked by yellow dashes are below 2.5 Å).

An interesting similarity in the coordination of c-di-AMP by the RCK_C domain was highlighted by He *et al*. A lone-pair donated by a water molecule is located in the center of c-di-AMP and coordinates the adenine base via a lone pair-π interaction [119] (Figure 24 B-D). Deletion of the residue that coordinates this water results in more than 300-fold weaker affinity for c-di-AMP in RCK_C_{SaCpaA} (His184) and abolishes binding completely in RCK_C_{SaKtrA} (Arg169) [115, 123]. Of note, these residues also affect c-di-AMP binding directly. In RCK_$C_{SgaBusR}$, the same lone pair-π interaction can be observed, as well. However, this water molecule is coordinated by two exceptionally strong water-water hydrogen bonds with a distance of only 2.5 Å that could potentially be low barrier hydrogen bonds [190]. This may explain, why BusR binds c-di-AMP with comparable affinity to KhtT and KtrA even in absence of the arginine that stacks between the bases and which was shown to be crucial for c-di-AMP binding [115, 125, 189]. However, it would need further experimental data to confirm this. For example, mutation of Thr165 to valine could interrupt the coordination of water molecules in direct vicinity to c-di-AMP without altering the geometry of the binding pocket.

4.1.2 Regulation of BusR by c-di-AMP

Binding of c-di-AMP needs to induce conformational changes that are propagated to adjacent domains and that result in diverse outcomes depending on the biological context of the RCK_C domain. While exact mechanisms are not completely understood, this work on BusR and previous work on KtrA suggest that the mechanisms involved significantly differ from each other between various RCK_C domains. The RCK_C domain from KtrA has been solved in a c-di-AMP bound state (*S. aureus* 4XTT) and an apo state (*B. subtilis* 4J91). Based on these structures it is thought that binding of c-di-AMP brings the monomers together and leads to a strong packing of the entire RCK_C domain [115]. This in agreement with work done on isolated RCK_C_{SaCpaA} domains that dimerize only in presence of c-di-AMP, indicating that c-di-AMP leads to a similar compaction movement in full length *S. aureus* CpaA [123]. For KtrA it has been observed that the RCK_N – RCK_C linker displays a certain degree of flexibility [111, 191]. Yet, it can be assumed from the structural data that the interlocked cross-over in form of an α-helix-hinge- β-sheet leads to enough rigidity to transfer such large conformational change to rearrange the octameric ring of KtrA in a disabling fashion [110, 115] (Figure 25). Unfortunately, structural data on full-length KtrA with c-di-AMP is missing so far. For the paralogues CabP and TrkH (chapter 2.2.2.7) it has been observed that binding of c-di-AMP interferes with the connection of the cytoplasmic RCK gating ring to the transmembrane channel, suggesting a dissociation of the ring upon c-di-AMP binding while for the predicted cation/proton antiporter CpeA and CpeB c-di-AMP induces complex formation [43, 114]. It is assumed that KtrA dissociates from KtrB upon binding of c-di-AMP, as well.

The situation is different for BusR. Binding of c-di-AMP does not induce any conformational changes that are propagated along the same protein chain. Instead, c-di-AMP binding leads to a restructuring of a transient interface, in particular a hydrophobic patch surrounding Trp159, between the RCK_C domain and the non-covalently DNA binding domain of another protomer (Figure 25). The residues involved in this patch are highly conserved in BusR but not in KtrA or similar proteins containing RCK_C domains. This transient connection is weakened upon binding of c-di-AMP to the RCK_C domain and allows for subsequent binding of the wHTH motif to the specific DNA sequence [189]. There is no data of KtrAB indicating such a direct interaction between RCK_C and the transmembrane channel. It is also important to note, that key residues that are involved in BusR signaling, are only conserved in BusR, but not in related RCK_C domains.

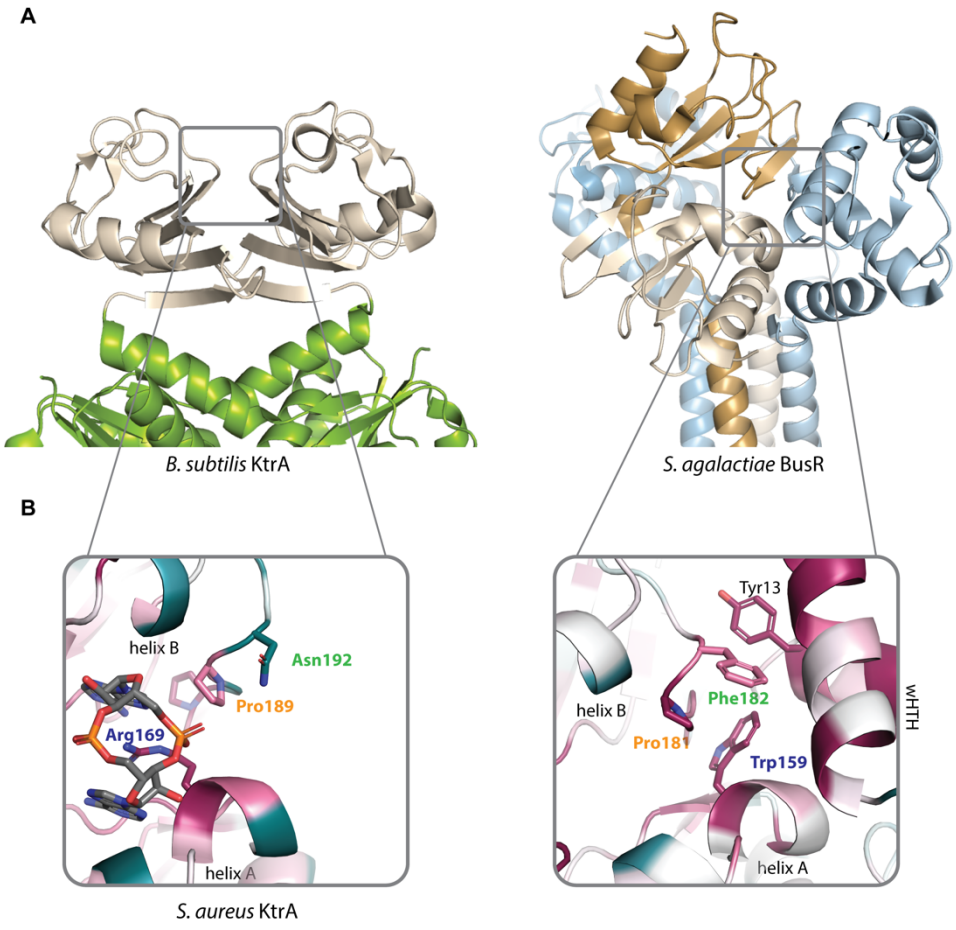

Figure 25. Differences in regulation by RCK_C domains. (A, left) Sections of the crystal structure of *B. subtilis* KtrA (pdb id: 4J90. RCK_N: green, RCK_C: wheat) and (right) and of *S. agalactiae* BusR (pdb id: 7B5T. RCK_C: wheat and brown, wHTH: light and dark blue). (B, left) Close-up on the c-di-AMP binding pocket of *S. aureus* KtrA and (right) *S. agalactiae* BusR. Residues are colored according to conservation generated with the ConSurf server from 150 sequences. Highly conserved residues are colored in dark purple, high variability is colored in cyan. Key residues important for signaling in BusR are highly conserved. Structurally equivalent residues in KtrA are either not conserved (Asn192 vs. Phe182) or are likely conserved for their role in c-di-AMP binding (Arg169 vs. Trp159).

4.1.3 DNA binding by BusR in contrast to other GntR family transcription factors

BusR is classified as GntR transcription factor due to its structurally highly conserved wHTH DNA binding domain. Among the GntR transcription factor family, BusR forms a new subclass based on its domain architecture and is therefore also the first structurally characterized member thereof.

Of all GntR family transcription factors the YtrA subclass shares most similarity with BusR in regard to the in regard to the $wHTH_{inhib}$ domains (chapter 2.3.1.4). In both cases, the wHTH domains are bridged by α-helices over a significant distance [166]. This is reflected in large DNAse I protected regions in footprint experiments on DNA substrates. For *S. agalactiae* BusR a footprint of 40 bp and for $YtrA_{SA}$ a 32 bp was observed [48, 192]. From structural data on *Corynebacterium glutamicum* CGL2947 it is clear that the α-helices in YtrA-like transcription factors can serve a dual role, by positioning the wHTH domains in respect to the binding site and by binding an effector molecule, which leads to conformational changes within the α-helices [166]. In this regard, the α-helices serve a regulatory function. In case of BusR no significant change or bending is observed between the free and DNA bound state [189]. The tetrameric coiled-coils form a central rigid platform upon which on either ends the DNA binding domains assemble. Ligand binding is not propagated via the coiled-coils. Instead, they act as a molecular ruler, serving as an additional layer of substrate recognition as it was shown by EMSAs [189].

Apart from the YtrA subfamily, the orientation of the wHTH domains in respect to the partnering wHTH from a second protomer within the protein is often very similar even among different subclasses of the GntR family. For instance, the wHTH domains from *E. coli* FadR, *A. fabrum* Atu1419 and *B. subtilis* NagR all show similar binding to the DNA despite very different C-terminal oligomerization domains [163, 164, 174] (Figure 26A; chapter 2.3.1). In particular, both wHTH domains bind side by side to the same major groove but turned around by 180° in respect to each other. BusR has four wHTH domains. Two domains that are close to each other also bind side by side to the same major groove, but in a parallel fashion. Therefore, the domain is 180° turned around in respect to NagR and other transcription factors of the GntR family (Figure 26A bottom).

As a result, on both sides of BusR two wHTH domains bind to two different DNA sequences. This leads to two distinct binding modes. A sequence specific interaction of the $wHTH_{inhib}$ domain buried deep in the major groove and further interacting with the minor groove, and a likely unspecific interaction of $wHTH_{free}$ with the minor groove [189] (Figure 26B). This is in contrast to Atu1419, which also forms a tetramer but all four wHTH domains interact with their target sequence in the same manner [174].

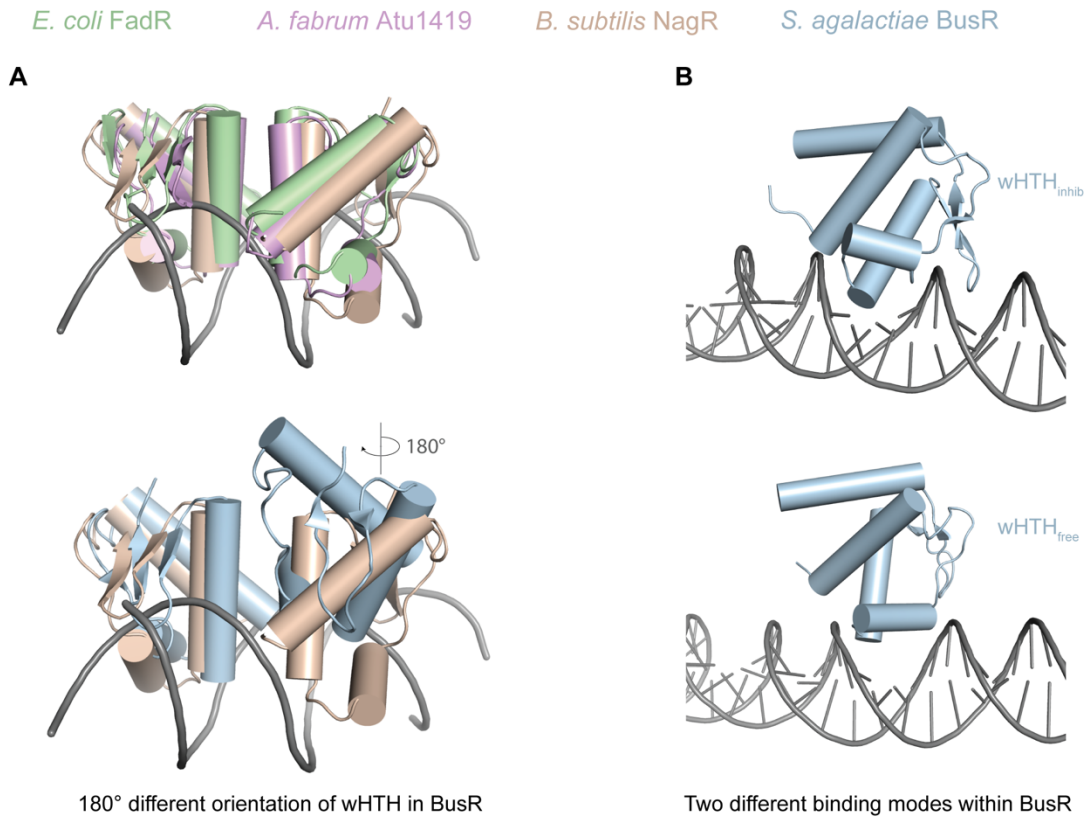

Figure 26. Comparison of the relative orientation of wHTH domains from various GntR proteins. (A, top) Superposition of *E. coli* FadR (pdb id: 1H9T, green), *A. fabrum* (pdb id: 6ZA3, pink) and *B. subtilis* NagR (pdb id: 4WWC, brown). The DNA (grey) derives from the NagR structure. (A, bottom) Superposition of NagR and *S. agalactiae* BusR (pdb id: 7OZ3, blue). All C-terminal effector binding domains are hidden (B, top) Close up on the $wHTH_{inhib}$ from BusR bound to the target DNA sequence (pdb id: 7OZ3, rest of protein hidden). (B, bottom) Same as B, top with the exception that $wHTH_{free}$ is displayed. The interaction with the target DNA is different between both domains.

It can be speculated, that $wHTH_{free}$ is not essential for target site binding but rather plays a vital role in finding the target site. In bacteria transcription factor accelerate the search for their binding site by 'facilitated diffusion' [193]. Instead of freely diffusing through the 3D space, the search includes non-specific one-dimensional sliding along the DNA. In fact, by single molecule tracking it was shown that transcription factors spend up to 99% of the time on DNA, so that transient interactions dominate the search [194]. It is possible that $wHTH_{free}$ is important for sliding and transient interactions with the DNA. However, experimentally dissecting the difference between $wHTH_{free}$ and $wHTH_{inhib}$ may prove difficult.

4.1.4 Transcriptional repression

BusR forms a stable tetramer under all states investigated so far as was shown by RALS and SAXS data [189]. The only other tetrameric GntR family member is the transcriptional repressor Atu1419 (chapter 2.3.1.2). The transcription factor binds to two inverted repeats that are spaced apart by 190 bp. Atu1419 induces DNA loop formation that leads to transcriptional repression by blocking access to the promotor [174]. In *S. agalactiae* two BusR binding sites in the promotor region of *busA* have been described that are 34 bp apart [48]. While this is significantly shorter than what is observed for Atu1419, it is still in good agreement with a loop formation model and raises the idea that this model of repression is also valid for BusR. In the DNA bound state of BusR one pair of wHTH interacts specifically with the DNA, while the second pair most likely interacts only non-specifically with the DNA [189]. From a structural perspective it cannot be completely ruled out that BusR may bind a second stretch of DNA as is necessary for loop formation. However, our experimental data do not support looping. Within this work, no 2:1 stoichiometry of a DNA:BusR complex necessary for this model could be observed in SAXS or RALS measurements with BusR and a DNA sequence containing a single binding site. The highly asymmetric electrostatic surface of BusR would lead to repulsion of a second DNA strand bound to the backside. Furthermore, no looped species could be observed in EMSAs using BusR and native DNA with two binding sites. On top of this biochemical evidence, structural studies by cryo-EM using the same native DNA showed, that both binding sites are occupied in an independent manner [189]. The *in vitro* data discourages a model of DNA loop formation. However, it remains to be seen whether additional factors present themselves *in vivo* that were not considered in this study and that could thus induce looping.

In absence of any observed cooperativity in form of looping or direct interaction, the question arises for the need of two binding sites arises. The response regulator BvgA of the two-component system BvgAS from *Bordetella pertussis* has two binding sites at the promotor for the gene *bipA*. Binding to the high affinity binding site activates transcription, while simultaneous occupation of the low affinity binding site abrogates the same [195]. In case of BusR, no activation of *busA* has been described and the affinity of BusR for both binding sites is at the same order of magnitude. Yet, it is possible that both binding sites may have different roles in *in vivo*. An *in vitro* transcription experiment would be highly desirable to further dissect the regulatory properties of both binding sites on the *busA* promotor activity in a BusR dependent manner. Even if it turns out that the binding site that is more downstream from the polymerase binding site is unable to repress transcription, it could still contribute to repression by locally enriching the BusR concentration in the vicinity of pAB2.

To discuss a different model of transcriptional repression it is worthwhile to compare BusR with transcription factors that are structurally closer related to BusR than the GntR family. While structurally distinct from the other members of the GntR family, BusR shares more significant similarity with the MerR family of transcription factors (chapter 2.3.2). Transcription factors of the MerR family are predominantly dimers. BrlR is an exception and has been has been discovered to be tetrameric. The central coiled-coil motif is distinct from BusR as it forms a dimer of two dimeric coiled-coils. Like BusR, BrlR adopts a head-to-tail arrangement [187]. Interestingly, as seen for BusR one of two wHTH motifs on either end is forming an interface with the effector binding domain of an antiparallel protomer. As this interface is in close proximity to both ligands that activate BrlR, c-di-GMP and pyocyanin, this interface is likely to adopt a regulatory function as seen for BusR. However, the exact mechanism of ligand induced DNA binding is not fully understood in absence of structural data on the BrlR-DNA complex.

A better understood member of the MerR family is the transcription factor BmrR. Just like BusR, BmrR binds between the -35 and -10 region of its target promotor and induces a strong bending of the DNA. In case of BmrR this allows for cooperative binding of the RNA polymerase on the opposite site of the DNA and transcriptional activation [158]. In case of BusR the binding sites are spaced apart by an additional major groove. The bend induced upon binding is less pronounced in BusR. Yet, a simultaneous binding of BusR and the RNA polymerase has been observed *in vitro* [138]. The question is, how would such a similar conformation lead to transcriptional activation in case of BmrR, but to repression in case of BusR? The structurally well characterized protein CueR, which belongs to the metalloregulators of the MerR family, can shed light on this. CueR binds in a similar manner to BmrR and facilitates transcription in a Cu(I) dependent manner. However, in absence of Cu(I) CueR also binds its target DNA at the same site but this apo state results in repression [196]. This repressed state further allows the RNA polymerase to bind but not to transition to an open complex and subsequent elongation. Instead, the RNA polymerase is arrested in a closed complex [197]. Based on double electron-electron resonance (DEER) it is postulated that binding of Cu(I) brings the DNA binding domains close together, squeezing the DNA more strongly and thereby allowing for the polymerase to transition to the open complex. The BusR-DNA state may resemble such a repressor state as observed for CueR. From a structural perspective it is very likely that BusR and a polymerase can bind simultaneously. The structure of *Thermus aquaticus* RNA polymerase holoenzyme bound to DNA (pdb id: 1L9Z) and BusR can be superimposed in respect to the DNA and their binding sites, without clashes or contacts within the proteins (Figure 27). The structure has been chosen as the polymerase has not progressed to a transcriptional competent open state but is merely bound to the promoter. The polymerase binds to the opposite face of the DNA. The bend of the DNA that is introduced by

BusR corresponds to the bend introduced by the RNA polymerase holoenzyme [189, 198]. This model implies that BusR does not repress transcription by blocking the promotor sight as is often the case for repressors that bind in the -35 and -10 region [159]. Instead, the RNA polymerase can still bind to the promotor-BusR complex but cannot transition to an open complex, which then results in transcriptional arrest. A possible advantage of such a trapped polymerase at promotor site could potentially be a rapid induction of gene expression after dissociation of BusR.

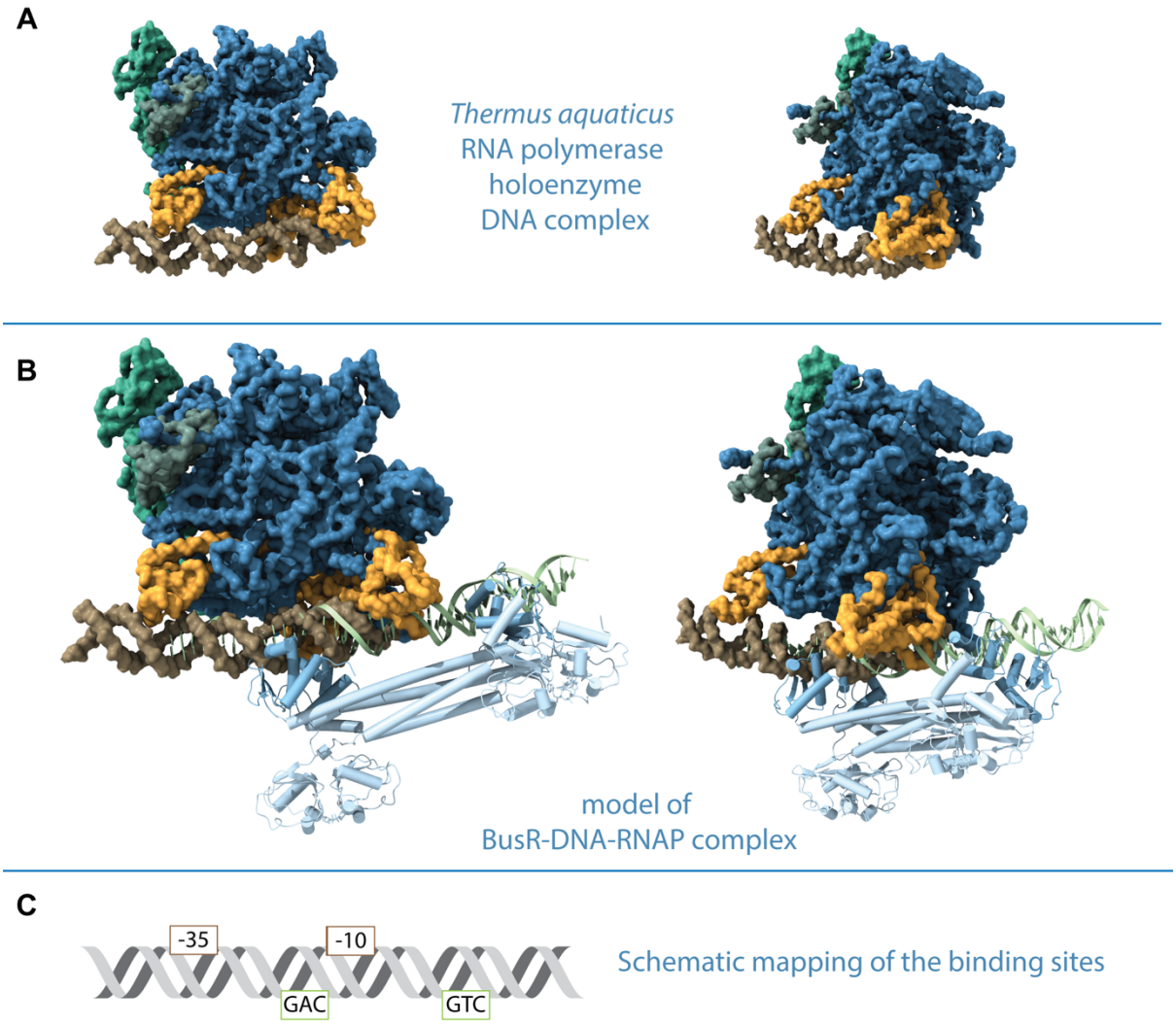

Figure 27. (A) Crystal structure of *Thermus aquaticus* RNA polymerase holoenzyme in complex with promotor DNA (pdb id: 1L9Z, σ^A-subunit: yellow, β- and β'-subunits: blue, ω-subunit: dark turquoise, α-subunits: light turquoise, DNA: brown). (B) Model of a putative BusR-RNAP-DNA complex (BusR in light blue, pdb id: 7B5Y) from two different angles. The DNA from the BusR structure (green) superimposes well with the DNA from the RNA polymerase structure. (C) Schematic overview of the positions of the binding sites for BusR (green) and the polymerase (brown) on the promotor.

Similar to BusR the nucleoid-associated protein Fis binds in between the -35 and -10 region and traps the RNAP at the promotor. RNAP with sigma factor σ^{70} are stopped from transitioning to an open complex while the sigma factor σ^{38} allows for transition to the open complex despite the presence of Fis [199]. Similar experiments should be conducted for BusR in the future.
The model of the ternary RNAP-BusR-DNA complex is very speculative and supporting data is insufficient. Yet, it can help to design future experiments that will help gain insights on the molecular mechanisms behind BusR mediated transcriptional repression.

4.1.5 Integration of ionic strength and c-di-AMP

Originally BusR was found to be a transcriptional repressor of *busA* that directly senses ionic strength directly and bind its target sequence accordingly. *In vitro* gel shift experiments with different ions showed a strict correlation between ionic strength and BusR dissociation from the *busA* promotor [138]. This would imply that following an osmotic upshift and a thereof resulting increased uptake of potassium, the cytoplasmic ionic strength would increase, displacing BusR from the promotor and allowing expression of BusA. The osmolyte transporter could then import compatible solutes to reestablish osmotic equilibrium, which would ultimately reenforce *busA* repression after reduction of the cytoplasmic ionic strength. In agreement it was shown that the *L. lactis busA* promotor activity increases moderately in *E. coli* in presence of BusR under increasing NaCl concentrations [79]. Such dual control is also seen for the activity of BusA, which is under direct control of c-di-AMP and ionic strength [132, 134]. Indeed, BusR displayed severe sensitivity in terms of stability at low ionic strength in absence of DNA, which could suggest large conformational changes in response to ionic strength (this work). Due to its mostly ionic nature, the wHTH-DNA interaction will be negatively affected by higher salt concentrations. In addition, higher salt concentrations could have a dual effect on BusR by further stabilizing the hydrophobic interaction between the RCK_C domain with the wHTH domain, which would disrupt the interaction with the DNA. While BusR has now been well established as c-di-AMP responsive transcription factor, it is plausible that BusR integrates both signals, ionic strength and c-di-AMP concentration, possibly via the same autoinhibitory hydrophobic patch [48, 79].

4.1.6 Two-layer regulation of BusA

Sikkema et al. showed that c-di-AMP acts as a backstop on *L. lactis* BusA activity, by inhibiting the transporter independent of the ionic strength [134] (chapter 2.2.3). Therefore, in *L. lactis, busA* is regulated both on the transcriptional level via BusR, as well as directly on the protein level by c-di-AMP. This is a theme for c-di-AMP regulation as observed before in case of KimA or KtrAB [118] (chapter 2.2.2.7). It will be interesting to investigate whether this form of regulation is valid only for *L. lactis* or whether it is conserved. In *B. subtilis* no homolog of *busR* exists and no binding of c-di-AMP

to the BusAA homolog OpuAA has been observed, despite its high sequence similarity to *B. subtilis* OpuBA and OpuCA from the same organism that both bind c-di-AMP [118, 200]. Interestingly, cell lysate DRaCALA experiments were not conclusive for c-di-AMP in case of OpuBA, while hydrogen deuterium exchange mass spectrometry and microscale thermophoresis experiments demonstrated c-di-AMP binding [118, 200]. It is therefore possible that *S. agalactiae* BusA, for which no binding was detected in a crude cell lysate DRaCALA experiment, does bind c-di-AMP after all [48]. The CBS domain of *S. agalactiae* and *L. lactis* BusA share high sequence similarity (similarity = 61.2 %, identity 37.2 %). Since no experimental structure for *S. agalactiae* BusA is yet available, the recently developed alphafold2 is a valuable tool. The artificial intelligence software that derives structural information from pairwise evolutionary correlations using a sophisticated neural network architecture, allows for unprecedented structure prediction accuracy [201]. A model of the CBS domain from *S. agalactiae* BusA superimposes nearly perfectly with its homolog from *L. lactis* with a RMSD of 0.93 Å (Figure 28). More importantly, all key contacts that coordinate c-di-AMP in *L. lactis* BusA are present in the model. These include hydrogen bonds to the main chain and neighboring isoleucine and leucin residues surrounding the adenine bases forming a well matching hydrophobic pocket. The only missing contact is the hydrogen bond between the 2'OH group of the ribose and serine 306 in *L. lactis* CBS_{BusA}. From a structural perspective and based on the computational model, it is very likely that c-di-AMP binding to BusA is not limited to the *L. lactis* protein. However, the true structure of *S. agalactiae* BusA CBS could be different from the model, especially in respect to the CBS interface, and it will therefore be inevitable to test c-di-AMP binding experimentally. A two-layer regulation of osmolyte import via BusA at the transcriptional and protein level would allow for a both an energy efficient and rapid response that is important for such a crucial aspect for the cell as osmolyte homeostasis.

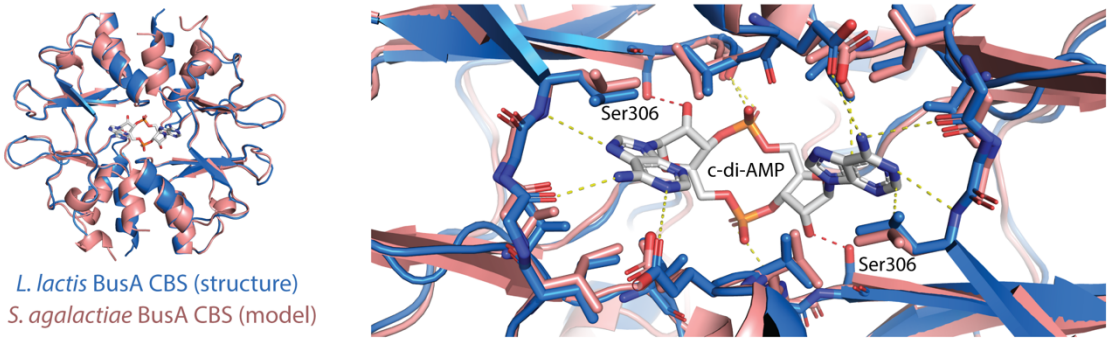

Figure 28. Alphafold2 model of *S. agalactiae* BusA CBS domain in comparison to the cryo-EM structure of *L. lactis* BusA CBS (pdb id: 7AHH). (left) Superposition of both CBS domains. (right) Close-up of the c-di-AMP binding pocket. Conserved protein-ligand coordination is colored in yellow while interactions missing in the model are colored in red. The model was created using the free Colaboratery version of alphafold2 and aligning both chains of the CBS domain individually to the *L. lactis* structure [201, 202].

4.2 c-di-AMP degradation

Second messengers are a crucial tool to rapidly react to different environmental conditions by regulating a multitude of cellular processes on multiple levels. For effective signaling, the levels of the second messenger in question have to be tightly regulated. This necessitates fast and specific enzymes for degradation. Degradation does not necessarily need to be regulated and could instead degrade at constant rate while synthesis rates are modulated according to changing stimuli. Yet, the regulation of degradation on the protein level would allow for faster and finer tuning of the c-di-AMP levels and help the cell save resources.

All PDEs that are physiologically relevant in c-di-AMP degradation have been shown to use, or are very likely to use, similar degradation mechanisms [42, 43, 74, 76]. Yet, the overall protein architecture varies significantly between the different PDEs. PgpH and GdpP both carry additional but distinct domains apart from the catalytic core, which can potentially regulate the c-di-AMP degradation by these PDE-types. Furthermore, both enzymes are membrane bound and could potentially sense and integrate changes in turgor directly via conformational changes within the transmembrane domains [42, 70]. PDE of the DhhP-type are soluble and have no additional domains, which makes regulation on the protein level for this type less likely. It was shown that their substrate specificity can vary and it was postulated that many DhhP-type PDEs rather catalyze the unregulated second step of degradation in c-di-AMP decay, the turnover of 5’-pApA to AMP, as was shown for TmPDE [74]. Furthermore, the inability of TmPDE to cleave longer nucleotide substrates like 5’-pApApA rules out the possibility of TmPDE being classified as nanoRNAse with exonuclease activity [74], highlighting its specificity for the degradation pathway of the second messenger c-di-AMP. The preference of 5′-pApA over c-di-AMP is not limited to TmPDE. Many DhhP-type PDEs from organisms including *L. lactis, T. maritima* or *S. pneumoniae*, that contain either a GdpP or PgpH homologs exhibit 5’-pApA cleavage specificity without physiologically relevant c-di-AMP turnover rates [69, 73, 74]. In contrast, DhhP-type PDEs from organisms that do not contain a GdpP or PgpH like *M. tuberculosis* or *B. burgdorferi*, do indeed degrade c-di-AMP to AMP [66, 75]. In this respect they are very similar to the newly discovered c-di-AMP specific PDE AtaC from *S. venezuelae*. In collaboration with the Tschowri group AtaC has been described as a monomeric and soluble PDE that specifically degrades c-di-AMP to AMP [43]. *In vivo* knock-out experiments on AtaC show that c-di-AMP levels significantly increase in absence of a functional copy, establishing AtaC as a physiologically relevant PDE catalyzing both steps of c-di-AMP degradation. This is very important as it was unknown beforehand how the large phylum of actinobacteria degrade c-di-AMP in absence of GdpP-type, PgpH-type or DhhP-type phosphodiesterases. A functional AtaC is import for growth and correct development of *S. venezuelae* while high levels of c-di-AMP lead to delay during sporulation [43].

If it is in general only the first step of degradation that is regulated and the second step is not, the open question remains how degradation is regulated in organisms like *S. venezuelae* that only uses AtaC for degradation for which no regulation has so far been observed. A direct regulation of AtaC is possible. Crosstalk between different second messengers is not uncommon and has been already studied to greater extend in case of c-di-AMP and (p)ppGpp (2.2.2.5). The lack of auxiliary domains limits the possibilities for allosteric control of AtaC and no allosteric effectors have been described so far. A competitive control of AtaC is plausible, too, and more investigations in this direction are needed in order to understand the c-di-AMP homeostasis in actinobacteria. Apart from a regulation on the post-translational level, AtaC may instead be regulated on the transcriptional level. AtaC expression increases slightly during the life cycle of *S. venezuelae* under standard conditions, which may indicate transcriptional control [43].

Even though AtaC is structurally not related to c-di-AMP degrading DhhP-type phosphodiesterases, they are highly similar in substrate specificity and the absence of obvious regulatory domains. It is possible that both enzymes evolved independently and are interchangeable. But in several organisms including *M. tuberculosis* or *M. smegmatis* both types of PDEs are utilized, hinting at distinct roles in c-di-AMP degradation that have to be yet discovered.

5 References

1. Chou, S.-H., et al., *Microbial Cyclic Di-Nucleotide Signaling*. 2020, Springer International Publishing. p. XVIII, 657.
2. Berthet, J., T.W. Rall, and E.W. Sutherland, *The relationship of epinephrine and glucagon to liver phosphorylase. IV. Effect of epinephrine and glucagon on the reactivation of phosphorylase in liver homogenates.* J Biol Chem, 1957. **224**(1): p. 463-75.
3. Okabayashi, T., A. Yoshimoto, and M. Ide, *Occurrence of Nucleotides in Culture Fluids of Microorganisms. V. Excretion of Adenosine Cyclic 3',5'-Phosphate by Brevibacterium Liquefaciens Sp. N.* J Bacteriol, 1963. **86**: p. 930-6.
4. Kim, H.S., et al., *Expression of the cpdA gene, encoding a 3',5'-cyclic AMP (cAMP) phosphodiesterase, is positively regulated by the cAMP-cAMP receptor protein complex.* J Bacteriol, 2009. **191**(3): p. 922-30.
5. Perlman, R.L. and I. Pastan, *Pleiotropic deficiency of carbohydrate utilization in an adenyl cyclase deficient mutant of Escherichia coli.* Biochem Biophys Res Commun, 1969. **37**(1): p. 151-7.
6. Deutscher, J., C. Francke, and P.W. Postma, *How phosphotransferase system-related protein phosphorylation regulates carbohydrate metabolism in bacteria.* Microbiol Mol Biol Rev, 2006. **70**(4): p. 939-1031.
7. Petersen, S. and G.M. Young, *Essential role for cyclic AMP and its receptor protein in Yersinia enterocolitica virulence.* Infect Immun, 2002. **70**(7): p. 3665-72.
8. Fuchs, E.L., et al., *The Pseudomonas aeruginosa Vfr regulator controls global virulence factor expression through cyclic AMP-dependent and -independent mechanisms.* J Bacteriol, 2010. **192**(14): p. 3553-64.
9. McDonough, K.A. and A. Rodriguez, *The myriad roles of cyclic AMP in microbial pathogens: from signal to sword.* Nat Rev Microbiol, 2011. **10**(1): p. 27-38.
10. Potrykus, K. and M. Cashel, *(p)ppGpp: still magical?* Annu Rev Microbiol, 2008. **62**: p. 35-51.
11. Irving, S.E., N.R. Choudhury, and R.M. Corrigan, *The stringent response and physiological roles of (pp)pGpp in bacteria.* Nat Rev Microbiol, 2021. **19**(4): p. 256-271.
12. Cashel, M. and J. Gallant, *Two compounds implicated in the function of the RC gene of Escherichia coli.* Nature, 1969. **221**(5183): p. 838-41.
13. Ronneau, S. and R. Hallez, *Make and break the alarmone: regulation of (p)ppGpp synthetase/hydrolase enzymes in bacteria.* FEMS Microbiol Rev, 2019. **43**(4): p. 389-400.
14. Winther, K.S., M. Roghanian, and K. Gerdes, *Activation of the Stringent Response by Loading of RelA-tRNA Complexes at the Ribosomal A-Site.* Mol Cell, 2018. **70**(1): p. 95-105 e4.
15. Ross, W., et al., *The magic spot: a ppGpp binding site on E. coli RNA polymerase responsible for regulation of transcription initiation.* Mol Cell, 2013. **50**(3): p. 420-9.
16. Ross, W., et al., *ppGpp Binding to a Site at the RNAP-DksA Interface Accounts for Its Dramatic Effects on Transcription Initiation during the Stringent Response.* Mol Cell, 2016. **62**(6): p. 811-823.
17. Sanchez-Vazquez, P., et al., *Genome-wide effects on Escherichia coli transcription from ppGpp binding to its two sites on RNA polymerase.* Proc Natl Acad Sci U S A, 2019. **116**(17): p. 8310-8319.
18. Hauryliuk, V., et al., *Recent functional insights into the role of (p)ppGpp in bacterial physiology.* Nat Rev Microbiol, 2015. **13**(5): p. 298-309.
19. Ross, P., et al., *Regulation of cellulose synthesis in Acetobacter xylinum by cyclic diguanylic acid.* Nature, 1987. **325**(6101): p. 279-81.
20. Ross, P., et al., *An unusual guanyl oligonucleotide regulates cellulose synthesis in Acetobacter xylinum.* FEBS Lett, 1985. **186**(2): p. 191-6.
21. Romling, U. and M.Y. Galperin, *Discovery of the Second Messenger Cyclic di-GMP.* Methods Mol Biol, 2017. **1657**: p. 1-8.

22. Jenal, U., A. Reinders, and C. Lori, *Cyclic di-GMP: second messenger extraordinaire.* Nat Rev Microbiol, 2017. **15**(5): p. 271-284.
23. Baraquet, C. and C.S. Harwood, *Cyclic diguanosine monophosphate represses bacterial flagella synthesis by interacting with the Walker A motif of the enhancer-binding protein FleQ.* Proc Natl Acad Sci U S A, 2013. **110**(46): p. 18478-83.
24. Boehm, A., et al., *Second messenger-mediated adjustment of bacterial swimming velocity.* Cell, 2010. **141**(1): p. 107-16.
25. Skotnicka, D., et al., *Cyclic Di-GMP Regulates Type IV Pilus-Dependent Motility in Myxococcus xanthus.* J Bacteriol, 2016. **198**(1): p. 77-90.
26. Steiner, S., et al., *Allosteric activation of exopolysaccharide synthesis through cyclic di-GMP-stimulated protein-protein interaction.* EMBO J, 2013. **32**(3): p. 354-68.
27. Romling, U., M.Y. Galperin, and M. Gomelsky, *Cyclic di-GMP: the first 25 years of a universal bacterial second messenger.* Microbiol Mol Biol Rev, 2013. **77**(1): p. 1-52.
28. McKee, R.W., et al., *The second messenger cyclic Di-GMP regulates Clostridium difficile toxin production by controlling expression of sigD.* J Bacteriol, 2013. **195**(22): p. 5174-85.
29. Li, W., et al., *Cyclic diguanylate monophosphate directly binds to human siderocalin and inhibits its antibacterial activity.* Nat Commun, 2015. **6**: p. 8330.
30. Valentini, M. and A. Filloux, *Multiple Roles of c-di-GMP Signaling in Bacterial Pathogenesis.* Annu Rev Microbiol, 2019. **73**: p. 387-406.
31. Hengge, R., *Principles of c-di-GMP signalling in bacteria.* Nat Rev Microbiol, 2009. **7**(4): p. 263-73.
32. Christen, M., et al., *Identification and characterization of a cyclic di-GMP-specific phosphodiesterase and its allosteric control by GTP.* J Biol Chem, 2005. **280**(35): p. 30829-37.
33. Galperin, M.Y., A.N. Nikolskaya, and E.V. Koonin, *Novel domains of the prokaryotic two-component signal transduction systems.* FEMS Microbiol Lett, 2001. **203**(1): p. 11-21.
34. Witte, G., et al., *Structural biochemistry of a bacterial checkpoint protein reveals diadenylate cyclase activity regulated by DNA recombination intermediates.* Mol Cell, 2008. **30**(2): p. 167-78.
35. Corrigan, R.M., et al., *Systematic identification of conserved bacterial c-di-AMP receptor proteins.* Proc Natl Acad Sci U S A, 2013. **110**(22): p. 9084-9.
36. Rubin, B.E., et al., *High-throughput interaction screens illuminate the role of c-di-AMP in cyanobacterial nighttime survival.* PLoS Genet, 2018. **14**(4): p. e1007301.
37. Blötz, C. and J. Stulke, *Glycerol metabolism and its implication in virulence in Mycoplasma.* FEMS Microbiol Rev, 2017. **41**(5): p. 640-652.
38. Kampf, J., et al., *Identification of c-di-AMP-Binding Proteins Using Magnetic Beads.* Methods Mol Biol, 2017. **1657**: p. 347-359.
39. Sureka, K., et al., *The cyclic dinucleotide c-di-AMP is an allosteric regulator of metabolic enzyme function.* Cell, 2014. **158**(6): p. 1389-1401.
40. He, Q., et al., *Structural and Biochemical Insight into the Mechanism of Rv2837c from Mycobacterium tuberculosis as a c-di-NMP Phosphodiesterase.* J Biol Chem, 2016. **291**(7): p. 3668-81.
41. Rao, F., et al., *YybT is a signaling protein that contains a cyclic dinucleotide phosphodiesterase domain and a GGDEF domain with ATPase activity.* J Biol Chem, 2010. **285**(1): p. 473-82.
42. Huynh, T.N., et al., *An HD-domain phosphodiesterase mediates cooperative hydrolysis of c-di-AMP to affect bacterial growth and virulence.* Proc Natl Acad Sci U S A, 2015. **112**(7): p. E747-56.
43. Latoscha, A., et al., *c-di-AMP hydrolysis by the phosphodiesterase AtaC promotes differentiation of multicellular bacteria.* Proc Natl Acad Sci U S A, 2020. **117**(13): p. 7392-7400.

44. Corrigan, R.M., et al., *c-di-AMP is a new second messenger in Staphylococcus aureus with a role in controlling cell size and envelope stress.* PLoS Pathog, 2011. **7**(9): p. e1002217.
45. Braun, F., et al., *Cyclic nucleotides in archaea: Cyclic di-AMP in the archaeon Haloferax volcanii and its putative role.* Microbiologyopen, 2019. **8**(9): p. e00829.
46. Du, B., et al., *Functional analysis of c-di-AMP phosphodiesterase, GdpP, in Streptococcus suis serotype 2.* Microbiol Res, 2014. **169**(9-10): p. 749-58.
47. Oppenheimer-Shaanan, Y., et al., *c-di-AMP reports DNA integrity during sporulation in Bacillus subtilis.* EMBO Rep, 2011. **12**(6): p. 594-601.
48. Devaux, L., et al., *Cyclic di-AMP regulation of osmotic homeostasis is essential in Group B Streptococcus.* PLoS Genet, 2018. **14**(4): p. e1007342.
49. Corrigan, R.M., et al., *Cross-talk between two nucleotide-signaling pathways in Staphylococcus aureus.* J Biol Chem, 2015. **290**(9): p. 5826-39.
50. Mehne, F.M., et al., *Cyclic di-AMP homeostasis in bacillus subtilis: both lack and high level accumulation of the nucleotide are detrimental for cell growth.* J Biol Chem, 2013. **288**(3): p. 2004-17.
51. Witte, C.E., et al., *Cyclic di-AMP is critical for Listeria monocytogenes growth, cell wall homeostasis, and establishment of infection.* mBio, 2013. **4**(3): p. e00282-13.
52. Gundlach, J., et al., *An Essential Poison: Synthesis and Degradation of Cyclic Di-AMP in Bacillus subtilis.* J Bacteriol, 2015. **197**(20): p. 3265-74.
53. Fahmi, T., G.C. Port, and K.H. Cho, *c-di-AMP: An Essential Molecule in the Signaling Pathways that Regulate the Viability and Virulence of Gram-Positive Bacteria.* Genes (Basel), 2017. **8**(8).
54. Commichau, F.M., et al., *Making and Breaking of an Essential Poison: the Cyclases and Phosphodiesterases That Produce and Degrade the Essential Second Messenger Cyclic di-AMP in Bacteria.* J Bacteriol, 2019. **201**(1).
55. Rosenberg, J., et al., *Structural and biochemical analysis of the essential diadenylate cyclase CdaA from Listeria monocytogenes.* J Biol Chem, 2015. **290**(10): p. 6596-606.
56. Tosi, T., et al., *Inhibition of the Staphylococcus aureus c-di-AMP cyclase DacA by direct interaction with the phosphoglucosamine mutase GlmM.* PLoS Pathog, 2019. **15**(1): p. e1007537.
57. Heidemann, J.L., et al., *Crystal structures of the c-di-AMP-synthesizing enzyme CdaA.* J Biol Chem, 2019. **294**(27): p. 10463-10470.
58. Gibhardt, J., et al., *An extracytoplasmic protein and a moonlighting enzyme modulate synthesis of c-di-AMP in Listeria monocytogenes.* Environ Microbiol, 2020. **22**(7): p. 2771-2791.
59. Rismondo, J., et al., *Phenotypes Associated with the Essential Diadenylate Cyclase CdaA and Its Potential Regulator CdaR in the Human Pathogen Listeria monocytogenes.* J Bacteriol, 2016. **198**(3): p. 416-26.
60. Zhu, Y., et al., *Cyclic-di-AMP synthesis by the diadenylate cyclase CdaA is modulated by the peptidoglycan biosynthesis enzyme GlmM in Lactococcus lactis.* Mol Microbiol, 2016. **99**(6): p. 1015-27.
61. Gundlach, J., et al., *Control of potassium homeostasis is an essential function of the second messenger cyclic di-AMP in Bacillus subtilis.* Sci Signal, 2017. **10**(475).
62. Müller, M., et al., *Structural analysis of the diadenylate cyclase reaction of DNA-integrity scanning protein A (DisA) and its inhibition by 3'-dATP.* Biochem J, 2015. **469**(3): p. 367-74.
63. Gandara, C., et al., *Activity and in vivo dynamics of Bacillus subtilis DisA are affected by RadA/Sms and by Holliday junction-processing proteins.* DNA Repair (Amst), 2017. **55**: p. 17-30.
64. Nicolas, P., et al., *Condition-dependent transcriptome reveals high-level regulatory architecture in Bacillus subtilis.* Science, 2012. **335**(6072): p. 1103-6.

65. Mehne, F.M., et al., *Control of the diadenylate cyclase CdaS in Bacillus subtilis: an autoinhibitory domain limits cyclic di-AMP production.* J Biol Chem, 2014. **289**(30): p. 21098-107.
66. Blötz, C., et al., *Identification of the Components Involved in Cyclic Di-AMP Signaling in Mycoplasma pneumoniae.* Front Microbiol, 2017. **8**: p. 1328.
67. Kellenberger, C.A., et al., *RNA-Based Fluorescent Biosensors for Live Cell Imaging of Second Messenger Cyclic di-AMP.* J Am Chem Soc, 2015. **137**(20): p. 6432-5.
68. Huynh, T.N. and J.J. Woodward, *Too much of a good thing: regulated depletion of c-di-AMP in the bacterial cytoplasm.* Curr Opin Microbiol, 2016. **30**: p. 22-29.
69. Bai, Y., et al., *Two DHH subfamily 1 proteins in Streptococcus pneumoniae possess cyclic di-AMP phosphodiesterase activity and affect bacterial growth and virulence.* J Bacteriol, 2013. **195**(22): p. 5123-32.
70. Rao, F., et al., *Unusual heme-binding PAS domain from YybT family proteins.* J Bacteriol, 2011. **193**(7): p. 1543-51.
71. Tan, E., et al., *Solution structure of the PAS domain of a thermophilic YybT protein homolog reveals a potential ligand-binding site.* J Biol Chem, 2013. **288**(17): p. 11949-59.
72. Ausmees, N., et al., *Genetic data indicate that proteins containing the GGDEF domain possess diguanylate cyclase activity.* FEMS Microbiol Lett, 2001. **204**(1): p. 163-7.
73. Bowman, L., et al., *New Insights into the Cyclic Di-adenosine Monophosphate (c-di-AMP) Degradation Pathway and the Requirement of the Cyclic Dinucleotide for Acid Stress Resistance in Staphylococcus aureus.* J Biol Chem, 2016. **291**(53): p. 26970-26986.
74. Drexler, D.J., et al., *Structural and Biophysical Analysis of the Soluble DHH/DHHA1-Type Phosphodiesterase TM1595 from Thermotoga maritima.* Structure, 2017. **25**(12): p. 1887-1897 e4.
75. Ye, M., et al., *DhhP, a cyclic di-AMP phosphodiesterase of Borrelia burgdorferi, is essential for cell growth and virulence.* Infect Immun, 2014. **82**(5): p. 1840-9.
76. Wang, F., et al., *Structural and biochemical characterization of the catalytic domains of GdpP reveals a unified hydrolysis mechanism for the DHH/DHHA1 phosphodiesterase.* Biochem J, 2018. **475**(1): p. 191-205.
77. Andrade, W.A., et al., *Group B Streptococcus Degrades Cyclic-di-AMP to Modulate STING-Dependent Type I Interferon Production.* Cell Host Microbe, 2016. **20**(1): p. 49-59.
78. Woodward, J.J., A.T. Iavarone, and D.A. Portnoy, *c-di-AMP secreted by intracellular Listeria monocytogenes activates a host type I interferon response.* Science, 2010. **328**(5986): p. 1703-5.
79. Pham, H.T., et al., *Enhanced uptake of potassium or glycine betaine or export of cyclic-di-AMP restores osmoresistance in a high cyclic-di-AMP Lactococcus lactis mutant.* PLoS Genet, 2018. **14**(8): p. e1007574.
80. Luo, Y. and J.D. Helmann, *Analysis of the role of Bacillus subtilis sigma(M) in beta-lactam resistance reveals an essential role for c-di-AMP in peptidoglycan homeostasis.* Mol Microbiol, 2012. **83**(3): p. 623-39.
81. St-Onge, R.J., et al., *Nucleotide second messenger-mediated regulation of a muralytic enzyme in Streptomyces.* Mol Microbiol, 2015. **96**(4): p. 779-95.
82. Commichau, F.M., et al., *A Delicate Connection: c-di-AMP Affects Cell Integrity by Controlling Osmolyte Transport.* Trends Microbiol, 2018. **26**(3): p. 175-185.
83. Massa, S.M., et al., *c-di-AMP Accumulation Impairs Muropeptide Synthesis in Listeria monocytogenes.* J Bacteriol, 2020. **202**(24).
84. Rumbaugh, K.P. and K. Sauer, *Biofilm dispersion.* Nat Rev Microbiol, 2020. **18**(10): p. 571-586.
85. Peng, X., et al., *Cyclic di-AMP mediates biofilm formation.* Mol Microbiol, 2016. **99**(5): p. 945-59.

86. Biswas, S. and I. Biswas, *Regulation of the glucosyltransferase (gtfBC) operon by CovR in Streptococcus mutans.* J Bacteriol, 2006. **188**(3): p. 988-98.
87. Townsley, L., et al., *Cyclic di-AMP Acts as an Extracellular Signal That Impacts Bacillus subtilis Biofilm Formation and Plant Attachment.* mBio, 2018. **9**(2).
88. Syed, A.K., et al., *Biofilm Formation by Staphylococcus aureus is Triggered by a Drop in the Levels of the Second Messenger cyclic-di-AMP.* bioRxiv, 2020: p. 2020.01.31.929125.
89. DeFrancesco, A.S., et al., *Genome-wide screen for genes involved in eDNA release during biofilm formation by Staphylococcus aureus.* Proc Natl Acad Sci U S A, 2017. **114**(29): p. E5969-E5978.
90. Fahmi, T., et al., *The Second Messenger c-di-AMP Regulates Diverse Cellular Pathways Involved in Stress Response, Biofilm Formation, Cell Wall Homeostasis, SpeB Expression, and Virulence in Streptococcus pyogenes.* Infect Immun, 2019. **87**(6).
91. Hu, J., et al., *Increased Excess Intracellular Cyclic di-AMP Levels Impair Growth and Virulence of Bacillus anthracis.* J Bacteriol, 2020. **202**(9).
92. Barker, J.R., et al., *STING-dependent recognition of cyclic di-AMP mediates type I interferon responses during Chlamydia trachomatis infection.* mBio, 2013. **4**(3): p. e00018-13.
93. Louie, A., V. Bhandula, and D.A. Portnoy, *Secretion of c-di-AMP by Listeria monocytogenes Leads to a STING-Dependent Antibacterial Response during Enterocolitis.* Infect Immun, 2020. **88**(12).
94. Ahn, J. and G.N. Barber, *STING signaling and host defense against microbial infection.* Exp Mol Med, 2019. **51**(12): p. 1-10.
95. Xia, P., et al., *The ER membrane adaptor ERAdP senses the bacterial second messenger c-di-AMP and initiates anti-bacterial immunity.* Nat Immunol, 2018. **19**(2): p. 141-150.
96. McFarland, A.P., et al., *Sensing of Bacterial Cyclic Dinucleotides by the Oxidoreductase RECON Promotes NF-kappaB Activation and Shapes a Proinflammatory Antibacterial State.* Immunity, 2017. **46**(3): p. 433-445.
97. Bejerano-Sagie, M., et al., *A checkpoint protein that scans the chromosome for damage at the start of sporulation in Bacillus subtilis.* Cell, 2006. **125**(4): p. 679-90.
98. Gundlach, J., et al., *Second Messenger Signaling in Bacillus subtilis: Accumulation of Cyclic di-AMP Inhibits Biofilm Formation.* Front Microbiol, 2016. **7**: p. 804.
99. Gibhardt, J., et al., *c-di-AMP assists osmoadaptation by regulating the Listeria monocytogenes potassium transporters KimA and KtrCD.* J Biol Chem, 2019. **294**(44): p. 16020-16033.
100. Whiteley, A.T., A.J. Pollock, and D.A. Portnoy, *The PAMP c-di-AMP Is Essential for Listeria monocytogenes Growth in Rich but Not Minimal Media due to a Toxic Increase in (p)ppGpp. [corrected].* Cell Host Microbe, 2015. **17**(6): p. 788-98.
101. Peterson, B.N., et al., *(p)ppGpp and c-di-AMP Homeostasis Is Controlled by CbpB in Listeria monocytogenes.* mBio, 2020. **11**(4).
102. Kruger, L., et al., *A meet-up of two second messengers: the c-di-AMP receptor DarB controls (p)ppGpp synthesis in Bacillus subtilis.* Nat Commun, 2021. **12**(1): p. 1210.
103. Choi, P.H., et al., *Structural and functional studies of pyruvate carboxylase regulation by cyclic di-AMP in lactic acid bacteria.* Proc Natl Acad Sci U S A, 2017. **114**(35): p. E7226-E7235.
104. Zhang, L., W. Li, and Z.G. He, *DarR, a TetR-like transcriptional factor, is a cyclic di-AMP-responsive repressor in Mycobacterium smegmatis.* J Biol Chem, 2013. **288**(5): p. 3085-96.
105. Kruger, L., et al., *Essentiality of c-di-AMP in Bacillus subtilis: Bypassing mutations converge in potassium and glutamate homeostasis.* PLoS Genet, 2021. **17**(1): p. e1009092.
106. Whatmore, A.M. and R.H. Reed, *Determination of turgor pressure in Bacillus subtilis: a possible role for K+ in turgor regulation.* J Gen Microbiol, 1990. **136**(12): p. 2521-6.
107. Sleator, R.D. and C. Hill, *Bacterial osmoadaptation: the role of osmolytes in bacterial stress and virulence.* FEMS Microbiol Rev, 2002. **26**(1): p. 49-71.

108. Zeden, M.S., et al., *Cyclic di-adenosine monophosphate (c-di-AMP) is required for osmotic regulation in Staphylococcus aureus but dispensable for viability in anaerobic conditions.* J Biol Chem, 2018. **293**(9): p. 3180-3200.
109. Zarrella, T.M., D.W. Metzger, and G. Bai, *Stress Suppressor Screening Leads to Detection of Regulation of Cyclic di-AMP Homeostasis by a Trk Family Effector Protein in Streptococcus pneumoniae.* J Bacteriol, 2018. **200**(12).
110. Vieira-Pires, R.S., A. Szollosi, and J.H. Morais-Cabral, *The structure of the KtrAB potassium transporter.* Nature, 2013. **496**(7445): p. 323-8.
111. Diskowski, M., et al., *Helical jackknives control the gates of the double-pore K(+) uptake system KtrAB.* Elife, 2017. **6**.
112. Oberkampf, M., et al., *c-di-AMP signaling is required for bile salts resistance and long-term colonization by Clostridioides difficile.* bioRxiv, 2021.
113. Rocha, R., et al., *Characterization of the molecular properties of KtrC, a second RCK domain that regulates a Ktr channel in Bacillus subtilis.* J Struct Biol, 2019. **205**(3): p. 34-43.
114. Bai, Y., et al., *Cyclic di-AMP impairs potassium uptake mediated by a cyclic di-AMP binding protein in Streptococcus pneumoniae.* J Bacteriol, 2014. **196**(3): p. 614-23.
115. Kim, H., et al., *Structural Studies of Potassium Transport Protein KtrA Regulator of Conductance of K+ (RCK) C Domain in Complex with Cyclic Diadenosine Monophosphate (c-di-AMP).* J Biol Chem, 2015. **290**(26): p. 16393-402.
116. Nelson, J.W., et al., *Riboswitches in eubacteria sense the second messenger c-di-AMP.* Nat Chem Biol, 2013. **9**(12): p. 834-9.
117. Tascon, I., et al., *Structural basis of proton-coupled potassium transport in the KUP family.* Nat Commun, 2020. **11**(1): p. 626.
118. Gundlach, J., et al., *Sustained sensing in potassium homeostasis: Cyclic di-AMP controls potassium uptake by KimA at the levels of expression and activity.* J Biol Chem, 2019. **294**(24): p. 9605-9614.
119. He, J., et al., *Cyclic di-AMP, a second messenger of primary importance: tertiary structures and binding mechanisms.* Nucleic Acids Res, 2020. **48**(6): p. 2807-2829.
120. Quintana, I.M., et al., *The KupA and KupB Proteins of Lactococcus lactis IL1403 Are Novel c-di-AMP Receptor Proteins Responsible for Potassium Uptake.* J Bacteriol, 2019. **201**(10).
121. Wang, X., et al., *A c-di-AMP riboswitch controlling kdpFABC operon transcription regulates the potassium transporter system in Bacillus thuringiensis.* Commun Biol, 2019. **2**: p. 151.
122. Moscoso, J.A., et al., *Binding of Cyclic Di-AMP to the Staphylococcus aureus Sensor Kinase KdpD Occurs via the Universal Stress Protein Domain and Downregulates the Expression of the Kdp Potassium Transporter.* J Bacteriol, 2016. **198**(1): p. 98-110.
123. Chin, K.H., et al., *Structural Insights into the Distinct Binding Mode of Cyclic Di-AMP with SaCpaA_RCK.* Biochemistry, 2015. **54**(31): p. 4936-51.
124. Fujisawa, M., Y. Wada, and M. Ito, *Modulation of the K+ efflux activity of Bacillus subtilis YhaU by YhaT and the C-terminal region of YhaS.* FEMS Microbiol Lett, 2004. **231**(2): p. 211-7.
125. Cereija, T.B., et al., *c-di-AMP, a likely master regulator of bacterial K(+) homeostasis machinery, activates a K(+) exporter.* Proc Natl Acad Sci U S A, 2021. **118**(14).
126. Huynh, T.N., et al., *Cyclic di-AMP targets the cystathionine beta-synthase domain of the osmolyte transporter OpuC.* Mol Microbiol, 2016. **102**(2): p. 233-243.
127. Schuster, C.F., et al., *The second messenger c-di-AMP inhibits the osmolyte uptake system OpuC in Staphylococcus aureus.* Sci Signal, 2016. **9**(441): p. ra81.
128. Locher, K.P., *Mechanistic diversity in ATP-binding cassette (ABC) transporters.* Nat Struct Mol Biol, 2016. **23**(6): p. 487-93.
129. Patzlaff, J.S., T. van der Heide, and B. Poolman, *The ATP/substrate stoichiometry of the ATP-binding cassette (ABC) transporter OpuA.* J Biol Chem, 2003. **278**(32): p. 29546-51.

130. van der Heide, T. and B. Poolman, *ABC transporters: one, two or four extracytoplasmic substrate-binding sites?* EMBO Rep, 2002. **3**(10): p. 938-43.
131. Obis, D., et al., *Genetic and biochemical characterization of a high-affinity betaine uptake system (BusA) in Lactococcus lactis reveals a new functional organization within bacterial ABC transporters.* J Bacteriol, 1999. **181**(20): p. 6238-46.
132. van der Heide, T., M.C. Stuart, and B. Poolman, *On the osmotic signal and osmosensing mechanism of an ABC transport system for glycine betaine.* EMBO J, 2001. **20**(24): p. 7022-32.
133. Karasawa, A., et al., *Physicochemical factors controlling the activity and energy coupling of an ionic strength-gated ATP-binding cassette (ABC) transporter.* J Biol Chem, 2013. **288**(41): p. 29862-71.
134. Sikkema, H.R., et al., *Gating by ionic strength and safety check by cyclic-di-AMP in the ABC transporter OpuA.* Sci Adv, 2020. **6**(47).
135. Stülke, J. and L. Krüger, *Cyclic di-AMP Signaling in Bacteria.* Annu Rev Microbiol, 2020. **74**: p. 159-179.
136. Ronzheimer, S., et al., *The GbsR Family of Transcriptional Regulators: Functional Characterization of the OpuAR Repressor.* Front Microbiol, 2018. **9**: p. 2536.
137. Romeo, Y., et al., *Osmoregulation in Lactococcus lactis: BusR, a transcriptional repressor of the glycine betaine uptake system BusA.* Mol Microbiol, 2003. **47**(4): p. 1135-47.
138. Romeo, Y., J. Bouvier, and C. Gutierrez, *Osmotic regulation of transcription in Lactococcus lactis: ionic strength-dependent binding of the BusR repressor to the busA promoter.* FEBS Lett, 2007. **581**(18): p. 3387-90.
139. Teixeira-Duarte, C.M., F. Fonseca, and J.H. Morais-Cabral, *Activation of a nucleotide-dependent RCK domain requires binding of a cation cofactor to a conserved site.* Elife, 2019. **8**.
140. Cong, X., et al., *Crystal structures of porcine STING(CBD)-CDN complexes reveal the mechanism of ligand recognition and discrimination of STING proteins.* J Biol Chem, 2019. **294**(30): p. 11420-11432.
141. Ereno-Orbea, J., I. Oyenarte, and L.A. Martinez-Cruz, *CBS domains: Ligand binding sites and conformational variability.* Arch Biochem Biophys, 2013. **540**(1-2): p. 70-81.
142. Mahmood, N.A., E. Biemans-Oldehinkel, and B. Poolman, *Engineering of ion sensing by the cystathionine beta-synthase module of the ABC transporter OpuA.* J Biol Chem, 2009. **284**(21): p. 14368-76.
143. Tkaczuk, K.L., et al., *Structural and functional insight into the universal stress protein family.* Evol Appl, 2013. **6**(3): p. 434-49.
144. Banerjee, A., et al., *A universal stress protein (USP) in mycobacteria binds cAMP.* J Biol Chem, 2015. **290**(20): p. 12731-43.
145. Dutta, A., M. Batish, and V. Parashar, *Structural basis of KdpD histidine kinase binding to the second messenger c-di-AMP.* J Biol Chem, 2021. **296**: p. 100771.
146. Commichau, F.M., et al., *A jack of all trades: the multiple roles of the unique essential second messenger cyclic di-AMP.* Mol Microbiol, 2015. **97**(2): p. 189-204.
147. Ren, A. and D.J. Patel, *c-di-AMP binds the ydaO riboswitch in two pseudo-symmetry-related pockets.* Nat Chem Biol, 2014. **10**(9): p. 780-6.
148. Jones, C.P. and A.R. Ferre-D'Amare, *Crystal structure of a c-di-AMP riboswitch reveals an internally pseudo-dimeric RNA.* EMBO J, 2014. **33**(22): p. 2692-703.
149. Gao, A. and A. Serganov, *Structural insights into recognition of c-di-AMP by the ydaO riboswitch.* Nat Chem Biol, 2014. **10**(9): p. 787-92.
150. Choi, P.H., et al., *Molecular basis for the recognition of cyclic-di-AMP by PstA, a PII-like signal transduction protein.* Microbiologyopen, 2015. **4**(3): p. 361-74.
151. Gundlach, J., et al., *Identification, characterization, and structure analysis of the cyclic di-AMP-binding PII-like signal transduction protein DarA.* J Biol Chem, 2015. **290**(5): p. 3069-80.

152. Campeotto, I., et al., *Complex structure and biochemical characterization of the Staphylococcus aureus cyclic diadenylate monophosphate (c-di-AMP)-binding protein PstA, the founding member of a new signal transduction protein family.* J Biol Chem, 2015. **290**(5): p. 2888-901.
153. Muller, M., K.P. Hopfner, and G. Witte, *c-di-AMP recognition by Staphylococcus aureus PstA.* FEBS Lett, 2015. **589**(1): p. 45-51.
154. Seshasayee, A.S., K. Sivaraman, and N.M. Luscombe, *An overview of prokaryotic transcription factors : a summary of function and occurrence in bacterial genomes.* Subcell Biochem, 2011. **52**: p. 7-23.
155. Fic, E., et al., *cAMP receptor protein from escherichia coli as a model of signal transduction in proteins--a review.* J Mol Microbiol Biotechnol, 2009. **17**(1): p. 1-11.
156. Lewis, M., *The lac repressor.* C R Biol, 2005. **328**(6): p. 521-48.
157. Liu, B., et al., *Structural basis of bacterial transcription activation.* Science, 2017. **358**(6365): p. 947-951.
158. Fang, C., et al., *The bacterial multidrug resistance regulator BmrR distorts promoter DNA to activate transcription.* Nat Commun, 2020. **11**(1): p. 6284.
159. Browning, D.F., M. Butala, and S.J.W. Busby, *Bacterial Transcription Factors: Regulation by Pick "N" Mix.* J Mol Biol, 2019. **431**(20): p. 4067-4077.
160. Haydon, D.J. and J.R. Guest, *A new family of bacterial regulatory proteins.* FEMS Microbiol Lett, 1991. **63**(2-3): p. 291-5.
161. Hoskisson, P.A. and S. Rigali, *Chapter 1: Variation in form and function the helix-turn-helix regulators of the GntR superfamily.* Adv Appl Microbiol, 2009. **69**: p. 1-22.
162. Jain, D., *Allosteric control of transcription in GntR family of transcription regulators: A structural overview.* IUBMB Life, 2015. **67**(7): p. 556-63.
163. Fillenberg, S.B., et al., *Structural insight into operator dre-sites recognition and effector binding in the GntR/HutC transcription regulator NagR.* Nucleic Acids Res, 2015. **43**(2): p. 1283-96.
164. van Aalten, D.M., C.C. DiRusso, and J. Knudsen, *The structural basis of acyl coenzyme A-dependent regulation of the transcription factor FadR.* EMBO J, 2001. **20**(8): p. 2041-50.
165. Okuda, K., et al., *Role of the aminotransferase domain in Bacillus subtilis GabR, a pyridoxal 5'-phosphate-dependent transcriptional regulator.* Mol Microbiol, 2015. **95**(2): p. 245-57.
166. Gao, Y.G., et al., *The structures of transcription factor CGL2947 from Corynebacterium glutamicum in two crystal forms: a novel homodimer assembling and the implication for effector-binding mode.* Protein Sci, 2007. **16**(9): p. 1878-86.
167. Jain, D. and D.T. Nair, *Spacing between core recognition motifs determines relative orientation of AraR monomers on bipartite operators.* Nucleic Acids Res, 2013. **41**(1): p. 639-47.
168. Lee, M.H., et al., *PlmA, a new member of the GntR family, has plasmid maintenance functions in Anabaena sp. strain PCC 7120.* J Bacteriol, 2003. **185**(15): p. 4315-25.
169. Hoskisson, P.A., et al., *DevA, a GntR-like transcriptional regulator required for development in Streptomyces coelicolor.* J Bacteriol, 2006. **188**(14): p. 5014-23.
170. Mistry, J., et al., *Pfam: The protein families database in 2021.* Nucleic Acids Res, 2021. **49**(D1): p. D412-D419.
171. Rigali, S., et al., *Subdivision of the helix-turn-helix GntR family of bacterial regulators in the FadR, HutC, MocR, and YtrA subfamilies.* J Biol Chem, 2002. **277**(15): p. 12507-15.
172. DiRusso, C.C. and T. Nystrom, *The fats of Escherichia coli during infancy and old age: regulation by global regulators, alarmones and lipid intermediates.* Mol Microbiol, 1998. **27**(1): p. 1-8.
173. Henry, M.F. and J.E. Cronan, Jr., *Escherichia coli transcription factor that both activates fatty acid synthesis and represses fatty acid degradation.* J Mol Biol, 1991. **222**(4): p. 843-9.

174. Vigouroux, A., et al., *Characterization of the first tetrameric transcription factor of the GntR superfamily with allosteric regulation from the bacterial pathogen Agrobacterium fabrum.* Nucleic Acids Res, 2021. **49**(1): p. 529-546.
175. Rigali, S., et al., *Extending the classification of bacterial transcription factors beyond the helix-turn-helix motif as an alternative approach to discover new cis/trans relationships.* Nucleic Acids Res, 2004. **32**(11): p. 3418-26.
176. Brown, N.L., et al., *The MerR family of transcriptional regulators.* FEMS Microbiol Rev, 2003. **27**(2-3): p. 145-63.
177. Lund, P.A., S.J. Ford, and N.L. Brown, *Transcriptional regulation of the mercury-resistance genes of transposon Tn501.* J Gen Microbiol, 1986. **132**(2): p. 465-80.
178. Chang, C.C., et al., *Structural basis of the mercury(II)-mediated conformational switching of the dual-function transcriptional regulator MerR.* Nucleic Acids Res, 2015. **43**(15): p. 7612-23.
179. Ahmed, M., et al., *A protein that activates expression of a multidrug efflux transporter upon binding the transporter substrates.* J Biol Chem, 1994. **269**(45): p. 28506-13.
180. Markham, P.N., J. LoGuidice, and A.A. Neyfakh, *Broad ligand specificity of the transcriptional regulator of the Bacillus subtilis multidrug transporter Bmr.* Biochem Biophys Res Commun, 1997. **239**(1): p. 269-72.
181. Bachas, S., et al., *Structural contributions to multidrug recognition in the multidrug resistance (MDR) gene regulator, BmrR.* Proc Natl Acad Sci U S A, 2011. **108**(27): p. 11046-51.
182. Kumaraswami, M., K.J. Newberry, and R.G. Brennan, *Conformational plasticity of the coiled-coil domain of BmrR is required for bmr operator binding: the structure of unliganded BmrR.* J Mol Biol, 2010. **398**(2): p. 264-75.
183. Heldwein, E.E. and R.G. Brennan, *Crystal structure of the transcription activator BmrR bound to DNA and a drug.* Nature, 2001. **409**(6818): p. 378-82.
184. Newberry, K.J., et al., *Structures of BmrR-drug complexes reveal a rigid multidrug binding pocket and transcription activation through tyrosine expulsion.* J Biol Chem, 2008. **283**(39): p. 26795-804.
185. Liao, J. and K. Sauer, *The MerR-like transcriptional regulator BrlR contributes to Pseudomonas aeruginosa biofilm tolerance.* J Bacteriol, 2012. **194**(18): p. 4823-36.
186. Liao, J., M.J. Schurr, and K. Sauer, *The MerR-like regulator BrlR confers biofilm tolerance by activating multidrug efflux pumps in Pseudomonas aeruginosa biofilms.* J Bacteriol, 2013. **195**(15): p. 3352-63.
187. Wang, F., et al., *BrlR from Pseudomonas aeruginosa is a receptor for both cyclic di-GMP and pyocyanin.* Nat Commun, 2018. **9**(1): p. 2563.
188. Chambers, J.R., et al., *BrlR from Pseudomonas aeruginosa is a c-di-GMP-responsive transcription factor.* Mol Microbiol, 2014. **92**(3): p. 471-87.
189. Bandera, A.M., et al., *BusR senses bipartite DNA binding motifs by a unique molecular ruler architecture.* Nucleic Acids Res, 2021.
190. Kemp, M.T., E.M. Lewandowski, and Y. Chen, *Low barrier hydrogen bonds in protein structure and function.* Biochim Biophys Acta Proteins Proteom, 2021. **1869**(1): p. 140557.
191. Szollosi, A., et al., *Dissecting the Molecular Mechanism of Nucleotide-Dependent Activation of the KtrAB K+ Transporter.* PLoS Biol, 2016. **14**(1): p. e1002356.
192. Lemmens, L., et al., *YtrASa, a GntR-Family Transcription Factor, Represses Two Genetic Loci Encoding Membrane Proteins in Sulfolobus acidocaldarius.* Front Microbiol, 2019. **10**: p. 2084.
193. Halford, S.E. and J.F. Marko, *How do site-specific DNA-binding proteins find their targets?* Nucleic Acids Res, 2004. **32**(10): p. 3040-52.
194. Stracy, M., et al., *Transient non-specific DNA binding dominates the target search of bacterial DNA-binding proteins.* Mol Cell, 2021. **81**(7): p. 1499-1514 e6.

195. Williams, C.L., et al., *BvgA functions as both an activator and a repressor to control Bvg phase expression of bipA in Bordetella pertussis.* Mol Microbiol, 2005. **56**(1): p. 175-88.
196. Stoyanov, J.V., J.L. Hobman, and N.L. Brown, *CueR (YbbI) of Escherichia coli is a MerR family regulator controlling expression of the copper exporter CopA.* Mol Microbiol, 2001. **39**(2): p. 502-11.
197. Martell, D.J., et al., *Metalloregulator CueR biases RNA polymerase's kinetic sampling of dead-end or open complex to repress or activate transcription.* Proc Natl Acad Sci U S A, 2015. **112**(44): p. 13467-72.
198. Murakami, K.S., S. Masuda, and S.A. Darst, *Structural basis of transcription initiation: RNA polymerase holoenzyme at 4 A resolution.* Science, 2002. **296**(5571): p. 1280-4.
199. Grainger, D.C., et al., *Selective repression by Fis and H-NS at the Escherichia coli dps promoter.* Mol Microbiol, 2008. **68**(6): p. 1366-77.
200. Hinkel, D. and E. Bremer, *Osmotisch bedingter Stress in Bacillus subtilis - C-di-AMP, der Regulator für die Aufnahme osmotischer Schutzsubstanzen?* Philipps-Universität Marburg, 2020.
201. Jumper, J., et al., *Highly accurate protein structure prediction with AlphaFold.* Nature, 2021.
202. Mirdita, M., M. Steinegger, and J. Soding, *MMseqs2 desktop and local web server app for fast, interactive sequence searches.* Bioinformatics, 2019. **35**(16): p. 2856-2858.

6 Supplement – full text publications

6.1 Supplement I - BusR Senses Bipartite DNA Binding Motifs by a Unique Molecular Ruler Architecture

Bandera, A. M.; Bartho J.; Lammens K.; Drexler D.; Kleinschwärzer J.; Hopfner K. P.; Witte G. BusR Senses Bipartite DNA Binding Motifs by a Unique Molecular Ruler Architecture. *Nucleic Acids Research*, **2021**, *49* (17), 10166–10177

DOI: https://doi.org/10.1093/nar/gkab736

URL: https://academic.oup.com/nar/advance-article/doi/10.1093/nar/gkab736/6357733

Nucleic Acids Research, 2021 **1**
https://doi.org/10.1093/nar/gkab736

BusR senses bipartite DNA binding motifs by a unique molecular ruler architecture

Adrian M. Bandera[1,2], Joseph Bartho[1,2], Katja Lammens[1,2], David Jan Drexler[1,2], Jasmin Kleinschwärzer[1,2], Karl-Peter Hopfner[1,2] and Gregor Witte[1,2,*]

[1]Gene Center, Ludwig-Maximilians-Universität München, Feodor-Lynen-Str. 25, D-81377 München, Germany and [2]Department of Biochemistry, Ludwig-Maximilians-Universität München, Feodor-Lynen-Str. 25, D-81377 München, Germany

Received February 24, 2021; Revised July 27, 2021; Editorial Decision July 28, 2021; Accepted August 12, 2021

ABSTRACT

The cyclic dinucleotide second messenger c-di-AMP is a major player in regulation of potassium homeostasis and osmolyte transport in a variety of bacteria. Along with various direct interactions with proteins such as potassium channels, the second messenger also specifically binds to transcription factors, thereby altering the processes in the cell on the transcriptional level. We here describe the structural and biochemical characterization of BusR from the human pathogen *Streptococcus agalactiae*. BusR is a member of a yet structurally uncharacterized subfamily of the GntR family of transcription factors that downregulates transcription of the genes for the BusA (OpuA) glycine-betaine transporter upon c-di-AMP binding. We report crystal structures of full-length BusR, its apo and c-di-AMP bound effector domain, as well as cryo-EM structures of BusR bound to its operator DNA. Our structural data, supported by biochemical and biophysical data, reveal that BusR utilizes a unique domain assembly with a tetrameric coiled-coil in between the binding platforms, serving as a molecular ruler to specifically recognize a 22 bp separated bipartite binding motif. Binding of c-di-AMP to BusR induces a shift in equilibrium from an inactivated towards an activated state that allows BusR to bind the target DNA, leading to transcriptional repression.

GRAPHICAL ABSTRACT

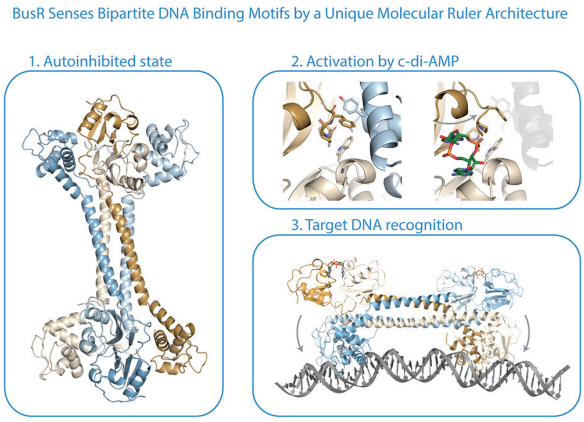

INTRODUCTION

The bacterial cyclic dinucleotide second messenger c-di-AMP was discovered in 2008 in the crystal structure of the DNA-integrity scanning protein DisA (1). Initially, DisA and c-di-AMP were identified as a checkpoint protein or signal for maintaining DNA-integrity in *Bacillus subtilis*, and to be responsible for delay in sporulation upon DNA-damage (2,3). The identification of c-di-AMP initiated a new field in microbial signaling research, which has since become well-established. The role of c-di-AMP in the context of the bacterial cell is now increasingly clear, but many signaling pathways are still to be explored in detail (4). Aside from its role in DNA maintenance, c-di-AMP has been linked to cell wall integrity, potassium and osmotic homeostasis, virulence, sporulation and biofilm formation (5–7). The c-di-AMP pathway is present in many gram-positive bacteria and also archaea, and occurs in a plethora of pathogens including *Staphylococcus aureus* (including MRSA), *Bacillus anthracis*, *Listeria monocytogenes*,

*To whom correspondence should be addressed. Tel: +49 89 2180 76988; Email: witte@genzentrum.lmu.de

Streptococcus pneumoniae and *Mycobacterium tuberculosis*, among others (8–11).

In brief, the cyclic dinucleotide is synthesized by di-adenylate cyclase domain (DAC) carrying proteins, can be bound by a variety of c-di-AMP receptors (proteins and riboswitches), and is either degraded by specific phospho-diesterases or is exported out of the cell. The group of DAC-proteins can be split up in three major classes, DacA, cdaS and DisA (1,12,13). Degradation of c-di-AMP is carried out by three families of phosphodiesterases (PDEs), namely PgpH-type PDEs belonging to the family of 7TMR membrane proteins with a cytosolic HD-domain that is the catalytically active PDE domain, the recently discovered actinobacterial manganese dependent PDE AtaC, and two types of DHH-type PDEs (14–17).

The correct concentration of c-di-AMP in cells is essential under normal growth conditions - both too low and too high concentrations result in severe effects on the viability of the cells (8,18–20). Altering c-di-AMP levels in the cells and thus disturbing its regulated processes has been shown to also alter resistance or susceptibility against antibiotics (21,22). For example, a methicillin resistant *S. aureus* strain that was depleted of c-di-AMP became sensitive again against β-lactam antibiotics (23). This renders the c-di-AMP pathway a remarkable target for antimicrobial therapies.

Once synthesized and available in the cells, c-di-AMP regulates many processes that are connected to K^+-homeostasis and osmotic regulators such as compatible solute importers (24,25). A viable cell needs to balance its turgor to cope with the continuously changing osmolarity of its environment. The turgor needs to be efficiently controlled as upshifts or downshifts of osmolarity would rapidly lead to dehydration or cell lysis. One approach used by many organisms in response to hyperosmotic stress is to rapidly increase the uptake of ions (26). In this respect, c-di-AMP has been shown to control potassium uptake on multiple levels. c-di-AMP binds to different subunits of potassium transporters (e.g. KtrAB, KtrCD, KimA, CpaA, KhtTU) and decreases or increases uptake or export of ions, respectively (27–32). Furthermore, gene expression of potassium transporters has been shown to be under the control of c-di-AMP, either via a c-di-AMP sensitive riboswitch (e.g. kimA, ktrAB, kdpFABC) or via a two-component system (e.g. kdpABC via kdpDE) (25,33–35). In many organsims, uptake of potassium is the first response to osmotic upshift. Meanwhile, compatible solutes, e.g. proline or glycine-betaine, are either imported or synthesized. C-di-AMP deficient strains of *S. aureus*, *L. monocytogenes* or *S. agalactiae* have been shown to acquire mutations that affect the uptake of osmolytes (21,36,37). Furthermore, c-di-AMP has been shown to repress gene transcription for osmolyte uptake systems, e.g. *busA* from *S. agalactiae* and *Lactococcus lactis*, as well as to decrease the activity of osmolyte transporters like OpuC and *L. lactis* BusA (37–40). These findings show that c-di-AMP is a key regulator of osmolyte homeostasis that regulates osmolarity at multiple levels.

To get more detailed molecular insights into how these processes are regulated by c-di-AMP, we here focus on the role of c-di-AMP in transcriptional regulation. Aside from the TetR-like transcription factor DarR, BusR is the second transcription factor that has recently been linked to c-di-AMP (37,39,41). BusR is a member of the GntR family, which can be split into several subfamilies according to their C-terminal effector and oligomerization domains. Prominent subfamilies include FadR, HutC, MocR, YtrA and AraR (42–44). Based on the current classifications for these subfamilies BusR cannot be sorted into any of these and most likely comprises a subfamily of its own. BusR satisfies the overall domain architecture of the GntR family with its N-terminal winged helix-turn-helix motif (wHTH) and a C-terminal effector binding motif, an RCK_C domain (regulator of K^+ conductance). This domain is known for binding c-di-AMP and is often utilized by c-di-AMP regulated potassium transporters (e.g. KtrA, KtrC, CpaA, KhtT) (27,28,32,45). In BusR, the wHTH and RCK_C domains are predicted to be connected by a coiled-coil region. *In vitro*, BusR represses the transcription of the *busA* operon in *L. lactis* in an osmolarity dependent manner (46,47). BusA is a glycine-betaine transporter crucial for responding to osmotic stress. A high amount of c-di-AMP leads to reduced expression of the transporter and thus less osmolyte uptake, while in the absence of c-di-AMP *busA* is constitutively expressed (37). Even though BusR is regulated by a second messenger which could imply a more global role, further targets of BusR have not yet been experimentally characterized. However, additional regulons for BusR in *L. lactis* subsp. *lactis* IO-1 were predicted by phylogenetic footprinting. These include *arsC*, an arsenic reductase, *hom (thrA)* and *thrB*. All three genes can be linked to osmotic homeostasis (48).

Here, we provide a biochemical and structural analysis of *Streptococcus agalactiae* BusR (SgaBusR). We present structures of apo, ligand bound and operator DNA bound states. We propose a mechanism for regulation and high binding specificity based on a molecular ruler guided site recognition, unseen in other GntR family members so far.

MATERIALS AND METHODS

Cloning, expression and purification of SgaBusR

The gene encoding BusR from *S. agalactiae* (DSM 16828) was cloned into a modified pET47b (Novagen) expression vector including an N-terminal (6x)His-MBP tag and a PreScission protease cleavage site (pET47b-MBP) (49). Point mutations were introduced by PCR amplification. For protein expression transformed *Escherichia coli* (DE3) Rosetta were grown in Turbo Broth™ (Molecular Dimensions) at 37°C to OD_{600} of 0.8, cooled down to 18°C and induced with 0.2 mM Isopropyl-β-D-thiogalactopyranosid (IPTG) at OD_{600} of 1.3 for overnight expression.

For selenomethionine expression, methionine auxotroph B834 Rosetta cells were grown in SelenoMethionine Medium Complete (Molecular Dimensions). Protein expression was induced at OD_{600} of 0.8. Purification of selenomethionine substituted protein was performed according to the purification of native protein with the exception of 5 mM β-mercaptoethanol in all buffers.

Cell pellets with overexpressed His-MBP-BusR constructs were resuspended in buffer A (100 mM NaP_i pH 6.5, 200 mM NaCl, 20 mM imidazole, 5% glycerol) and

lysed by sonication. The lysate was cleared by centrifugation and filtration and loaded onto a 5 ml Ni-NTA column (Cytiva). The sample was washed with buffer HS (100 mM NaP_i pH 6.5, 1 M NaCl, 20 mM imidazole, 5% (v/v) glycerol) and buffer B_{50} (100 mM NaP_i pH 6.5, 200 mM NaCl, 50 mM imidazole, 5% (v/v) glycerol) and eluted with buffer B (100 mM NaP_i pH 6.5, 200 mM NaCl, 500 mM imidazole, 5% (v/v) glycerol). PreScission protease was added to the eluent prior to dialysis against buffer A at 8°C overnight. The protein was loaded onto a 5 ml Heparin column (Cytiva) and eluted using buffer HS and directly passed through a 5 ml Ni-NTA column (Cytiva) for removal of any non-digested species. The flow-through was collected and as a polishing step size exclusion chromatography (SEC) was conducted using a HiLoad Superdex S200 column (Cytiva, S75 for small constructs) preequilibrated in buffer SEC (30 mM NaP_i pH 6.5, 200 mM NaCl, 3% (v/v) glycerol). For all samples intended for crystallization trials buffer H (30 mM HEPES pH 7.0, 200 mM NaCl) was used for SEC instead. All steps were analyzed by SDS-PAGE. Protein concentration was determined spectrophotometrically using the theoretical molar extinction coefficient calculated from amino acid composition (50). All concentrations are given in tetramers unless otherwise stated. The protein was concentrated to 10 mg/ml and flash frozen in liquid nitrogen and stored at -80°C. RCK_C constructs were purified in an altered way. After Ni-NTA, samples were directly applied to size exclusion chromatography using buffer H. For crystallization of the ligand bound state, the His-tag was removed by PreScission protease (Cytiva) cleavage prior to size exclusion chromatography.

Small-angle X-ray scattering

Small-angle scattering data were either obtained by batch mode data collection, i.e. a sample (between 1 and 14 mg/ml) and the respective buffer (30 mM HEPES pH 7.5, 100 mM NaCl) were measured in alternating steps, or in size-exclusion chromatography coupled SAXS (SEC-SAXS) with the running buffer as reference. Full length BusR was measured in 20 mM HEPES pH 7.5, 200 mM NaCl, 3% glycerol (v/v). BusR:c-di-AMP:pAB1 was measured in 20 mM HEPES pH 6.5, 100 mM NaCl, 3% glycerol (v/v). Measurements were done at the P12 SAXS beamline at the PETRA III storage ring (EMBL Hamburg, DESY Hamburg). Data were processed using CHROMIXS and PRIMUS of the ATSAS suite (51) and analyzed as reviewed in (52,53). Data were checked for aggregation by Guinier-plot analysis (Guinier approximation in the $s^*R_G < 1.3$ region). Theoretical scattering curves were calculated from atomic models using CRYSOL (51). SAXS data have been deposited into the SASBDB database with accession numbers SASDK74 (RCK_C domain dimer), SASDK84 (BusR) and SASDK94 (BusR:cdiAMP:pAB1-complex).

Crystallization and structure determination

All crystals were obtained using hanging-drop vapor diffusion in a 1:1 mixture of purification buffer and crystallization solution at 20°C. Full-length selenomethionine substituted BusR crystals were grown at 7 mg/ml in 150 mM magnesium-acetate and 6% D + trehalose. Crystals were subjected to mother liquor containing 35% ethylene glycol and subsequently flash frozen in liquid nitrogen. Apo His_6-RCK_C crystals were grown at 6 mg/mL in 0.1 M Bis–Tris pH 6.5, 18% (w/v) PEG MME 5000. For the ligand bound state 4.5 mg/mL BusR RCK_C (no His_6-tag) was co-crystallized with 1 mM c-di-AMP in 100 mM sodium-acetate pH 4.6, 3% PEG 4000. 30% PEG 400 was used as cryoprotectant for both crystals. Crystals were measured at the EMBL Hamburg P13 and P14 beamlines at PETRA III storage ring (DESY Hamburg) at 100 K. Data were indexed, integrated and scaled using XDS/XSCALE (54). HKL2MAP (55)/SHELX (56) were used for experimental phasing of the full length dataset collected at selenium peak wavelength. Initial model building was done automatically using Buccaneer (57). Manual building was continued in COOT (58) and refinement was performed in PHENIX (59). Phases for the RCK_C constructs were obtained by molecular replacement using the RCK_C domain of the full-length structure as search model in PHASER/PHENIX (59). Data collection and refinement statistics are provided in Supplementary Table S1. Buried surface area between substructures was calculated using the PISA server (60).

Cryo-electron microscopy

A 152 bp long DNA substrate containing pAB1 and pAB2 (called pAB) was amplified from genomic DNA by PCR and purified by PCR clean up (Macherey & Nagel). 0.4 mg/ml of BusR were incubated with 0.2 mg/mL DNA and 100 μM c-di-AMP in 20 mM HEPES pH 6.5, 100 mM NaCl. Prior to grid preparation β-octyl glucoside was added to a final concentration of 0.05%. 4.5 μl of sample was applied to plasma cleaned (GloCube, Quorum) QuantiFoil R2/1 200 mesh holey carbon grids (Quantifoil) and plunge frozen in liquid ethane using a Leica EM GP. Data was acquired using a Titan Krios transmission electron microscope (Thermo Fisher Scientific) operated at 300 keV, with a Gatan K2 Summit detector operated in counting mode, and Gatan GIF Quantum energy filter. EPU software (TFS) was used for automated acquisition. 9381 micrographs with a nominal magnification of 130 000×, calibrated pixel size of 1.046 Å, defocus range of −1.1 to −2.6 μm, and a total dose of 45 $e^-/Å^2$ over 40 frames were collected. For data processing all micrographs were aligned using Motioncor2 (61). The subsequent steps were done in cryoSPARC v3.2 (62). Local CTF estimation was done with CTFFIND4 implemented in cryoSPARC. Initial particles were picked using blob picker. These particles were 2D classified, and high quality and diverse classes were selected and low pass filtered to 20 Å for training of the topaz neural network picker embedded in cryoSPARC (63,64). The topaz picked particles were extracted and resubjected to 2D classification and topaz training. Final extraction was done with a box size of 256 pixels and particles were subjected to 2D classification. Classes of good resolution were selected and used to generate an initial 3D model (C1). The best volume was used as a reference in Relion 3.1 for further 3D classification (65). The best 3D classes were selected and used for 3D refinement. After polishing and CTF Refinement,

fixed angle 3D classification was performed using a mask that excludes the protruding DNA. 3D refinement and post processing using the same mask resulted in a final resolution estimate of 4.46 Å. Model building was done by using the crystallographic full-length structure of BusR and the c-di-AMP bound RCK_C domain structure (both this work). These models were rigid body fitted into the cryo-EM map using UCSF Chimera. Coot was used for further building. The linker between the coiled-coils and the RCK_C domain was manually built into the density. An ideal B-DNA based on the sequence of pAB2 was generated and bent to fit the density. Data collection and refinement statistics are provided in Supplementary Table S2.

Static-light scattering

Size exclusion chromatography coupled right angle light scattering (SEC-RALS) was performed using an ÄKTA micro, a Superdex S200 10/300 increase column (Cytiva), a right-angle light scattering detector and a refractive index detector (Malvern/Viscotek). Assays were performed at 20°C in buffer K (30 mM KP_i pH 6.5, 20 mM KCl) for BusR-DNA or DNA alone and buffer SEC for BusR alone or with c-di-AMP. BSA was used as a standard for calibration. Data evaluation was done with the OmniSEC software package (Malvern).

Electrophoretic mobility shift assays

Electrophoretic mobility shift assay (EMSA) was done with 5′-6-FAM labelled DNA (Supplementary Table S3). 6% polyacrylamide gels were cast in 100 mM KP_i pH 6.5 and pre-run at 80 V for 90 min at 8°C. For detailed concentrations refer to the figure legends. BusR, DNA and nucleotides were incubated in 100 mM KP_i pH 6.5, 20 mM KCl for 30 min at 20°C before being separated on gel for 90 min at 8°C and 45 V. Gels were imaged using a Typhoon imager (Cytiva). For EMSAs with pAB containing both binding sites the respective promotor region of *busA* was amplified by PCR from genomic DNA and cloned into a pUC19 vector. For the control the pAB1 GAC binding sites were deleted by site directed mutagenesis. The DNA was then amplified with 5′-6-FAM labelled primers for subsequent use in EMSAs.

Isothermal titration calorimetry

Isothermal titration calorimetry experiments were conducted in buffer SEC using protein concentrations of 20 μM and a 20-fold excess of ligand in the syringe. The experiment was performed at 20°C, consisting of 19 injections of 2 μl, spaced 150 s apart. Control experiments were done by titrating buffer to buffer and ligand to buffer and were subtracted from the measurement using the Malvern software package. The binding parameters represent average values with SD ($n = 3$).

Surface plasmon resonance

For surface plasmon resonance (SPR) experiments (Biacore X100, Cytiva) neutravidin was coupled to flow cell 1 and 2 of a CM5 chip using amino reactive EDC/NHS coupling chemistry in HBS-EP + buffer (150 mM NaCl, 10 mM HEPES–NaOH pH 7.4, 3 mM EDTA, 0.05% v/v surfactant P20). Biotin labelled pAB1 sequence was coupled to flow cell 2 and an unspecific DNA of equal length was coupled to flow cell 1 (serving as a reference). Raw data shown are reference subtracted (FC2-FC1). Assays were conducted in buffer S (100 mM NaP_i pH 6.5, 20 mM KCl, 200 mM NaCl, 3 mM EDTA, 0.05% v/v surfactant P20) and steady-state affinities were derived from single cycle kinetic experiments using the Biacore X100 evaluation software.

RESULTS AND DISCUSSION

Oligomerization and c-di-AMP binding

BusR from *S. agalactiae* has been described to negatively regulate expression of the osmolyte uptake system BusA in a c-di-AMP dependent manner. Our aim is to understand the molecular mechanisms how BusR translates c-di-AMP levels to reduced expression of BusA. C-di-AMP binding capabilities of BusR including specificities have been demonstrated by DRaCALA experiments before, but neither binding affinities nor stoichiometry or its mechanism of regulation are yet known (39). To this end, we expressed and purified *S. agalactiae* BusR to homogeneity. BusR elutes as a single monodisperse peak from a size-exclusion chromatography column at an elution volume that is incompatible with a monomeric species. We therefore analyzed BusR without ligand (apo) and BusR with c-di-AMP (cplx) by SEC-coupled static light scattering and determined a molecular weight of BusR of Mw(apo) = 97.0 kDa ($Mw^{theoretical}$ = 23.8 kDa) and Mw(cplx) = 96.3 kDa in the c-di-AMP bound state (Supplementary Figure S1). Thus, BusR is a stable tetramer in solution, in agreement with SAXS data (Supplementary Figure S2), and the oligomeric state is not altered upon binding of the ligand c-di-AMP. To thermodynamically characterize binding of c-di-AMP to BusR we performed isothermal titration calorimetry (ITC) and titrated BusR with the putative ligand c-di-AMP, and c-di-GMP and 5′-pApA as controls. The resulting ITC data convincingly show specific and high affinity binding of c-di-AMP even in high phosphate and high salt buffer (that is needed as c-di-AMP decreases BusR's stability in absence of DNA), with a dissociation constant $K_D = 112 \pm 7$ nM and a stoichiometry of $n = 1.7$. This indicates that one tetramer of BusR binds two molecules of c-di-AMP (Figure 1C, Supplementary Figure S3).

Crystal structure of BusR

In order to understand the molecular mechanisms of BusR signaling we crystallized selenomethionine substituted full-length BusR and solved its structure to 2.8 Å resolution by single-wavelength anomalous diffraction experiment. As the protein was recombinantly expressed and purified from *E. coli*, that lack DAC domain proteins and the entire c-di-AMP pathway, our structure represents the apo state. The asymmetric unit contains the physiological functional tetramer of BusR (Figure 1A). Each monomer contains

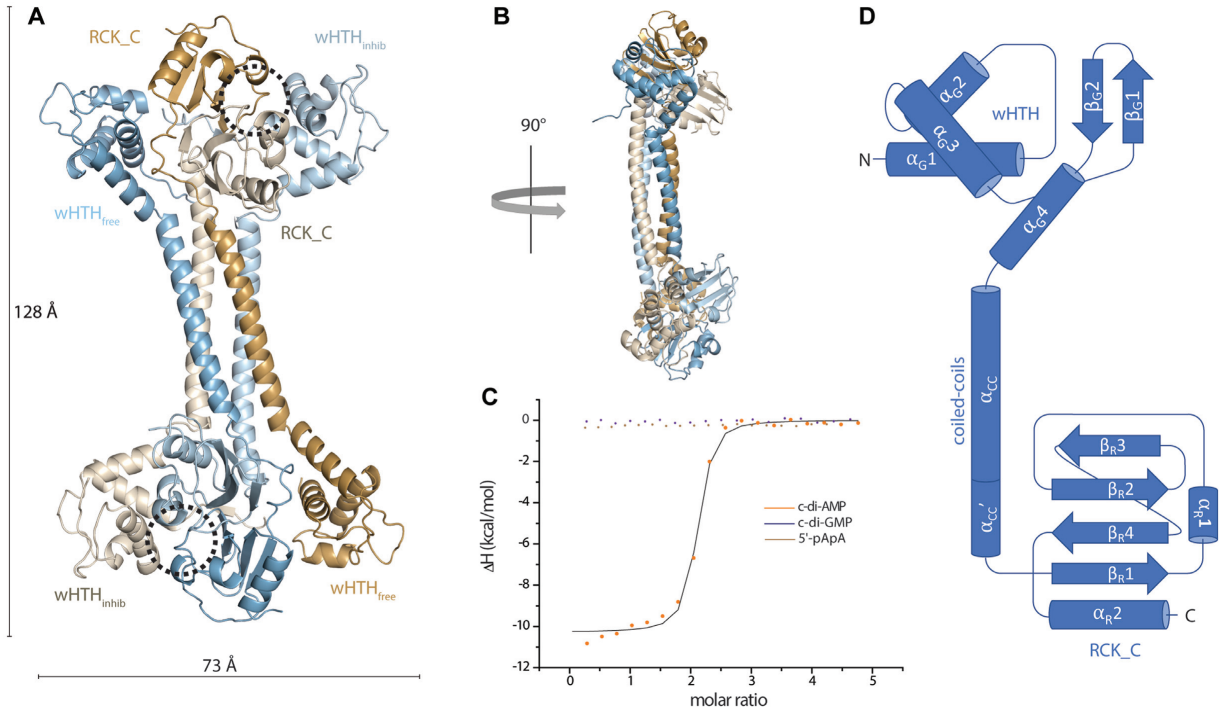

Figure 1. Crystal structure of apo *S. agalactiae* BusR and ligand binding. (**A**) Cartoon representation of the tetrameric crystal structure of apo BusR, colored by chain. The respective domains are labelled to illustrate the antiparallel head-to-tail arrangement. The ligand binding pocket is highlighted by a dashed circle. (**B**) Side view of the apo crystal structure, rotated by 90°. (**C**) Binding curve and fits of ITC measurements of BusR titrated with c-di-AMP (orange, $K_D = 112 \pm 7$ nM), 5′-pApA (brown, no binding) and c-di-GMP (blue, no binding) ($n = 3$). (**D**) Schematic overview of the secondary structure of a single BusR monomer from the apo crystal structure. The helix elongation of the central coiled-coils labelled α_{CC}' is only present in the light blue and light brown colored monomers (see panel A and B), while unstructured in the others.

an N-terminal wHTH domain and a C-terminal effector binding RCK_C domain. Both domains are linked by a long α-helix (α_{CC}). The DNA binding domain consists of a two stranded winged helix-turn-helix motif, following the pattern of α_G1–α_G2–α_G3–β_G1–β_G2, followed by an additional C-terminal helix α_G4. The four central α_{CC}-helices of the four monomers constitute a four-stranded coiled-coil motif, thereby forming a robust tetramerization interface. The four monomers are arranged in a 2-parallel 2-antiparallel head-to-tail arrangement, forming an overall shape resembling a dumbbell. The RCK_C domains form a dimer on each side of the BusR dumbbell. Each of these dimers is flanked by the two wHTH motifs of the antiparallel strands. The interfaces between the RCK_C dimer and its neighbouring wHTH motifs differ significantly resulting in two distinct DNA binding domain arrangements that we refer to as wHTH$_{inhib}$ and wHTH$_{free}$. The interface between the RCK_C domain and wHTH$_{inhib}$ is approx. 50% larger in buried surface area (wHTH$_{free}$: area = 902 Å^2 versus wHTH$_{inhib}$: area = 1353 Å^2). The RCK_C – wHTH$_{inhib}$ interface is stabilized by a hydrophobic region around Trp159. In contrast, wHTH$_{free}$ is only loosely connected to the neighbouring RCK_C via a protruding loop connecting α_{CC} and the distal RCK_C. The significance of this observation will be addressed below.

The overall shape of BusR with two separated DNA-binding platforms, led us to the idea that the interconnecting coiled-coil domain might serve as a molecular ruler to increase binding site specificity, and the observation of two different wHTH versus RCK_C orientations on each side of the dumbbell suggests that these interactions might be taking part in c-di-AMP mediated activation of BusR.

Binding of c-di-AMP to BusR increases affinity for operator DNA

We next addressed the question of how c-di-AMP alters the DNA binding properties of BusR. Using DNA footprinting experiments is has been recently shown that there are two quite large binding sequences of BusR in the promotor sequence of *busA* (37). One binding site is closer to the start codon (here named pAB1) and the other binding site overlaps with the −35 and −10 element (pAB2). A comparison of these two sequences shows that they share a motif with 22 nucleotides of random sequence flanked by an inverted repeat: 5′-GAC-N_{22}-GTC-3′. We observed no major differences in the binding of these sequences in our binding experiments with BusR (Supplementary Figure S4B) and therefore confined ourselves to pAB1. This does not imply that the binding sites may not have different roles *in vivo*.

So far, it has been shown that expression levels of BusA are negatively regulated by BusR and c-di-AMP *in vivo* (37). To further characterize BusR biding *in vitro* we performed electrophoretic mobility shift assays (EMSA). Upon increasing concentration of c-di-AMP in presence of BusR and pAB1, the free DNA is shifted towards a complex band, showing that the affinity of BusR for pAB1 is strongly increased in presence of the second messenger (Figure 2C). At these conditions maximum binding is achieved at 1 μM of c-di-AMP. This capability to sense low c-di-AMP concentrations allows for a sensitive and rapid regulation of BusR activity (i.e. repression of *busA*). SPR experiments confirm this result and display an increase in binding affinity of BusR for pAB1 from $K_D = 577 \pm 55$ nM in absence to $K_D = 5 \pm 0.4$ nM in presence of c-di-AMP (Figure 2D, Supplementary Figure S5). We assume that the dissociation constant for this binding likely represents an upper limit due to the influence of the high salt and phosphate condition used in the experimental setup. The effect of c-di-AMP is highly specific, as control experiments with c-di-GMP and 5′-pApA show no impact on the affinity of BusR to DNA in an EMSA (Figure 2C), in line with the results from ITC. This finding raised the question of how c-di-AMP binding alters the affinity of BusR for DNA on a molecular basis and whether the observed RCK_C – $wHTH_{inhib}$ interface is a key element in this regulatory event.

Atomic resolution structure of the RCK_C domain

While our full-length structure revealed the overall domain architecture of BusR, it lacks the necessary resolution to thoroughly describe ligand binding. In order to understand the effect of c-di-AMP on DNA binding of BusR we focused on the isolated RCK_C domains. We purified and crystallized a construct comprising only the RCK_C domain (Leu135 to end) and solved its ligand-free and c-di-AMP bound structure to 1 and 1.2 Å resolution, respectively. The crystal of the apo state only contains one monomer in the asymmetric unit. However, a symmetry related copy is present that generates the dimeric assembly as common to RCK_C domains and as observed in our full-length structure. To probe whether the BusR RCK_C domain is monomeric in solution and dimerizes upon c-di-AMP binding we conducted small-angle X-ray scattering measurements. The scattering data show that the RCK_C domain on its own is dimeric in solution even in the absence of c-di-AMP (Supplementary Figure S2G). The crystal of the RCK_C domain in the c-di-AMP bound state contains the physiological dimer in the asymmetric unit with one moiety of c-di-AMP bound. The c-di-AMP binding pocket is localized in the cleft between α_R1 of the two RCK_C subunits in a conserved hydrophobic and narrow pocket formed by residues Ile153, Gly154, Val158, Ala164, Thr165, Ile166, Pro181 and the main chain of Trp159 and Gly180. Residues Asn157 and His160 form a polar rim around the pocket (Supplementary Figure S6). The high-resolution structure of the RCK_C domain explains very well the high specificity of BusR for c-di-AMP and how it discriminates its ligand even from structurally closely related molecules such as its linearized variant 5′-pApA, or c-di-GMP. The adenine base, especially its amino group forms hydrogen bonds to the peptide backbone of Ile166 while Ala164 at the same time prevents a larger group at C2 of the adenine base, thus preventing c-di-GMP from binding. The 2′-OH group of the ribose is coordinated via a hydrogen bond by Asp157 and the phosphate group forms a hydrogen bond with His160. The individual monomers are identical and the resulting assembly is symmetric, therefore all protein-ligand interactions are mirrored on the opposite site of c-di-AMP (Supplementary Figure S6).

Autoinhibition mediated by the RCK_C domain

The large interface between $wHTH_{inhib}$ and the RCK_C domain observed in our full-length structure and the fact that it positions the ligand binding site in close proximity to one of the wHTH motifs, raises the idea that it might play a role in regulation. Furthermore, in the observed conformation, the DNA recognition helix α_G3 of $wHTH_{inhib}$ is buried in the interface and thus incapable to bind to DNA. At the core of the interface the residues Trp159 (RCK_C, chain A), Pro181, Phe182 (RCK_C, chain B) and Tyr13 ($wHTH_{inhib}$) are forming a hydrophobic pocket (Supplementary Figure S7). Intriguingly, these residues of the hydrophobic patch are highly conserved among homologs of BusR (Supplementary Figure S8). This may not be surprising for Tyr13 that is involved in DNA binding or Pro181 that is an integral part of the c-di-AMP binding pocket. However, it is notable for residues Trp159 and Phe182 as their sidechains are not involved in either one. Phe182 is often found to be replaced by a tyrosine, which however is a residue of comparable chemical properties.

The apo and c-di-AMP bound crystal structure of the RCK_C domain show that c-di-AMP binding induces a subtle rotation of the RCK_C domains that results in a widening of the binding pocket (Figure 2A). This movement pushes residues Pro179, Gly180, Pro181 and Phe182 (chain A) further out in respect to Trp159 (chain B) of the opposing chain. When we transfer this movement to the full-length structure this has two implications. Firstly, it weakens the hydrophobic patch and secondly, it leads to steric clashes of Pro181 and Phe182 with $wHTH_{inhib}$, especially Tyr13 (Figure 2B). Thus, it seems that this interface locks $wHTH_{inhib}$ in an autoinhibited state in absence of c-di-AMP, restricting movement of $wHTH_{inhib}$ and thus impairing high affinity binding to the operator sequence.

To test this hypothesis and the relevance of this interface *in vitro* we mutated Trp159 to alanine, thereby weakening the hydrophobic patch. Indeed, the Trp159Ala mutant shows a c-di-AMP uncoupled DNA-binding: The mutant has higher affinity for its target DNA in absence of c-di-AMP in EMSAs and SPR measurements compared to wildtype BusR, while addition of c-di-AMP to the mutant affects the DNA affinity only marginally (Figure 2C, D). In comparison, wt BusR requires presence of 1 μM c-di-AMP to reach the same shift in EMSA as Trp159Ala (no c-di-AMP).

The conservation of the hydrophobic pocket, the high-resolution crystal structures of the apo and ligand bound state, and the c-di-AMP decoupled elevated affinity of the Trp159Ala mutant indicate that the hydrophobic patch surrounding Trp159 is important for signaling. It arrests BusR in an autoinhibited state that is released upon binding of c-di-AMP to allow for DNA binding and subsequent tran-

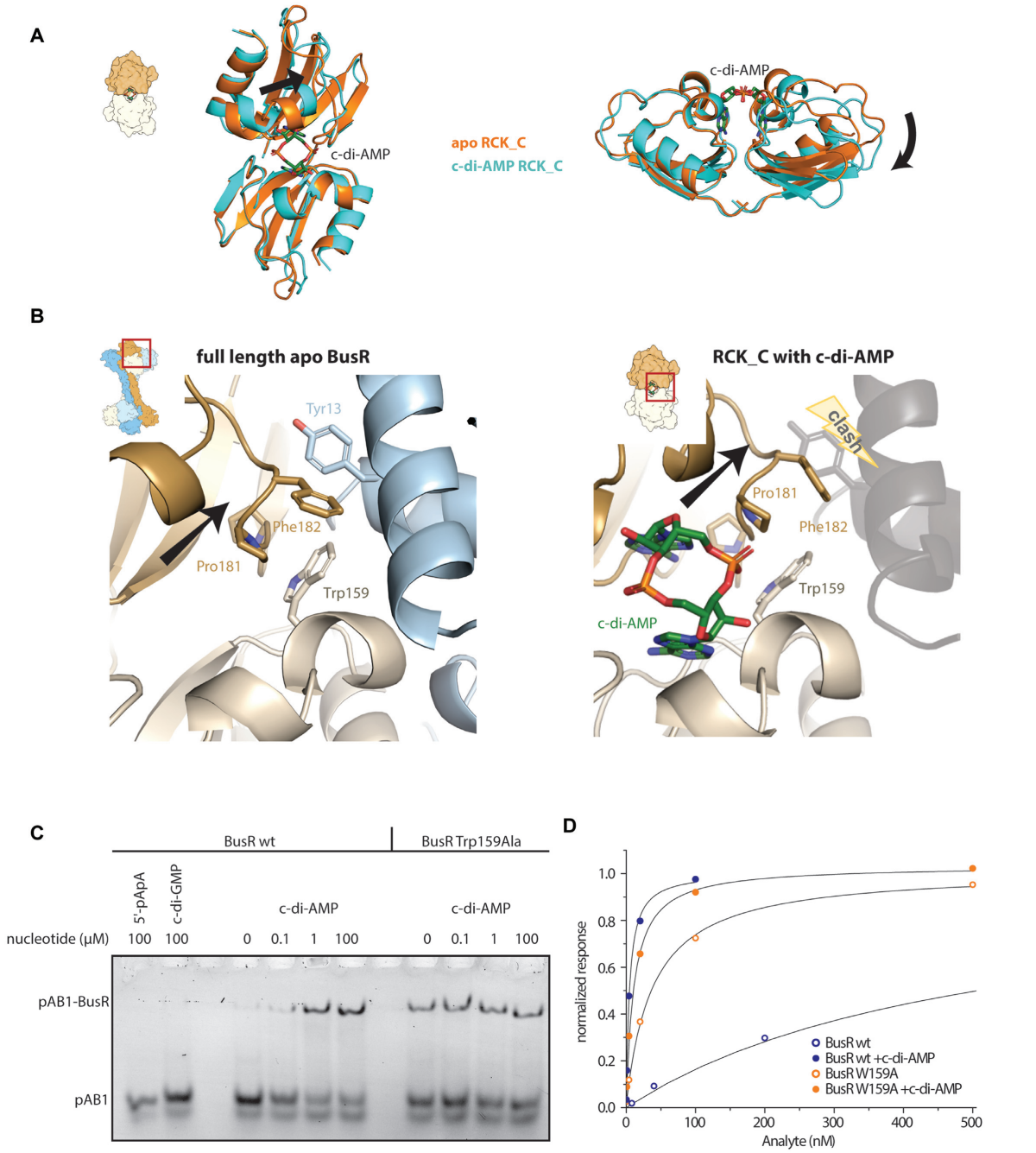

Figure 2. Release of autoinhibition upon c-di-AMP binding to BusR. (**A**) Front and side view of superimposed crystal structures of apo RCK_C domain (orange) and ligand bound RCK_C domain (cyan, c-di-AMP in dark green). Ligand induced movement of the monomers in respect to each other is indicated by a black arrow (1.31 Å rmsd for apo RCK_C compared to ligand bound RCK_C). (**B**) Close-up on RCK_C – $wHTH_{inhib}$ interface in the full-length (left) and c-di-AMP bound RCK_C (right) crystal structure. In the full-length apo state a tight interface is formed around residues Trp159 (RCK_C chain A, light brown), Pro179-Phe182 (RCK_C chain B, dark brown) and Tyr13 ($wHTH_{inhib}$, blue). Binding of c-di-AMP induces rotational movement (black arrow) of the RCK_C monomers in respect to each other that would cause sterical clashes with helices α_G1 and α_G3 (grey and transparent), which frees the $wHTH_{inhib}$ domain for subsequent DNA binding. (**C**) EMSA experiments: c-di-AMP titrated to 100 nM wt BusR leads to increased affinity for operator DNA (20 nM), while related nucleotides show no effect. The mutation of Trp159Ala disturbs the RCK_C–$wHTH_{inhib}$ interface and thereby allows for DNA binding of BusR in absence of c-di-AMP ($n = 3$). (**D**) Steady-state affinity binding fits of SPR measurements using a single site binding model. Titration of BusR and BusR Trp159Ala to pAB1 in presence and absence of c-di-AMP (10 μM) ($n = 3$).

scriptional control. To our knowledge this mechanism is different from other RCK_C domains and unique to BusR, which further becomes apparent by the fact that Trp159 and Phe182 are not conserved in paralogous and structurally highly similar RCK_C domains as for example *S. aureus* KtrA (pdb code 4xtt, (66)) (Supplementary Figure S9).

DNA binding

The idea of a molecular ruler in combination with two sides of regulated (i.e. partially flexible) DNA-binding domains in a transcription factor render the structure of the dsDNA-bound BusR even more interesting. Thus, to visualize this ternary complex of c-di-AMP activated BusR on dsDNA, we solved two complex structures by single-particle cryo-electron microscopy. One structure contains BusR bound to pAB1 at a resolution of 7.1 Å (Supplementary Figure S10) and the other structure was determined using the whole promotor sequence (pAB, two BusR binding sites). In the reconstruction only BusR and the DNA in proximity to the binding site are visible and thus pAB1- and pAB2-bound BusR cannot be distinguished. However, the latter structure yields data up to 4.5 Å resolution and thus provides more details in the protein domains (Supplementary Figure S11). The higher resolution likely resulted from thinner ice after plunge freezing of the larger sample. As expected, BusR binds to the DNA as a tetramer, which reflects the oligomeric assembly we observed by SEC-RALS and SAXS in solution (Supplementary Figures S1 and S2). Compared to the crystal structure, BusR undergoes major structural rearrangements upon binding to dsDNA (Figure 3A). The central coiled-coils align in an 'X'-like fashion relative to the dsDNA. BusR has a strikingly asymmetric surface charge distribution, with one predominantly positively charged side and a mainly negative charge on the opposite side (Supplementary Figure S12). This positively charged side of the BusR is facing the negatively charged DNA in the complex. In our structure, BusR induces a bending of the DNA by ∼18°. The DNA is also slightly bend to the side, thereby breaking the C2 symmetry of the complex.

C-di-AMP can be unambiguously identified in the ligand binding site within the RCK_C domain and the RCK_C–$wHTH_{inhib}$ interface surrounding Trp159 is completely dissolved. In comparison to the crystal structure, the RCK_C domains tilt by 70° relative to the coiled-coils away from $wHTH_{inhib}$ in the direction of $wHTH_{free}$. This rotation of the RCK_C dimer creates space for $wHTH_{inhib}$ to undergo a rotation of 60° towards the DNA. The rotation of $wHTH_{inhib}$ allows the helices α_{CC} and α_G4, which are interrupted in the apo state, to reseal to a single prolonged α-helix, spanning the entire molecule (video abstract). This brings the two equivalent DNA binding domains into the same position as the two binding motifs (5′-GAC-3′) that are spaced apart by three turns of DNA. While the resolution of the EM density is not good enough to determine the register of the DNA directly, it can be deduced from the lower resolution BusR:c-di-AMP:pAB1 structure, as the whole dsDNA density (46 bp) is visible. The Helices α_G2 and α_G3 of $wHTH_{inhib}$ plunge deep into the major groove, in close contact to the motif sequence, while the 'wing' of $wHTH_{inhib}$ (loop between β_G1 and β_G2) reaches into the minor groove (Figure 3B). We mutated residues that are close to the binding motif and are likely to interact with the DNA. These mutants, Lys36Ala and Arg38Ala (α_G2), Arg53Ala and Lys54Ala (α_G3) and Gly70Ile and Gly72Ile (loop between β_G2 and β_G3) all show a severely diminished binding in EMSAs (Supplementary Figure S3), while behaving identical to the wildtype during purification, proving their importance for binding site recognition. In the reverse experiment, mutating one (or both) of the two binding motifs to a random nucleotide sequence of equal length, BusR binding in EMSAs is also heavily compromised, indicating the importance of the 5′-GAC-3′ motif in the binding site (Figure 3C).

While the release of $wHTH_{inhib}$ leads to a sequence specific binding, $wHTH_{free}$ contributes to the protein-DNA interaction differently. The second DNA binding domain undergoes a major rearrangement: It rotates alongside the RCK_C domains by 90°. In this complex, $wHTH_{free}$ faces the DNA in the same orientation as $wHTH_{inhib}$ but is positioned one quarter of a DNA turn (90°) further inwards, towards the middle of the DNA sequence (Figure 3A, Supplementary Figure S4A). Thus, $wHTH_{free}$ is not in direct proximity to the binding motif. The whole domain is slightly displaced and further away from the DNA and the wing does not reach into the minor groove (Figure 3B). Based on our structure, $wHTH_{free}$ appears to be limited to phosphate backbone contacts. Our structure suggests that $wHTH_{free}$ contributes in a rather sequence independent binding mode. This hypothesis is supported by sequence alignments of the four so far experimentally determined binding sequences of BusR (*S. agalactiae, L. lactis* and *Tetragenococcus halophilus)* showing a highly conserved target binding motif 5′-GAC-3′ for $wHTH_{inhib}$, while the $wHTH_{free}$ binding region is not very conserved (Supplementary Figure S4A), and also differs between pAB1 and pAB2.

As shown above, the two binding motif sequences are crucial for recognition by BusR, but even more striking is the need for their relative positioning in respect to each other. The distance between these two sites is 22 bp for all the four experimentally determined binding sequences. Including both flanking binding sequences, it sums up to three turns of the DNA double helix. This leads to positioning of both binding sequences facing to the same side of the DNA. It is tempting to speculate that the coiled-coil spacer serves as a molecular ruler to increase the specificity of BusR to specific sites in fixed distance to each other. To experimentally address the relevance of this spacing, we used dsDNA that contains additional 5 bp in the middle between the binding sequences in EMSAs. The +5 bp not only increase the distance between the binding motifs but turns the around on the dsDNA by 180° with respect to each other. Neither this DNA-segment is recognized by BusR, nor a −10 bp DNA with shorter middle segment, having both binding sequences facing to the same direction again but closer together (Figure 3C). This illustrates that both the recognition of the correct DNA sequence and the relative spacing of these sites is essential for BusR-DNA binding. In this sense, the coiled-coils in the center of BusR resemble a molecular ruler, adding a second layer of specificity to the transcription factor.

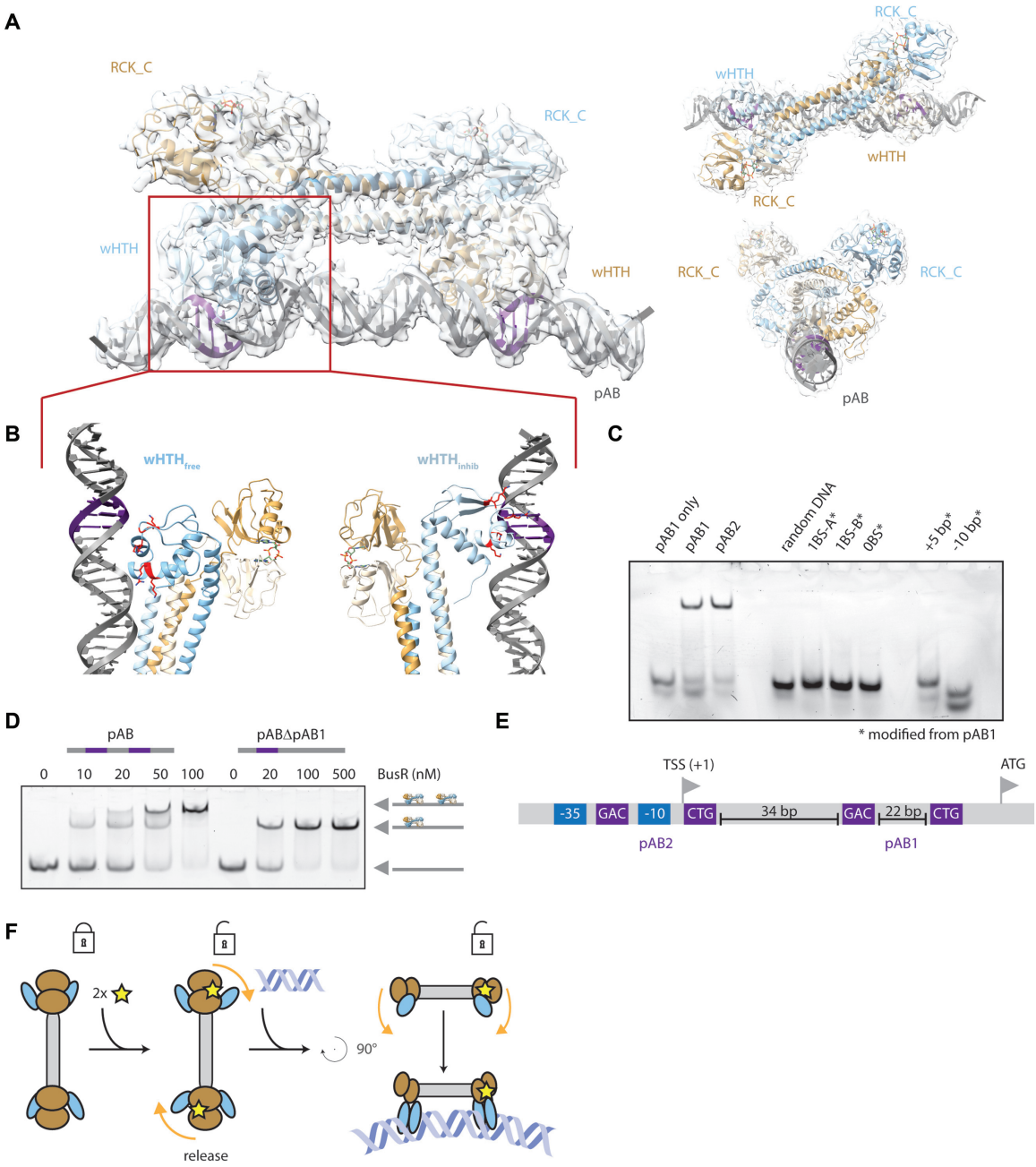

Figure 3. BusR bound to operator DNA. (**A**) cryoEM structure of BusR bound to operator DNA pAB depicted as side view (left), top view (top right) and front view (bottom right). The binding motifs are colored in purple. Large domain rearrangement occurs from apo to DNA bound BusR. The RCK_C–wHTH$_{inhib}$ interface is broken and all four wHTH motifs rotate backwards to face and bind the DNA. (**B**) The DNA binding domain shows great variability in its interaction with the DNA. The wHTH$_{free}$ rather interacts with the phosphate backbone instead of the bases (left part, for reasons of better visibility wHTH$_{inhib}$ is not shown), whereas wHTH$_{inhib}$ is deeply buried in the major groove with its wing bound to the minor groove (right part, wHTH$_{free}$ is not shown). (**C**) BusR distinguishes its native substrate (pAB1 or pAB2) from non-target DNA. Alterations to the DNA severely disrupt binding of BusR in EMSAs. Deletion of one (BS-A or BS-B) or both binding motifs (0BS) from pAB1 abolishes DNA binding in EMSAs. Also changes to the position of the binding motifs, either by elongation of the DNA in between the binding motifs by 5 base pairs (+5 bp) or by shortening of the distance in between by 10 base pairs (−10 bp) prevents BusR from recognizing its substrate (BusR = 100 nM, DNA = 20 nM, c-di-AMP = 10 μM, $n = 3$). (**D**) EMSA with the promoter region containing both pAB1 and pAB2. Two complex bands are observed upon titration of BusR. A control with only one binding site present results in the lower complex band, indicating that this is a BusR:DNA complex of 1:1 stochiometry and linear instead of looped DNA (20 nM DNA, 10 μM c-di-AMP; $n = 3$). (**E**) Schematic overview of the two binding sites of BusR within the promotor region of BusA. Included are the −35 and −10 transcriptional elements, the transcriptional start site (TSS) and the start codon (ATG). (**F**) Schematic representation of the domain rearrangement and mechanism. Two molecules of c-di-AMP bind to the RCK_C domains. Consequently, the adjacent wHTH$_{inhib}$ domain is released and can now freely rotate towards the DNA. Upon binding the DNA is bent by 18°.

BusR–DNA complex organization

The recently described tetrameric GntR family transcription factor Atu1419 from *Agrobacterium fabrum* binds to two binding sites that are 190 bp apart and bends the DNA around the protein causing DNA loop repression (67). This raises the idea that BusR might induce DNA loop formation, as well. To analyze BusR with respect to this looping option we performed cryo-EM with a rather long ds-DNA containing both binding sites as substrate for cryoEM (BusR:c-di-AMP:pAB). In this dataset we could observe free DNA, and DNA with one or two copies of BusR. We could not identify any loop formation in the micrographs nor during further processing (e.g. no 2D classes with respective assemblies, S11B). In parallel, we tested the ability of BusR to bind to multiple copies of its operator ds-DNA sequence by SEC-RALS. In presence of a 3-fold excess of pAB1 towards BusR we still observe only a 1:1 stoichiometry (Supplementary Figure S1D). Furthermore, we conducted band shift assays with dsDNA spanning both binding sites (Figure 3D). In presence of BusR two complex bands can be observed and increasing concentration of BusR leads to a shift of the lower complex band towards the upper complex band. While the upper complex band most likely represents a 2:1 BusR-DNA complex, the lower complex band can represent a linear or looped BusR-DNA complex. As a control we tested the same substrate lacking one binding site (ΔpAB1) by mutating both its GAC binding motifs, thus preventing loop formation. Band shifts with ΔpAB1 result in the loss of the upper complex while retaining the same position of the lower complex band. Because a looped complex is likely to behave differently than a linear complex this indicates that the lower complex band rather represents a linear complex. Based on our observations under the conditions used, we thus conclude BusR, apart from its similarity to Atu1419 in respect to its oligomeric state and the presence of two binding sites, does not induce loop formation *in vitro*.

To our knowledge the quaternary assembly and the mode of regulation is strikingly different from other members of the GntR family and BusR represents a subfamily of its own. BusR shares more overall structural similarity to the MerR family of transcription factors, especially to the c-di-GMP responsive MerR family transcription factor BrlR. Like BusR, BrlR is a dumbbell shaped tetramer with a head-to-tail arrangement and a central coiled-coil motif joining the distal ligand and DNA binding domains. Except for the overall shape, the two transcription factors share little in common. The coiled-coils of BrlR are formed by a dimer of dimers and form a less rigid tetramerization interface compared to BusR. BrlR has two c-di-GMP binding sites structurally unrelated to the c-di-AMP binding site in BusR. While we observe c-di-AMP binding to a regulatory subunit (RCK_C), followed by large conformational changes leading to DNA binding, in BrlR c-di-GMP binding occurs directly at the wHTH domain and the coiled-coil motif, followed by only subtle movement. In this respect, in BrlR binding of c-di-GMP rather resembles an induced or stabilized fit while BusR moves from autoinhibited to activated state upon c-di-AMP binding. Lacking a dsDNA bound structure of BlrR, we refer to BmrR, another transcriptional activator of the MerR family. BmrR dimerizes via a coiled-coil motif. A high degree of conformational plasticity is exhibited by the coiled-coils between apo and DNA bound state (68). Upon binding BmrR strongly bends the DNA in a clamp-like fashion, introducing a significant kink in the DNA that allows for the polymerase to bind subsequently (69). In contrast, the tetrameric coiled-coil of BusR is highly rigid and can be perfectly superimposed from apo to DNA bound state. This rigidity is further transferred to the DNA binding domain upon resealing of helix α_{CC} and α_G4. We believe that the tetrameric coiled coil mediated assembly is less a means of bending the DNA for transcriptional activation as in case of BmrR and the MerR family, but it adds a second layer of specificity by acting as a molecular ruler between two binding sites separated by a specific distance.

In summary, our biochemical and structural data provide a possible molecular mechanism for the c-di-AMP triggered inactivation of *busA* gene expression by BusR. It explains how the input signal c-di-AMP is translated to gene repression through reconfiguration of the BusR tetramer upon binding of c-di-AMP to the RCK_C dimer. BusR resides in an autoinhibited state by a hydrophobic patch that locks its wHTH domain and prevents high affinity binding to its target in absence of c-di-AMP. This state is shifted to a DNA binding activated state upon binding of its native ligand c-di-AMP. Binding of the second messenger induces movement involving residues of the hydrophobic patch surrounding Trp159 that releases the wHTH domain and allows for strong binding to its operator DNA. This ultimately results in blocking transcription of *busA* and less osmolyte uptake as demonstrated before (37,39). High specificity and selectivity for the downregulated gene is provided by the sequence specificity of the DNA binding domains and the ultimate need for two binding sites in a fixed distance that corresponds to the length of the coiled-coil ruler, achieved by the so far unique domain arrangement of BusR.

DATA AVAILABILITY

MX and cryoEM structures have been deposited in the RCSB PDB. Accession numbers: 7B5T (BusR fl), 7B5W (RCK_C domain ligand free), 7B5U (RCK_C with c-di-AMP), 7OZ3 (cryoEM structure of BusR-DNA complex (pAB)), 7B5Y (cryoEM structure of the BusR-pAB1 complex). SAXS data have been deposited in the SASBDB with accession numbers SASDK74 (BusR RCK_C domain dimer), SASDK84 (BusR full-length protein), and SASDK94 (BusR:c-di-AMP:pAB1 complex). Other datasets generated and/or analysed during the current study are available from the corresponding author on reasonable request.

SUPPLEMENTARY DATA

Supplementary Data are available at NAR Online.

ACKNOWLEDGEMENTS

Synchrotron SAXS and MX data were collected at beamlines P12 (SAXS), and P13/P14 (MX) operated by EMBL Hamburg at the PETRA III storage ring (DESY, Hamburg,

Germany). We thank G. Bourenkov, C. Jeffries and the staff of EMBL Hamburg for discussions and outstanding on-site support. We also thank J. Basquin (MPI, Munich) for initial crystal testing, D. Kostrewa for help with data analysis, and members of the Hopfner lab for insightful discussions and great support.
Author contributions: A.M.B. performed most experiments, structure determination, model building and wrote the manuscript with contributions from all other authors. J.B. and K.L. supported cryoEM sample preparation, data collection and evaluation, J.K. optimized EMSAs, D.J.D. and K.P.H. participated in data evaluation and discussion of results, G.W. designed and supervised the overall study, evaluated MX/SAXS data and analysed results. All authors contributed to and approved the final manuscript.

FUNDING

DFG [GRK1721 to G.W., K.P.H.]; DFG [HO2489/8-1]; Gottfried Wilhelm Leibniz-Prize (to K.P.H.); DFG [WI 3717/3-1 to G.W.]. Funding for open access charge: funding money and LMU Munich.
Conflict of interest statement. None declared.

REFERENCES

1. Witte,G., Hartung,S., Büttner,K. and Hopfner,K.P. (2008) Structural biochemistry of a bacterial checkpoint protein reveals diadenylate cyclase activity regulated by DNA recombination intermediates. *Mol. Cell*, **30**, 167–178.
2. Bejerano-Sagie,M., Oppenheimer-Shaanan,Y., Berlatzky,I., Rouvinski,A., Meyerovich,M. and Ben-Yehuda,S. (2006) A checkpoint protein that scans the chromosome for damage at the start of sporulation in *Bacillus subtilis*. *Cell*, **125**, 679–690.
3. Oppenheimer-Shaanan,Y., Wexselblatt,E., Katzhendler,J., Yavin,E. and Ben-Yehuda,S. (2011) c-di-AMP reports DNA integrity during sporulation in Bacillus subtilis. *EMBO Rep.*, **12**, 594–601.
4. Römling,U. (2008) Great times for small molecules: c-di-AMP, a second messenger candidate in Bacteria and Archaea. *Sci. Signal*, **1**, pe39.
5. Stülke,J. and Krüger,L. (2020) Cyclic di-AMP signaling in bacteria. *Annu. Rev. Microbiol.*, **74**, 159–179.
6. Xiong,Z.Q., Fan,Y.Z., Song,X., Liu,X.X., Xia,Y.J. and Ai,L.Z. (2020) The second messenger c-di-AMP mediates bacterial exopolysaccharide biosynthesis: a review. *Mol. Biol. Rep.*, **47**, 9149–9157.
7. Zarrella,T.M. and Bai,G. (2020) The many roles of the bacterial second messenger cyclic di-AMP in adapting to stress cues. *J. Bacteriol.*, **203**, e00348-20.
8. Woodward,J.J., Iavarone,A.T. and Portnoy,D.A. (2010) c-di-AMP secreted by intracellular *Listeria monocytogenes* activates a host type I interferon response. *Science*, **328**, 1703–1705.
9. Corrigan,R.M., Abbott,J.C., Burhenne,H., Kaever,V. and Gründling,A. (2011) c-di-AMP is a new second messenger in *Staphylococcus aureus* with a role in controlling cell size and envelope stress. *PLoS Pathog.*, **7**, e1002217.
10. Braun,F., Thomalla,L., van der Does,C., Quax,T.E.F., Allers,T., Kaever,V. and Albers,S.V. (2019) Cyclic nucleotides in archaea: Cyclic di-AMP in the archaeon *Haloferax volcanii* and its putative role. *Microbiologyopen*, **8**, e00829.
11. Bai,Y., Yang,J., Eisele,L.E., Underwood,A.J., Koestler,B.J., Waters,C.M., Metzger,D.W. and Bai,G. (2013) Two DHH subfamily 1 proteins in Streptococcus pneumoniae possess cyclic di-AMP phosphodiesterase activity and affect bacterial growth and virulence. *J. Bacteriol.*, **195**, 5123–5132.
12. Bai,Y., Yang,J., Zhou,X., Ding,X., Eisele,L.E. and Bai,G. (2012) Mycobacterium tuberculosis Rv3586 (DacA) is a diadenylate cyclase that converts ATP or ADP into c-di-AMP. *PLoS One*, **7**, e35206.
13. Mehne,F.M., Gunka,K., Eilers,H., Herzberg,C., Kaever,V. and Stülke,J. (2013) Cyclic di-AMP homeostasis in bacillus subtilis: both lack and high level accumulation of the nucleotide are detrimental for cell growth. *J. Biol. Chem.*, **288**, 2004–2017.
14. Huynh,T.N., Luo,S., Pensinger,D., Sauer,J.D., Tong,L. and Woodward,J.J. (2015) An HD-domain phosphodiesterase mediates cooperative hydrolysis of c-di-AMP to affect bacterial growth and virulence. *Proc. Natl. Acad. Sci. U.S.A.*, **112**, E747–E756.
15. Latoscha,A., Drexler,D.J., Al-Bassam,M.M., Bandera,A.M., Kaever,V., Findlay,K.C., Witte,G. and Tschowri,N. (2020) c-di-AMP hydrolysis by the phosphodiesterase AtaC promotes differentiation of multicellular bacteria. *Proc. Natl. Acad. Sci. U.S.A.*, **117**, 7392–7400.
16. Rao,F., See,R.Y., Zhang,D., Toh,D.C., Ji,Q. and Liang,Z.X. (2010) YybT is a signaling protein that contains a cyclic dinucleotide phosphodiesterase domain and a GGDEF domain with ATPase activity. *J. Biol. Chem.*, **285**, 473–482.
17. Drexler,D.J., Muller,M., Rojas-Cordova,C.A., Bandera,A.M. and Witte,G. (2017) Structural and biophysical analysis of the soluble DHH/DHHA1-type phosphodiesterase TM1595 from *Thermotoga maritima*. *Structure*, **25**, 1887–1897.
18. Luo,Y. and Helmann,J.D. (2012) Analysis of the role of *Bacillus subtilis* sigma(M) in beta-lactam resistance reveals an essential role for c-di-AMP in peptidoglycan homeostasis. *Mol. Microbiol.*, **83**, 623–639.
19. Song,J.H., Ko,K.S., Lee,J.Y., Baek,J.Y., Oh,W.S., Yoon,H.S., Jeong,J.Y. and Chun,J. (2005) Identification of essential genes in Streptococcus pneumoniae by allelic replacement mutagenesis. *Mol. Cells*, **19**, 365–374.
20. Chaudhuri,R.R., Allen,A.G., Owen,P.J., Shalom,G., Stone,K., Harrison,M., Burgis,T.A., Lockyer,M., Garcia-Lara,J., Foster,S.J. *et al.* (2009) Comprehensive identification of essential *Staphylococcus aureus* genes using transposon-mediated differential hybridisation (TMDH). *BMC Genomics*, **10**, 291.
21. Whiteley,A.T., Garelis,N.E., Peterson,B.N., Choi,P.H., Tong,L., Woodward,J.J. and Portnoy,D.A. (2017) c-di-AMP modulates *Listeria monocytogenes* central metabolism to regulate growth, antibiotic resistance and osmoregulation. *Mol. Microbiol.*, **104**, 212–233.
22. Witte,C.E., Whiteley,A.T., Burke,T.P., Sauer,J.D., Portnoy,D.A. and Woodward,J.J. (2013) Cyclic di-AMP is critical for *Listeria monocytogenes* growth, cell wall homeostasis, and establishment of infection. *mBio*, **4**, e00282-13.
23. Dengler,V., McCallum,N., Kiefer,P., Christen,P., Patrignani,A., Vorholt,J.A., Berger-Bachi,B. and Senn,M.M. (2013) Mutation in the C-di-AMP cyclase dacA affects fitness and resistance of methicillin resistant *Staphylococcus aureus*. *PLoS One*, **8**, e73512.
24. Commichau,F.M., Gibhardt,J., Halbedel,S., Gundlach,J. and Stülke,J. (2018) A delicate connection: c-di-AMP affects cell integrity by controlling osmolyte transport. *Trends Microbiol.*, **26**, 175–185.
25. Gundlach,J., Herzberg,C., Kaever,V., Gunka,K., Hoffmann,T., Weiss,M., Gibhardt,J., Thurmer,A., Hertel,D., Daniel,R. *et al.* (2017) Control of potassium homeostasis is an essential function of the second messenger cyclic di-AMP in *Bacillus subtilis*. *Sci. Signal*, **10**, eaal3011.
26. Bremer,E. and Kramer,R. (2019) Responses of microorganisms to osmotic stress. *Annu. Rev. Microbiol.*, **73**, 313–334.
27. Corrigan,R.M., Campeotto,I., Jeganathan,T., Roelofs,K.G., Lee,V.T. and Gründling,A. (2013) Systematic identification of conserved bacterial c-di-AMP receptor proteins. *Proc. Natl. Acad. Sci. U.S.A.*, **110**, 9084–9089.
28. Bai,Y., Yang,J., Zarrella,T.M., Zhang,Y., Metzger,D.W. and Bai,G. (2014) Cyclic di-AMP impairs potassium uptake mediated by a cyclic di-AMP binding protein in Streptococcus pneumoniae. *J. Bacteriol.*, **196**, 614–623.
29. Gundlach,J., Krüger,L., Herzberg,C., Turdiev,A., Poehlein,A., Tascon,I., Weiss,M., Hertel,D., Daniel,R., Hänelt,I. *et al.* (2019) Sustained sensing in potassium homeostasis: Cyclic di-AMP controls potassium uptake by KimA at the levels of expression and activity. *J. Biol. Chem.*, **294**, 9605–9614.
30. Chin,K.H., Liang,J.M., Yang,J.G., Shih,M.S., Tu,Z.L., Wang,Y.C., Sun,X.H., Hu,N.J., Liang,Z.X., Dow,J.M. *et al.* (2015) Structural insights into the distinct binding mode of cyclic di-AMP with SaCpaA_RCK. *Biochemistry*, **54**, 4936–4951.
31. Gibhardt,J., Hoffmann,G., Turdiev,A., Wang,M., Lee,V.T. and Commichau,F.M. (2019) c-di-AMP assists osmoadaptation by

regulating the *Listeria monocytogenes* potassium transporters KimA and KtrCD. *J. Biol. Chem.*, **294**, 16020–16033.
32. Cereija,T.B., Guerra,J.P.L., Jorge,J.M.P. and Morais-Cabral,J.H. (2021) c-di-AMP, a likely master regulator of bacterial K(+) homeostasis machinery, activates a K(+) exporter. *Proc. Natl. Acad. Sci. U.S.A.*, **118**, e2020653118.
33. Nelson,J.W., Sudarsan,N., Furukawa,K., Weinberg,Z., Wang,J.X. and Breaker,R.R. (2013) Riboswitches in eubacteria sense the second messenger c-di-AMP. *Nat. Chem. Biol.*, **9**, 834–839.
34. Wang,X., Cai,X., Ma,H., Yin,W., Zhu,L., Li,X., Lim,H.M., Chou,S.H. and He,J. (2019) A c-di-AMP riboswitch controlling kdpFABC operon transcription regulates the potassium transporter system in Bacillus thuringiensis. *Commun Biol*, **2**, 151.
35. Moscoso,J.A., Schramke,H., Zhang,Y., Tosi,T., Dehbi,A., Jung,K. and Gründling,A. (2016) Binding of cyclic di-AMP to the *Staphylococcus aureus* sensor kinase KdpD occurs via the universal stress protein domain and downregulates the expression of the Kdp potassium transporter. *J. Bacteriol.*, **198**, 98–110.
36. Zeden,M.S., Schuster,C.F., Bowman,L., Zhong,Q., Williams,H.D. and Gründling,A. (2018) Cyclic di-adenosine monophosphate (c-di-AMP) is required for osmotic regulation in Staphylococcus aureus but dispensable for viability in anaerobic conditions. *J. Biol. Chem.*, **293**, 3180–3200.
37. Devaux,L., Sleiman,D., Mazzuoli,M.V., Gominet,M., Lanotte,P., Trieu-Cuot,P., Kaminski,P.A. and Firon,A. (2018) Cyclic di-AMP regulation of osmotic homeostasis is essential in Group B Streptococcus. *PLoS Genet.*, **14**, e1007342.
38. Schuster,C.F., Bellows,L.E., Tosi,T., Campeotto,I., Corrigan,R.M., Freemont,P. and Gründling,A. (2016) The second messenger c-di-AMP inhibits the osmolyte uptake system OpuC in Staphylococcus aureus. *Sci. Signal*, **9**, ra81.
39. Pham,H.T., Nhiep,N.T.H., Vu,T.N.M., Huynh,T.N., Zhu,Y., Huynh,A.L.D., Chakrabortti,A., Marcellin,E., Lo,R., Howard,C.B. *et al.* (2018) Enhanced uptake of potassium or glycine betaine or export of cyclic-di-AMP restores osmoresistance in a high cyclic-di-AMP *Lactococcus lactis* mutant. *PLoS Genet.*, **14**, e1007574.
40. Sikkema,H.R., van den Noort,M., Rheinberger,J., de Boer,M., Krepel,S.T., Schuurman-Wolters,G.K., Paulino,C. and Poolman,B. (2020) Gating by ionic strength and safety check by cyclic-di-AMP in the ABC transporter OpuA. *Sci. Adv.*, **6**, eabd7697.
41. Zhang,L., Li,W. and He,Z.G. (2013) DarR, a TetR-like transcriptional factor, is a cyclic di-AMP-responsive repressor in *Mycobacterium smegmatis*. *J. Biol. Chem.*, **288**, 3085–3096.
42. Rigali,S., Derouaux,A., Giannotta,F. and Dusart,J. (2002) Subdivision of the helix-turn-helix GntR family of bacterial regulators in the FadR, HutC, MocR, and YtrA subfamilies. *J. Biol. Chem.*, **277**, 12507–12515.
43. Hoskisson,P.A. and Rigali,S. (2009) Chapter 1: variation in form and function the helix-turn-helix regulators of the GntR superfamily. *Adv. Appl. Microbiol.*, **69**, 1–22.
44. Jain,D. (2015) Allosteric control of transcription in GntR family of transcription regulators: a structural overview. *IUBMB Life*, **67**, 556–563.
45. Blotz,C., Treffon,K., Kaever,V., Schwede,F., Hammer,E. and Stülke,J. (2017) Identification of the components involved in cyclic di-AMP signaling in *Mycoplasma pneumoniae*. *Front Microbiol*, **8**, 1328.
46. Romeo,Y., Obis,D., Bouvier,J., Guillot,A., Fourcans,A., Bouvier,I., Gutierrez,C. and Mistou,M.Y. (2003) Osmoregulation in *Lactococcus lactis*: BusR, a transcriptional repressor of the glycine betaine uptake system BusA. *Mol. Microbiol.*, **47**, 1135–1147.
47. Romeo,Y., Bouvier,J. and Gutierrez,C. (2007) Osmotic regulation of transcription in *Lactococcus lactis*: ionic strength-dependent binding of the BusR repressor to the busA promoter. *FEBS Lett.*, **581**, 3387–3390.
48. Poorinmohammad,N., Hamedi,J. and Masoudi-Nejad,A. (2020) Genome-scale exploration of transcriptional regulation in the nisin Z producer *Lactococcus lactis* subsp. lactis IO-1. *Sci. Rep.*, **10**, 3787.
49. Gibson,D.G., Young,L., Chuang,R.Y., Venter,J.C., Hutchison,C.A. 3rd and Smith,H.O. (2009) Enzymatic assembly of DNA molecules up to several hundred kilobases. *Nat. Methods*, **6**, 343–345.
50. Pace,C.N., Vajdos,F., Fee,L., Grimsley,G. and Gray,T. (1995) How to measure and predict the molar absorption coefficient of a protein. *Protein Sci.*, **4**, 2411–2423.
51. Franke,D., Petoukhov,M.V., Konarev,P.V., Panjkovich,A., Tuukkanen,A., Mertens,H.D.T., Kikhney,A.G., Hajizadeh,N.R., Franklin,J.M., Jeffries,C.M. *et al.* (2017) ATSAS 2.8: a comprehensive data analysis suite for small-angle scattering from macromolecular solutions. *J. Appl. Crystallogr.*, **50**, 1212–1225.
52. Mertens,H.D. and Svergun,D.I. (2010) Structural characterization of proteins and complexes using small-angle X-ray solution scattering. *J. Struct. Biol.*, **172**, 128–141.
53. Putnam,C.D., Hammel,M., Hura,G.L. and Tainer,J.A. (2007) X-ray solution scattering (SAXS) combined with crystallography and computation: defining accurate macromolecular structures, conformations and assemblies in solution. *Q. Rev. Biophys.*, **40**, 191–285.
54. Kabsch,W. (2010) Xds. *Acta Crystallogr. D. Biol. Crystallogr.*, **66**, 125–132.
55. Pape,T. and Schneider,T.R. (2004) HKL2MAP: a graphical user interface for macromolecular phasing with SHELX programs. *J. Appl. Crystallogr.*, **37**, 843–844.
56. Sheldrick,G.M. (2010) Experimental phasing with SHELXC/D/E: combining chain tracing with density modification. *Acta Crystallogr. D. Biol. Crystallogr.*, **66**, 479–485.
57. Cowtan,K. (2006) The Buccaneer software for automated model building. 1. Tracing protein chains. *Acta Crystallogr. D. Biol. Crystallogr.*, **62**, 1002–1011.
58. Emsley,P., Lohkamp,B., Scott,W.G. and Cowtan,K. (2010) Features and development of Coot. *Acta Crystallogr. D. Biol. Crystallogr.*, **66**, 486–501.
59. Liebschner,D., Afonine,P.V., Baker,M.L., Bunkoczi,G., Chen,V.B., Croll,T.I., Hintze,B., Hung,L.W., Jain,S., McCoy,A.J. *et al.* (2019) Macromolecular structure determination using X-rays, neutrons and electrons: recent developments in Phenix. *Acta Crystallogr. D Struct. Biol.*, **75**, 861–877.
60. Krissinel,E. and Henrick,K. (2007) Inference of macromolecular assemblies from crystalline state. *J. Mol. Biol.*, **372**, 774–797.
61. Zheng,S.Q., Palovcak,E., Armache,J.P., Verba,K.A., Cheng,Y. and Agard,D.A. (2017) MotionCor2: anisotropic correction of beam-induced motion for improved cryo-electron microscopy. *Nat. Methods*, **14**, 331–332.
62. Punjani,A., Rubinstein,J.L., Fleet,D.J. and Brubaker,M.A. (2017) cryoSPARC: algorithms for rapid unsupervised cryo-EM structure determination. *Nat. Methods*, **14**, 290–296.
63. Bepler,T., Morin,A., Rapp,M., Brasch,J., Shapiro,L., Noble,A.J. and Berger,B. (2019) Positive-unlabeled convolutional neural networks for particle picking in cryo-electron micrographs. *Nat. Methods*, **16**, 1153–1160.
64. Bepler,T., Kelley,K., Noble,A.J. and Berger,B. (2020) Topaz-Denoise: general deep denoising models for cryoEM and cryoET. *Nat. Commun.*, **11**, 5208.
65. Scheres,S.H. (2012) RELION: implementation of a Bayesian approach to cryo-EM structure determination. *J. Struct. Biol.*, **180**, 519–530.
66. Kim,H., Youn,S.J., Kim,S.O., Ko,J., Lee,J.O. and Choi,B.S. (2015) Structural studies of potassium transport protein KtrA regulator of conductance of K+ (RCK) C domain in complex with cyclic diadenosine monophosphate (c-di-AMP). *J. Biol. Chem.*, **290**, 16393–16402.
67. Vigouroux,A., Meyer,T., Naretto,A., Legrand,P., Aumont-Nicaise,M., Di Cicco,A., Renoud,S., Dore,J., Levy,D., Vial,L. *et al.* (2021) Characterization of the first tetrameric transcription factor of the GntR superfamily with allosteric regulation from the bacterial pathogen *Agrobacterium fabrum*. *Nucleic. Acids. Res.*, **49**, 529–546.
68. Kumaraswami,M., Newberry,K.J. and Brennan,R.G. (2010) Conformational plasticity of the coiled-coil domain of BmrR is required for bmr operator binding: the structure of unliganded BmrR. *J. Mol. Biol.*, **398**, 264–275.
69. Fang,C., Li,L., Zhao,Y., Wu,X., Philips,S.J., You,L., Zhong,M., Shi,X., O'Halloran,T.V., Li,Q. *et al.* (2020) The bacterial multidrug resistance regulator BmrR distorts promoter DNA to activate transcription. *Nat. Commun.*, **11**, 6284.

Supplemental Data

BusR Senses Bipartite DNA Binding Motifs by a Unique Molecular Ruler Architecture

Adrian M. Bandera, Joseph Bartho, Katja Lammens, David Jan Drexler, Jasmin Kleinschwärzer, Karl-Peter Hopfner and Gregor Witte

Supplemental Figures

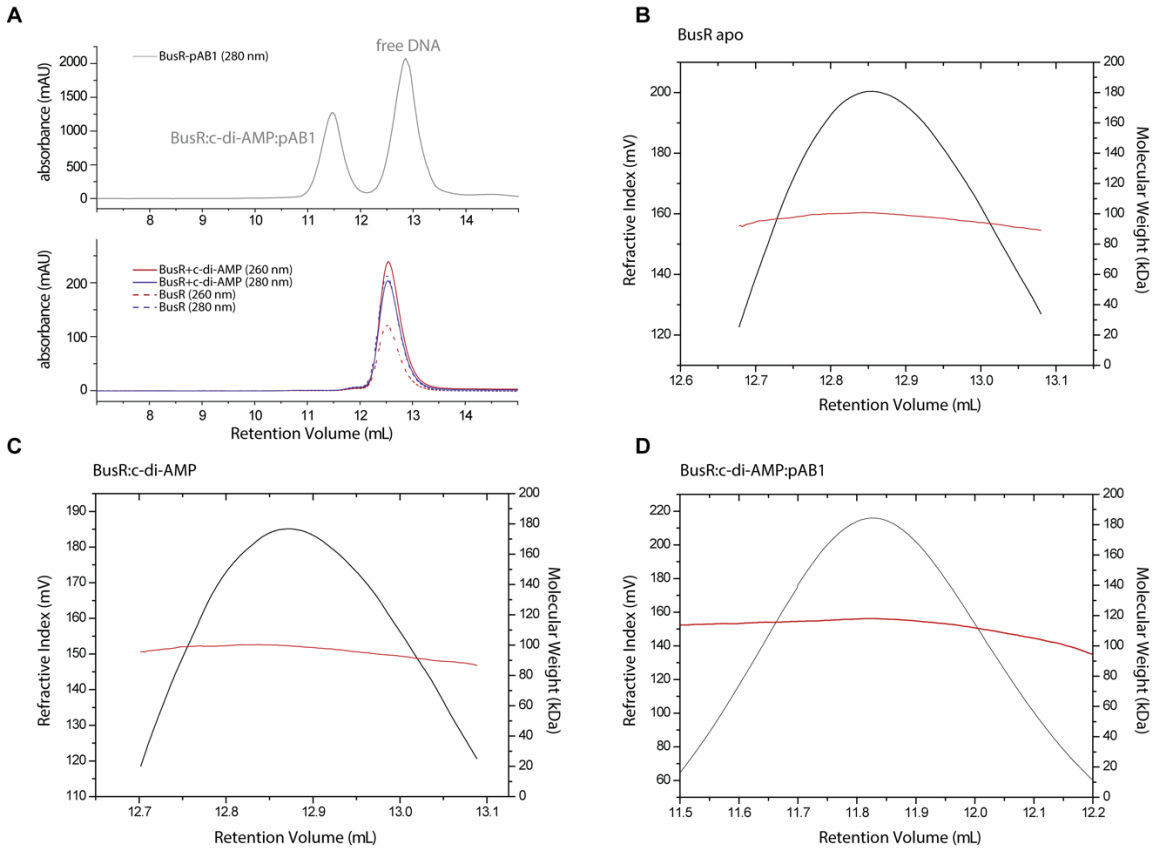

Figure S 1. Determination of Molecular weight and oligomeric state by static light scattering.
Molecular weight determined by size-exclusion chromatography coupled right-angle light scattering using a 24 mL 10/300 Superdex S200 increase column (Cytiva) and an additional refractive index detector (Viscotek).
(A) UV-profile for the BusR:c-di-AMP:pAB1 complex (grey, top), for BusR (dashed line, bottom) at 260 nm (red) and 280 nm (blue) and for BusR with c-di-AMP bound (straight line, bottom). Panels B – D show the refractive Index and the molecular weight for the main peak fractions. (B) BusR has an experimental weight of 97 kDa (Mw/Mn = 1.001, n=1) that corresponds to a tetramer (theoretical Mw = 95.4 kDa). (C) Addition of c-di-AMP does not alter the oligomeric state (measured Mw = 96.3 kDa, theoretical Mw = 96.7 kDa, Mw/Mn = 1.002). (D) A tetramer of BusR binds to a single molecule of double stranded pAB1 – DNA. Experiment conducted in presence of 3-fold excess of DNA (exp. Mw = 116.5 kDa, theoretical Mw (BusR:pAB1) = 123.4 kDa, Mw (BusR:$(pAB1)_2$) = 151.4 kDa, Mw/Mn = 1.000)

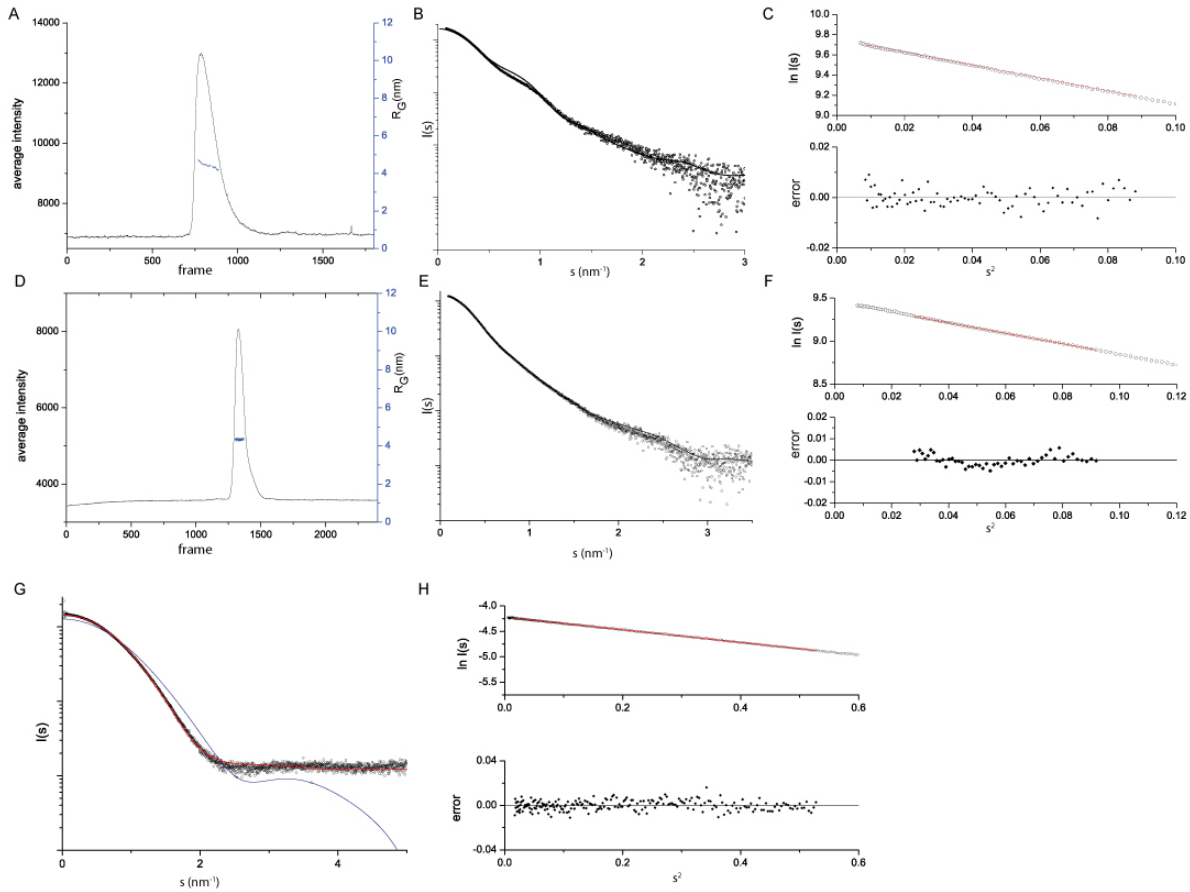

Figure S 2. Small-angle X-ray scattering of BusR.
(A) Chromatogram (average sample scattering vs. retention time = frames) of a size-exclusion coupled SAXS (SEC-SAXS) experiment with 5 mg/mL sample of BusR on a Superdex S200 5/150GL column (20 mM HEPES pH 7.6, 200 mM NaCl, 3% v/v glycerol) with approximated R_G values (blue) of the peak frames.
(B) Averaged sample scattering curve after buffer correction (circles) and the theoretical scattering curve (line) of BusR calculated from our crystal structure using CRYSOL.
(C) Guinier analysis of the scattering data from (B) in the Guinier region $s*R_G<1.3$ (globular particles), indicating that the sample is free of aggregation as can be seen by the homogenous error distribution of the linear regression. (R_G^{BusR} = 4.4 nm)
(D) Chromatogram of SEC-SAXS experiment with a complex of BusR:pAB1:c-di-AMP on a Superdex S200 10/300GL column (20 mM HEPES pH6.5, 100 mM NaCl, 3% glycerol (v/v)) with approximated R_G values (blue) of the peak frames.
(E) Averaged sample scattering curve after buffer correction (circles) and the theoretical scattering curve (line) of the BusR:pAB1:c-di-AMP complex calculated from our cryo-EM structure (χ^2 = 5.8)
(F) shows the Guinier analysis of the scattering data from (E) in the Guinier region with errors ($R_G^{complex}$ = 4.28 nm)
(G) Scattering curve of the isolated RCK_C domain in solution (batch measurement, buffer 100 mM NaCl, 30 mM HEPES, pH 7.5) with calculated scattering curves of a RCK_C monomer (blue) and RCK_C dimer (red, χ^2 = 5.8). The scattering curve is only compatible with the presence of RCK_C dimers in solution.
(H) Guinier analysis of the scattering data from (G) with errors ($R_G^{RCK\_C\_dimer}$ = 1.9 nm).

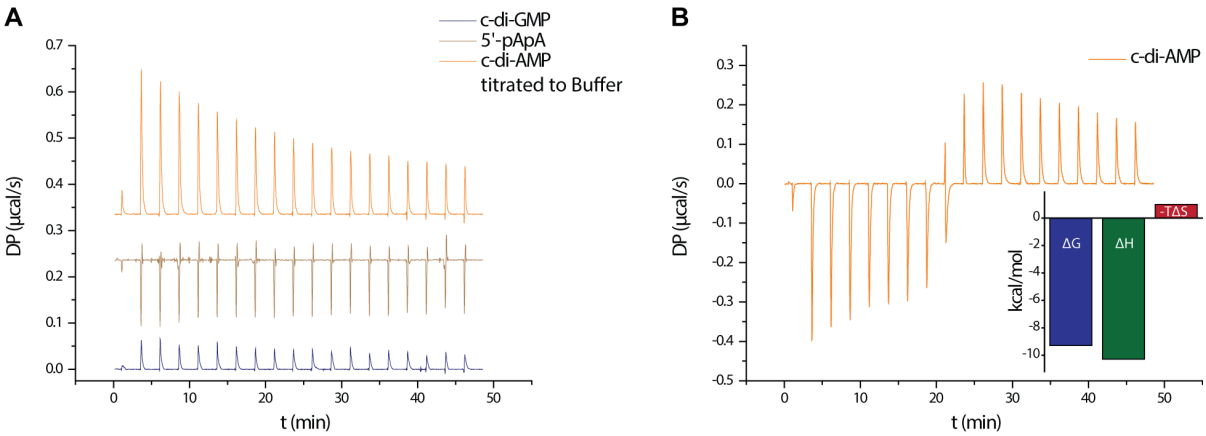

Figure S 3. Raw data for binding analysis of c-di-AMP by ITC, related to Figure 1(C).
(A) ITC measurement raw data of 20 µM full length BusR titrated with 400 µM c-di-GMP (blue) or 5'-pApA (brown). A control of c-di-AMP titrated to buffer results in a strong signal and is therefore displayed as well (orange) and is used as control reference for correction of (B) – see Fig. 1C.
(B) ITC measurement raw data (uncorrected) of 400 µM c-di-AMP titrated to 20 µM full length BusR and respective corresponding signature plot of the corrected data – Fig. 1C.

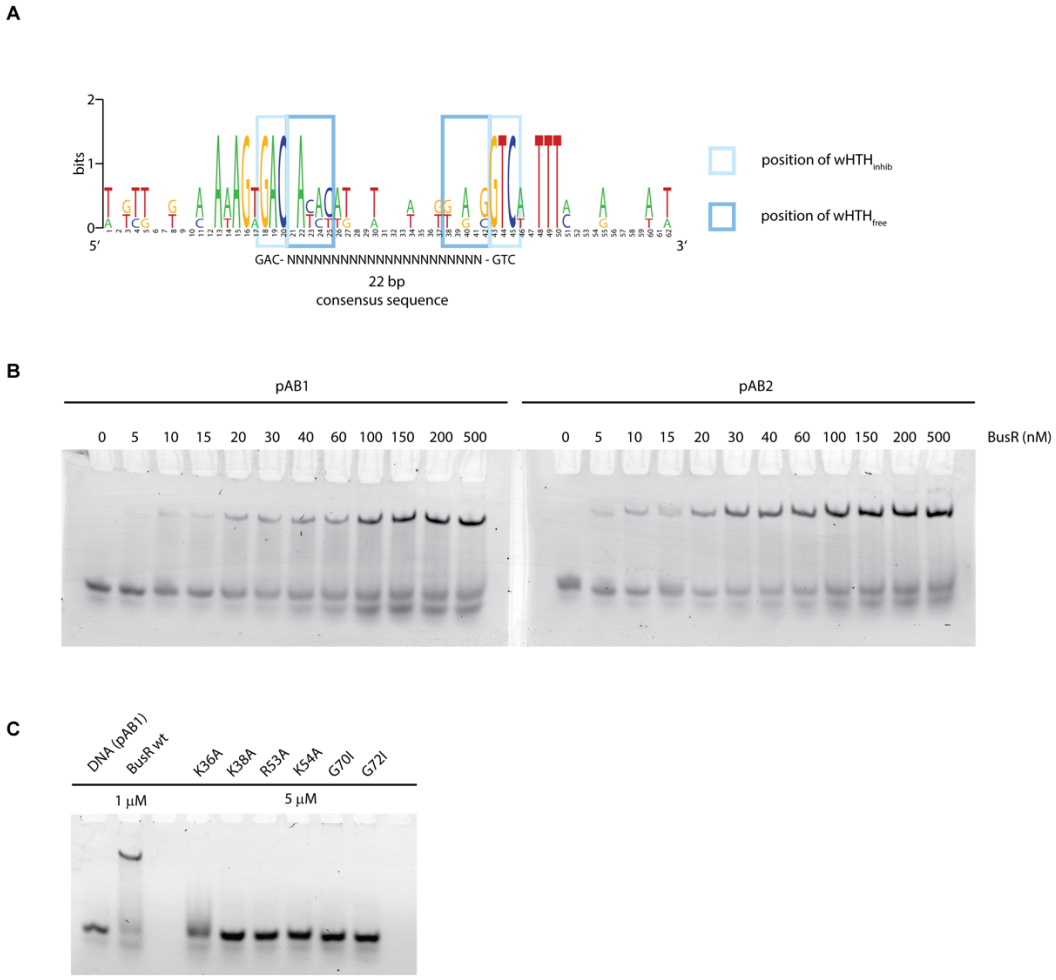

Figure S 4. Additional experimental data on BusR DNA binding by EMSA.
(A) Logo plot of aligned binding sites of four experimentally confirmed operator sequences of BusR from *Lactococcus lactis, Tetragenococcus halophilus*, and two sequences from *Streptococcus agalactiae* (created with the Berkeley WebLogo server[1]).
(B) BusR titrated to pAB1-DNA (left) and pAB2-DNA (right) in presence of c-di-AMP (20 nM DNA, 10 µM c-di-AMP, n = 3). Both binding sites are bound with comparable affinity.
(C) BusR mutants with point mutations in the wHTH motif in comparison to BusR wt by EMSA. The depicted mutants all show severe binding deficiency compared to the wildtype (20 nM DNA, 10 µM c-di-AMP, n = 3).

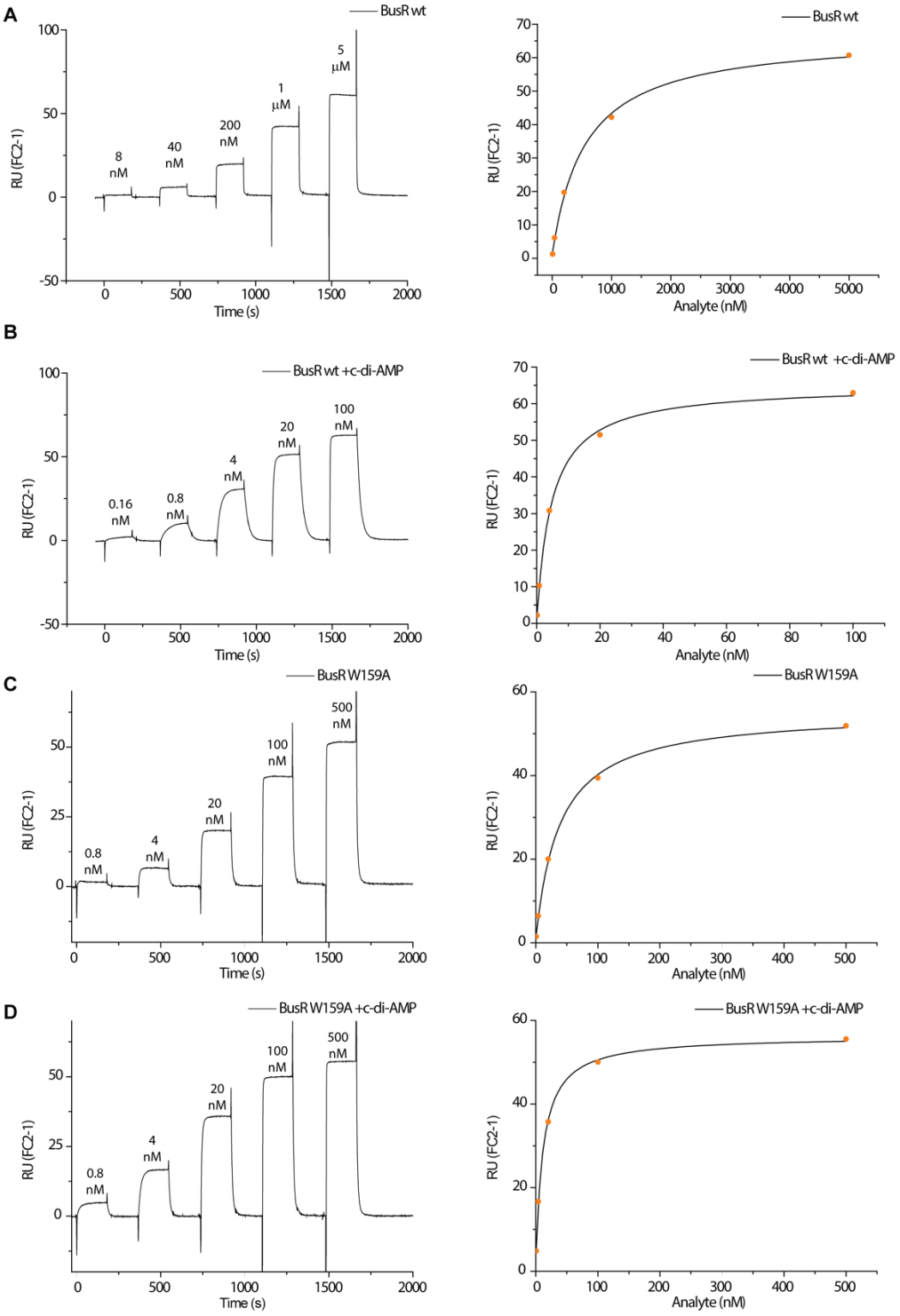

Figure S 5. Raw data of BusR DNA binding by SPR.
Representative SPR raw data (left) of BusR titrated to pAB1 (on chip) in single-cycle assays and their corresponding steady state affinity fit for a 1:1 binding model (right). For all experiments we performed independent triplicate measurements.
(A) BusR wt (0.8 nM – 5 µM analyte concentration) in absence of c-di-AMP, K_D = 577 ± 55 nM.
(B) BusR wt (0.16 nM – 100 nM) in presence of 10 µM c-di-AMP (10 µM), K_D = 5.1 ± 0.4 nM.
(C) BusR W159A (0.8 nM – 500 nM) in absence of c-di-AMP, K_D = 11 ± 2 nM.
(D) BusR W159A (0.8 nM – 500 nM) in presence of c-di-AMP (10 µM), K_D = 34 ± 8 nM.

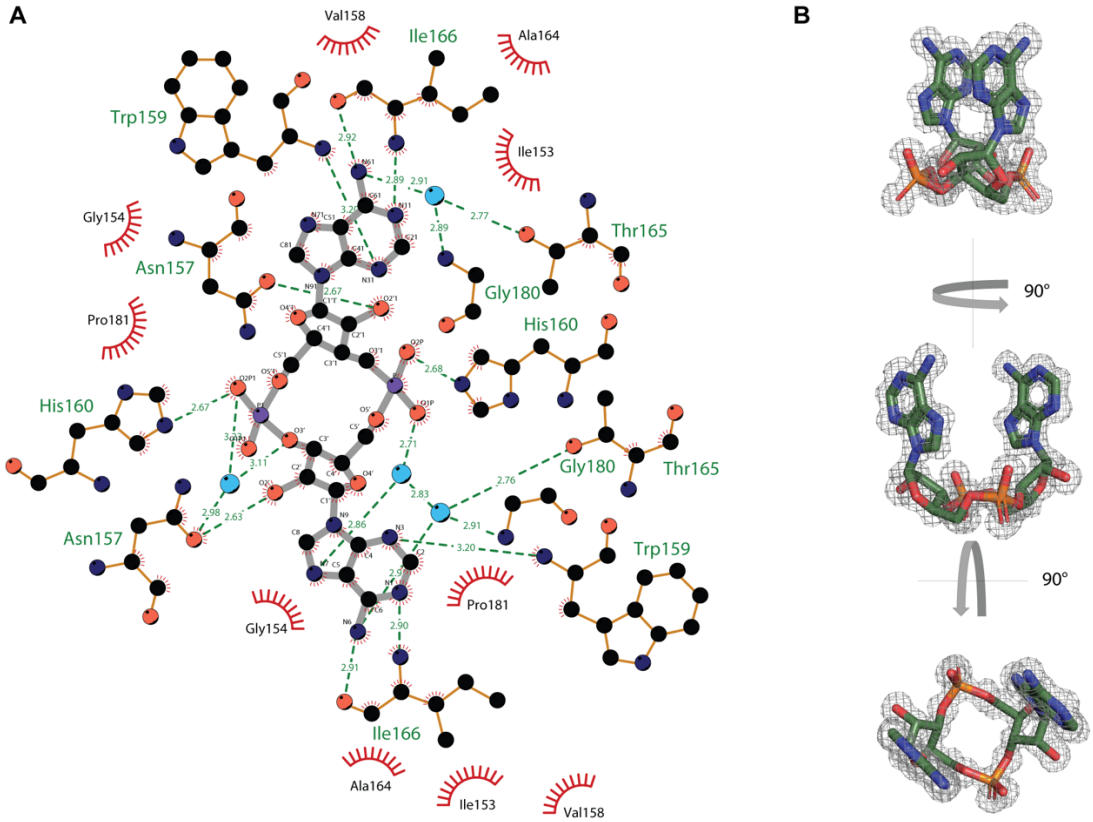

Figure S 6. Ligand coordination plot and polder map, related to figure 2.
(A) Schematic plot of the c-di-AMP coordination by the RCK_C domain, calculated with ligplot [2].
(B) Polder map of c-di-AMP in the binding pocket at 3σ contour level from different angles [3].

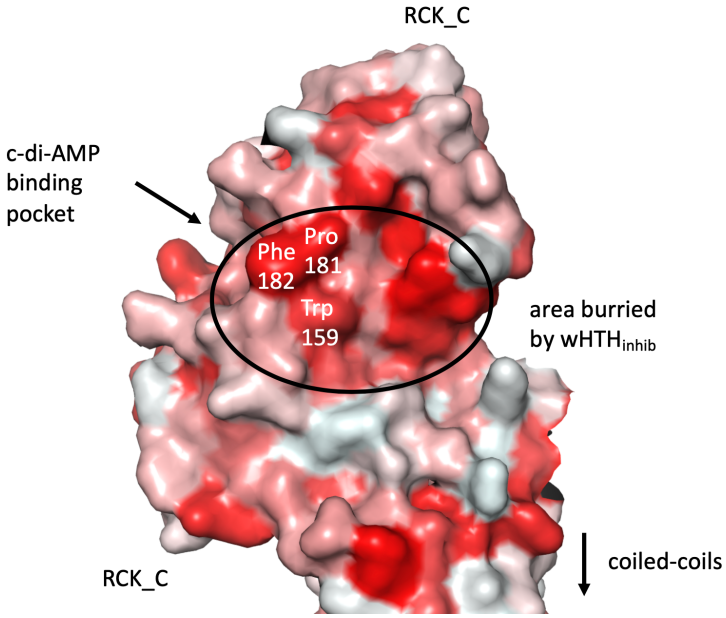

Figure S 7. Hydrophobicity of the RCK_C – wHTH$_{inhib}$ interface.
Side view of the RCK_C domain of full length BusR as surface representation colored according to hydrophobicity (red = hydrophobic). Both DNA binding domains have been omitted for clarity reasons. The circle indicates the area that is buried in the interface with wHTH$_{inhib}$.

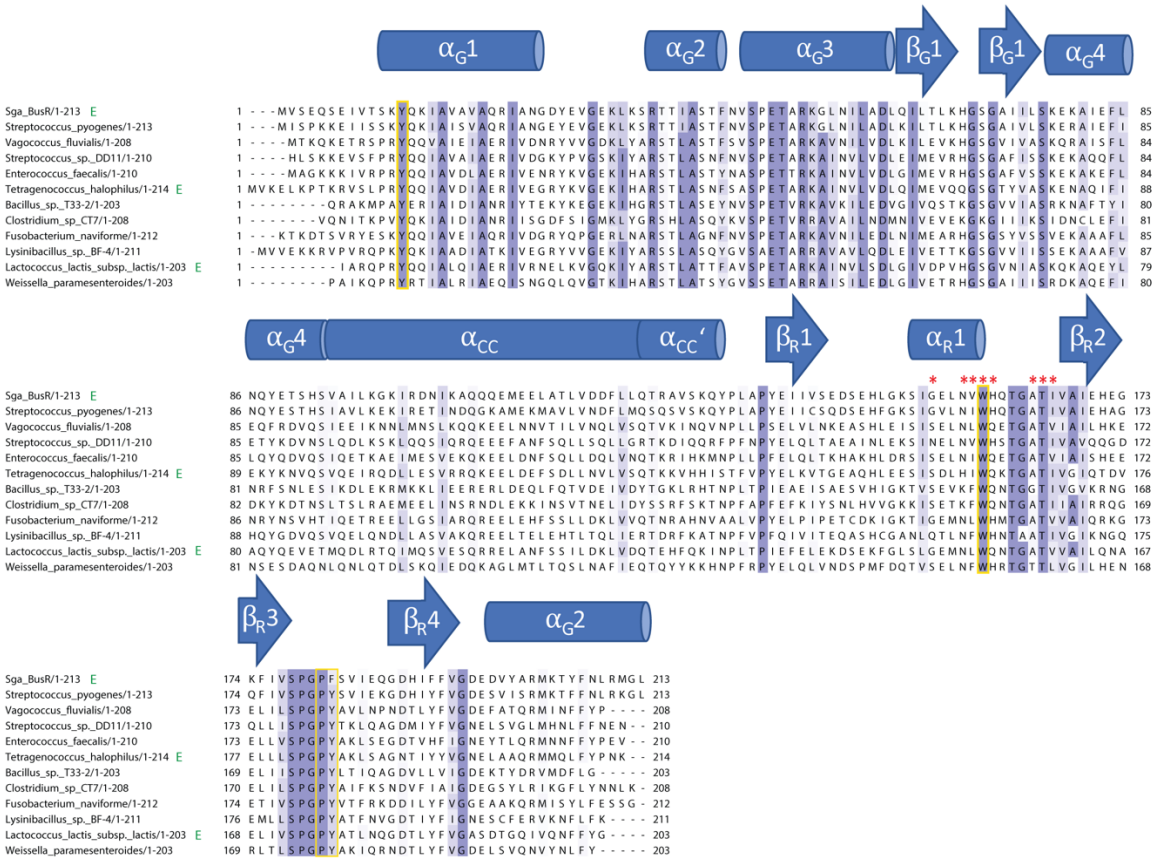

Figure S 8. Multiple Sequence Alignment of BusR homologues.
Putative BusR sequences from different species. The resulting sequences include also experimentally described homologues (green E). The resulting multiple sequence alignment is colored according to conservation. Residues involved in the RCK_C - wHTH$_{inhib}$ signaling interface are highlighted with a yellow box. Residues involved in c-di-AMP coordination are marked by a red asterisk.

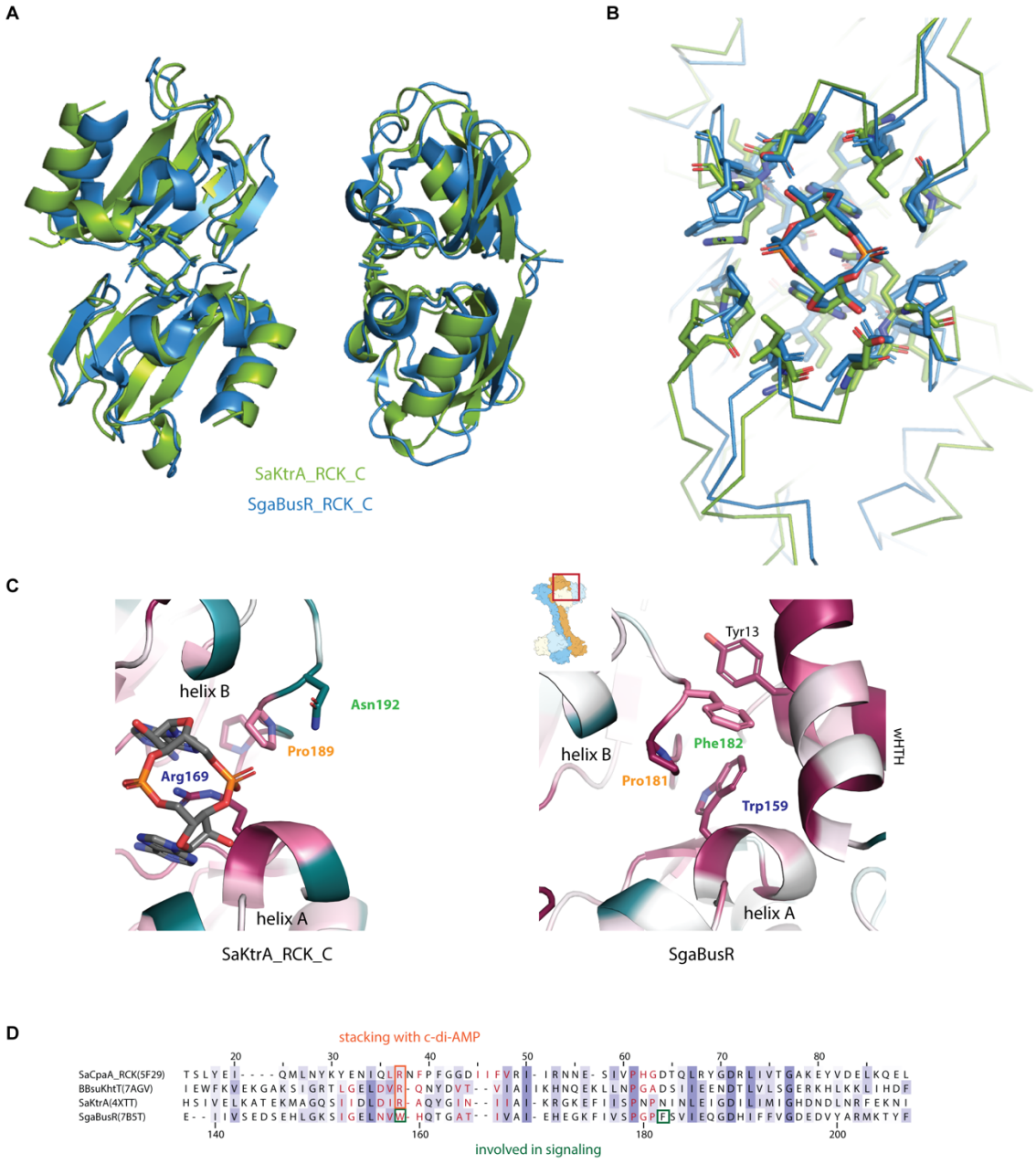

Figure S 9. Comparison of RCK_C domains from *S. agalactiae* BusR and *S. aureus* KtrA.
(A) Superposition of the RCK_C domains from the different proteins BusR and KtrA shows a high structural similarity (RMSD = 1.379 Å).
(B) Stick representation of the c-di-AMP binding sites. The ligand binding sites share very similar main chain geometry while most sidechains are not conserved
(C) Close-up on "signaling residues" in SaKtrA (left) and their counterpart in apo BusR (right). Residues are colored according to conservation generated with the ConSurf server from 150 sequences. Highly conserved residues are colored in dark purple, high variability is presented in cyan. While SaKtrA Arg169 stacks with c-di-AMP, the sidechain of BusR Trp159 is not involved in c-di-AMP coordination but coordinates a conserved hydrophobic patch including Tyr13, Phe182 and Pro181. SaKtrA Phe192, the equivalent of BusR Phe182 is not conserved, as no regulatory hydrophobic patch exists.
(D) Sequence alignment of c-di-AMP binding and similar structurally characterized RCK_C domains.

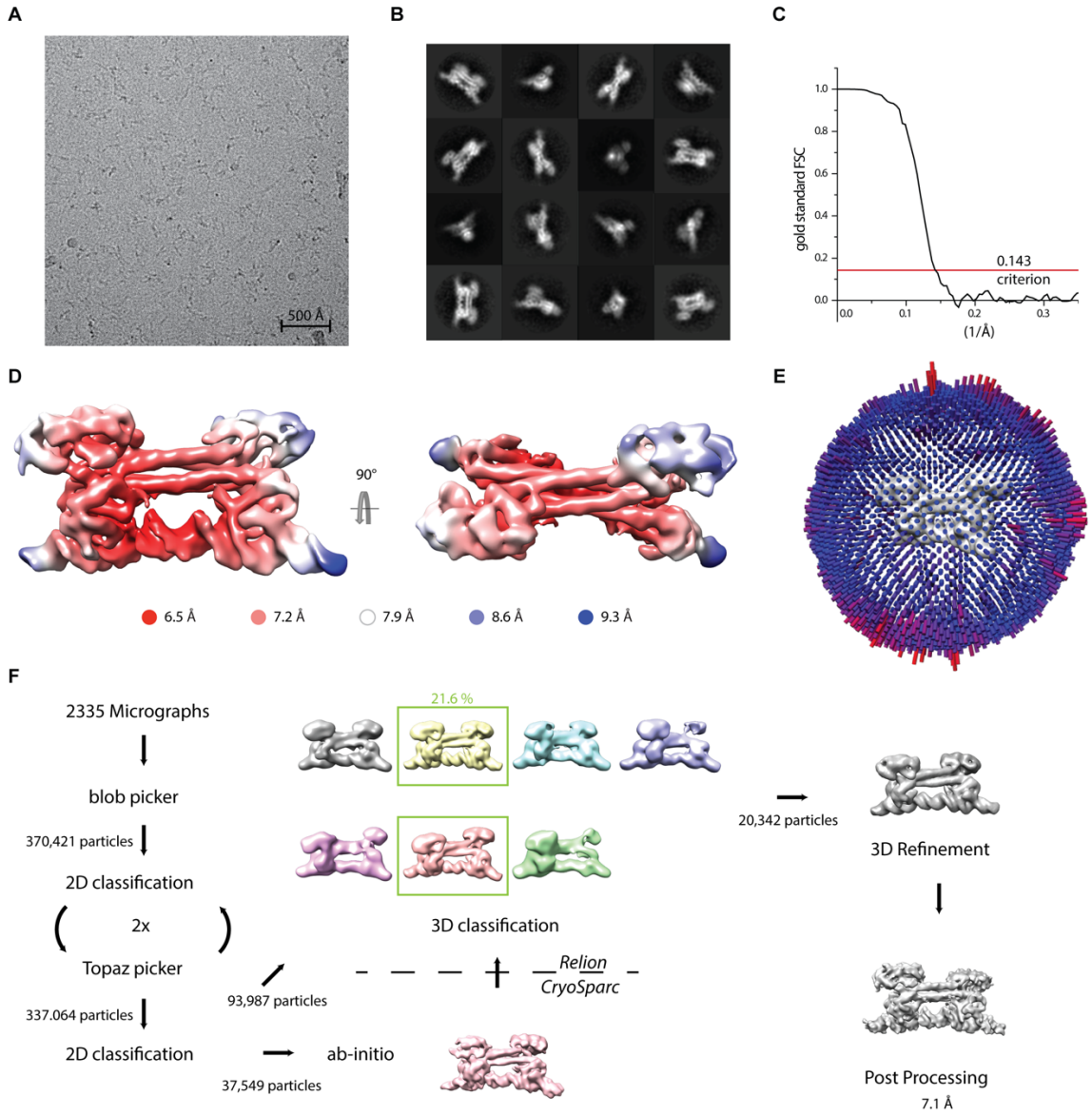

Figure S 10. CryoEM processing of the BusR:c-di-AMP:pAB1 complex.
(A) Representative micrograph at 30° tilt angle.
(B) 16 distinct and highly populated 2D classes from the final reconstruction.
(C) Gold-standard Fourier shell correlation curve. The red line represents the 0.143 criterion which proposes 7.1 Å average resolution.
(D) Variability in local resolution ranging from 6.5 Å (dark red) to 9.3 Å (dark blue). Calculated using Relion 3.1
(E) Overall angular distribution of the particles used for final reconstruction.
(F) Schematic Processing scheme leads to the final reconstruction with 20,342 particles and C1 symmetry.

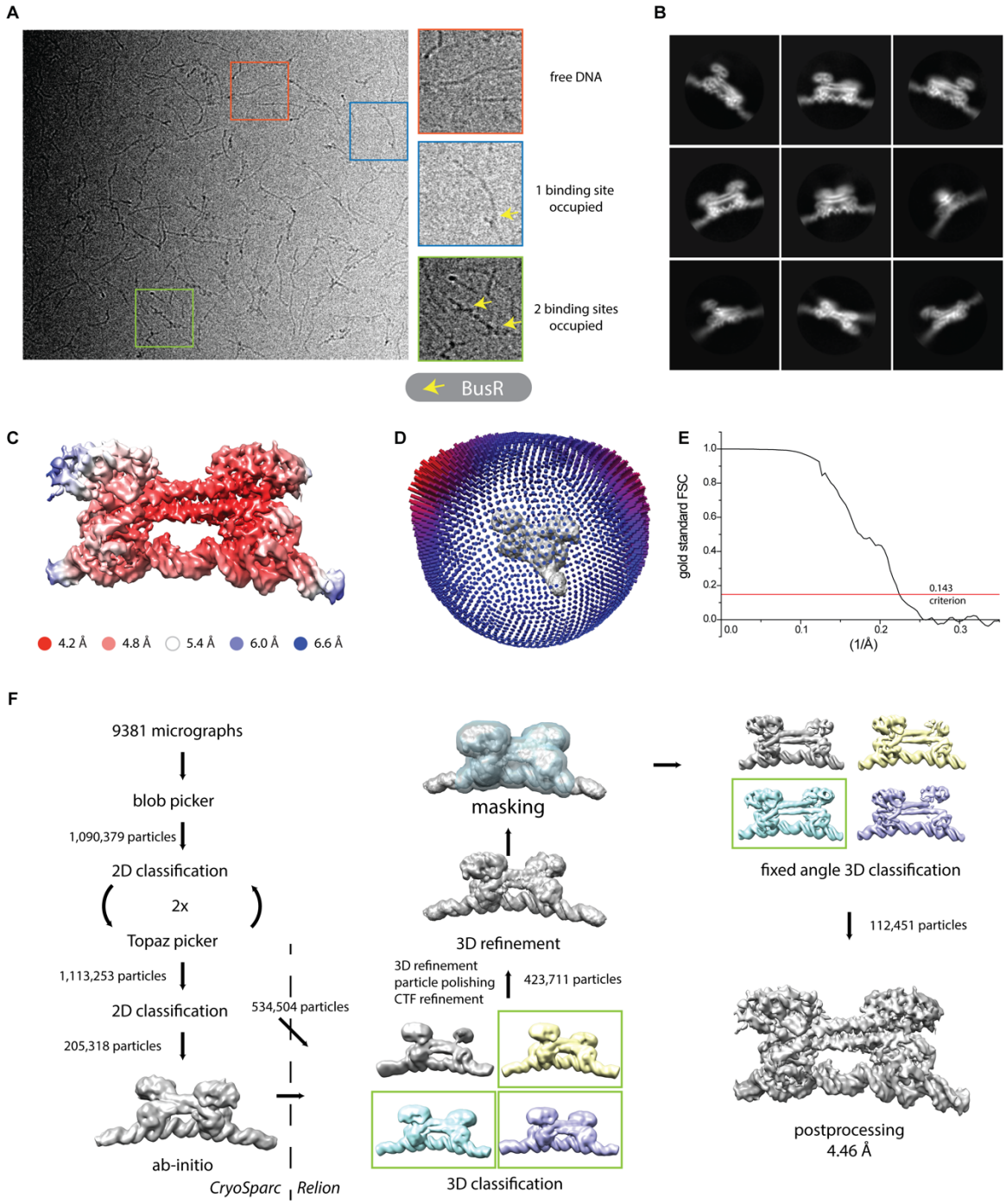

Figure S 11. CryoEM processing of the BusR:c-di-AMP:pbusA complex and additional data related to figure 3
(A) representative micrograph and highlighted observed species.
(B) Representative 2D classes from the final reconstruction.
(C) Variability in local resolution. Resoltion ranging from 4.2 Å (dark red) to 6.6 Å (dark blue) according to Relion 3.1.2.
(D) Overall angular distribution of the particles used for final reconstruction.
(E) Gold-standard Fourier shell correlation curve. The red line represents the 0.143 criterion which proposes 4.46 Å average resolution (calculated using Relion 3.1)
(F) Complete processing scheme for BusR:c-di-AMP:pAB.

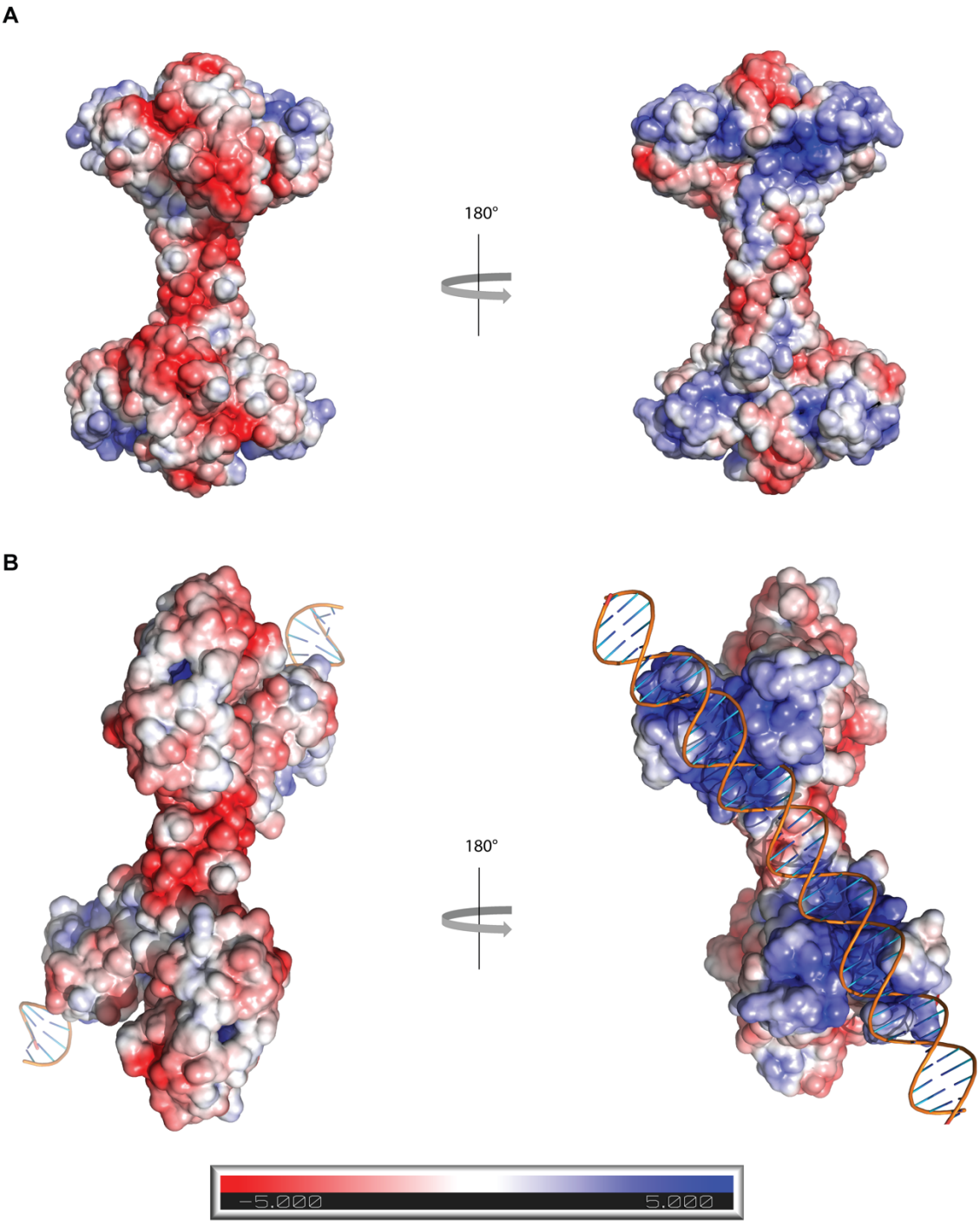

Figure S 12. Surface accessible electrostatic surface of BusR.
All solvent accessible electrostatic surfaces (ranging from -5 KT/e to 5 KT/e) were calculated using the Adaptive Poisson-Boltzmann Solver (APBS) plug-in in pymol [4].
(A) Apo BusR reveals an asymmetric distribution of electrostatic potential.
(B) When bound to DNA the negative charge of the DNA's phosphate backbone is directed towards the positively charged surface of BusR surrounding the DNA. The DNA was removed from the model during APBS calculation.

Table S1. Crystallographic Data and Refinement Statistics

Protein	BusR_fl_wt	RCK_C-cdA	His_6-RCK_C
Data collection			
Beamline	EMBL-P13	EMBL-P14	EMBL-P13
Wavelength (Å)	0.9797	0.9763	0.9
Resolution range	48.22 - 2.802 (2.902 - 2.802)	17.48 - 1.2 (1.23 - 1.2)	18.0 - 1.001 (1.03 - 1.00)
Space group	I 4	P 1 21 1	C 1 2 1
Cell dimensions			
a, *b*, *c* (Å)	114.18 114.18240.48	33.16 60.95 35.71	46.26 40.41 41.01
α, β, γ (°)	90 90 90	90 101.73 90	90 103.21 90
Total reflections	518066 (36988)	285772 (16873)	251457 (15270)
Unique reflections	74011 (5409)	41498 (2859)	39372 (2881)
Multiplicity	6.9 (6.83)	6.9 (5.9)	6.4 (5.3)
Completeness (%)	99.1 (97.7)	95.4 (88.3)	99.1 (97.0)
I/sigma(I)	19.4 (1.02)	36.6 (14.9)	21.6 (1.9)
Wilson B-factor	101.5	12.6	14.4
R-meas	8.0 (164.6)	3.4 (11)	3.2 (96.6)
CC1/2	100.0 (61.5)	100 (99.3)	100 (77.3)
Refinement			
Resolution	2.8	1.2	1.0
Reflections used in refinement	37333 (3694)	41497	39369
Reflections used for R-free	1827 (154)	1923	1906
R-work	25.7 (41.2)	13.1 (11.4)	19.9 (34.3)
R-free	26.9 (42.9)	15.5 (13.4)	22.6 (34.6)
Molecules (asu)	1 tetramer	1 dimer	1 monomer
Number of non-hydrogen atoms	6528	1585	898
macromolecules	6506	1307	794
solvent	22	278	104
Protein residues	828	157	97
RMS(bonds)	0.005	0.006	0.009
RMS(angles)	0.96	1.28	1.28
Ramachandran favored (%)	95.1	98.69	96.84
Ramachandran allowed (%)	4.8	1.31	2.11
Ramachandran outliers (%)	0.1	0.00	1.05
Rotamer outliers (%)	3.5	0.00	0.00
Clashscore	11.5	1.96	0.00
Average B-factor	127.9	12.90	20.38
macromolecules	128.0	10.26	19.08
solvent	98.1	25.33	30.28
Number of TLS groups	12		
PDB ID	7B5T	7B5U	7B5W

rmsd, root-mean-square deviation. asu, asymmetric unit. Values in parentheses are for the last resolution shell

Table S2. EM Data Collection, 3D Reconstruction, and Model Refinement Statistics

	S. agalactiae **BusR:c-di-AMP:pAB complex**	***S. agalactiae*** **BusR:c-di-AMP: pAB1**
Data collection and processing		
Magnification	130000	130000
Voltage (kV)	300	300
Electron exposure (e^{-}/Å^2)	45	45
Defocus range (μm)	-1.1 to -2.6	-1.0 to -2.8
Pixel size (Å)	1.046	1.059
Symmetry imposed	C1	C1
Initial particle images (no.)	1,090,379	370,421
Final particle images (no.)	112,451	20,342
Map resolution (Å) / FSC threshold	4.46 / 0.143	7.1 / 0.143
Map-resolution range (Å)	4.2 - 6.6	6.5 - 9.3
Refinement		
Initial model used (PDB code)	This work	This work
Model resolution (Å)	4.0	7.1
FSC threshold	0 / 0.143 / 0.5	0 / 0.143 / 0.5
Model-resolution range (Å)	3.8 / 3.9 / 4.5	5.5 / 6.3 / 7.7
Map-sharpening *B* factor (Å^2)	- 177.2	-492.7
Model composition		
Nonhydrogen	8209	8434
Protein residues	804	818
Nucleotides	88	92
Ligands	c-di-AMP (2x)	c-di-AMP (2x)
Mean *B* factors (Å^2)		
Protein	127.7	226.7
Ligand	141.9	319.5
Nucleotide	158.5	256.3
R.m.s. deviations		
Bond lengths (Å)	0.009	0.009
Bond angles (°)	1.35	1.6
Validation		
MolProbity score	1.75	2.46
Clashscore	8.38	13.56
Poor rotamers (%)	0.29	3.26
Ramachandran plot		
Favored (%)	95.7	93.46
Allowed (%)	4.3	5.93
Disallowed (%)	0	0.62
PDB ID	7OZ3	7B5Y

Table S 3. Oligos (5′ – 3′)

purpose	name	sequence	modification
cloning	Sga BusR f	TCTTGAAGTCCTCTTTCAGGGACCCATGGTTTCTGAACAATCTGAAATTGTAACATC	
	Sga BusR r	TGGCACCAGAGCGAGCTCAAGCCCCATCCTTAAGTTAAAATAGGTTTTCA	
	Sga RCK_C f	CTTGAAGTCCTCTTTCAGGGACCCCTAGCACCATATGAAATTATTG	
	QC W159A f	TAGGAGAATTAAATGTAGCGCATCAAACTGGTGCGAC	
	QC W159A r	GTCGCACCAGTTTGATGCGCTACATTTAATTCTCCTA	
	QC_K36A f	GTTGGAGAGAAGTTGGCATCTAGAACAACTATT	
	QC_K36A r	AATAGTTGTTCTAGATGCCAACTTCTCTCCAAC	
	QC_R38A f	GAGAAGTTGAAATCTGCAACAACTATTGCTTCA	
	QC_R38A r	TGAAGCAATAGTTGTTGCAGATTTCAACTTCTC	
	QC_R53A f	TCACCAGAAACAGCAGCTAAGGGTCTTAATATT	
	QC_R53A r	AATATTAAGACCCTTAGCTGCTGTTTCTGGTGA	
	QC_K54A f	CCAGAAACAGCACGTGCGGGTCTTAATATTTTA	
	QC_K54A r	CTAAAATATTAAGACCCGCACGTGCTGTTTCTGG	
	QC_G70I f	TTAACTTTAAAGCATATCAGTGGAGCCATTATT	
	QC_G70I r	AATAATGGCTCCACTGATATGCTTTAAAGTTAA	
	QC_G72I f	TTAAAGCATGGCAGTATAGCCATTATTCTTTCT	
	QC_G72I r	AGAAAGAATAATGGCTATACTGCCATGCTTTAA	
	QC_pAB1_BS1-f	GAGTAAAAAAGTATGTACCCTTTTACGATAAC	
	QC_pAB1_BS1-r	GTTATCGTAAAAGGGTACATACTTTTTTACTC	
	QC_pAB1_BS2-f	GTGTCTTATCTATAAAGTATGGTTGAGTTATCG	
	QC_pAB1_BS2-r	CGATAACTCAACCATACTTTATAGATAAGACAC	
Cloning & Amplification For cryoEM	pAB_f	ATAAAGCTTCTCTAAGCAAGGTG	
	pAB_r	ATAGGATCCGTGTCTTATCTATAAAGTG	
EMSA	pAB1_for	ATAAAGTGACGTTAAAGTATCGTAAAAGGGTAGTCACTTTTTTACT	5′-FAM
	pAB1_rev	AGTAAAAAAGTGACTACCCTTTTACGATACTTTAACGTCACTTTAT	
	pAB1_f 0BS_for	ATAAAGTATGGTTAAAGTATCGTAAAAGGGTACATACTTTTTTACT	5′-FAM
	pAB1_r 0BS_rev	AGTAAAAAAGTATGTACCCTTTTACGATACTTTAACCATACTTTAT	
	pAB1_1BS-A_for	ATAAAGTATGGTTAAAGTATCGTAAAAGGGTAGTCACTTTTTTACT	5′-FAM
	pAB1_1BS-A_rev	AGTAAAAAAGTGACTACCCTTTTACGATACTTTAACCATACTTTAT	
	pAB1_1BS-B_for	ATAAAGTGACGTTAAAGTATCGTAAAAGGGTACATACTTTTTTACT	5′-FAM
	pAB1_1BS-B_rev	AGTAAAAAAGTATGTACCCTTTTACGATACTTTAACGTCACTTTAT	
	pAB1_f_5bp_for	ATAAAGTGACGTTAAAGTATCGTCGATTAAAAGGGTAGTCACTTTTTTACT	5′-FAM
	pAB1_r_5bp_rev	AGTAAAAAAGTGACTACCCTTTTAATCGACGATACTTTAACGTCACTTTAT	
	pAB1_f_-10bp_for	ATAAAGTGACGTTAAAAGGGTAGTCACTTTTTTACT	5′-FAM
	pAB1_r_-10bp_rev	AGTAAAAAAGTGACTACCCTTTTAACGTCACTTTAT	
	ref_f	GGTCATACTTCCTAAGTCACCGGTATGGTAAGCAGGTAGACCTTCGA	5′-FAM
	ref_r	TCGAAGGTCTACCTGCTTACCATACCGGTGACTTAGGAAGTATGACC	
	pbusA_FAM_f	AAGCTTCTCTAAGCAAGGTG	5'FAM
	pbusA_FAM_r	GGATCCGTGTCTTATCTATAAAGTG	5'FAM
cryoEM & SAXS	pAB1_EM_f	CGGTAAAGTGACGTTAAAGTATCGTAAAAGGGTAGTCACTTTTCGG	
	pAB1_EM_r	CCGAAAAGTGACTACCCTTTTACGATACTTTAACGTCACTTTACCG	

Supplemental Methods

A second cryoEM structure of the BusR:DNA complex was solved using shorter DNA with only a single binding site. For grid preparation full-length BusR was incubated with excess c-di-AMP and pAB1 DNA and purified via size exclusion chromatography (Superdex S200 10/300) equilibrated in 20 mM HEPES pH 6.5, 100 mM NaCl. Peak fractions, corresponding to approx. 0.5 mg/mL were pooled. Prior to grid preparation β-octyl glucoside was added to a final concentration of 0.05%. 4.5 µL of sample was applied to plasma cleaned (GloCube, Quorum) UltrAuFoil R2/2 200 mesh grids (Quantifoil), then plunge frozen in liquid ethane using a Leica EM GP. Data was acquired using a Titan Krios transmission electron microscope (Thermo Fisher Scientific) operated at 300 keV, with a Gatan K2 Summit detector operated in counting mode, and Gatan GIF Quantum energy filter. EPU software (TFS) was used for automated acquisition. 3 Datasets at different tilt angles of 20°, 25° and 30° were collected with a total of 2,335 micrographs, with a nominal magnification of 130,000x, calibrated pixel size of 1.059 Å, defocus range of -1.0 to -2.8 µm, and a total dose of 46 $e^-/Å^2$ over 40 frames. For data processing all micrographs were aligned using Motioncor2 [5]. The subsequent steps were done in cryoSPARC v2.15 [6]. Local CTF estimation was done with Patch CTF implemented in cryoSPARC. Initial particles were picked using blob picker. These particles were 2D classified, and high quality and diverse classes were selected and low pass filtered to 20 Å for training of the topaz neural network picker embedded in cryoSPARC [7,8]. The topaz picked particles were extracted and resubjected to 2D classification and topaz training. Final extraction was done with a box size of 220 pixels and particles were subjected to 2D classification. Classes of good resolution were selected and used to generate three initial 3D models (C1 symmetry). The best volume was used as a reference in Relion 3.1 for further 3D classification [9]. The best 3D classes were selected and used for 3D refinement followed by post processing.

Model building was done by using the crystallographic full-length structure of BusR (this work) and dissecting every monomer into the wHTH domain and the RCK_C domain. The coiled-coil domain

with parts of all four monomers was taken as a single entity. These models were rigid body fitted into the cryo-EM map using UCSF Chimera. Coot was used for further building. The linker between the coiled-coils and the RCK_C domain was freely built into the density. An ideal B-DNA based on the sequence of pAB1 was generated and bent to fit the map.

Supplemental References

1 Crooks, G. E., Hon, G., Chandonia, J. M. & Brenner, S. E. WebLogo: a sequence logo generator. *Genome Res* **14**, 1188-1190, doi:10.1101/gr.849004 (2004).

2 Wallace, A. C., Laskowski, R. A. & Thornton, J. M. LIGPLOT: a program to generate schematic diagrams of protein-ligand interactions. *Protein Eng* **8**, 127-134, doi:10.1093/protein/8.2.127 (1995).

3 Liebschner, D. *et al.* Polder maps: improving OMIT maps by excluding bulk solvent. *Acta Crystallogr D Struct Biol* **73**, 148-157, doi:10.1107/S2059798316018210 (2017).

4 Baker, N. A., Sept, D., Joseph, S., Holst, M. J. & McCammon, J. A. Electrostatics of nanosystems: application to microtubules and the ribosome. *Proc Natl Acad Sci U S A* **98**, 10037-10041, doi:10.1073/pnas.181342398 (2001).

5 Zheng, S. Q. *et al.* MotionCor2: anisotropic correction of beam-induced motion for improved cryo-electron microscopy. *Nat Methods* **14**, 331-332, doi:10.1038/nmeth.4193 (2017).

6 Punjani, A., Rubinstein, J. L., Fleet, D. J. & Brubaker, M. A. cryoSPARC: algorithms for rapid unsupervised cryo-EM structure determination. *Nat Methods* **14**, 290-296, doi:10.1038/nmeth.4169 (2017).

7 Bepler, T. *et al.* Positive-unlabeled convolutional neural networks for particle picking in cryo-electron micrographs. *Nat Methods* **16**, 1153-1160, doi:10.1038/s41592-019-0575-8 (2019).

8 Bepler, T., Kelley, K., Noble, A. J. & Berger, B. Topaz-Denoise: general deep denoising models for cryoEM and cryoET. *Nat Commun* **11**, 5208, doi:10.1038/s41467-020-18952-1 (2020).

9 Scheres, S. H. RELION: implementation of a Bayesian approach to cryo-EM structure determination. *J Struct Biol* **180**, 519-530, doi:10.1016/j.jsb.2012.09.006 (2012).

6.2 Supplement II - Structural and Biophysical Analysis of the Soluble DHH/DHHA1-Type Phosphodiesterase TM1595 from *Thermotoga maritima*

Drexler, D.*; Müller, M.*; Rojas-Cordova, C. A.; Bandera, A. M.; Witte, G. Structural and Biophysical Analysis of the Soluble DHH/DHHA1-Type Phosphodiesterase TM1595 from Thermotoga maritima. *Structure* **2017**, *25* (12), 1887-1897.e4.

* contributed equally

DOI: https://doi.org/10.1016/j.str.2017.10.001

URL: https://www.sciencedirect.com/science/article/pii/S0969212617303295

Short Article

Structure

Structural and Biophysical Analysis of the Soluble DHH/DHHA1-Type Phosphodiesterase TM1595 from *Thermotoga maritima*

Graphical Abstract

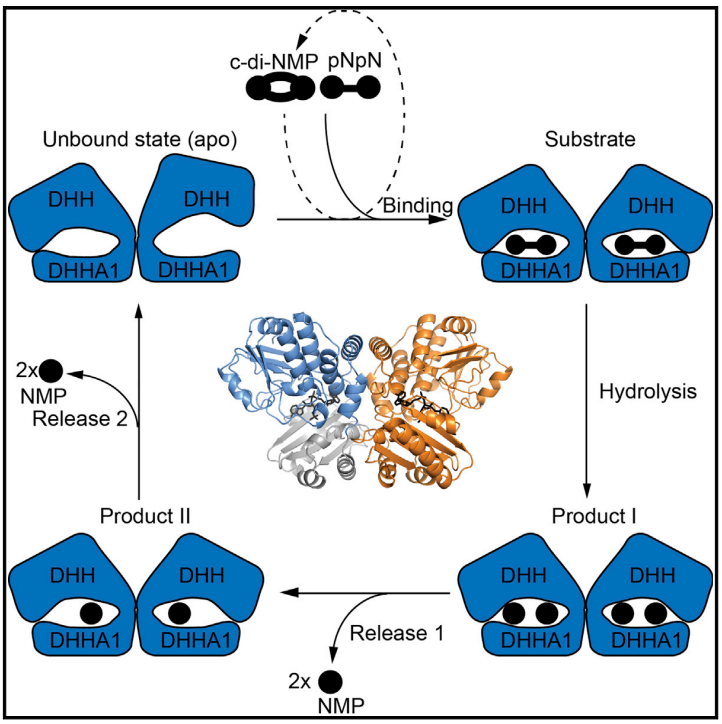

Highlights

- Crystal structures of a *T. maritima* DHH/DHHA1-type PDE in different reaction states
- Biophysical and biochemical characterization of PDE activity and substrate binding
- TmPDE has high affinity for linear dinucleotides consistent with structural data
- The data support a two-step degradation mechanism of c-di-AMP

Authors

David Jan Drexler, Martina Müller, Carlos Alberto Rojas-Cordova, Adrian Maurice Bandera, Gregor Witte

Correspondence

witte@genzentrum.lmu.de

In Brief

In their paper Drexler et al., 2017 describe the biochemical and structural investigation of a soluble DHH-type phosphodiesterase and provide experimental evidence for a probable two-step decay of c-di-AMP with the analyzed phosphodiesterase being responsible for the second step in hydrolysis.

Drexler et al., 2017, Structure *25*, 1887–1897
December 5, 2017
https://doi.org/10.1016/j.str.2017.10.001

Structure
Short Article

Structural and Biophysical Analysis of the Soluble DHH/DHHA1-Type Phosphodiesterase TM1595 from *Thermotoga maritima*

David Jan Drexler,[1,4] Martina Müller,[1,2,4] Carlos Alberto Rojas-Cordova,[1,3] Adrian Maurice Bandera,[1] and Gregor Witte[1,5,*]
[1]Gene Center and Department of Biochemistry, Ludwig-Maximilians-Universität München, Feodor-Lynen-Str. 25, 81377 Munich, Germany
[2]Present address: CRELUX GmbH, Am Klopferspitz 19a, 82152 Planegg-Martinsried, Germany
[3]Present address: EMBL Heidelberg, Meyerhofstraße 1, 69117 Heidelberg, Germany
[4]These authors contributed equally
[5]Lead Contact
*Correspondence: witte@genzentrum.lmu.de
https://doi.org/10.1016/j.str.2017.10.001

SUMMARY

The concentration of messenger molecules in bacterial cells needs to be tightly regulated. This can be achieved by either controlling the synthesis rate, degradation, or export by specific transporters, respectively. The regulation of the essential second messenger c-di-AMP is achieved by modulation of the diadenylate cyclase activity as well as by specific phosphodiesterases that hydrolyze c-di-AMP in the cell. We provide here structural and biochemical data on the DHH-type phosphodiesterase TmPDE (TM1595) from *Thermotoga maritima*. Our analysis shows that TmPDE is preferentially degrading linear dinucleotides, such as 5′-pApA, 5′-pGpG, and 5′-pApG, compared with cyclic dinucleotide substrates. The high-resolution structural data provided here describe all steps of the PDE reaction: the ligand-free enzyme, two substrate-bound states, and three post-reaction states. We can furthermore show that Pde2 from *Streptococcus pneumoniae* shares both structural features and substrate specificity based on small-angle X-ray scattering data and biochemical assays.

INTRODUCTION

Nucleotide second messengers are key components in cellular signaling that link signals to cellular responses. To achieve robust signaling that allows fast reaction to environmental or metabolic changes, the cellular levels of the messenger molecules are often regulated in both their synthesis and degradation, or they are even exported from the cell. In the case of the bacterial second messenger 3′,5′-cyclic di-adenosine monophosphate (c-di-AMP), the synthesis of the messenger molecule is carried out by DAC (di-adenylate cyclase) domain proteins that selectively synthesize c-di-AMP from two molecules of ATP (Witte et al., 2008). c-di-AMP is involved in a variety of processes in the cell, most of them related to potassium homeostasis or cell wall biogenesis, reviewed for example in Corrigan and Gründling (2013). Remarkably, c-di-AMP is the first second messenger that has been described to be essential for the bacteria synthesizing it, as total knockouts of DAC domain proteins are for example lethal in *Bacillus subtilis* (Mehne et al., 2013), *Staphylococcus aureus* (Corrigan et al., 2013), and *Listeria monocytogenes* (Witte et al., 2013). *In vivo* experiments in different organisms showed that the cellular level of c-di-AMP needs to be tightly regulated, as even small changes lead to drastic effects in the viability of the cells. For quite some time the essentiality of c-di-AMP could not be pinpointed, but a recent study in *B. subtilis* showed that c-di-AMP is, in fact, a key component in controlling potassium homeostasis (Gundlach et al., 2017). The c-di-AMP pathway is also an interesting target for antimicrobial therapies (Müller et al., 2015a), because the pathway influences sensitivity to antibiotic treatment (Dengler et al., 2013; Whiteley et al., 2017) and is found in many pathogenic bacteria such as *L. monocytogenes* (Woodward et al., 2010), *Mycobacterium tuberculosis* (Bai et al., 2012), *Streptococcus pneumoniae* (Kamegaya et al., 2011), and *S. aureus*, including methicillin-resistant *S. aureus*. The regulation of c-di-AMP synthesis is controlled by expression levels or activity of the respective proteins. For example, *B. subtilis* CdaS is expressed prior to sporulation (Nicolas et al., 2012), and also direct regulation of the DAC domains via ligand interactions was observed, as described for the DAC prototype DNA-integrity scanning protein A (DisA) from *Thermotoga maritima* and *B. subtilis.* DisA switches off its c-di-AMP synthesis upon binding to recombination intermediate DNA structures and likely acts as a checkpoint protein that ensures genome integrity prior to sporulation of the bacteria (Bejerano-Sagie et al., 2006; Oppenheimer-Shaanan et al., 2011; Witte et al., 2008). Another example is the regulation of the membrane protein CdaA by CdaR (Mehne et al., 2013). In addition to limited synthesis, a decrease in the total cellular c-di-AMP levels can also be achieved by selective degradation of the messenger molecule by c-di-AMP-specific phosphodiesterases (PDE) that degrade c-di-AMP to AMP and/or 5′-pApA. In bacteria, two types of c-di-AMP PDEs have been identified so far.

The first PDE that was characterized in detail is the multidomain membrane-associated DHH/DHHA1-type phosphodiesterase GdpP, which is encoded by YybT in *B. subtilis* (Figure 1A) (Rao et al., 2010). GdpP carries two additional regulatory

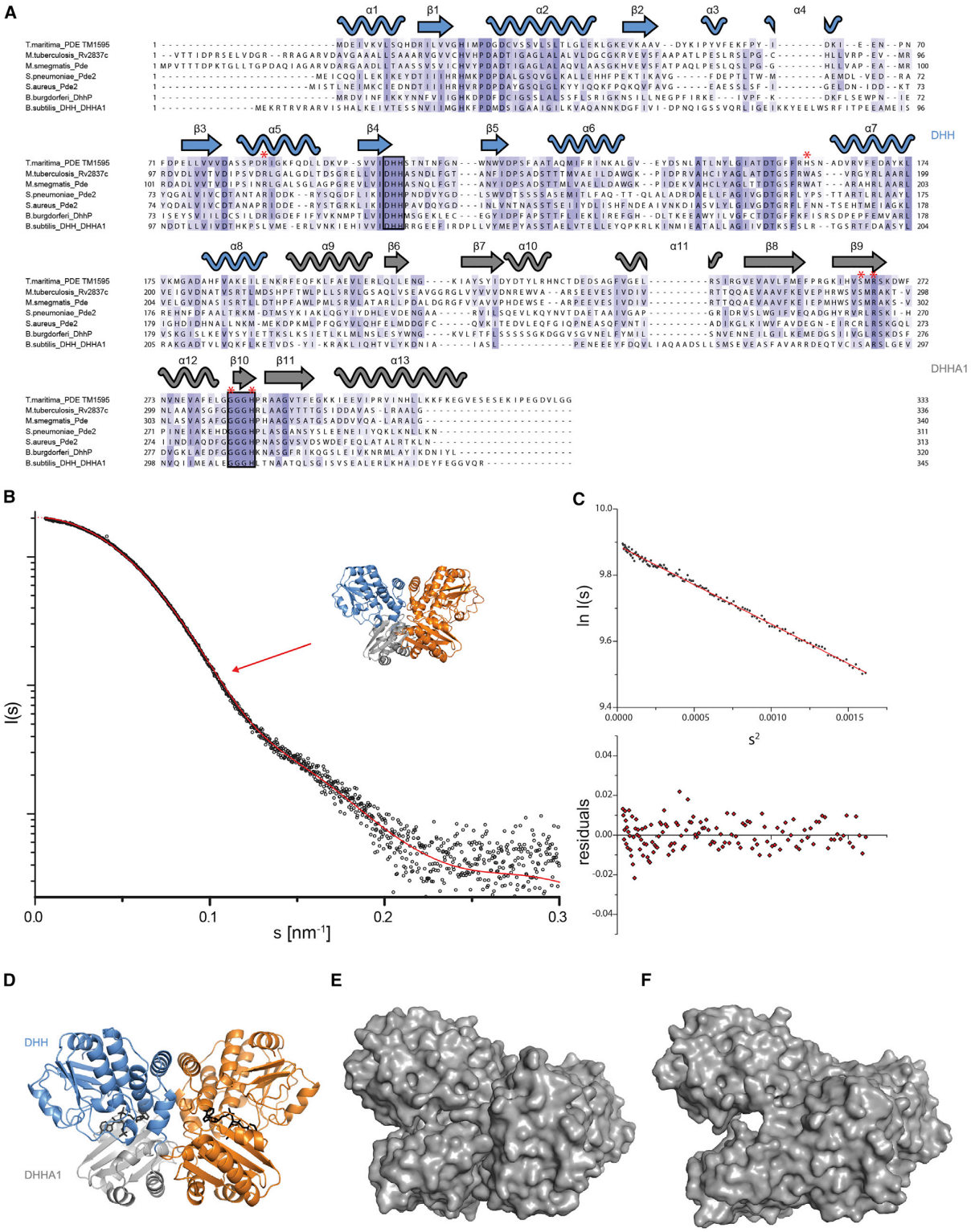

(legend on next page)

domains in addition to the two active PDE domains DHH and DHHA1; a sensory PAS (Per-Arnt-Sim) domain and a degenerated GGDEF domain. Whereas the former has been shown to bind Heme and nitric oxide, thereby affecting the PDE activity (Rao et al., 2011), the latter motif originally derives from proteins involved in c-di-GMP signaling but in this case binds and hydrolyzes ATP. GdpP has been shown to specifically hydrolyze c-di-AMP to 5′-pApA in presence of Mn^{2+} but also shows c-di-GMP phosphodiesterase activity resulting in 5′-pGpG (Rao et al., 2010). DHH/DHHA1-type PDEs also occur as soluble proteins comprising just the DHH/DHHA1 domains without the regulatory domains (Figure 1A), such as in *S. pneumoniae* (Pde2) (Bai et al., 2013), *M. tuberculosis* (CnpB/PDE/Rv2837c) (He et al., 2016), *M. smegmatis* (PDE) (Tang et al., 2015), and *S. aureus* (Pde2) (Bowman et al., 2016). Although these proteins belong to the DHH/DHH1A group, they have interestingly been reported to possess altered product specificity as they degrade c-di-AMP as well as 5′-pApA to AMP. Even though it was shown that *S. aureus* Pde2 might degrade c-di-AMP to 5′-pApA, it has a clear preference for the hydrolysis of the second step, i.e., 5′-pApA to 2 AMP (Bowman et al., 2016). In contrast, the biochemistry of the other PDEs mentioned above remains somewhat uncertain. In addition to the DHH/DHHA1-type PDEs, a second class of c-di-AMP-specific phosphodiesterases has been identified in *L. monocytogenes* (Huynh et al., 2015). *L. monocytogenes* PgpH is a member of the HD superfamily, named after the His-Asp residues that are functionally important as they coordinate the catalytically essential metal ions. PgpH and homologs are integral membrane proteins that belong to the 7TM-7TMR_HD family and consist of a seven transmembrane helix domain and a cytoplasmatic HD domain and (Huynh and Woodward, 2016). PgpH-type PDEs also show preferential hydrolysis of one of the 3′-5′-phosphodiester bonds in c-di-AMP, resulting in the linear product 5′-pApA. Of note, both DHH- and HD-type phosphodiesterases occur in bacteria with c-di-AMP pathways; some species have both of them (e.g., *L. monocytogenes*), whereas others have only one representative, most commonly DHH-type enzymes (Huynh and Woodward, 2016). As PgpH and GdpP are obviously responsible for the first step in c-di-AMP hydrolysis (its linearization to 5′-pApA), it is tempting to speculate that the soluble DHH-type PDEs carry out its subsequent hydrolysis from 5′-pApA to 2 AMP. Structural studies of the intracellular domain of the *L. monocytogenes* PgpH HD domain PDE (Huynh et al., 2015) and the soluble DHH domain phosphodiesterases from *M. tuberculosis* (He et al., 2016) suggest a similar mechanism of hydrolysis in which the two-metal-ion catalytic center facilitates the attack of the phosphodiester by an activated water molecule. To gain a more detailed view on the mechanism and biophysical properties of the second step in c-di-AMP degradation, we solved crystal structures of the soluble DHH-type PDE from *T. maritima* (TM1595) in different nucleotide-bound states and performed biochemical and biophysical assays to determine the kinetic and thermodynamic properties of nucleotide binding.

RESULTS AND DISCUSSION

Protein Characterization

Based on sequence homology searches we identified a putative c-di-AMP phosphodiesterase in *T. maritima*. The 37.5 kDa protein encoded by TM_1595 is highly similar to known DHH/DHHA1-PDEs and thus will be referred to as TmPDE (Figure 1A). We recombinantly expressed TmPDE in *Escherichia coli* and purified it to homogeneity. For comparative reasons we also purified the Pde2 protein from *S. pneumoniae* (SpPde2), which has been described to possess c-di-AMP phosphodiesterase activity (Bai et al., 2013). Both purified PDEs elute as single peaks in size-exclusion chromatography (SEC) with a hydrodynamic radius corresponding to a dimeric form of the PDEs. To unambiguously determine the molecular weight in solution we also performed analytical SEC coupled right-angle laser light scattering (SEC-RALS) and small-angle X-ray scattering (SAXS). The respective molecular weights derived from these methods indicate that TmPDE forms a dimeric assembly in solution (Figures 1B, 1C, and S1).

Product Specificity and Phosphodiesterase Activity

To analyze the phosphodiesterase activity of both TmPDE and SpPde2, we individually incubated the proteins with c-di-AMP, 5′-pApA, 5′-pApG, or 5′-pGpG, and analyzed the products by liquid chromatography (LC; see the STAR Methods). The reaction partners showed well-separated peaks, allowing their integration and Michaelis-Menten-like kinetic evaluation. Interestingly, we could detect robust and fast phosphodiesterase activity of both PDEs when using the linear substrates 5′-pApA (K_M = 204 ± 10 μM; k_{cat} = 0.14 s^{-1}), 5′-pApG (K_M = 355 ± 36 μM, k_{cat} = 0.26 ± 0.02 s^{-1}), and 5′-pGpG (similar activity, but no detectable saturation in the K_M assays). The cyclic dinucleotide c-di-AMP, however, was only degraded to a small extent under the various conditions tested, and only the use of 1,000-fold higher protein concentration yielded detectable

Figure 1. Multiple Sequence Alignment and Overall Structural Characterization of TmPDE

(A) Sequence alignment of PDEs from different species. Secondary structure elements from TmPDE are shown above, with the DHH domain in light blue and DHHA1 domain in gray. Nucleotide-binding residues are marked by asterisks and the highly conserved active site is outlined. For *B. subtilis* GdpP only the C-terminal DHH/DHHA1 domain is shown, the other sequences represent the full-length proteins.

(B) Buffer-corrected SAXS curve of a 7 mg/mL TmPDE wild-type sample shown as black circles with the theoretical scattering curve shown in red of TmPDE (in apo state, inset) obtained using CRYSOL (Svergun et al., 1995) (χ^2 = 2.3).

(C) Guinier plot analysis ln I(s) versus s^2 of the SAXS-data from (C). The radius of gyration was determined from linear regression (red) of data in the Guinier region ($s*R_G < 1.3$), R_G = 2.67 nm. The lower panel shows the residuals of the linear regression. The linearity of the Guinier plot indicates that the TmPDE sample is not aggregating.

(D) Crystal structure of the biological dimer of TmPDE D80N D154N mutant in the 5′-pApG-bound state shown in cartoon representation. The DHH and DHHA1 domains of one monomer are colored light blue and gray, respectively, whereas the other monomer is colored orange. 5′-pApG is shown as black sticks.

(E) Surface representation of the TmPDE D80 D154N mutant in 5′-pApG-bound state in which both binding sites are closed.

(F) Surface representation of the TmPDE apo structure in the same orientation as shown in (E) with one open binding site.

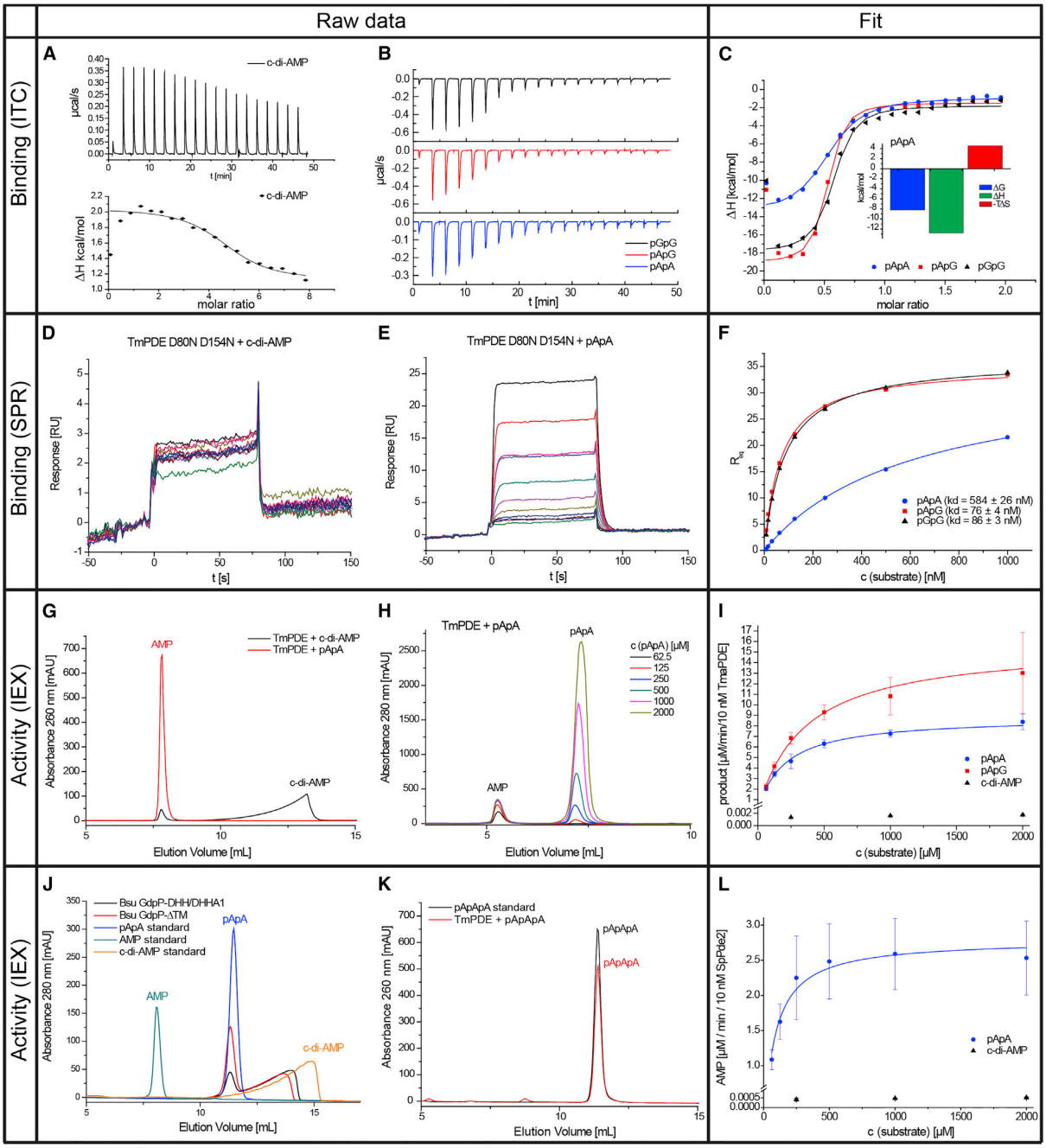

Figure 2. Binding and Activity of TmPDE with Different Ligands

(A) ITC measurement of 20 μM TmPDE D80N D154N mutant titrated with 200 μM c-di-AMP and the respective binding curve fit (K_D = 4.58 ± 1.93 μM).

(B) ITC measurement raw data of 20 μM TmPDE D80N D154N mutant titrated with 250 μM ligand: 5′-pGpG (black), 5′-pApG (red), and 5′-pApA (blue).

(C) Binding curves and fits of ITC titrations of the TmPDE D80N D154N mutant with 5′-pGpG (K_D = 247 ± 59 nM) (black), 5′-pApG (K_D = 191 ± 36 nM) (red), and 5′-pApA (K_D = 860 ± 94 nM) (blue). The inset shows a representative signature plot of the ITC measurement with 5′-pApA with ΔG = −8.26 kcal/mol, ΔH = −12.8 kcal/mol, and –TΔS = 4.55 kcal/mol (similar values were observed for the other linear 5′-pNpNs).

(D) SPR measurement of the TmPDE D80N D154N mutant (on chip) with injections of 8–1,000 μM c-di-AMP.

(E) SPR measurement of the TmPDE D80N D154N mutant (on chip) with injections of 8–1,000 μM 5′-pApA.

(F) Steady-state affinity fits for SPR measurements of the TmPDE D80N D154N mutant titrated with 5′-pGpG (K_D = 86 ± 3 nM) (black), 5′-pApG (K_D = 76 ± 4 nM) (red), and 5′-pApA (K_D = 584 ± 26 nM) (blue).

(legend continued on next page)

amounts of AMP (Figures 2 and S2). This extremely low turnover did not allow for reliable determination of kinetic parameters for either TmPDE or SpPde2. This finding is in agreement with data from Bowman et al. (2016) showing that soluble DHH/DHHA1-type PDEs prefer the hydrolysis of 5′-pApA over the direct hydrolysis of c-di-AMP. Indeed, the turnover of c-di-AMP for both TmPDE and SpPde2 is almost negligible in comparison with the 5′-pApA substrate. In contrast, the DHH/DHHA1-type GdpP-type protein from *B. subtilis* (Figure 2J) and *S. pneumoniae* SpPde1 (not shown) clearly show degradation of c-di-AMP to 5′-pApA, despite the homologous catalytic domains. A truncated *B. subtilis* GdpP construct lacking the regulatory domains (GdpP-DHH/DHHA1) also hydrolyzes c-di-AMP to 5′-pApA, thus excluding the regulatory domains of GdpP as a reason for the ligand specificity (Figure 2J). To elucidate differences between PDE and GdpP phosphodiesterases, we modeled *B. subtilis* GdpP based on sequence alignment and our TmPDE structure using SWISS-MODEL (Biasini et al., 2014). As expected, the GdpP model shows a similar overall structure (Figure S3E), whereas analysis of the active site reveals that the modeled ligand 5′-pApA does not fit into the GdpP model structure due to steric hindrance of residues L191 and N314 (Figure S3F). This could be a reason for the incomplete hydrolysis of c-di-AMP to 5′-pApA in GdpP-like phosphodiesterases, although this assumption is only based on a structure prediction and remains to be verified.

To be able to monitor substrate binding to the protein, we produced an inactive mutant of TmPDE that can bind the substrate(s) but lacks catalytic activity. Site-directed mutagenesis of two acidic residues abolished binding of the catalytically essential active site Mn^{2+} ions in the active site, which are necessary for activating the water molecule that performs the nucleophilic attack on the 3′-5′-phosphodiester (Rao et al., 2010). These respective aspartate residues were identified by homology analysis and mutated to asparagine (i.e., D80N D154N; Figures 3A and 3B) instead of alanine, as described previously (Rao et al., 2010), to have a more conservative mutation. The resulting mutant and wild-type proteins showed identical elution profiles and molecular weight in SEC-RALS, and also show similar SAXS curves, suggesting that the mutations did not alter overall protein conformation or oligomeric state (Figures S1A, S1G, and S1H). In the LC-based assays we were not able to detect any turnover of 5′-pApA or c-di-AMP by TmPDE D80N D154N, confirming that this mutant is completely inactive under the assay conditions used.

We performed surface plasmon resonance (SPR) experiments to rule out mechanistic differences in c-di-AMP or 5′-pApA hydrolysis, which might lead to the apparent inactivity *in vitro* and to further characterize the product binding of TmPDE. The inactive mutant TmPDE D80N D154N was immobilized on the SPR chip, and different concentrations of the respective cyclic and linear nucleotides were injected over the chip's surface. The resulting binding curves determined from the sensorgrams (Figures 2D–2F and S2E–S2G) indicate that TmPDE D80N D154N is not capable of binding c-di-AMP or c-di-GMP under the conditions tested. In contrast, linear products were bound with K_D values in the nanomolar range (Figures 2D–2F and 4B), some of them with high on-off rates beyond the resolution of the SPR instrument, as indicated by the abrupt rise and fall in the respective sensorgrams (Figure 2E). To further determine thermodynamic parameters of the substrate binding, we also performed isothermal titration calorimetry (ITC). Using c-di-AMP as a ligand, the integrated heat curves only showed a low-affinity binding (K_D = 4.58 ± 1.93 μM) in an endothermic reaction. In contrast, the linear substrates clearly show high-affinity binding and parameters indicative of enthalpy-driven substrate binding with 5′-pGpG (K_D = 247 ± 59 nM), 5′-pApG (K_D = 191 ± 36 nM), and 5′-pApA (K_D = 860 ± 94 nM) (Figures 2A–2C and 4B).

These biophysical data, in combination with the *in vitro* activity assays, strongly argue that the native substrate of TmPDE (and SpPde2) is in fact a linear dinucleotide (e.g., 5′-pApA, 5′-pApG, and 5′-pGpG as tested here), and that cyclic derivatives are bound only to a much lower extent. The fast on-off kinetics suggest that the active site is readily accessible by diffusion from the bulk solvent. Because there is only one active site in the DHH-DHHA1 domain phosphodiesterase, the full degradation of c-di-AMP to two molecules of AMP would require either reorientation (rotation) of the intermediate 5′-pApA within the active site or its release and rebinding. With respect to the previously described hydrolysis of c-di-AMP by SpPde2 and Rv2837c, and the binding affinities determined here, we can confirm that, for c-di-AMP hydrolysis, orders of magnitude higher concentrations are needed in the assays. Using higher concentrations of c-di-AMP certainly increases the probability of c-di-AMP binding to TmDPE/SpPde2 and might potentially lead to the linearized product 5′-pApA, which is then degraded much more rapidly to two molecules of AMP due to the higher affinity to the DHH active site as seen in Figure S2A. This might explain why c-di-AMP PDE activity has been described for some of the soluble DHH-type PDEs in literature. To rule out that TmPDE has

(G) Ion-exchange chromatography runs on Mono Q 5/50 GL column of the reaction products after 1 hr incubation from 100 μL reactions containing 2 μM TmPDE + 250 μM 5′-pApA (red) and 250 μM c-di-AMP (black).
(H) Representative chromatograms of the activity assays of TmPDE (10 nM) with substrate 5′-pApG (62.5–2000 μM) after 25 min at 20°C analyzed by ion-exchange chromatography with a Mono Q 5/50 GL column.
(I) Michaelis-Menten kinetics of the reactions from TmPDE (10 nM) with substrates 5′-pApA (62.5–2,000 μM) (blue) and 5′-pApG (62.5–2,000 μM) (red) after 25 min at 20°C. 5′-pApA, K_M = 204 ± 10 μM; 5′-pApG, K_M = 355 ± 36 μM. Also shown are the data points for c-di-AMP (black). Shown are mean values with errors from three independent experiments.
(J) Ion-exchange chromatography runs on Resource Q column of the reaction products from 100 μL reactions containing 1 μM *B. subtilis* GdpP-ΔTM + 250 μM c-di-AMP (red) and 1 μM *B. subtilis* GdpP-DHH/DHHA1 + 250 μM c-di-AMP (black) after 1 hr at 20°C. Also shown are the standards AMP (green), 5′-pApA (blue), and c-di-AMP (orange).
(K) Ion-exchange chromatography runs on Mono Q 5/50 GL column of the reaction products from a 100 μL reaction containing 100 nM TmPDE + 250 μM 5′-pApApA (red) after 1 hr at 20°C and the respective standard 5′-pApApA (shown in black).
(L) Michaelis-Menten kinetics of the reactions from SpPde2 with 5′-pApA (62.5–2,000 μM) (blue). K_M = 97 ± 8 μM after 25 min incubation at 20°C. Also shown are the data points for c-di-AMP (black). Shown are mean values with errors from three independent experiments.

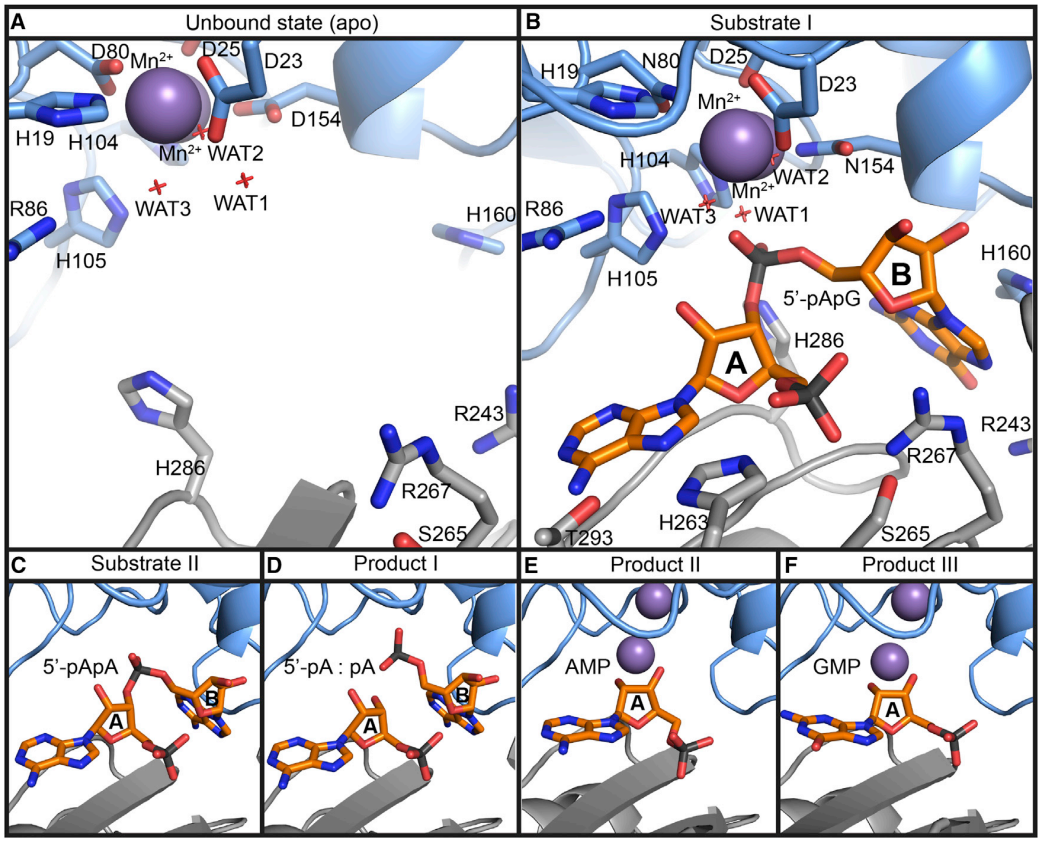

Figure 3. Active Site of TmPDE in Different Ligand-Bound (Reaction Intermediate) States

(A) Detailed view on the empty active site of TmPDE. Substrate-binding residues are shown as sticks and manganese ions are shown as purple spheres.

(B) Detailed view of the active site of TmPDE D80N D154N crystallized with 5′-pApG. The bound ligand and the interacting residues are shown as sticks and the manganese ions (modeled, see main text) as purple spheres.

(C) TmPDE D80N D154N with 5′-pApA in the nucleotide binding cleft. The positions for the 5′- and 3′-nucleotides are labeled with A and B in the sugar ring.

(D) TmPDE D80N D154N with two molecules of AMP in site A and site B resulting from 5′-pApA cleavage. The phosphate of nucleotide in position B has moved up, in agreement with the S_N2-mechanism.

(E) Wild-type TmPDE with AMP and Mn^{2+} ions at site A. The second AMP, c.f., D has already left site B.

(F) TmPDE D80N D154N after hydrolysis of 5′-pGpG and only one GMP (site A) left in the active site.

even higher specificity for longer RNAs, such that it might serve as nanoRNase, we also tested 5′-pApApA as a substrate (Figure 2K). TmPDE showed almost no cleavage of the trinucleotide, despite a doubled reaction time and a ten times higher protein concentration compared with the 5′-pApA experiment.

Structural Determination of TmPDE in Different Ligand-Bound States

To obtain structural information that allows a description of the putative substrate recognition and PDE mechanism, we crystallized wild-type TmPDE in absence of ligands (apo-) and in the product-bound form II (AMP/Mn^{2+}). We also crystallized the mutant TmPDE D80N D154N in the presence of different linear dinucleotides, trapping the enzyme in different reaction intermediate states (substrates I and II, products I–III).

We used datasets collected from TmPDE product state crystals (containing Mn^{2+}, AMP, or GMP) diffracting to 1.9 Å to phase the data by single-wavelength anomalous diffraction. The obtained map showed readily interpretable electron density for the two molecules in the asymmetric unit. This allowed us to build the almost complete structure of TmPDE with good validation statistics, and the final model comprises residues 1–319 for both chains in the asymmetric unit, 501 water molecules and 6 Mn^{2+} ions (numbers for TmPDE/AMP-Mn^{2+}, i.e., product II) (Table 1). The refined model was subsequently used to determine the structures of apo TmPDE and the substrate and product complexes by molecular replacement. These structures were then refined and yielded similar statistics (Table 1).

Overall Structural Properties of TmPDE

One chain of TmPDE consists of the two clearly separated domains DHH (residues 1–190) and DHHA1 (residues 194–end), connected by a linker between helices α8 and α9 (Figure 1 and Movie S1). Monomeric TmPDE has overall dimensions of

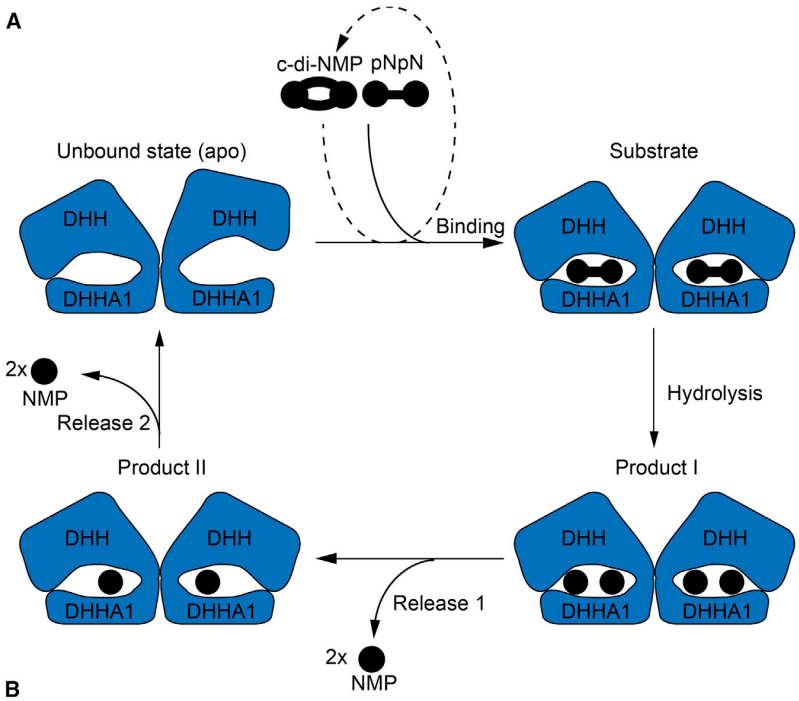

B

	K_D (ITC) [nM]	K_D (SPR) [nM]	k_{on} [$M^{-1}s^{-1}$]	k_{off} [s^{-1}]	K_M [μM]	k_{cat} [s^{-1}]
pApA	860 ± 94	584 ± 26	> $5x10^5$	0.33	204 ± 10	0.14
pApG	191 ± 36	76 ± 4	> $10x10^5$	0.07	355 ± 36	0.26 ± 0.02
pGpG	247 ± 59	86 ± 3	> $6x10^5$	0.04	/	/
c-di-AMP	4580 ± 1930	n.b.	n.b.	n.b.	n.t.	n.t.
c-di-GMP	/	n.b.	n.b.	n.b.	n.t.	n.t.

n.b. = not binding
n.t. = no (significant) turnover

Figure 4. Schematic Representation of the Hydrolysis Reaction of TmPDE

(A) The reaction cycle based on available structures: The pre-reaction state of TmPDE shows one open active site in the dimer. 5′-pNpN ligands bind tightly to TmPDE, whereas c-di-NMPs bind much weaker. The bound ligand is hydrolyzed resulting in two NMP molecules in the active site. The two NMPs are then released separately (3′ nucleotide followed by the 5′ nucleotide) prior to binding of the next substrate.

(B) The table summarizes all results of binding experiments and activity assays. K_D values are calculated from ITC and SPR experiments, k_{on} and k_{off} from SPR measurements. The errors represent the error of the individual fit of the binding model to the experimental data. K_M and k_{cat} values from Mono Q activity assays are mean values and errors of three independent experiments. Please note that 5′-pGpG is hydrolyzed with approximately similar activity, but the assay does not allow for determination of parameters.

approximately 55 × 35 × 30 Å. The eponymous active site containing the highly conserved DHH motif is located in the cleft between DHH and DHHA1. The two domains share high structural similarity with the DHH/DHHA1 structures of nanoRNases (Srivastav et al., 2014; Uemura et al., 2013) and also the PDE from *M. tuberculosis* Rv2837c (He et al., 2016). The DHH domain comprising residues 1–192 consists of a five-stranded parallel β sheet domain flanked by helices (α1–α8). It harbors the catalytically active residues (see below) and is responsible for metal ion coordination. The smaller C-terminal DHHA1 domain (residues 195–end) is connected to the DHH domain via a flexible linker domain and has a DHH similar fold comprising a central mixed β sheet domain (β6–β11) surrounded by helices (α9–α13). The dimeric assembly is mainly achieved by a large number of contacts between the α helices, creating a continuous helical central part in the dimer whereas the β sheet domains face outward.

The crystal packing (5′-pApA-structure with one molecule per asymmetric unit in $C222_1$) and the arrangement of the molecules in the asymmetric units of the other structures suggest that TmPDE forms a butterfly-shaped dimer with overall dimensions of 80 × 55 × 40 Å. The interactions of the DHH/DHHA1 domains and the linker region, with many hydrophobic interactions mediated by, e.g., helices α7–α9, results in outward facing clefts of the active sites, with the monomers having an approximately 60° tilt with respect to each other. This arrangement creates a large buried surface area of approximately 2,050 $Å^2$. In contrast, the only other possible dimeric assembly has inward facing active sites and a much lower buried surface area of approximately 800 $Å^2$. To experimentally validate the biological assembly, we collected solution scattering data of wild-type TmPDE and also of the D54N D180N mutant. The shapes of the averaged scattering curves are only compatible with the theoretical scattering curves of the respective butterfly-shaped dimers (Figures 1B, S1G, and S1H). We also collected SAXS data from the homologous *S. pneumoniae* Pde2 (Figures S1C–S1F), which we also used as a reference in our biochemical assays. Lacking a high-resolution structure of SpPde2, we performed *ab initio* modeling using the SpPde2 SAXS data. All *ab initio* models of independent runs (n = 20) were highly similar, and the final averaged shape shows a good fit and similarity to our crystallographic TmPDE dimer (description below, Figure S1E).

Because the linker between DHH and DHHA1 domains allows the cleft to open and consequently change its accessibility to the bulk solvent, the active site of TmPDE is certainly able to harbor and degrade more substrates than tested here. This is in agreement with data on the mycobacterial phosphodiesterase Rv2837c (He et al., 2016) and nanoRNases (Srivastav et al., 2014), which show that these enzymes can degrade various small nucleic acid substrates.

Substrate Coordination and Mn^{2+}-Activated 3′-5′-Phosphodiester Bond Cleavage

To characterize substrate binding, cleavage, and release, we determined the structures of the nucleotide-free state, two substrate-bound, and three product-bound states of TmPDE. The

Table 1. Crystallographic Data and Refinement Statistics

	Unbound State (Apo)	Substrate I 5′-pApA	Substrate II 5′-pApG	Product I pApA	Product II AMP/Mn^{2+}	Product III GMP/Mn^{2+}
Protein	wild-type	D80N D154N	D80N D154N	D80N D154N	wild-type	D80N D154N
Data Collection						
Beamline	EMBL P14	ESRF ID30A MASSIF-1	EMBL P13	EMBL P13	EMBL P14	SLS X06SA
Wavelength (Å)	0.9763	0.9660	1.1999	1.1999	1.5498 (SAD)	1.2999 (SAD)
Space group	C 2	C 2 2 2_1	C 2 2 2_1	C 2 2 2_1	P 2_1 2_1 2_1	P 2_1 2_1 2_1
Cell dimensions						
a, b, c (Å)	132.7, 54.9, 108.6	71.7, 87.8, 122.4	70.4, 88.3, 124.3	71.4, 87.6, 121.9	55.3, 106.8, 134.1	55.9, 105.6, 134.5
α, β, γ (°)	90, 118, 90	90, 90, 90	90, 90, 90	90, 90, 90	90, 90, 90	90, 90, 90
Resolution	95–1.7 (1.74–1.70)	50–1.7 (1.74–1.70)	62–1.55 (1.59–1.55)	60.9–1.55 (1.59–1.50)	50–1.9 (1.95–1.90)	50–1.9 (1.95–1.90)
$CC_{1/2}$	99.8 (65.9)	99.9 (75.0)	100 (75.5)	100 (75.8)	99.9 (66.1)	99.9 (74.6)
R_{meas}	11.7 (101)	5.5 (76.6)	3.7 (82.8)	4.5 (121)	10 (85.5)	7.2 (130.5)
I/σI	13.3 (2.0)	21.4 (2.25)	19.2 (1.87)	19.7 (1.67)	14.3 (2.5)	17.4 (1.9)
Completeness (%)	96.5 (95.9)	98.8 (97.8)	98.4 (95.4)	99.5 (98.3)	95.2 (92.1)	99.7 (99.9)
Redundancy	6.9 (6.8)	9.9 (4.5)	4.5 (4.3)	6.6 (6.3)	6.7 (6.6)	6.9 (6.9)
Refinement						
Resolution	20–1.75	44–1.7	50–1.55	41–1.55	49–1.9	46–1.9
No. of reflections	67,550	42,286	106,907	106,661	115,140	62,479
R_{work}/R_{free}	16.4/19.0	17.3/19.6	15.8/18.3	16.8/19.5	16.4/20.4	16.3/20.3
Molecules (asu)	2	1	1	1	2	2
No. of atoms						
Protein	5,118	2,606	2,620	2,639	5,130	5,144
Nucleotides/ligands	-/87	45/44	46/94	46/62	46/11	48/28
Water	527	249	279	295	501	551
RMSD						
Bond lengths (Å)	0.004	0.006	0.006	0.006	0.007	0.010
Bond angles (°)	0.691	0.763	0.811	0.849	0.821	1.004
Ramachandran plot (%)						
Favored	98	99	97	98	98	99
Allowed	2	1	3	2	2	1
Outliers	–	–	–	–	–	–
PDB ID	5O25	5O4Z	5O58	5O70	5O1U	5O7F

RMSD, root-mean-square deviation; asu, asymmetric unit.

mutant TmPDE D80N D154N has reduced activity due to impaired coordination of the catalytically essential Mn^{2+} ions, thus we will describe the metal ion coordination on the basis of the apo state structure. Here, we could clearly identify the Mn^{2+} ions in the active site owing to density in the anomalous difference map, and we used the apo structure to model the Mn^{2+} ions and respective water molecules in the other representations of TmPDE structures. Even though all nucleotide ligands were already clearly visible in the mF_o-DF_c difference density of the ligand-bound states after replacement, we also confirmed the presence and nature of the ligand in the product state I (AMP:AMP) structure by anomalous difference electron density map visualizing the phosphate (Figure S3A), and by calculation of Polder maps (Liebschner et al., 2017) with the ligand atoms omitted (Figure S3B). As mentioned before, the active site mutations do not alter the behavior or structure of TmPDE in solution, suggesting that the mutations only affect the active site.

As described previously for other DHH/DHHA1-phosphodiesterases, the 3′-5′-phosphodiester bond is attacked by a water molecule that is activated by divalent cations (Mn^{2+}) (He et al., 2016; Uemura et al., 2013). The nucleophilic attack for the S_N2-reaction is carried out by the activated water WAT1 from the "backside" of the phosphate and facilitates the planar intermediate state before the final cleavage. Consistent with this, our D80N D154N mutant, crystallized in the presence of 5′-pApA, shows that the 3′-5′-phosphodiester bond is in the ideal orientation for an attack by activated WAT1 (distance 1.7 Å; Figure S3C). The putative reaction mechanism of TmPDE is also in good agreement with data on Rv2837 (He et al., 2016), and also

remarkably similar to the EAL domain described for a light-regulated c-di-GMP phosphodiesterase (Barends et al., 2009).

Unbound State (Apo Form)

Interestingly, our ligand-free structure reveals that the dimeric DHH/DHHA1 assembly has a slightly asymmetric shape, whereas the ligand-bound structures show almost identical conformations in the two chains. Specifically, one-half of the dimer has a more open cleft, whereas the other half of the PDE is rather closed and slightly shifted and rotated (Figures 1E and 1F). This might indicate that TmPDE is dynamic during its reaction cycle, such that the open form of the empty enzyme facilitates substrate binding, and that substrate binding leads to closure of the active site (Movie S1). A readily accessible active site would provide a structural basis for the relatively fast on-rate of substrate binding (Figure 4B). Interestingly, our ITC experiments show a stoichiometry of n = 0.5 for substrate binding to the inactive enzyme (Figure 2C), this raises the possibility that TmPDE might function in a flip-flop-like manner in solution, i.e., only one site is active per cycle, in agreement with the half-open apo structure. In contrast, the crystal structures of ligand- and product-bound states argue for two active sites, but might be influenced by crystallization conditions and/or packing. We cannot exclude an alternating active site in the dimer at this stage but the conclusions drawn for the reaction chemistry and substrate preference for linear dinucleotides (see below) remain untouched by this possibility.

In the active site of TmPDE, two manganese ions are coordinated by a dense network of highly conserved residues; His-19 and Asp-23 coordinate Mn^{2+} 1, Asp-25, His-104, and Asp-154 coordinate Mn^{2+} 2, and Asp-80 coordinates both Mn^{2+} 1 and 2. The ligand binding site is further occupied by bulk solvent and some ordered water molecules. In this state, the enzyme is ready to bind its dinucleotide substrate.

Substrate-Bound Pre-reactive States (Substrates I and II)

The substrate-bound structures of TmPDE D80N D154N with 5′-pApA (substrate I, Figures 3C) and 5′-pApG (substrate II, Figure 3B) reveal that TmPDE dimer is symmetrical and has closed active site clefts compared with the apo state. The dinucleotides are oriented with the 3′-5′-phosphodiester bond facing the position of the two modeled manganese ions, where highly coordinated water molecules are located instead. The bases of substrate molecules are coordinated by a network of polar and stacking interactions (Figure 3B) that correctly position the substrate. In particular, the 3′-base (site B) is stacked by His-160 and the loop comprising residues 154–160 closes the active site pocket. The 5′-base (site A) stacks on top of the GGG stretch sheets (β10 and β11; Figure 3B). In good agreement with SPR and ITC data showing different thermodynamic parameters for 5′-pApG and 5′-pApA binding, we can identify differences in the base stabilization in the structures. The guanine base forms additional interactions compared with the adenine substrate; Arg-243 of the DHHA1 domain contacts O6 and Asn-162 contacts N2 of the base (Figure S3D). These additional guanine-specific interactions manifest in both (1) slightly tighter K_D values for the binding of 5′-pApG and 5′-pGpG compared with 5′-pApA, and (2) a lower turnover (higher K_M) for the 5′-pApG substrate, indicating either a lower overall activity or a slower rate of substrate-product exchange.

Post-reactive State Formation and Product Release (Products I–III)

Directly after the phosphodiester bond cleavage of the 5′-pApA substrate, two molecules of AMP are present in the active site (product state I, Figure 3D). The 5′-phosphate of the nucleotide in site B has moved up, consistent with the directionality of the S_N2-reaction carried out by the activated water WAT1. In the next step (product state II, Figure 3E), only the AMP moiety in site A remains present in the binding cleft, kept in position by the GGG stretch, whereas the nucleotide from site B has already been released from the cleft. The 5′-phosphate of molecule A is tightly bound by His-263 and Arg-267 in the DHHA1 domain. The base is stacked by Arg-86 (DHH domain) and Thr-293 (DHHA1 domain) and is located on the surface of the GGG/AAA-stretch motif of the DHHA1 domain (β10 and β11). The analogous situation resulting from 5′-pGpG-cleavage can be seen in Figure 3F, where only the GMP remained bound in site A (product state III). Of note, our AMP structure contains three Mn^{2+} ions in the active site. Two of them (Mn^{2+} 1, Mn^{2+} 2) are in good agreement with structures of DHH/DHHA1 enzymes described above and also in (Srivastav et al., 2014). In contrast, Mn^{2+} 3 is less coordinated (sugar 2′ and 3′-OH, His-105, His-286), and has a lower occupancy in the structure. We assume that the third Mn^{2+} ion is bound in the active site due to the high Mn^{2+} concentration in the crystallization conditions and thus has no physiological relevance.

Conclusion

The structural and biochemical data provide a mechanistic framework for the phosphodiesterase activity of *T. maritima* PDE (summarized in Figure 4A). After high-affinity binding of the linear dinucleotide substrate to the ligand-free catalytic site, the phosphodiester bond is hydrolyzed in a S_N2 reaction by an activated water molecule resulting in two NMPs. The nucleotide in position B leaves the cleft prior to the one in site A, and the active site is then ready for the next cycle. The reported structures and biophysical data for TmPDE and SpPde2 suggest that linear dinucleotides are the main substrate for the soluble DHH-type PDEs and supports the idea of a two-step degradation of c-di-AMP in bacteria.

STAR★METHODS

Detailed methods are provided in the online version of this paper and include the following:

- KEY RESOURCES TABLE
- CONTACT FOR REAGENT AND RESOURCE SHARING
- METHOD DETAILS
  - Experimental Model and Subject Details
  - Cloning, Expression and Purification
  - TmPde Crystallization
  - Data Collection and Processing
  - Phasing, Model Building and Refinement
  - Small-Angle X-ray Scattering
  - Static Light Scattering
  - Enzymatic Activity Assay
  - Surface Plasmon Resonance
  - Isothermal Titration Calorimetry
- DATA AND SOFTWARE AVAILABILITY

CellPress

SUPPLEMENTAL INFORMATION

Supplemental Information includes three figures, one table, and one movie and can be found with this article online at https://doi.org/10.1016/j.str.2017.10.001.

AUTHOR CONTRIBUTIONS

D.J.D. and M.M. performed and evaluated most of the experiments. C.A.R.C. purified protein and helped with crystallization. A.M.B. purified GdpP and performed assays. G.W. supervised data evaluation, performed experiments, designed research, and wrote the manuscript with the help of D.J.D. and M.M. All authors approved the final version of the manuscript.

ACKNOWLEDGMENTS

We thank the staff of the EMBL Hamburg Beamlines at PETRA3 P12, P13, and P14 (EMBL/DESY Hamburg, Germany) for outstanding scientific support; data of the TmPDE/5′-pApA complex were collected at the automated MASSIF-1 beamline ID30A (ESRF Grenoble, France) and data on the product state III at SLS X06SA (Swiss Light Source, Switzerland). We thank Karl-Peter Hopfner for valuable discussions and support, and Sandra Schuller, Katja Lammens, Robert Byrne, and Dirk Kostrewa for discussions. This work was funded by grants from the Deutsche Forschungsgemeinschaft (DFG) WI 3717/2-1, WI 3717/3-1 (SPP1879), and GRK1721 (A10) to G.W.; A.M.B., D.J.D., and M.M. received support from the DFG GRK1721 research training group.

Received: July 17, 2017
Revised: September 7, 2017
Accepted: September 29, 2017
Published: October 26, 2017

REFERENCES

Adams, P.D., Afonine, P.V., Bunkoczi, G., Chen, V.B., Davis, I.W., Echols, N., Headd, J.J., Hung, L.W., Kapral, G.J., Grosse-Kunstleve, R.W., et al. (2010). PHENIX: a comprehensive Python-based system for macromolecular structure solution. Acta Crystallogr. D Biol. Crystallogr. *66*, 213–221.

Afonine, P.V., Grosse-Kunstleve, R.W., Echols, N., Headd, J.J., Moriarty, N.W., Mustyakimov, M., Terwilliger, T.C., Urzhumtsev, A., Zwart, P.H., and Adams, P.D. (2012). Towards automated crystallographic structure refinement with phenix.refine. Acta Crystallogr. D Biol. Crystallogr. *68*, 352–367.

Bai, Y., Yang, J., Eisele, L.E., Underwood, A.J., Koestler, B.J., Waters, C.M., Metzger, D.W., and Bai, G. (2013). Two DHH subfamily 1 proteins in *Streptococcus pneumoniae* possess cyclic di-AMP phosphodiesterase activity and affect bacterial growth and virulence. J. Bacteriol. *195*, 5123–5132.

Bai, Y., Yang, J., Zhou, X., Ding, X., Eisele, L.E., and Bai, G. (2012). *Mycobacterium tuberculosis* Rv3586 (DacA) is a diadenylate cyclase that converts ATP or ADP into c-di-AMP. PLoS One *7*, e35206.

Barends, T.R., Hartmann, E., Griese, J.J., Beitlich, T., Kirienko, N.V., Ryjenkov, D.A., Reinstein, J., Shoeman, R.L., Gomelsky, M., and Schlichting, I. (2009). Structure and mechanism of a bacterial light-regulated cyclic nucleotide phosphodiesterase. Nature *459*, 1015–1018.

Bejerano-Sagie, M., Oppenheimer-Shaanan, Y., Berlatzky, I., Rouvinski, A., Meyerovich, M., and Ben-Yehuda, S. (2006). A checkpoint protein that scans the chromosome for damage at the start of sporulation in *Bacillus subtilis*. Cell *125*, 679–690.

Biasini, M., Bienert, S., Waterhouse, A., Arnold, K., Studer, G., Schmidt, T., Kiefer, F., Gallo Cassarino, T., Bertoni, M., Bordoli, L., et al. (2014). SWISS-MODEL: modelling protein tertiary and quaternary structure using evolutionary information. Nucleic Acids Res. *42*, W252–W258.

Blanchet, C.E., Spilotros, A., Schwemmer, F., Graewert, M.A., Kikhney, A., Jeffries, C.M., Franke, D., Mark, D., Zengerle, R., Cipriani, F., et al. (2015). Versatile sample environments and automation for biological solution X-ray scattering experiments at the P12 beamline (PETRA III, DESY). J. Appl. Crystallogr. *48*, 431–443.

Bowman, L., Zeden, M.S., Schuster, C.F., Kaever, V., and Gründling, A. (2016). New insights into the cyclic di-adenosine monophosphate (c-di-AMP) degradation pathway and the requirement of the cyclic dinucleotide for acid stress resistance in *Staphylococcus aureus*. J. Biol. Chem. *291*, 26970–26986.

Corrigan, R.M., Campeotto, I., Jeganathan, T., Roelofs, K.G., Lee, V.T., and Gründling, A. (2013). Systematic identification of conserved bacterial c-di-AMP receptor proteins. Proc. Natl. Acad. Sci. USA *110*, 9084–9089.

Corrigan, R.M., and Gründling, A. (2013). Cyclic di-AMP: another second messenger enters the fray. Nat. Rev. Microbiol. *11*, 513–524.

Dengler, V., McCallum, N., Kiefer, P., Christen, P., Patrignani, A., Vorholt, J.A., Berger-Bachi, B., and Senn, M.M. (2013). Mutation in the C-di-AMP cyclase dacA affects fitness and resistance of methicillin resistant *Staphylococcus aureus*. PLoS One *8*, e73512.

Emsley, P., and Cowtan, K. (2004). Coot: model-building tools for molecular graphics. Acta Crystallogr. D Biol. Crystallogr. *60*, 2126–2132.

Franke, D., Petoukhov, M.V., Konarev, P.V., Panjkovich, A., Tuukkanen, A., Mertens, H.D.T., Kikhney, A.G., Hajizadeh, N.R., Franklin, J.M., Jeffries, C.M., et al. (2017). ATSAS 2.8: a comprehensive data analysis suite for small-angle scattering from macromolecular solutions. J. Appl. Crystallogr. *50*, 1212–1225.

Gundlach, J., Herzberg, C., Kaever, V., Gunka, K., Hoffmann, T., Weiss, M., Gibhardt, J., Thurmer, A., Hertel, D., Daniel, R., et al. (2017). Control of potassium homeostasis is an essential function of the second messenger cyclic di-AMP in *Bacillus subtilis*. Sci. Signal. *10*, https://doi.org/10.1126/scisignal.aal3011.

He, Q., Wang, F., Liu, S., Zhu, D., Cong, H., Gao, F., Li, B., Wang, H., Lin, Z., Liao, J., et al. (2016). Structural and biochemical insight into the mechanism of Rv2837c from *Mycobacterium tuberculosis* as a c-di-NMP phosphodiesterase. J. Biol. Chem. *291*, 3668–3681.

Huynh, T.N., Luo, S., Pensinger, D., Sauer, J.D., Tong, L., and Woodward, J.J. (2015). An HD-domain phosphodiesterase mediates cooperative hydrolysis of c-di-AMP to affect bacterial growth and virulence. Proc. Natl. Acad. Sci. USA *112*, E747–E756.

Huynh, T.N., and Woodward, J.J. (2016). Too much of a good thing: regulated depletion of c-di-AMP in the bacterial cytoplasm. Curr. Opin. Microbiol. *30*, 22–29.

Jeffries, C.M., Graewert, M.A., Blanchet, C.E., Langley, D.B., Whitten, A.E., and Svergun, D.I. (2016). Preparing monodisperse macromolecular samples for successful biological small-angle X-ray and neutron-scattering experiments. Nat. Protoc. *11*, 2122–2153.

Kabsch, W. (2010). Xds. Acta Crystallogr. D Biol. Crystallogr. *66*, 125–132.

Kamegaya, T., Kuroda, K., and Hayakawa, Y. (2011). Identification of a *Streptococcus pyogenes* SF370 gene involved in production of c-di-AMP. Nagoya J. Med. Sci. *73*, 49–57.

Liebschner, D., Afonine, P.V., Moriarty, N.W., Poon, B.K., Sobolev, O.V., Terwilliger, T.C., and Adams, P.D. (2017). Polder maps: improving OMIT maps by excluding bulk solvent. Acta Crystallogr. D Struct. Biol. *73*, 148–157.

McCoy, A.J., Grosse-Kunstleve, R.W., Adams, P.D., Winn, M.D., Storoni, L.C., and Read, R.J. (2007). Phaser crystallographic software. J. Appl. Crystallogr. *40*, 658–674.

Mehne, F.M., Gunka, K., Eilers, H., Herzberg, C., Kaever, V., and Stülke, J. (2013). Cyclic di-AMP homeostasis in *Bacillus subtilis*: both lack and high level accumulation of the nucleotide are detrimental for cell growth. J. Biol. Chem. *288*, 2004–2017.

Mertens, H.D., and Svergun, D.I. (2010). Structural characterization of proteins and complexes using small-angle X-ray solution scattering. J. Struct. Biol. *172*, 128–141.

Müller, M., Deimling, T., Hopfner, K.P., and Witte, G. (2015a). Structural analysis of the diadenylate cyclase reaction of DNA-integrity scanning protein A (DisA) and its inhibition by 3′-dATP. Biochem. J. *469*, 367–374.

Müller, M., Hopfner, K.P., and Witte, G. (2015b). c-di-AMP recognition by *Staphylococcus aureus* PstA. FEBS Lett. *589*, 45–51.

Nicolas, P., Mader, U., Dervyn, E., Rochat, T., Leduc, A., Pigeonneau, N., Bidnenko, E., Marchadier, E., Hoebeke, M., Aymerich, S., et al. (2012).

Condition-dependent transcriptome reveals high-level regulatory architecture in *Bacillus subtilis*. Science *335*, 1103–1106.

Oppenheimer-Shaanan, Y., Wexselblatt, E., Katzhendler, J., Yavin, E., and Ben-Yehuda, S. (2011). c-di-AMP reports DNA integrity during sporulation in *Bacillus subtilis*. EMBO Rep. *12*, 594–601.

Pape, T., and Schneider, T.R. (2004). HKL2MAP: a graphical user interface for macromolecular phasing with SHELX programs. J. Appl. Crystallogr. *37*, 843–844.

Pettersen, E.F., Goddard, T.D., Huang, C.C., Couch, G.S., Greenblatt, D.M., Meng, E.C., and Ferrin, T.E. (2004). UCSF Chimera – a visualization system for exploratory research and analysis. J. Comput. Chem. *25*, 1605–1612.

Putnam, C.D., Hammel, M., Hura, G.L., and Tainer, J.A. (2007). X-ray solution scattering (SAXS) combined with crystallography and computation: defining accurate macromolecular structures, conformations and assemblies in solution. Q. Rev. Biophys. *40*, 191–285.

Rao, F., Ji, Q., Soehano, I., and Liang, Z.X. (2011). Unusual heme-binding PAS domain from YybT family proteins. J. Bacteriol. *193*, 1543–1551.

Rao, F., See, R.Y., Zhang, D., Toh, D.C., Ji, Q., and Liang, Z.X. (2010). YybT is a signaling protein that contains a cyclic dinucleotide phosphodiesterase domain and a GGDEF domain with ATPase activity. J. Biol. Chem. *285*, 473–482.

Schrodinger, LLC. (2015). The PyMOL Molecular Graphics System, Version 1.8.

Sheldrick, G.M. (2010). Experimental phasing with SHELXC/D/E: combining chain tracing with density modification. Acta Crystallogr. D Biol. Crystallogr. *66*, 479–485.

Srivastav, R., Kumar, D., Grover, A., Singh, A., Manjasetty, B.A., Sharma, R., and Taneja, B. (2014). Unique subunit packing in mycobacterial nanoRNase leads to alternate substrate recognitions in DHH phosphodiesterases. Nucleic Acids Res. *42*, 7894–7910.

Svergun, D., Barberato, C., and Koch, M.H.J. (1995). CRYSOL - a program to evaluate X-ray solution scattering of biological macromolecules from atomic coordinates. J. Appl. Crystallogr. *28*, 768–773.

Tang, Q., Luo, Y., Zheng, C., Yin, K., Ali, M.K., Li, X., and He, J. (2015). Functional analysis of a c-di-AMP-specific phosphodiesterase MsPDE from *Mycobacterium smegmatis*. Int. J. Biol. Sci. *11*, 813–824.

Uemura, Y., Nakagawa, N., Wakamatsu, T., Kim, K., Montelione, G.T., Hunt, J.F., Kuramitsu, S., and Masui, R. (2013). Crystal structure of the ligand-binding form of nanoRNase from *Bacteroides fragilis*, a member of the DHH/DHHA1 phosphoesterase family of proteins. FEBS Lett. *587*, 2669–2674.

Whiteley, A.T., Garelis, N.E., Peterson, B.N., Choi, P.H., Tong, L., Woodward, J.J., and Portnoy, D.A. (2017). c-di-AMP modulates *Listeria monocytogenes* central metabolism to regulate growth, antibiotic resistance and osmoregulation. Mol. Microbiol. *104*, 212–233.

Winn, M.D., Ballard, C.C., Cowtan, K.D., Dodson, E.J., Emsley, P., Evans, P.R., Keegan, R.M., Krissinel, E.B., Leslie, A.G., McCoy, A., et al. (2011). Overview of the CCP4 suite and current developments. Acta Crystallogr. D Biol. Crystallogr. *67*, 235–242.

Witte, C.E., Whiteley, A.T., Burke, T.P., Sauer, J.D., Portnoy, D.A., and Woodward, J.J. (2013). Cyclic di-AMP is critical for *Listeria monocytogenes* growth, cell wall homeostasis, and establishment of infection. MBio *4*, e00282-13.

Witte, G., Hartung, S., Büttner, K., and Hopfner, K.P. (2008). Structural biochemistry of a bacterial checkpoint protein reveals diadenylate cyclase activity regulated by DNA recombination intermediates. Mol. Cell *30*, 167–178.

Woodward, J.J., Iavarone, A.T., and Portnoy, D.A. (2010). c-di-AMP secreted by intracellular *Listeria monocytogenes* activates a host type I interferon response. Science *328*, 1703–1705.

CellPress

STAR★METHODS

KEY RESOURCES TABLE

REAGENT or RESOURCE	SOURCE	IDENTIFIER
Bacterial and Virus Strains		
E. coli BL21 (DE3) Rosetta (expression strain)	Novagene	
T. maritima MSB8 (used for genomic DNA prep.)	DSMZ; DSM 3109	https://www.dsmz.de/
B. subtilis subsp. subtilis	DSMZ; DSM 402	https://www.dsmz.de/ used for colony PCR
S. pneumoniae	DSMZ; DSM 11865	https://www.dsmz.de/ genomic DNA used for PCR
Chemicals, Peptides, and Recombinant Proteins		
5′-pApA	Biolog	Cat #P 033
5′-pApG	Biolog	Cat #P 082
5′-pGpG	Biolog	Cat #P 023
c-di-AMP	Biolog	Cat #C 088
c-di-GMP	Biolog	Cat #C 057
AMP	Sigma-Aldrich	Cat #A1752-1G
Deposited Data		
TmPDE pre-reaction state (apo)	This paper	PDB 5O25
TmPDE D80ND154N + 5′-pApA	This paper	PDB 5O4Z
TmPDE D80ND154N + 5′-pApG	This paper	PDB 5O58
TmPDE D80ND154N + pA : pA	This paper	PDB 5O70
TmPDE D80ND154N + GMP/Mn^{2+}	This paper	PDB 5O7F
TmPDE AMP/Mn^{2+}	This paper	PDB 5O1U
SAXS data (TmPDE wildtype)	This paper	SASBDB SASDCD7
SAXS data (TmPDE D80N D154N)	This paper	SASBDB SASDCC7
SAXS data (SpPde2)	This paper	SASBDB SASDCB7
Oligonucleotides		
RNA sequence: 5′-pApApA_ligand: AAA	Metabion	N/A
Primers for cloning, see Table S1	Metabion	N/A
Recombinant DNA		
Plasmid: pET-M11-SUMO1	EMBL Heidelberg	N/A
Software and Algorithms		
XDS/XSCALE	(Kabsch, 2010)	http://xds.mpimf-heidelberg.mpg.de/
SHELX CDE	(Sheldrick, 2010)	http://shelx.uni-ac.gwdg.de/SHELX/
HKL2MAP	(Pape and Schneider, 2004)	http://webapps.embl-hamburg.de/hkl2map/
PHENIX suite	(Adams et al., 2010)	https://www.phenix-online.org/
CCP4 suite	(Winn et al., 2011)	http://www.ccp4.ac.uk/
PHASER	(McCoy et al., 2007)	(included in CCP4 and PHENIX)
PyMOL	(Schrodinger, 2015)	https://www.pymol.org/
SWISS-MODEL	(Biasini et al., 2014)	https://swissmodel.expasy.org/interactive
UCSF Chimera	(Pettersen et al., 2004)	https://www.cgl.ucsf.edu/chimera/
ATSAS (includes CRYSOL)	(Franke et al., 2017)	https://www.embl-hamburg.de/biosaxs/software.html
PEAQ-ITC Analysis Software	Malvern	Provided with the instrument

(*Continued on next page*)

Continued		
REAGENT or RESOURCE	SOURCE	IDENTIFIER
Biacore X100+ Data Evaluation Software	GE Lifesciences	Provided with the instrument
Origin Pro	OriginLabs	http://www.originlab.de/
Other		
Columns (IEX, SEC, Affinity)	GE Healthcare Life Sciences	http://www.gelifesciences.com/webapp/wcs/stores/servlet/Home/en/GELifeSciences-de/

CONTACT FOR REAGENT AND RESOURCE SHARING

Further information and requests for resources and reagents should be directed to and will be fulfilled by the Lead Contact Gregor Witte (witte@genzentrum.lmu.de)

METHOD DETAILS

Experimental Model and Subject Details

B. subtilis subsp. subtilis (DSM 402) and *T. maritima* MSB8 (DSM 3109) cells were purchased from the DSMZ (Germany) and used either for genomic DNA preparation or directly for colony PCR. *S. pneumoniae* (DSM 11865) genomic DNA was purchased from DSMZ (Germany).

Cloning, Expression and Purification

T. maritima PDE (TM_1595), *S. pneumoniae* Pde2 (SPD_1153), *B. subtilis* GdpP-ΔTM (GdpP without transmembrane part) and *B. subtilis* GdpP-DHH/DHHA1 (active site domains only) were cloned into separate pET28 M11 SUMO1 vectors (EMBL Heidelberg) via the AgeI/NotI for the first or BamHI/NotI for the latter constructs restriction sites, respectively. A GSG-linker was introduced in between the SenP2 cleavage-site and the start of the TmPDE gene to facilitate tag cleavage. Recombinant expression of all proteins containing a His_6-SUMO tag was performed in *E. coli* Rosetta BL21(DE3) after induction with 0.2 mM IPTG (for TmPDE and BsuGdpP) or 0.1 mM IPTG (for SpPde2) at 18°C. Cells were harvested after 18 hours and lysed in buffer A (50 mM Tris-HCl, 300 mM NaCl, 10 mM imidazole, 5% v/v glycerol, pH 7.5) by sonication. After clarification of the lysate by centrifugation, the supernatant was loaded onto a Ni-NTA column (Qiagen). The column was washed with buffer A and followed by buffer B (50 mM Tris-HCl, 300 mM NaCl, 30 mM imidazole, 5% v/v glycerol, pH 7.5) prior to elution of the proteins with buffer C (50 mM Tris-HCl, 300 mM NaCl, 250 mM imidazole, 5% v/v glycerol, pH 7.5). SenP2 was added at a ratio of 1:500 (w:w) to TmPDE and SpPde2 in order to cleave the His_6-SUMO tag during dialysis into buffer D (20 mM Tris-HCl, 150 mM NaCl, 5% v/v glycerol, pH 7.5). After separating the tag from the proteins with the aid of a second Ni-column, TmPDE and SpPde2 were concentrated and loaded onto a HiLoad Superdex 200 column (GE Healthcare) equilibrated with buffer D. The peak fractions were pooled, concentrated, flash frozen in liquid nitrogen and stored at -80°C. TmPDE mutants were created by site-directed mutagenesis using overlap extension PCR. Mutant proteins were expressed and purified as described for the wild-type protein.

TmPde Crystallization

For determination of the product state structure, TmPDE at a concentration of 10 mg/mL was supplemented with 1 mM $MnCl_2$ and 1 mM AMP. Crystals were grown by hanging-drop vapor diffusion at 20°C after mixing 1 μL protein with 1 μL reservoir solution (0.1 M HEPES-NaOH pH 7.8, 25% w/v PEG4000, 0.2 M $CaCl_2$) with a total reservoir volume of 300 μL. Crystals were cryo-protected by transfer into mother liquor supplemented with 25% v/v ethylene glycol prior to flash cooling in liquid nitrogen. Crystals of apo TmPDE were grown similarly, but the protein was concentrated to 15 mg/mL and the reservoir solution contained 0.1 M Tris-HCl pH 7.5, 25% w/v PEG4000, 0.2 M $MgCl_2$. Cryo-protection was achieved by addition of 25% v/v PEG400 to the reservoir solution. Crystals of the inactive mutant TmPDE D80N D154N with 5′-pApA were grown by hanging-drop vapor diffusion with 10 mg/mL protein, 1.5 mM 5′-pApA and 1.5 mM $MnCl_2$ and a reservoir solution of 2.2 M ammonium sulfate and 0.1 M sodium citrate. Crystals were cryo-protected by soaking in reservoir solution supplemented with 25% v/v glycerol. Crystals of the inactive mutant TmPDE D80N D154N with 5′-pApG were obtained by sitting-drop vapor diffusion with 13 mg/mL protein, 1.5 mM 5′-pApG and 5 mM $MnCl_2$ and a reservoir solution of 20% w/v 2-propanol, 0.1 M sodium acetate pH 4.6 and 0.2 M $CaCl_2$. Crystals of the inactive mutant TmPDE D80N D154N with GMP (product III) were obtained by sitting-drop vapor diffusion with 13 mg/mL protein, 1.5 mM 5′-pGpG and 5 mM $MnCl_2$ and a reservoir solution of 30% w/v PEG4000, 0.1 M Tris pH 8.5 and 0.2 M $MgCl_2$. For both the 5′-pApG and 5′-pGpG complexes cryo-protection was achieved by the addition of 50% v/v ethylene glycol to the reservoir solution.

CellPress

Data Collection and Processing

Diffraction data of the AMP/Mn^{2+}-TmPDE and apo TmPDE crystals were collected at the EMBL P14 beamline at PETRA III (DESY Hamburg, Germany). Diffraction data of the TmPDE D80N D154N mutant with 5′-pApA were measured at the ESRF ID30A MASSIF-1 (ESRF Grenoble, France). TmPDE with 2 AMP (product state II) and 5′-pApG were collected at the EMBL P13 beamline at PETRA III (DESY Hamburg, Germany). Diffraction data of the TmPDE mutant crystallized in presence of 5′-pGpG (GMP state) were collected at SLS X06SA (Swiss Light Source, Villigen, Switzerland). All data were indexed and scaled using XDS and XSCALE, respectively (Kabsch, 2010).

Phasing, Model Building and Refinement

Phases were determined by the use of a single anomalous diffraction dataset collected from TmPDE-AMP/Mn^{2+} crystals. Identification of Mn^{2+} sites, phasing and solvent flattening was performed using SHELXCDE (Sheldrick, 2010) through the HKL2MAP GUI (Pape and Schneider, 2004). The relatively high resolution allowed automatic model building with PHENIX (Adams et al., 2010) followed by manual model building in COOT (Emsley and Cowtan, 2004) and automatic refinement in PHENIX (Afonine et al., 2012). The product state III was phased similarly. The structures of the apo TmPDE and both TmPDE D80N D154N nucleotide complexes were phased by molecular replacement with PHASER (McCoy et al., 2007) within the CCP4 suite (Winn et al., 2011) using the DHH and DHHA1 domains as separate search models. Model building and refinement was performed with Coot and PHENIX as described above. All crystallographic figures were prepared with PyMOL (Schrodinger, 2015). Morphing in Movie S1 was prepared in Chimera (Pettersen et al., 2004) using the apo state and 5′-pApA bound state of TmPDE to illustrate the potential dynamics of the ligand-binding cleft.

Small-Angle X-ray Scattering

Small-angle X-ray scattering experiments were performed at the EMBL P12 beamline at PETRA III (DESY Hamburg, Germany). To remove potential aggregates, all samples were additionally purified by size-exclusion chromatography and centrifuged prior to measurements. Size-exclusion chromatography coupled SAXS was performed for the TmPDE D80N D154N mutant (Blanchet et al., 2015; Jeffries et al., 2016). The running buffer of the chromatography step was used as a buffer reference for buffer subtraction of the protein sample scattering data. Proteins in batch mode were measured at different concentrations and all data sets were analyzed using the ATSAS software package (Franke et al., 2017) as described in (Mertens and Svergun, 2010; Putnam et al., 2007). Calculation of theoretical scattering curves from crystal structures was performed using CRYSOL (Svergun et al., 1995). Figures of *ab initio* models with docked crystal structures were prepared with UCSF Chimera (Pettersen et al., 2004). Scattering data of SpPde2, wild type TmPDE and TmPDE D80N D154N have been deposited in the SASBDB.

Static Light Scattering

Size-exclusion chromatography coupled light scattering was performed using an ÄKTA micro chromatography system equipped with a Superdex 200 10/300 Increase column (GE Healthcare Life Sciences) and a right-angle laser light scattering device and refractive index detector (Malvern/Viscotek). BSA (66 kDa) was used to calibrate the system. Evaluation was performed using the OmniSEC software (Malvern/Viscotek) provided with the instrument.

Enzymatic Activity Assay

To check the activity of TmPDE and SpPde2 we used a LC-based assay to quantify the reaction products. A 100 μL reaction mix containing 50 mM Tris pH 8.5, 20 mM KCl, 0.1 mM $MnCl_2$, 62.5-2000 μM c-di-AMP or 5′-pApA, and 10 nM-10 μM enzyme (monomer concentration) was incubated at room temperature for 15-60 min. This was then quickly diluted with assay buffer A (50 mM Tris-HCl pH 9.0) and the nucleotides were separated from the protein by spin concentrators (30 kDa cutoff). 500 μL of the flow-through was loaded on to a Mono Q 5/50 GL column (GE Lifesciences) equilibrated with buffer A (50 mM Tris-HCl pH 9.0). A linear gradient to 50% buffer B (50 mM Tris-HCl pH 9, 1 M NaCl) over 30 column volumes was used to elute the reaction products. The peaks were then compared to standard nucleotides (AMP, 5′-pApA, c-di-AMP). The individual chromatogram peaks were integrated using Origin (OriginLabs). Please note, for assays shown in Figures 2G, 2J, and S2A–S2D a linear gradient to 35% buffer B over 28 column volumes was used.

Surface Plasmon Resonance

c-di-AMP and 5′-pApA binding was analyzed by SPR using a Biacore X100+ as previously described (Müller et al., 2015b). 5278 RU TmPDE D80N D154N were coupled to flow cell 2 (FC2) of an activated CM-5 (GE Life sciences) chip using amino reactive EDC/NHS coupling chemistry. FC1 was only activated and blocked with ethanolamine to serve as a reference for unspecific binding of the analyte to the chip and the reported data therefore correspond to RU(FC2-FC1). Different concentrations of nucleotides in HBS-EP buffer (150 mM NaCl, 10 mM HEPES-NaOH pH 7.4, 3 mM EDTA, 0.05% v/v surfactant P20) were injected to monitor binding of c-di-AMP and nucleotide substrates. Data were analyzed using the Biacore X100 Evaluation software. All experiments were repeated at least once to confirm the robustness of the assay.

Isothermal Titration Calorimetry

ITC data were collected using a Malvern PEAQ-ITC system with 20 μM TmPDE D80N D154N in HBS-EP buffer in the cell. The respective nucleotide at a concentration of 200 μM in HBS-EP buffer was titrated into the cell by 19 injections of 2 μL, spaced 150 s apart, at

25°C. Data evaluation was performed with the Malvern software package. All experiments were repeated at least once to confirm the robustness of the assay.

DATA AND SOFTWARE AVAILABILITY

Coordinates and structure factors have been deposited in the PDB under ID codes 5O25, 5O4Z, 5O58, 5O70, 5O1U, and 5O7F. SAXS data have been deposited in the SASBDB under ID codes SASDCB7, SASDCC7, and SASDCD7.

Structure, Volume *25*

Supplemental Information

Structural and Biophysical Analysis of the Soluble DHH/DHHA1-Type Phosphodiesterase TM1595 from *Thermotoga maritima*

David Jan Drexler, Martina Müller, Carlos Alberto Rojas-Cordova, Adrian Maurice Bandera, and Gregor Witte

Table S1. Primers used in this study, Related to STAR Methods.

Name	Length	Orientation	T_m [°C]	Sequence (5'3')
TmPDE_AgeI_GSG_fwd	51	forward	56	TAATAAACCGGTGGATCCGGCTCTGGCTGGACGAGATCGTCAAAGTGCTC
TmPDE NotI_rev	35	reverse	60	TAATAAGCGGCCGCTCATCCCCCCAGTACGTCTCC
TmPDE D80N_fwd	33	forward	67	CTTCTTGTGGTGGTCAACGCCTCCTCTCCCGAC
TmPDE D80N_rev	33	reverse	69	GTCGGGAGAGGAGGCGTTGACCACCACAAGAAG
TmPDE D154N_fwd	31	forward	64	CTTGGGATCGCAACCAACACAGGGTTTTTCA
TmPDE D154N_rev	31	reverse	63	TGAAAAACCCTGTGTTGGTTGCGATCCCAAG
SpPdeI_Lys51_BamHI_fwd	33	forward	49	TAATAAGGATCCAAGAAACTGAGAGTGCATTAT
SpPdeI_Lys51_NotI_rev	35	reverse	48	TAATAAGCGGCCGCTCATTCTTCTTTCTCCTTTTC
SpPdeII_Lys51_BamHI_fwd	33	forward	51	TAATAAGGATCCATGGAGATTTGCCAACAAATT
SpPdeII_Lys51_NotI_rev	35	reverse	47	TAATAAGCGGCCGCTCAGTTTTTAAGCAAGTTTTT
BsGdpP_K1_BamHI_F	33	forward	46	TAATAAGGATCCATTGGAATCATGCTTTTTAAT
BsGdpP_NotI_R	32	reverse	53	TAATAAGCGGCCGCTCATCTCTGTACGCCTCC
GdpP DHH/DHHA1 B.s. C1 for	31	forward	63	TAAGGATCCATGGAGAAACGAACAAGGGTGC
GdpP DHH/DHHA1 B.s. C1 rev	32	reverse	67	TAAGCGGCCGCTCATCTTTGAACCCCTCCTTC

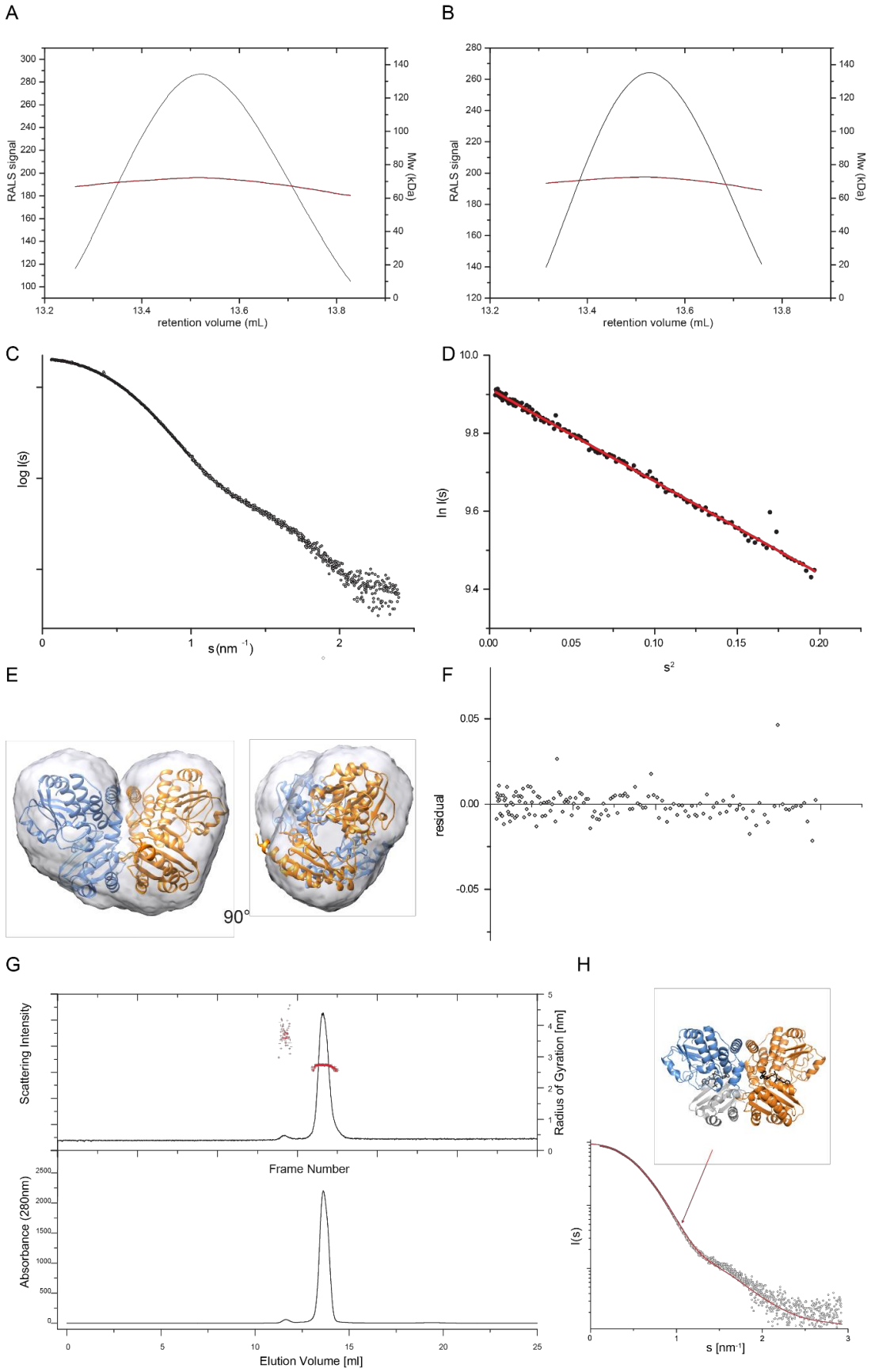
A
RALS signal
Mw (kDa)
retention volume (mL)
B
RALS signal
Mw (kDa)
retention volume (mL)
C
log I(s)
s(nm -1)
D
ln I(s)
s2
E
90°
F
residual
G
Scattering Intensity
Radius of Gyration [nm]
Frame Number
Absorbance (280nm)
Elution Volume [ml]
H
I(s)
s [nm-1]

Figure S1. Molecular weight determination of TmPDE wt (and mutant) and SAXS data, Related to Figure 1.

Molecular weight determination by size-exclusion coupled right-angle light scattering. Panel A and B show the TmPDE peaks of a run using a 24ml 10/300 S200 increase column (GE Healthcare) and their respective molecular weight determined by RALS for wildtype TmPDE (A) and TmPDE D80N D154N (B). Both proteins show molecular weights of approx. 70 kDa and thus TmPDE is dimeric in solution (the monomer Mw of the construct is 37.8 kDa). The mutation does not change the oligomeric state in solution.

(C) buffer corrected small-angle X-ray scattering curve of a 7 mg/mL *S. pneumoniae* Pde2 sample

(D) Guinier plot analysis, data from (C), R_G=2.7nm was determined from the slope of the linear regression for $s*R_G<1.3$ (Guinier approximation).The sample is free of aggregates as judged from linearity of the Guinier region

(E) final averaged *ab initio* shape of *S. pneumoniae* Pde2 calculated from 20 DAMMIF models (NSD 0.81) with docked TmPDE dimer in two orientations.

(F) shows the respective residuals of the linear regression of the Guinier plot (D)

(G) Chromatogram of SEC-coupled SAXS measurements of the TmPDE D80N D154N mutant using a Superdex 200 10/300 column. Shown are scattering intensity and radius of gyration (top) and absorbance at 280nm (bottom) versus elution volume.

(H) Averaged and buffer corrected SAXS curve (grey points) derived from the main peak (RG=2.7nm, panel B). Also shown is the theoretical scattering curve (red) calculated with CRYSOL (Svergun et al., 1995) of the “butterfly” shaped TmPDE D80N D154N dimer shown as cartoon model.

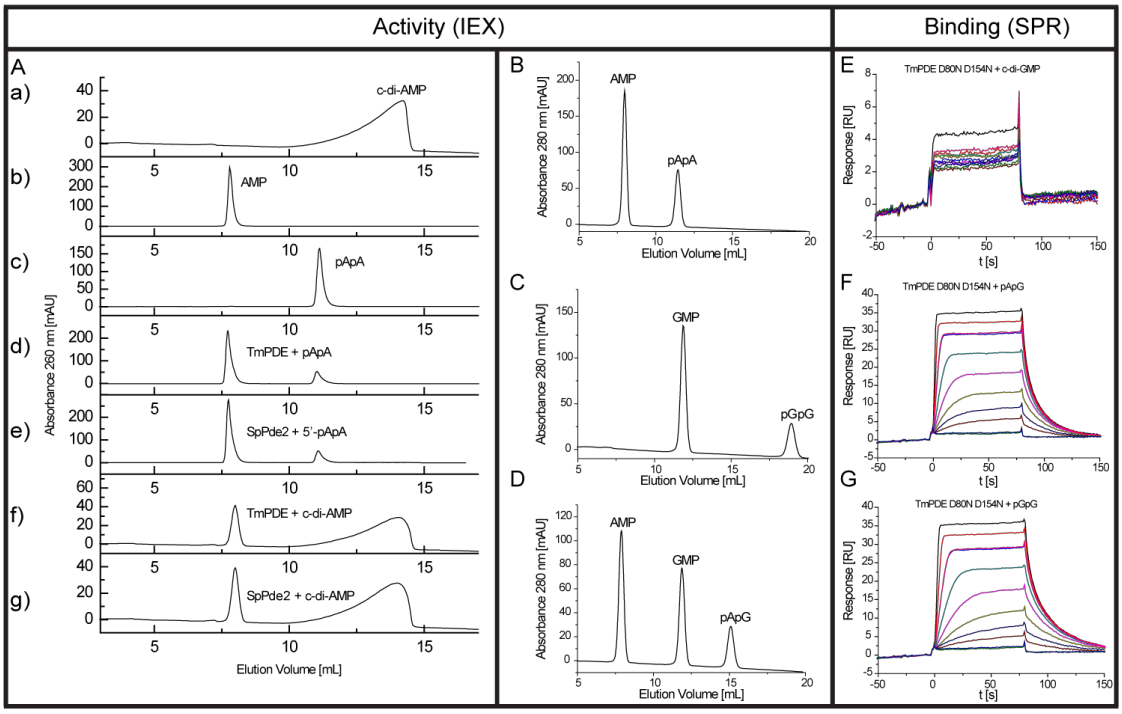

Figure S2. IEX experiments and SPR raw data, Related to Figure 2.

(A) Ion Exchange chromatography on Mono-Q column. From top:
a) 125 µM c-di-AMP standard; b) 250 µM AMP standard; c) 125 µM 5'-pApA standard; d) Reaction of 10 nM TmPDE with 125 µM 5'-pApA; e) Reaction of 25 nM SpPde2 with 125 µM 5'-pApA; f) Reaction of 10 µM TmPDE with 250 µM c-di-AMP; g) Reaction of 10 µM SpPde2 with 250 µM c-di-AMP. (t=25 min reaction time at 20 °C).
(B) Ion exchange chromatography on Mono-Q 5/50 GL column of the reaction products from 100 µL reactions with 10 nM TmPDE + 125 µM 5'-pApA after 25 min incubation.
(C) Ion exchange chromatography on Mono-Q 5/50 GL column of the reaction products from 100 µL reactions with 10 nM TmPDE + 125 µM 5'-pGpG after 25 min incubation.
(D) Ion exchange chromatography on Mono-Q 5/50 GL column of the reaction products from 100 µL reactions with 10 nM TmPDE + 125 µM 5'-pApG after 25 min incubation.
(E) SPR measurements of TmPDE D80N 154N mutant (on chip) with injections of 8 – 1000 µM c-di-GMP analyte concentrations.
(F) SPR measurements of TmPDE D80N 154N mutant (on chip) with injections of 8 – 1000 µM 5'-pApG analyte concentrations.
(G) SPR measuremenst of TmPDE D80N 154N mutant (on chip) with injections of 8 – 1000 µM 5'-pGpG analyte concentrations.

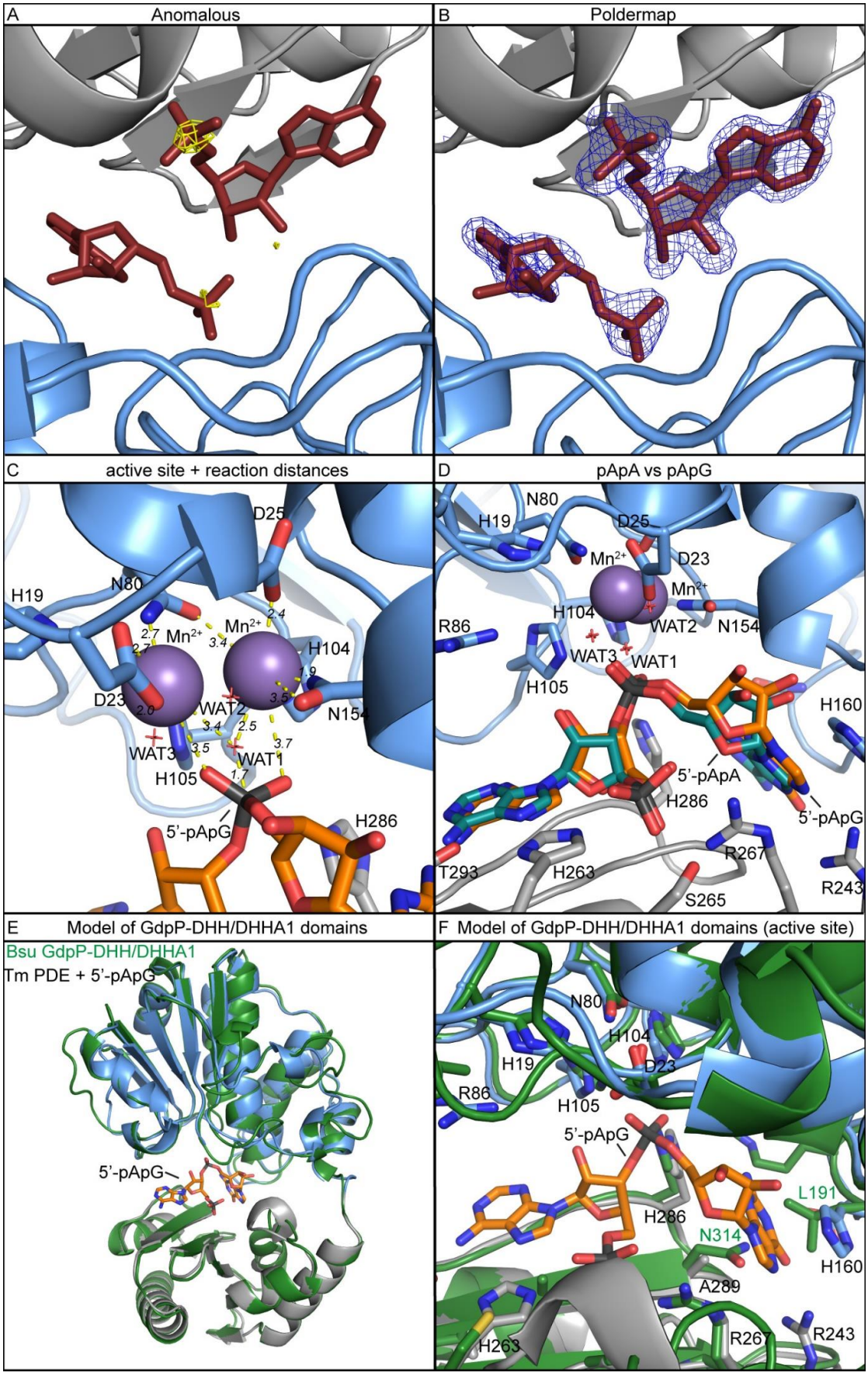
A
Anomalous
B
Poldermap
C
active site + reaction distances
D25
H19
N80
Mn2+
Mn2+
H104
D23
WAT2
N154
WAT3
WAT1
H105
5'-pApG
H286
D
pApA vs pApG
N80
H19
D25
Mn2+
D23
Mn2+
H104
R86
WAT2
N154
WAT3
WAT1
H105
H160
5'-pApA
H286
5'-pApG
T293
H263
R267
S265
R243
E
Model of GdpP-DHH/DHHA1 domains
Bsu GdpP-DHH/DHHA1
Tm PDE + 5'-pApG
5'-pApG
F
Model of GdpP-DHH/DHHA1 domains (active site)
N80
H104
H19
D23
R86
H105
5'-pApG
L191
H286
N314
H160
A289
H263
R267
R243

Figure S3. Detailed view on the active site of TmPDE, Related to Figure 3.

(A) Active site of TmPDE D80N D154N shown in cartoon representation, DHH domain (light blue) and DHHA1 domain (grey) with hydrolyzed 5'-pApA (i.e. 2 AMP in red) and anomalous difference map (yellow) shown at 3.7σ contour level clearly defining the phosphate positions.
(B) Active site of TmPDE D80N D154N shown in cartoon representation, DHH domain (light blue) and DHHA1 domain (grey) with hydrolyzed 5'-pApA (2 AMP, red) and the respective Polder map (dark blue) shown at 4σ contour level.
(C) Close-up view on the active site of TmPDE D80N D154N shown in cartoon representation, DHH domain (light blue), DHHA1 domain (grey), with interacting residues and 5'-pApG shown as sticks, water molecules as red crosses and manganese ions (purple) as spheres. Distances are given in Å and shown as dashed lines (yellow).
(D) Active site superposition of TmPDE D80N D154N with 5'-pApA and 5'-pApG, respectively. TmPDE is shown in cartoon representation, DHH domain (light blue), DHHA1 domain (grey), with interacting residues, 5'-pApA (cyan) and 5'-pApG (orange) shown as sticks, water molecules as red crosses and manganese ions (purple) as spheres.
(E) Overall structure superposition of the modelled GdpP DHH/DHHA1 domains (green, based on the TmPDE D80N D154N structure with 5'-pApG as template using SWISS-MODEL) and the template. Protein structures are shown in cartoon representation, TmPDE DHH domain (light blue), DHHA1 domain (grey) and 5'-pApG (orange) shown as sticks.
(F) Active site close-up of the superposition of the modelled GdpP DHH/DHHA1 domain (green) and TmPDE D80N D154N (with 5'-pApG) illustrate a potential clash between L191 and N314 (site B) of the GdpP-model and the second base of the ligand.

6.3 Supplement III - c-di-AMP hydrolysis by the phosphodiesterase AtaC promotes differentiation of multicellular bacteria

Latoscha A.*; Drexler D.*; Al-Bassam M. M.; Bandera A. M.; Kaever V.; Findlay K. C.; Witte G.; Tschowri N. C-di-AMP hydrolysis by the phosphodiesterase AtaC promotes differentiation of multicellular bacteria. *PNAS* **2020**, *117* (35), 7392-7400.

* contributed equally

DOI: https://doi.org/10.1073/pnas.1917080117
URL: https://www.pnas.org/content/117/13/7392

c-di-AMP hydrolysis by the phosphodiesterase AtaC promotes differentiation of multicellular bacteria

Andreas Latoscha[a,1], David Jan Drexler[b,c,1], Mahmoud M. Al-Bassam[d], Adrian M. Bandera[b,c], Volkhard Kaever[e], Kim C. Findlay[f], Gregor Witte[b,c,2], and Natalia Tschowri[a,2]

[a]Department of Microbiology, Humboldt-Universität zu Berlin, 10115 Berlin, Germany; [b]Gene Center, Ludwig-Maximilians-Universität München, 81377 München, Germany; [c]Department of Biochemistry, Ludwig-Maximilians-Universität München, 81377 München, Germany; [d]Department of Pediatrics, University of California San Diego, La Jolla, CA 92093; [e]Research Core Unit Metabolomics, Medizinische Hochschule Hannover, 30625 Hannover, Germany; and [f]Department of Cell and Developmental Biology, John Innes Centre, Norwich Research Park, Norwich NR4 7UH, United Kingdom

Edited by Caroline S. Harwood, University of Washington, Seattle, WA, and approved February 11, 2020 (received for review October 1, 2019)

Antibiotic-producing *Streptomyces* use the diadenylate cyclase DisA to synthesize the nucleotide second messenger c-di-AMP, but the mechanism for terminating c-di-AMP signaling and the proteins that bind the molecule to effect signal transduction are unknown. Here, we identify the AtaC protein as a c-di-AMP-specific phosphodiesterase that is also conserved in pathogens such as *Streptococcus pneumoniae* and *Mycobacterium tuberculosis*. AtaC is monomeric in solution and binds Mn^{2+} to specifically hydrolyze c-di-AMP to AMP via the intermediate 5′-pApA. As an effector of c-di-AMP signaling, we characterize the RCK_C domain protein CpeA. c-di-AMP promotes interaction between CpeA and the predicted cation/proton antiporter, CpeB, linking c-di-AMP signaling to ion homeostasis in Actinobacteria. Hydrolysis of c-di-AMP is critical for normal growth and differentiation in *Streptomyces*, connecting ionic stress to development. Thus, we present the discovery of two components of c-di-AMP signaling in bacteria and show that precise control of this second messenger is essential for ion balance and coordinated development in *Streptomyces*.

c-di-AMP | *Streptomyces* | phosphodiesterase | development | osmostress

Bacteria use mono-, di-, and trinucleotides as second messengers to control fundamental physiological functions in response to signal sensing (1). Among these molecules, cyclic di-3′,5′-adenosine monophosphate (c-di-AMP) is the only nucleotide messenger that must be precisely balanced since both its depletion and overproduction can be toxic (2). Its core function is to control cellular integrity by setting homeostasis of osmolytes that in many bacteria are used for osmoregulation (3, 4). Changes in external osmolarity trigger water fluxes across the membrane, which can lead to cell dehydration or swelling and, finally, collapse or burst when osmobalance mechanisms fail to respond properly (5). As a key component of these mechanisms, c-di-AMP directly targets transport systems for osmoactive and osmoprotective substances such as potassium ions and low-molecular-weight compatible solutes in many bacteria (6–10).

c-di-AMP also plays a central role in host–pathogen interactions and bacterial virulence (11). Secreted c-di-AMP is recognized by hosts' innate immunity receptors STING, DDX41, ERAdP, and RECON to regulate type I interferon immune response and NF-κB pathways, respectively (12–16). Modulation of intracellular c-di-AMP has been reported to affect virulence of *Streptococcus pyogenes* (17), *Listeria monocytogenes* (18), *Streptococcus pneumoniae* (19), and *Mycobacterium tuberculosis*. Thus, the molecule is considered an attractive antimicrobial target (20).

c-di-AMP synthesis out of two ATP molecules is catalyzed by the diadenylate cyclase (DAC) activity of the DisA_N domain (Pfam PF02457), which was identified in the structural and biochemical analysis of the DNA integrity scanning protein A (DisA) of *Thermotoga maritima* (21). DisA is mainly present in sporulating Firmicutes and Actinobacteria (22) and has a conserved domain organization consisting of an N-terminal DAC domain and a C-terminal DNA-binding helix–hairpin–helix domain separated by a linker region (21). c-di-AMP hydrolysis is mediated by the DHH-DHHA1 domain containing the Asp–His–His motif. The multidomain membrane-associated GdpP protein in *Bacillus subtilis* was the first characterized DHH-DHHA1-type phosphodiesterase (PDE) (23). In addition, HD domains, which contain a catalytic His–Asp motif and were first identified in the PgpH protein in *L. monocytogenes*, also degrade c-di-AMP (18).

Most Actinobacteria contain DisA for c-di-AMP synthesis; however, the majority of them do not encode DHH-DHHA1 domain–containing or HD-type c-di-AMP PDEs. Hence, we wondered how actinomycetes balance intracellular c-di-AMP levels. Within Actinobacteria, *Streptomyces* are the most extensively studied mycelial organisms and the richest natural source of antibiotics (24). For growth and reproduction, *Streptomyces* undergo a complex developmental life cycle, which involves the conversion between three morphologically and physiologically distinct forms of cell existence. During exponential growth, they proliferate by extension and branching of vegetative hyphae. The switch to the stationary phase and onset of the reproductive phase are marked by the erection of aerial hyphae. These filaments

Significance

Bacteria use the nucleotide cyclic di-3′,5′-adenosine monophosphate (c-di-AMP) for adaptation to changing environments and host–pathogen interactions. Enzymes for nucleotide synthesis and degradation and proteins for binding of the second messenger are key components of signal transduction pathways. It was long unknown how the majority of Actinobacteria, one of the largest bacterial phyla, stop c-di-AMP signals and which proteins bind the molecule to elicit cellular responses. Here, we identify a c-di-AMP phosphodiesterase that bacteria evolved to terminate c-di-AMP signaling and a protein that forms a complex with c-di-AMP in *Streptomyces*. We also demonstrate that balance of c-di-AMP is critical for developmental transitions from filaments to spores in multicellular bacteria.

Author contributions: A.L., D.J.D., M.M.A.-B., A.M.B., G.W., and N.T. designed research; A.L., D.J.D., M.M.A.-B., A.M.B., K.C.F., and G.W. performed research; A.L., D.J.D., M.M.A.-B., A.M.B., V.K., G.W., and N.T. analyzed data; and A.L., D.J.D., G.W., and N.T. wrote the paper.

The authors declare no competing interest.

This article is a PNAS Direct Submission.

Data deposition: Small-angle scattering data have been deposited in the Small Angle Scattering Biological Data Bank (SASBDB) with accession numbers SASDH25 (AtaC) and SASDH35 (CpeA).

[1]A.L. and D.J.D. contributed equally to this work.

[2]To whom correspondence may be addressed. Email: witte@genzentrum.lmu.de or natalia.tschowri@hu-berlin.de.

This article contains supporting information online at https://www.pnas.org/lookup/suppl/doi:10.1073/pnas.1917080117/-/DCSupplemental.

First published March 18, 2020.

elongate and divide into unigenomic prespore compartments that ultimately mature into chains of spores. Completion of the developmental program is easily visible by eye since mature *Streptomyces* spores accumulate a spore pigment. For example, our model species, the chloramphenicol producer *S. venezuelae*, is characterized by a green spore pigment such that colonies turn green at the end of the life cycle (25, 26). Importantly, antibiotic production and morphological differentiation are coregulated in *Streptomyces*. Hence, studying their developmental biology also provides a better understanding of the control of their secondary metabolism.

In this work, we identified and characterized the PDE superfamily protein AtaC as a c-di-AMP–specific hydrolase unrelated to canonical c-di-AMP PDEs. AtaC is broadly distributed in bacteria and the only known c-di-AMP PDE in most actinomycetes. Among others, pathogens such as the causative agent of pneumonia, *S. pneumoniae*, contain an AtaC homolog that we characterize here to be a functional c-di-AMP hydrolase. Our biochemical and structural analyses show that AtaC is a monomeric Mn^{2+}-dependent PDE with high affinity for c-di-AMP. Moreover, we provide direct biochemical evidence that *Streptomyces* DisA is an active DAC and that c-di-AMP produced by DisA is crucial for survival under ionic stress conditions. Further, we show that accumulation of c-di-AMP in the *S. venezuelae ataC* mutant results in profound developmental and growth defects and report the identification of the RCK_C domain (RCK stands for regulator of conductance of K^+) containing protein CpeA as a c-di-AMP binding protein in *Streptomyces*. Overall, in this study we identified and functionally characterized core components of c-di-AMP signaling in *Streptomyces* and linked c-di-AMP regulation to ion homeostasis to control differentiation in multicellular bacteria.

Results

DisA Synthesizes c-di-AMP in *S. venezuelae*. DisA is the sole DAC protein encoded in the *S. venezuelae* genome and is conserved in all sequenced *Streptomyces* strains. To demonstrate DisA DAC activity, we purified N-terminally His-tagged DisA and an inactive $DisA_{D86A}$ that carries an alanine instead of aspartate in the active site (21). We included His-tagged *B. subtilis* DisA ($DisA_{Bsu}$) as a positive control for enzymatic activity (21). [^{32}P]-labeled ATP was added as a substrate for in vitro DAC assays, and the reactions were separated by thin-layer chromatography (TLC). DisA synthesized c-di-AMP, whereas the mutated $DisA_{D86A}$ failed, demonstrating that *S. venezuelae* DisA is a functional DAC, which requires the conserved catalytic aspartate D_{86} for activity (Fig. 1*A*).

In vivo, DisA is the major source for c-di-AMP during onset of sporulation (14 to 16 h) and the sporulation phase (18 to 20 h) (Fig. 1*B*) (27). However, we reproducibly detected low c-di-AMP levels in Δ*disA* during vegetative growth (10 and 12 h), suggesting that *S. venezuelae* might contain a non–DAC domain enzyme capable of c-di-AMP production (Fig. 1*B*). The presence of c-di-AMP throughout the wild-type *S. venezuelae* life cycle suggested that *disA* expression is constitutive. To confirm this, we complemented the *disA* mutant by chromosomal insertion of a C-terminally FLAG-tagged *disA* under control of its native promoter. Using a monoclonal anti-FLAG antibody, we detected constant DisA-FLAG expression in all developmental stages, which correlated with c-di-AMP production in the wild type under the conditions tested (Fig. 1*C* and *SI Appendix*, Fig. S1*A*).

Altogether, our data show that DisA is a functional DAC in vitro and in vivo and the major enzyme for c-di-AMP production during *S. venezuelae* sporulation.

The Phosphodiesterase Superfamily Protein AtaC (Vnz_27310) Degrades c-di-AMP. Streptomycetes do not possess PDEs with a DHH-DHHA1 domain or a PgpH-type HD domain, known to degrade c-di-AMP in other bacteria (18, 23), raising the question of how

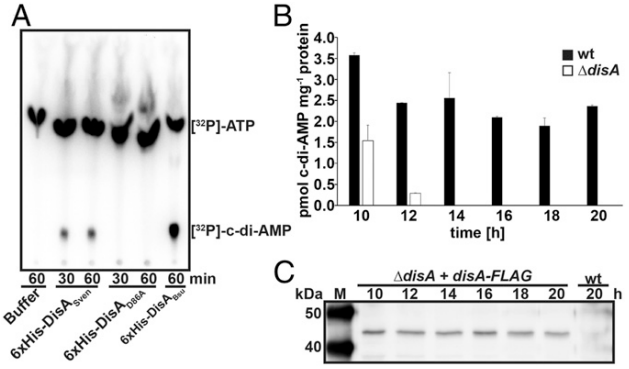

Fig. 1. DisA is an active diadenylate cyclase in vitro and in vivo. (*A*) TLC of DAC assay with purified 6xHis-$DisA_{Sven}$ and 6xHis-$DisA_{D86A}$ and [^{32}P]-ATP as the substrate. Migration of [^{32}P]-ATP in buffer is shown in lane 1. 6xHis-$DisA_{Bsu}$ served as a positive control for DAC activity. (*B*) Intracellular c-di-AMP levels in *S. venezuelae* wild type (wt) and Δ*disA* during late vegetative growth (10 to 12 h), early sporulation (14 to 16 h), and sporulation (18 to 20 h). Data are presented as the mean of biological replicates ± SD ($n = 3$). (*C*) Expression profile of DisA-FLAG in a *disA* mutant complemented with *disA-FLAG* under the control of the *disA* promoter grown in liquid sporulation medium (MYM). DisA-FLAG was detected using a monoclonal anti-FLAG antibody. Wild type served as a negative control.

S. venezuelae removes c-di-AMP from the cytoplasm. To find a potentially novel c-di-AMP PDE, we used interproscan (28) to search for Pfam PF01663, which is associated with putative type I phosphodiesterases/nucleotide pyrophosphatases. Among others, we found two proteins (Vnz_27310 and Vnz_31010) belonging to the phosphodiesterase and metallophosphatase superfamilies, respectively, that we selected for in vitro PDE activity tests.

Purified N-terminally His-tagged Vnz_27310 and Vnz_31010 were assayed in vitro using [^{32}P]-labeled c-di-AMP as a substrate. While we could not detect [^{32}P]-c-di-AMP cleavage activity for Vnz_31010, Vnz_27310 clearly degraded c-di-AMP to 5′-pApA and finally to AMP (Fig. 2*A*), so that we named Vnz_27310 AtaC for actinobacterial PDE targeting c-di-AMP. The addition of unlabeled c-di-AMP but not of c-di-GMP or cAMP competed with [^{32}P]-c-di-AMP and led to reduced cleavage of the radiolabeled substrate, showing specificity for c-di-AMP (Fig. 2*A*). We analyzed the kinetics of c-di-AMP hydrolysis activity of AtaC using anion exchange chromatography assays and determined a catalytic rate constant (k_{cat}) of 0.2 s^{-1} (*SI Appendix*, Fig. S2 *A* and *B*), while only a negligible c-di-GMP hydrolysis activity was detected (*SI Appendix*, Fig. S2*C*). We also compared AtaC-dependent hydrolysis of the linear dinucleotides 5′-pApG and 5′-pGpG to the hydrolysis of 5′-pApA and observed a high hydrolysis activity for 5′-pApA ($k_{cat} = 2.1\ s^{-1}$), whereas the other substrates tested were only degraded to a small extent (Fig. 2*B* and *SI Appendix*, Fig. S2 *D*–*F*).

Using the PATRIC database (https://www.patricbrc.org), we examined the distribution of the here discovered c-di-AMP PDE (PGF_00172869) and found at least 5,374 prokaryotic species containing homologs to AtaC (Dataset S1), including pathogens such as *S. pneumoniae* and *M. tuberculosis*. AtaC from *S. pneumoniae* ($AtaC_{Spn}$; sequence ID: CVN04004.1) and from *M. tuberculosis* ($AtaC_{Mtu}$; sequence ID: CNE38097.1) share 41 and 47%, respectively, identical residues with AtaC from *S. venezuelae*. In agreement with the high degree of protein identity, enzyme assays data shown in Fig. 2*C* demonstrate that $AtaC_{Spn}$ is a PDE that hydrolyzes c-di-AMP and $AtaC_{Mtu}$ likely has the same function.

In summary, we identified and functionally characterized a c-di-AMP hydrolase in *Streptomyces* and a c-di-AMP signaling component in pathogens and showed that AtaC is a conserved

MICROBIOLOGY

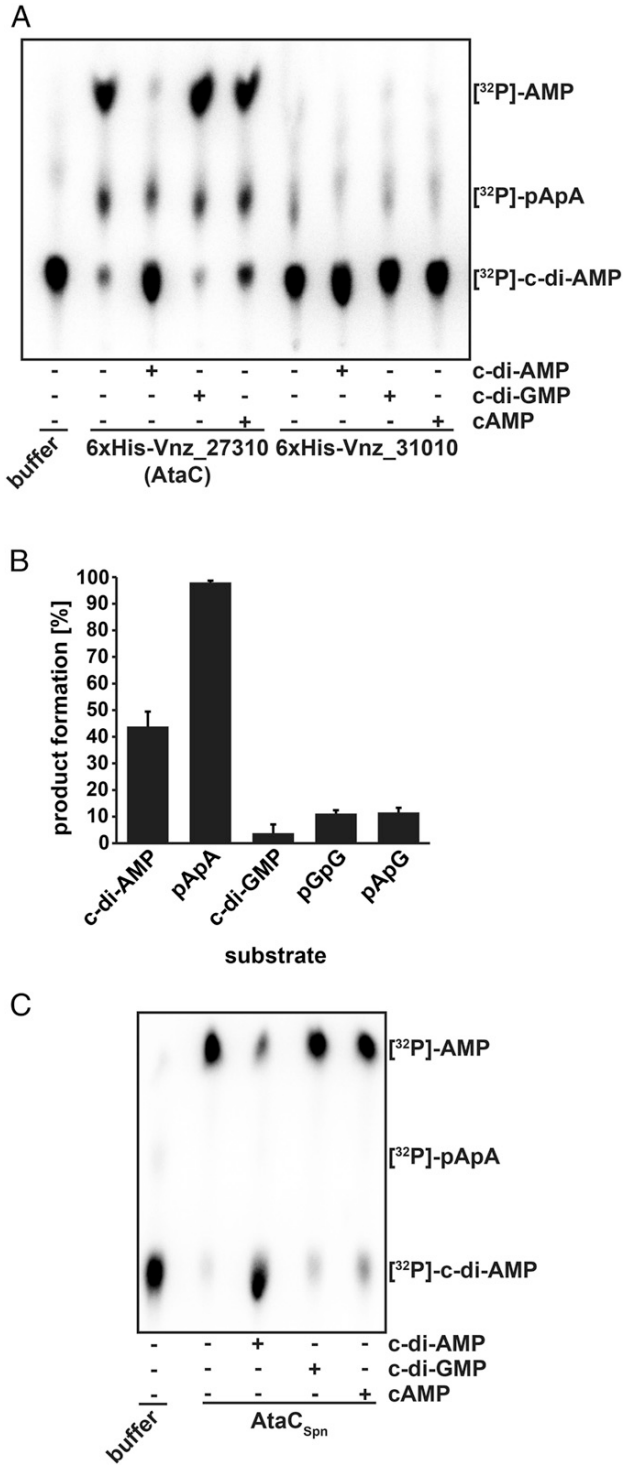

Fig. 2. AtaC is a c-di-AMP-specific PDE. TLC of the PDE assay of AtaC and Vnz_31010 from *S. venezuelae* (*A*) and *S. pneumoniae* ($AtaC_{Spn}$) (*C*) with [^{32}P]-c-di-AMP. Radioactively labeled c-di-AMP in buffer migrates as shown in lane 1. In samples used for competition, unlabeled c-di-AMP, c-di-GMP, or cAMP (indicated by +) were added in excess before starting the reaction with [^{32}P]-c-di-AMP. (*B*) AtaC activity assay by ion exchange chromatography runs on a 1 mL Resource Q column of the reaction products after 1 h incubation from 100 µL reactions containing 100 nM AtaC + 250 µM c-di-AMP, 5′-pApA, c-di-GMP, 5′-pGpG, or 5′-pApG ($n = 3$).

phosphodiesterase that efficiently and specifically hydrolyzes c-di-AMP to AMP via the intermediate 5′-pApA.

AtaC Is a Monomeric Mn^{2+}-Dependent Phosphodiesterase. To further characterize the c-di-AMP hydrolysis mechanism of AtaC and to gain some structural insights into this PDE, we used HHpred (29) and found two close structural homologs. The core domain of a phosphonoacetate hydrolase (PhnA) from *Sinorhizobium meliloti* 1021 (ref. 30 and Protein Data Bank [PDB] code 3SZY) showed the highest similarity and served as a template for the structural model of AtaC including the putative active site. The predicted active site comprises three aspartates (D68, D227, and D269), three histidines (H231, H270, and H384), and one threonine (T108) (Fig. 3*A*).

Our size exclusion chromatography (SEC) coupled multiangle laser light scattering data show that AtaC is a monomer in solution with a determined molecular weight of 43.7 kDa (*SI Appendix*, Fig. S3*A*). The calculated ab initio shape of AtaC from SEC-SAXS (size exclusion coupled small-angle X-ray scattering) data superimposes well with the HHpred model structure (Fig. 3*B*), and the measured SAXS curve of AtaC is similar to the theoretical scattering curve of our AtaC model (*SI Appendix*, Fig. S3 *B–D*), indicating that AtaC and PhnA have a similar shape in solution.

The enzymatic reaction of the PhnA-class hydrolases is known to be catalyzed by two metal ions in the active site (30), so we tested the metal binding for AtaC by thermal unfolding assays using a nano differential scanning fluorimetry (nanoDSF) assay and observed protein stabilization upon addition of manganese ions (Mn^{2+}) (Fig. 3*C*). Based on the structural similarity to PhnA, we identified potential metal-binding residues in AtaC and generated a variant, $AtaC_{D269N}$, that we expected to lack Mn^{2+} coordination but retain nucleotide binding, as shown for DHH-DHHA1-type PDEs (23, 31). nanoDSF data confirmed the stability of $AtaC_{D269N}$ with a melting temperature comparable to the wild-type protein when incubated with ethylenediaminetetraacetic acid (EDTA) (Fig. 3*D*). Moreover, $AtaC_{D269N}$ behaved identically to the wild-type protein during purification and final SEC. In line with our predictions, $AtaC_{D269N}$ failed to bind Mn^{2+} (Fig. 3*E*) and did not hydrolyze c-di-AMP, as shown using ion exchange chromatography-based assays (*SI Appendix*, Fig. S4*A*). However, $AtaC_{D269N}$ was still capable of c-di-AMP binding, as confirmed by nanoDSF experiments that showed a shift in the melting curve with increasing ligand concentration (Fig. 3*F*). Using isothermal titration calorimetry (ITC) analysis, we determined the dissociation constant (K_D) of $AtaC_{D269N}$ for c-di-AMP to be 949 ± 360 nM, whereas binding of c-di-GMP could not be detected (Fig. 3 *G* and *H* and *SI Appendix*, Fig. S4*B*).

Altogether, our combined structural analysis and biochemical data strongly suggest that AtaC uses a similar metal ion-dependent mechanism as its structural homolog PhnA for substrate cleavage.

AtaC Hydrolyzes c-di-AMP In Vivo. We quantified c-di-AMP in cell extracts isolated from wild-type *S. venezuelae* and the *ataC* null mutant using liquid chromatography tandem mass spectrometry (LC-MS/MS). Our data show that c-di-AMP levels are elevated in the *ataC* mutant during all developmental stages when compared to the wild type, demonstrating that AtaC degrades c-di-AMP in vivo and thus is an important component of c-di-AMP metabolism in *S. venezuelae* (Fig. 4*A*). Western blot analysis showed that AtaC levels slightly increase during the life cycle (Fig. 4*B* and *SI Appendix*, Fig. S1*B*).

Inactivation of AtaC Delays *S. venezuelae* Development. To investigate the physiological functions of *disA* and *ataC* and thus of c-di-AMP in *S. venezuelae*, we first analyzed the developmental phenotypes of mutant strains. Colonies of *S. venezuelae* Δ*disA*

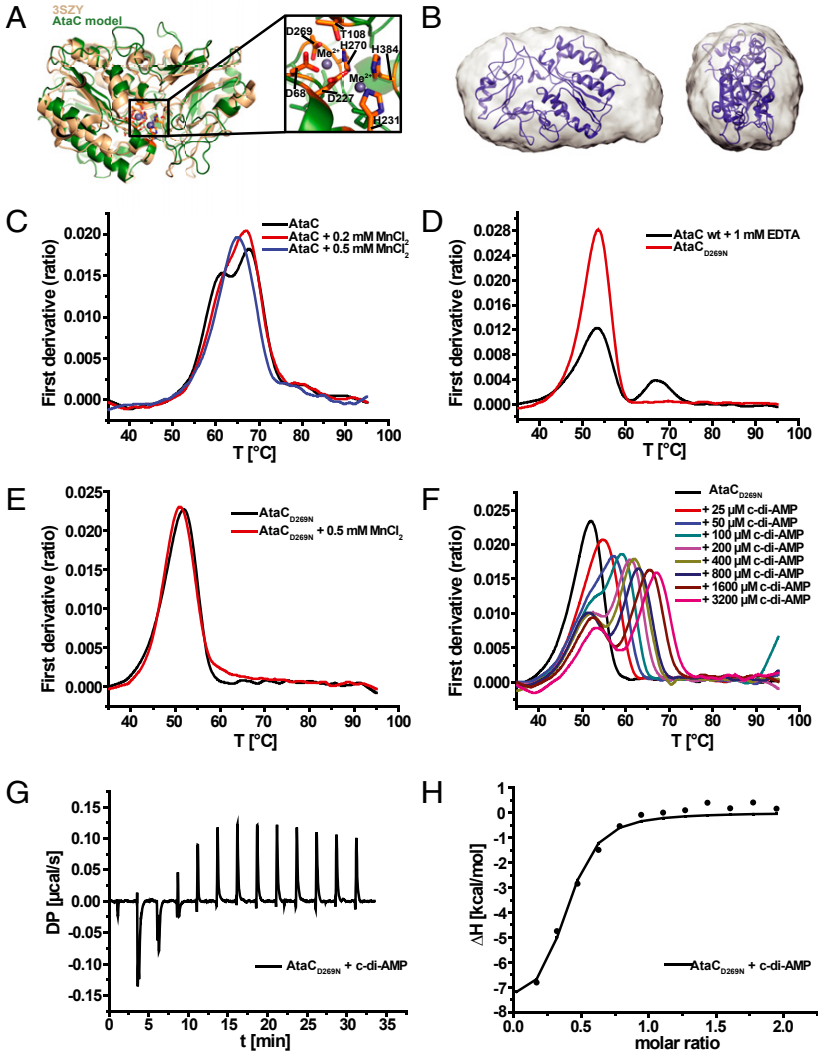

Fig. 3. AtaC is a monomeric Mn^{2+}-dependent PDE. (*A*) Model of AtaC obtained from HHpred/MODELER (green) superimposed with best-match 3SZY (beige). The close-up shows the predicted active site, annotated with all of the most conserved residues. (*B*) Modeled structure from *A* superimposed with the final averaged and filtered ab initio shape (16 ab initio models averaged) from SEC-SAXS with the front view (*Left*) and side view (*Right*). (*C*) nanoDSF thermal shift first-derivative curves of 10 μM apo AtaC (black), 10 μM AtaC + 0.2 mM $MnCl_2$ (red), and 10 μM AtaC + 0.5 mM $MnCl_2$ (blue). (*D*) nanoDSF thermal shift first-derivative curves of 10 μM AtaC + 1 mM EDTA (black) and 10 μM $AtaC_{D269N}$ (red). (*E*) nanoDSF thermal shift first-derivative curves of 10 μM $AtaC_{D269N}$ (black) and $AtaC_{D269N}$ + 0.5 mM $MnCl_2$ (red). (*F*) nanoDSF thermal shift first-derivative curves of 10 μM $AtaC_{D269N}$ + c-di-AMP (25 to 3,200 μM). (*G*) ITC measurement raw data of 23 μM $AtaC_{D269N}$ mutant titrated with 231 μM c-di-AMP. (*H*) Binding curve and fit of ITC titration of the $AtaC_{D269N}$ mutant with c-di-AMP (K_D = 949 ± 360 nM; n = 3).

became green (Fig. 5*A*), and scanning electron microscopy (SEM) confirmed that the *disA* mutant produced spore chains with morphology identical to those of the wild type (Fig. 5*B*). Thus, neither the DisA protein nor the c-di-AMP produced by DisA is required for differentiation.

In contrast, the *ataC* mutant showed a severe delay in development. After 4 d, the Δ*ataC* strain developed aerial hyphae but did not turn green like the wild type (Fig. 5*A*), and SEM imaging showed mainly undifferentiated aerial hyphae, in contrast to the fully sporulated hyphae seen in the wild type (Fig. 5*B*). Moreover, many of the aerial hyphae of the *ataC* mutant had lysed. After extended incubation (7 d), the aerial hyphae of the *ataC* mutant had largely sporulated, with sporadic nondifferentiated and lysed filaments still detected (Fig. 5*B*).

The lysed hyphae seen in the SEMs led us to analyze the growth of the Δ*ataC* strain in liquid maltose–yeast extract–malt extract (MYM) medium. As shown in Fig. 5*C*, the *ataC* mutant grew slower than the wild type in the exponential phase but reached a similar final optical density at 578 nm after 20 h. Notably, deletion of *disA* had no effect on growth (Fig. 5*C*). Using a heat resistance assay, we found that neither spores formed by the *ataC* mutant nor those produced by Δ*disA* and $disA_{D86A}$ strains were defective in spore viability (*SI Appendix*, Fig. S5*A*).

We could fully complement the defects of Δ*ataC* in development and growth by introduction of the *ataC* wild-type allele under the control of its native promoter from the pIJ10770 vector (32) that integrates into the chromosomal $attB_{\phi BT1}$ site (Fig. 5 *A* and *C* and *SI Appendix*, Fig. S5*B*). In contrast, expression of $ataC_{D269N}$, which cannot cleave c-di-AMP (*SI Appendix*, Fig. S4*A*) from the same integrative vector, did not restore the developmental defects caused by *ataC* deletion (Fig. 5*A*), showing that the cleavage of c-di-AMP by AtaC is crucial for normal development of *Streptomyces*.

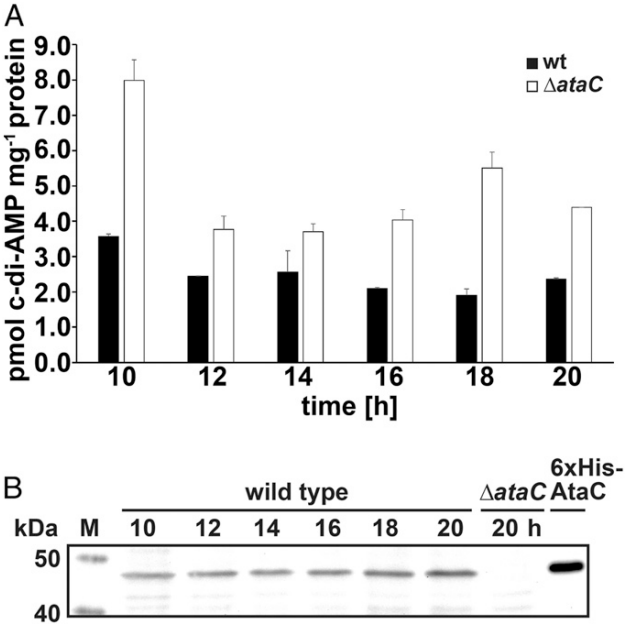

Fig. 4. AtaC hydrolyzes c-di-AMP in vivo and is expressed during the life cycle of *S. venezuelae*. (*A*) Intracellular c-di-AMP levels in *S. venezuelae* wild type and Δ*ataC* during late vegetative growth (10 to 12 h), early sporulation (14 to 16 h), and sporulation (18 to 20 h). Data are presented as the mean of biological replicates ± SD ($n = 3$). (*B*) Expression profile of AtaC in *S. venezuelae* wild type grown in a liquid sporulation medium (MYM). AtaC was detected using a polyclonal anti-AtaC antiserum. Protein samples harvested from Δ*ataC* served as negative control. Purified 6xHis-AtaC served as the positive control.

Altogether, these results demonstrate that elevated levels of c-di-AMP impair growth and development, whereas reduced levels of c-di-AMP do not affect differentiation under standard growth conditions.

The *disA* Mutant Is More Susceptible to Ionic Stress. Since regulation of osmotic balance is a major function of c-di-AMP in many bacteria (3), we next investigated the osmotic stress resistance of strains with altered c-di-AMP levels due to mutations in either *ataC* or *disA*. We spotted serially diluted spores on nutrient agar (NA) medium plates supplemented with 0.5 M NaCl and a control plate without extra added NaCl. On both plates, growth of the Δ*ataC* strain was slightly impaired, resulting in smaller colony size compared to the wild type (Fig. 5*D*). This phenotype reflects the growth defect of the mutant (Fig. 5*C*) and could be complemented by expression of the wild-type allele from pIJ10770 (Fig. 5*D*).

In contrast, when grown on NA plates containing 0.5 M NaCl, Δ*disA* and $disA_{D86A}$ showed pronounced reduction in growth. Expression of wild-type *disA* from pIJ10770 fully complemented the growth defect of Δ*disA* (Fig. 5*D*). The identical Δ*disA* and $disA_{D86A}$ phenotypes demonstrate that c-di-AMP produced by DisA is crucial for osmotic stress resistance in *S. venezuelae* (Fig. 5*D*).

In summary, our data revealed that accumulation of c-di-AMP due to *ataC* inactivation delays development and slows down *Streptomyces* growth in the exponential phase. On the other hand, depletion of c-di-AMP due to *disA* inactivation renders *S. venezuelae* highly susceptible to ionic stress.

The RCK_C Domain Protein CpeA (Vnz_28055) Binds c-di-AMP. RCK_C domains are established direct targets of c-di-AMP that have the $(I/L)(I/L)X_2DX_1RX_5N(I/L)(I/L)$ signature for ligand binding (Fig. 6*A*) (33). We found the RCK_C domain protein CpeA (Vnz_28055) with a putative c-di-AMP binding motif (Fig. 6*A*) in 93 *Streptomyces* species for which complete genome sequences are available (34). We purified N-terminally His-tagged CpeA and applied differential radial capillary action of ligand assays (DRaCALA) to probe interaction between CpeA and c-di-AMP. DRaCALA allows visualization of protein-bound radiolabeled ligand as a concentrated spot or ring after the application of the protein-ligand mixture onto nitrocellulose (35). With this assay, we confirmed that CpeA binds [^{32}P]-labeled c-di-AMP (Fig. 6*B*).

In competition experiments, we found that unlabeled c-di-AMP interfered with binding of [^{32}P]-c-di-AMP to CpeA, while excess of c-di-GMP, cAMP, 5′-pApA, or ATP still allowed [^{32}P]-c-di-AMP-CpeA complex formation (Fig. 6*B*). NanoDSF analysis revealed that addition of c-di-AMP in the micromolar range significantly increased the melting point of CpeA. In contrast, high concentrations of other nucleotides such as 5′-pApA, ATP, AMP, or cAMP were needed for CpeA stabilization to the same extent, and c-di-GMP even destabilized the protein (Fig. 6*C* and *SI Appendix*, Fig. S6). Taken together, these data indicate that CpeA specifically binds c-di-AMP. To determine the K_D, we analyzed c-di-AMP binding through surface plasmon resonance (SPR) assays. Since we faced protein instability problems during CpeA coupling to the chip and using ITC, we applied biotinylated c-di-AMP on chip and CpeA as a ligand in SPR analysis. We determined a K_D of 37 μM, probably reflecting an upper limit for the K_D as the biotin at the 2′-OH of the ribose moiety likely interferes with binding of c-di-AMP to CpeA (*SI Appendix*, Fig. S7*A*). SAXS and static light scattering experiments showed that CpeA is a stable dimer in solution and does not dissociate at concentrations down to 260 nM, as observed in analytical size exclusion chromatography (*SI Appendix*, Fig. S7 *B–E*), independent of the presence of c-di-AMP. In summary, we could identify CpeA as a c-di-AMP binding protein in the genus *Streptomyces*.

cpeA forms a conserved operon with *cpeB (vnz_28050)*. Some *Streptomyces* species, such as *S. venezuelae*, contain the small open reading frame *cpeC (vnz_28045)* in the same operon (Fig. 6*D*). CpeB is a structural homolog of the sodium/proton antiporter NapA (PDB code 5BZ3_A) from *Thermus thermophilus* (36), as predicted with 100% probability using HHpred (29). To test whether CpeA and CpeB form a functional interacting unit, we used a bacterial two-hybrid system in which an interaction between bait and target proteins reconstitutes a functional adenylate cyclase (Cya) that allows the *Escherichia coli cya* mutant to utilize maltose as a carbon source (37). We found that CpeA and CpeB form a complex (Fig. 6*E*). The interaction between these two proteins was strongly enhanced when enzymatically active DisA-FLAG was coexpressed, while coexpression of the inactive $DisA_{D86A}$-FLAG variant had no effect (Fig. 6*E*), demonstrating that c-di-AMP produced by DisA stimulates CpeA-CpeB interaction. These data are consistent with our model that c-di-AMP controls ion transport activity of CpeB by stimulating complex formation with the regulatory unit, CpeA. Thus, we renamed Vnz_28055-28045 to CpeABC for cation proton exchange components A, B, and C. However, c-di-AMP–dependent cation flux via CpeB remains to be proven.

Discussion

In this work, using the chloramphenicol producer *S. venezuelae* as a model and a combination of bioinformatic, biochemical, structural, and genetic analyses, we identified AtaC as a c-di-AMP–specific PDE. AtaC is widely distributed in bacteria and represents the only c-di-AMP PDE in the majority of Actinobacteria and a c-di-AMP signaling component in pathogens, such as *S. pneumoniae* (Fig. 2 and Dataset S1).

AtaC is a soluble, single-domain phosphodiesterase superfamily protein that is monomeric in solution (*SI Appendix*, Fig.

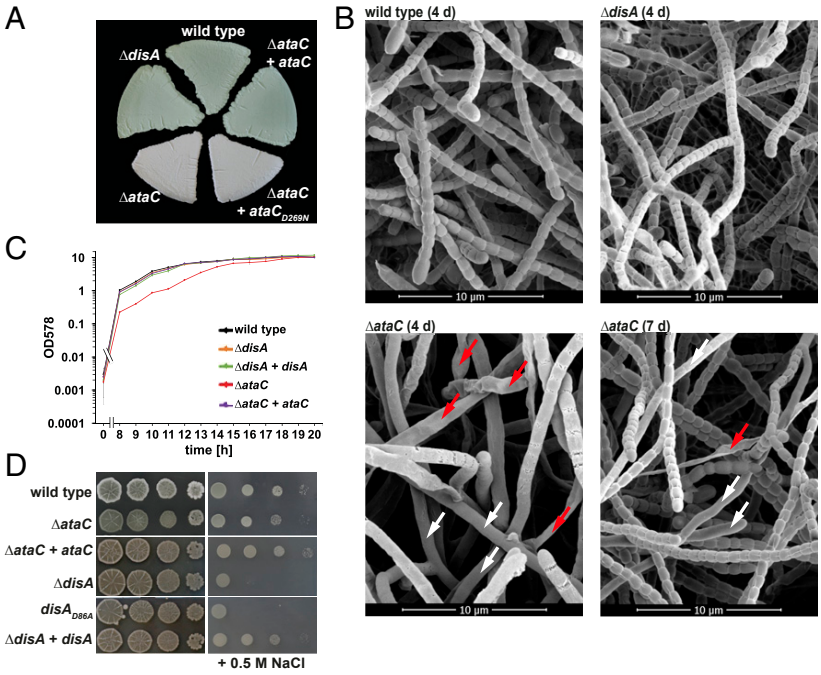

Fig. 5. Mutagenesis of c-di-AMP-metabolizing enzymes impacts development and ionic stress resistance in *S. venezuelae*. (*A*) Green morphologies of *S. venezuelae* wild type and Δ*disA* indicate the formation of mature spores after 4 d of growth at 30 °C on a solid sporulation medium (MYM agar). *S. venezuelae* Δ*ataC* failed to accumulate the spore pigment and remained white after the same incubation time. The wild-type *ataC* allele complements the phenotype of Δ*ataC*, while the enzymatically inactive variant *ataC*$_{D269N}$ does not. (*B*) Scanning electron micrographs showing that after 4 d of incubation on MYM, *S. venezuelae* wild type and Δ*disA* formed spores, but Δ*ataC* consisted predominantly of nonsporulating aerial hyphae (white arrows) and formed flat, likely lysed hyphae (red arrows). After 7 d of growth, Δ*ataC* produced wild-type–like spore chains, but occasional nondifferentiated and lysed hyphae were still detectable. (*C*) Deletion of *ataC* leads to a growth defect in *S. venezuelae*. c-di-AMP mutants were grown in a liquid sporulation medium (MYM) at 30 °C, and optical density was measured at 578 nm. Δ*ataC* growth is delayed by 3 h and can be restored by expression of the wild-type allele under the control of its native promoter from the *attB*$_{\phi BT1}$ site. (*D*) Osmotic stress resistance of c-di-AMP mutants. Serial dilutions of spores were spotted on NA without additional salt or supplemented with 0.5 M NaCl and grown at 30 °C for ∼2 d. Δ*disA* and *disA*$_{D86A}$ (expressing inactive DisA) are hypersensitive to salt stress.

S3). In solution, AtaC is structurally similar to the alkaline phosphatase superfamily domain of the C–P bond-cleaving enzyme PhnA from *S. meliloti* 1021 (Fig. 3*A*) (30). As described for DHH-DHHA1 domain-containing proteins GdpP and DhhP and the HD domain PDE PgpH, AtaC binds Mn^{2+} to hydrolyze c-di-AMP, and we showed that residue D269 participates in metal ion coordination and is crucial for hydrolysis activity (Fig. 3 *C*–*E*) (18, 23, 38). AtaC has a k_{cat} of 0.2 s^{-1}, which is comparable to the reported k_{cat} of GdpP (0.55 s^{-1}). Hydrolytically inactive $AtaC_{D269N}$ has a dissociation constant of 0.9 µM, which is highly similar to the K_D of wild-type PgpH (0.3 to 0.4 µM) (Fig. 3 *G* and *H*) (18, 23). Since we determined the AtaC dissociation constant using a protein carrying the D269N mutation lacking Mn^{2+} coordination, the K_D value represents an upper limit as the metal ions bound by the wild-type protein likely contribute to protein stability and c-di-AMP binding. However, while PgpH- and GdgP-type PDEs hydrolyze c-di-AMP exclusively to the linear 5′-pApA, AtaC cleaves c-di-AMP and the intermediate product 5′-pApA to AMP, which has also been shown for some DhhP-type PDEs (Fig. 2 *A* and *B* and *SI Appendix*, Fig. S2 *A*, *B*, and *D*) (18, 23, 38). The substrate specificity of AtaC is strictly dependent on two adenosine bases as it shows only weak hydrolysis activity for 5′-pApG and 5′-pGpG, in contrast to the DhhP-type PDE TmPDE, which does not distinguish between different nucleobases (Fig. 2*B* and *SI Appendix*, Fig. S2 *E* and *F*) (31).

In *Streptomyces*, AtaC and the DAC DisA are important regulators of c-di-AMP (Figs. 1*B* and 4*A*). On standard growth medium, elevation of intracellular c-di-AMP in Δ*ataC* interferes with growth and ordered hyphae-to-spores transition, while reduction of the second messenger in Δ*disA* does not have any noticeable consequences on these cell functions. On the other hand, when incubated at high external NaCl concentrations, Δ*disA* is severely inhibited in growth, whereas Δ*ataC* grows similarly to the wild type (Fig. 5), indicating that c-di-AMP stimulates an osmoprotective function. We found that the RCK_C domain protein CpeA binds c-di-AMP and that ligand binding induces interaction between CpeA and CpeB, a structural homolog of the Na^+/H^+ antiporter NapA from *T. thermophilus* and a member of the large monovalent cation/proton antiporter (CPA) superfamily (36) (Fig. 6). Na^+/H^+ antiporters exist in all living cells, where they regulate intracellular pH, sodium levels, and cell volume (39). In some bacteria, Na^+/H^+ antiporters use the proton motive force to extrude sodium out of the cell and are activated at alkaline pH (40). However, in *Staphylococcus aureus*, the CPA family transporter CpaA has a cytosolic RCK_C domain that binds c-di-AMP to regulate transport activity (6, 41). Similarly, the regulatory RCK_C domain proteins KtrA and KtrC bind c-di-AMP to control the activity of the corresponding potassium transport units KtrB and KtrD, respectively (33). Thus, in agreement with this general concept and our data, we propose that c-di-AMP sensed by the regulatory RCK_C domain protein CpeA induces CpeA-CpeB complex formation to activate sodium export via CpeB in *Streptomyces*. At low c-di-AMP, CpeB is presumably inactive, allowing accumulation of toxic Na^+ ions in the cell and leading to growth defects of Δ*disA* on NaCl-containing medium. However, on the other hand, likely constant activity of CpeB at high c-di-AMP in Δ*ataC* may result in continuous proton influx affecting

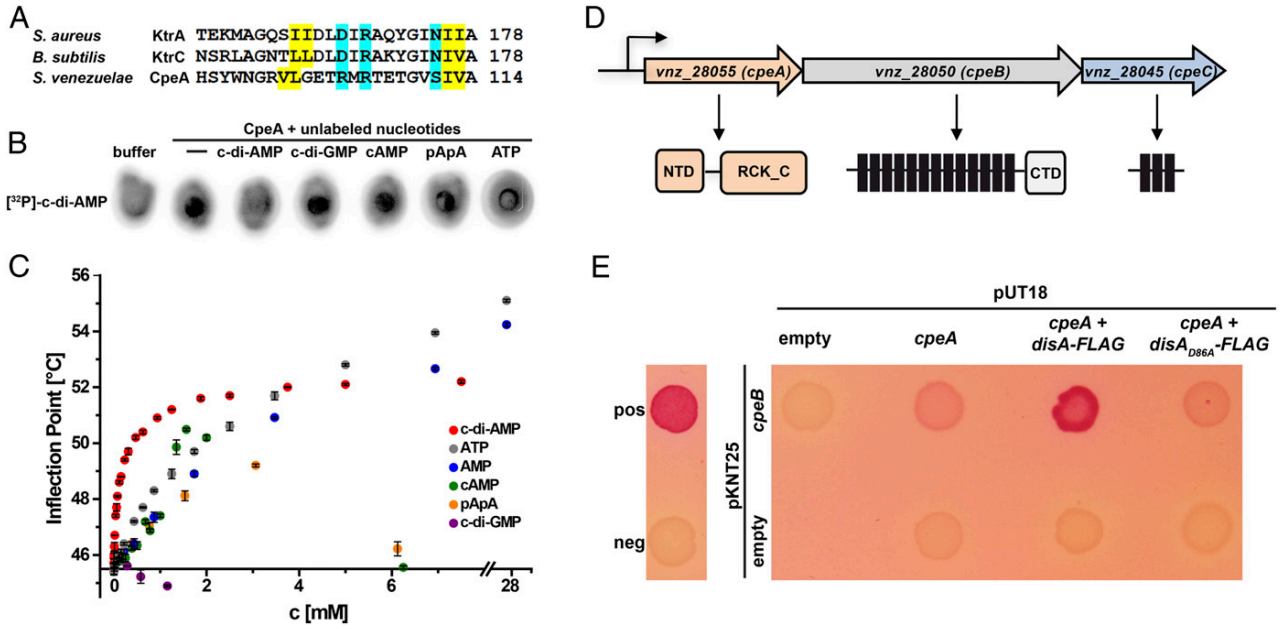

Fig. 6. CpeA (Vnz_28055) binds c-di-AMP and interacts with CpeB (Vnz_28050) in a c-di-AMP-stimulating manner. (*A*) Alignment of the c-di-AMP binding regions in RCK_C domains was generated using Clustal Omega (49). C-di-AMP binding residues in KtrA (*S. aureus*; ref. 50), KtrC (*B. subtilis*; ref. 51), and conserved amino acids in CpeA are highlighted. Amino acids that form the hydrophobic patch are shown in yellow; residues involved in hydrophilic coordination are highlighted in cyan. (*B*) CpeA binds [^{32}P]-c-di-AMP in DRaCALAs. Binding of the radiolabeled ligand is indicated by dark spots centered on the nitrocellulose. In competition assays, excess (100 μM) of unlabeled c-di-AMP, c-di-GMP, cAMP, 5′-pApA, or ATP was added to the binding reaction containing [^{32}P]-c-di-AMP and 6xHis-CpeA. (*C*) Inflection points from nanoDSF thermal shift assays of 20 μM CpeA with different concentrations of c-di-AMP, ATP, AMP, cAMP, 5′-pApA, and c-di-GMP (0 to 10 mM) at a heating rate of 1.5 K/min. Shown are mean values of $n = 3$ independent experiments with SD. (*D*) *cpeA (vnz_28055), cpeB (vnz_28050)* and *cpeC (vnz_28045)* form an operon in *S. venezuelae*. CpeA has an N-terminal domain (NTD) of unknown function and a C-terminal RCK_C domain. CpeB is a predicted structural homolog of the Na^+/H^+ antiporter NapA (36). It consists of 13 transmembrane (TM) domains and a cytosolic fraction at the C terminus (CTD). CpeC is a predicted membrane protein with 3 TM domains. (*E*) Adenylate cyclase–based two-hybrid assays revealing that CpeA and CpeB interact in vivo and that c-di-AMP production by coexpressed DisA-FLAG stimulates protein–protein interaction. Using pKNT25 and pUT18, the T25 and T18 fragments of adenylate cyclase were attached to the C termini of CpeB and CpeA, respectively. *disA-FLAG* and *disA$_{D86A}$-FLAG* were expressed from pUT18-*cpeA*. The leucin zipper part of the yeast GCN4 protein was used as a positive control. Spotted cotransformants were grown for 24 h at 26 °C.

intracellular pH and thus important cellular functions, causing growth and developmental defects.

In summary, in this study we identified AtaC as a component of c-di-AMP metabolism in bacteria and uncovered CpeA as a potential link between c-di-AMP and ion balance in *Streptomyces*. In nature, these bacteria primarily inhabit the upper layer of the soil, where they often face fluctuating osmotic conditions through desiccation and rainfall. The c-di-AMP pathway described here is likely crucial for adaptation in such a challenging ecosystem.

Materials and Methods

For a full explanation of the experimental protocols, see Extended Experimental Procedures in *SI Appendix*.

Bacterial Strains and Plasmids. All strains, plasmids, and oligonucleotides used in this study are listed in *SI Appendix*, Table S1. Plasmids and strains were constructed as described in *SI Appendix*.

Protein Overexpression and Purification. *E. coli* BL21 (DE3) pLysS and Rosetta (DE3) were used for protein overexpression. Cultures were grown in the presence of required antibiotics at 37 °C and induced with isopropyl-β-D-thiogalactopyranosid (IPTG) in the logarithmic phase and transferred for growth at 16 °C overnight. Strains overexpressing 6xHis-AtaC, 6xHis-AtaC$_{D269N}$, 6xHis-Vnz_31010, and 6xHis-AtaC$_{Spn}$ were supplemented with $MnCl_2$ (18). Cultures were harvested and lysed using a French press, and the proteins were purified via nickel–nitrilotriacetic acid (Ni-NTA) chromatography. 6xHis-DisA variants and 6xHis-CpeA were dialyzed twice in DisA cyclase buffer (ref. 42 and *SI Appendix*), and tested PDEs were dialyzed twice in PDE buffer (*SI Appendix*) with 5 to 10% glycerol (18) at 4 °C. Dialyzed proteins were stored at −20 °C. For characterization of biophysical properties of 6xHis-AtaC and 6xHis-AtaC$_{D269N}$, the protein elution was concentrated prior to size exclusion chromatography, flash frozen in liquid nitrogen, and stored at −80 °C.

Biochemical Characterization of DisA and AtaC Variants. Biochemical assays using radioactive-labeled substrates were conducted as described in ref. 34. For DAC assays, 5 μM 6xHis-tagged DisA$_{Sven}$, DisA$_{D86A}$, or DisA$_{Bsu}$ were incubated with 83 nM [^{32}P]-ATP (Hartmann Analytic) in DisA cyclase buffer. For PDE assays, 100 nM 6xHis-AtaC or 8 μM 6xHis-Vnz_31010 were mixed with 2 nM [^{32}P]-c-di-AMP (Hartmann Analytic, synthesized using purified 6xHis-DisA$_{Bsu}$) in PDE buffer. For competition, 100 μM unlabeled c-di-AMP, c-di-GMP, or cAMP were added on ice prior to starting the PDE reactions with [^{32}P]-c-di-AMP.

Alternatively, enzymatic activity of 6xHis-AtaC and 6xHis-AtaC$_{D269N}$ was detected by separation of nonlabeled reaction products by anion exchange chromatography as described in ref. 31. Reaction solutions contained 50 mM Tris (pH = 7.5), 20 mM NaCl, 100 μM $MnCl_2$, 62.5 to 2,000 μM ligand (c-di-NMP, 5′-pNpN; N = A or G), and 100 nM to 10 μM of 6xHis-AtaC and were incubated at 37 °C for 1 h. The reaction was stopped by separating the reaction products from the protein by ultrafiltration (Centricon, 30 kDa cut-off). The filtrate was diluted to 500 μL with running buffer A (50 mM Tris, pH 9) and loaded on a 1 mL Resource Q anion exchange column (GE Healthcare Life Sciences). A linear gradient to 40% running buffer B (50 mM Tris, 1 M NaCl, pH = 9) over 20 column volumes was used to separate the nucleotides. The product peaks were identified by comparison to nucleotide standards, c-di-NMP, pNpN, N = A or G, obtained from BioLog.

Differential Radial Capillary Action of Ligand Assay. DRaCALAs were performed using 5 μg of purified 6xHis-CpeA (Vnz_28055) as described in Roelofs et al. (35) with minor modifications. For competition, reactions were incubated with 42 nM [^{32}P]-c-di-AMP for 5 min at room temperature prior to addition

of 100 μM of nonlabeled nucleotides. Samples were spotted on nitrocellulose after 10 min reaction at room temperature.

Western Blotting. For detection of FLAG-tagged DisA, Western blot analysis was performed as described in ref. 34 using 5 μg total protein of *S. venezuelae* Δ*disA* expressing the FLAG-tagged *disA* allele from the Φ_{BT1} integration site under the control of the native promoter. Anti-FLAG primary antibody (Sigma) and the anti-mouse IgG-HRP (Thermo Fisher Scientific) were used for detection. AtaC was detected in the wild-type strain (10 μg total protein) using polyclonal rabbit anti-AtaC antiserum as the primary antibody (generated by Pineda GmbH using purified 6xHis-AtaC) and donkey anti-rabbit-HRP as the secondary antibody (GE Healthcare). Enhanced chemiluminescent detection reagent (Perkin-Elmer) was used for visualization.

c-di-AMP Extraction and Quantification. The nucleotide extraction protocol from ref. 2 was adapted to *Streptomyces*. Wild-type, Δ*disA*, and Δ*ataC* strains were grown in MYM. Samples for c-di-AMP extraction and for determination of the protein concentration were taken every 2 h after initial growth for 10 h. c-di-AMP was extracted using acetonitrile/methanol from cells disrupted with the BeadBlaster (Biozym). Samples were analyzed using LC-MS/MS as described in ref. 2.

Bacterial Adenylate Cyclase Two-Hybrid (BACTH) Assays. The BACTH system was used to assay c-di-AMP–dependent protein–protein interaction between CpeA and CpeB in vivo (37). Plasmids expressing C-terminal fusions of CpeA and CpeB to T18 and T25 fragments of *cyaA* from *Bordetella pertussis*, respectively, were transformed into *E. coli* W3110 lacking *cya* (43). *disA*-FLAG or $disA_{D86A}$-FLAG was introduced into the pUT18-*cpeA* plasmid directly downstream of the T18 fragment (for details see *SI Appendix*). Cotransformants were spotted on MacConkey agar supplemented with maltose (1%), ampicillin (100 μg/mL), and kanamycin (50 μg/mL). Red colonies indicate cAMP-dependent fermentation of maltose, which occurs upon direct interactions of the proteins fused to the otherwise separate adenylate cyclase domains.

Small-Angle X-Ray Scattering. Size-exclusion chromatography coupled small-angle X-ray scattering data (44, 45) for AtaC was collected at beamline P12 operated by the European Molecular Biology Laboratory (EMBL) Hamburg at the PETRA III storage ring of the Deutsches Elektronen Synchroton (DESY), Hamburg, Germany. CHROMIXS of the ATSAS Suite (46) was used for analysis and processing of the chromatogram results. In brief, after choosing an appropriate buffer region and averaging of the respective frames, the protein scattering frames from the elution peak were buffer subtracted and averaged. Buffer-corrected SEC-SAXS data and batch samples (for buffer subtraction, etc.) were analyzed using PRIMUS of the ATSAS suite. The theoretical scattering curve of the AtaC model derived from HHpred/MODELER was obtained using CRYSOL (47). Ab initio models were calculated using DAMMIF and averaged using DAMAVER as described earlier (31).

Label-Free Thermal Shift Assays (nanoDSF). Label-free thermal shift assay experiments of AtaC were performed with a Tycho NT.6 instrument (NanoTemper Technologies). The samples were heated in a glass capillary at a rate of 30 K/min, and the internal fluorescence at 330 and 350 nm was recorded. Data analysis, data smoothing, and calculation of derivatives was done using the internal evaluation features of the Tycho instrument. Thermal shift assays with CpeA were performed in a Prometheus NT.48 (NanoTemper Technologies) with a 1.5 K/min heating rate (20 °C to 95 °C) in 20 mM Tris HCl (pH = 7.5), 160 mM NaCl, 5% glycerol, and 10 mM $MgCl_2$.

Bioinformatic Characterization of AtaC and Its Abundance in Prokaryotes. AtaC was identified as a member of the phosphodiesterase family of proteins by annotation of the *S. venezuelae* genome with interproscan (version 5.27-66.0; ref. 28) and searching for proteins harboring type I phosphodiesterase/nucleotide pyrophosphatase domain (Pfam PF01663).

Scanning Electron Microscopy. SEM was performed as previously described (48).

Data Availability Statement. Small-angle scattering data have been deposited in the Small Angle Scattering Biological Data Bank (SASBDB) with accession numbers SASDH25 (AtaC; https://www.sasbdb.org/data/SASDH25) and SASDH35 (CpeA; https://www.sasbdb.org/data/SASDH35). All data discussed in the paper will be made available to readers.

ACKNOWLEDGMENTS. We are grateful to Mark J. Buttner and Fabian M. Commichau for helpful discussion and critical reading of the manuscript and thank Matt Bush for technical support with scanning electron micrographs. We thank the staff of the EMBL Hamburg beamline P12 at PETRA3 (EMBL/DESY, Hamburg, Germany) for outstanding scientific support. We also acknowledge Anna-Lena Hagemann and Annette Garbe for technical support with LC-MS/MS funded by the Deutsche Forschungsgemeinschaft (DFG) Priority Program SPP 1879 (Grant KA 730/9-1). We acknowledge the use of the Prometheus instrument in the Bioanalytics unit of the Ludwig-Maximilians-Universität München Biocenter and discussions with Franziska Tippel and Beate Kern (NanoTemper Technologies). Research in G.W.'s lab is funded by DFG Grant GRK1721 and the DFG Priority Program SPP 1879 (Grant WI 3717/3-1). Research in N.T.'s lab is funded by the DFG Emmy Noether Program (Grant TS 325/1-1) and the DFG Priority Program SPP 1879 (Grants TS 325/2-1 and TS 325/2-2).

1. R. Hengge *et al.*, Recent advances and current trends in nucleotide second messenger signaling in bacteria. *J. Mol. Biol.* **431**, 908–927 (2019).
2. J. Gundlach *et al.*, An essential poison: Synthesis and degradation of cyclic di-AMP in *Bacillus subtilis*. *J. Bacteriol.* **197**, 3265–3274 (2015).
3. F. M. Commichau, J. Gibhardt, S. Halbedel, J. Gundlach, J. Stülke, A delicate connection: c-di-AMP affects cell integrity by controlling osmolyte transport. *Trends Microbiol.* **26**, 175–185 (2018).
4. J. Gundlach *et al.*, Control of potassium homeostasis is an essential function of the second messenger cyclic di-AMP in *Bacillus subtilis*. *Sci. Signal.* **10**, eaal3011 (2017).
5. E. Bremer, R. Krämer, Responses of microorganisms to osmotic stress. *Annu. Rev. Microbiol.* **73**, 313–334 (2019).
6. R. M. Corrigan *et al.*, Systematic identification of conserved bacterial c-di-AMP receptor proteins. *Proc. Natl. Acad. Sci. U.S.A.* **110**, 9084–9089 (2013).
7. C. F. Schuster *et al.*, The second messenger c-di-AMP inhibits the osmolyte uptake system OpuC in *Staphylococcus aureus*. *Sci. Signal.* **9**, ra81 (2016).
8. J. Gundlach *et al.*, Sustained sensing in potassium homeostasis: Cyclic di-AMP controls potassium uptake by KimA at the levels of expression and activity. *J. Biol. Chem.* **294**, 9605–9614 (2019).
9. H. T. Pham *et al.*, Enhanced uptake of potassium or glycine betaine or export of cyclic-di-AMP restores osmoresistance in a high cyclic-di-AMP *Lactococcus lactis* mutant. *PLoS Genet.* **14**, e1007574 (2018).
10. I. M. Quintana *et al.*, The KupA and KupB proteins of *Lactococcus lactis* IL1403 are novel c-di-AMP receptor proteins responsible for potassium uptake. *J. Bacteriol.* **201**, e00028-19 (2019).
11. L. Devaux, P. A. Kaminski, P. Trieu-Cuot, A. Firon, Cyclic di-AMP in host-pathogen interactions. *Curr. Opin. Microbiol.* **41**, 21–28 (2018).
12. J. J. Woodward, A. T. Iavarone, D. A. Portnoy, c-di-AMP secreted by intracellular *Listeria monocytogenes* activates a host type I interferon response. *Science* **328**, 1703–1705 (2010).
13. A. P. McFarland *et al.*, RECON-dependent inflammation in hepatocytes enhances *Listeria monocytogenes* cell-to-cell spread. *mBio* **9**, e00526-18 (2018).
14. K. Parvatiyar *et al.*, The helicase DDX41 recognizes the bacterial secondary messengers cyclic di-GMP and cyclic di-AMP to activate a type I interferon immune response. *Nat. Immunol.* **13**, 1155–1161 (2012).
15. J. R. Barker *et al.*, STING-dependent recognition of cyclic di-AMP mediates type I interferon responses during *Chlamydia trachomatis* infection. *mBio* **4**, e00018-13(2013).
16. P. Xia *et al.*, The ER membrane adaptor ERAdP senses the bacterial second messenger c-di-AMP and initiates anti-bacterial immunity. *Nat. Immunol.* **19**, 141–150 (2018).
17. T. Fahmi, S. Faozia, G. C. Port, K. H. Cho, The second messenger c-di-AMP regulates diverse cellular pathways involved in stress response, biofilm formation, cell wall homeostasis, SpeB expression, and virulence in *Streptococcus pyogenes*. *Infect. Immun.* **87**, e00147-19 (2019).
18. T. N. Huynh *et al.*, An HD-domain phosphodiesterase mediates cooperative hydrolysis of c-di-AMP to affect bacterial growth and virulence. *Proc. Natl. Acad. Sci. U.S.A.* **112**, E747–E756 (2015).
19. Y. Bai *et al.*, Two DHH subfamily 1 proteins in *Streptococcus pneumoniae* possess cyclic di-AMP phosphodiesterase activity and affect bacterial growth and virulence. *J. Bacteriol.* **195**, 5123–5132 (2013).
20. R. J. Dey *et al.*, Inhibition of innate immune cytosolic surveillance by an *M. tuberculosis* phosphodiesterase. *Nat. Chem. Biol.* **13**, 210–217 (2017).
21. G. Witte, S. Hartung, K. Büttner, K. P. Hopfner, Structural biochemistry of a bacterial checkpoint protein reveals diadenylate cyclase activity regulated by DNA recombination intermediates. *Mol. Cell* **30**, 167–178 (2008).
22. R. M. Corrigan, A. Gründling, Cyclic di-AMP: Another second messenger enters the fray. *Nat. Rev. Microbiol.* **11**, 513–524 (2013).
23. F. Rao *et al.*, YybT is a signaling protein that contains a cyclic dinucleotide phosphodiesterase domain and a GGDEF domain with ATPase activity. *J. Biol. Chem.* **285**, 473–482 (2010).
24. K. F. Chater, Recent advances in understanding *Streptomyces*. *F1000Res.* **5**, 2795 (2016).
25. M. J. Bush, N. Tschowri, S. Schlimpert, K. Flärdh, M. J. Buttner, c-di-GMP signalling and the regulation of developmental transitions in *streptomycetes*. *Nat. Rev. Microbiol.* **13**, 749–760 (2015).

MICROBIOLOGY

26. N. Tschowri, Cyclic dinucleotide-controlled regulatory pathways in *Streptomyces* species. *J. Bacteriol.* **198**, 47–54 (2016).
27. R. J. St-Onge *et al*., Nucleotide second messenger-mediated regulation of a muralytic enzyme in *Streptomyces*. *Mol. Microbiol.* **96**, 779–795 (2015).
28. E. Quevillon *et al*., InterProScan: Protein domains identifier. *Nucleic Acids Res.* **33**, W116–W120 (2005).
29. A. Hildebrand, M. Remmert, A. Biegert, J. Söding, Fast and accurate automatic structure prediction with HHpred. *Proteins* **77** (suppl. 9), 128–132 (2009).
30. V. Agarwal, S. A. Borisova, W. W. Metcalf, W. A. van der Donk, S. K. Nair, Structural and mechanistic insights into C-P bond hydrolysis by phosphonoacetate hydrolase. *Chem. Biol.* **18**, 1230–1240 (2011).
31. D. J. Drexler, M. Muller, C. A. Rojas-Cordova, A. M. Bandera, G. Witte, Structural and biophysical analysis of the soluble DHH/DHHA1-type phosphodiesterase TM1595 from *Thermotoga maritima*. *Structure* **25**, 1887–1897.e4 (2017).
32. S. Schlimpert *et al*., Two dynamin-like proteins stabilize FtsZ rings during *Streptomyces* sporulation. *Proc. Natl. Acad. Sci. U.S.A.* **114**, E6176–E6183 (2017).
33. M. Schrecker, D. Wunnicke, I. Hänelt, How RCK domains regulate gating of K+ channels. *Biol. Chem.* **400**, 1303–1322 (2019).
34. M. M. Al-Bassam, J. Haist, S. A. Neumann, S. Lindenberg, N. Tschowri, Expression patterns, genomic conservation and input into developmental regulation of the GGDEF/EAL/HD-GYP domain proteins in *Streptomyces*. *Front. Microbiol.* **9**, 2524 (2018).
35. K. G. Roelofs, J. Wang, H. O. Sintim, V. T. Lee, Differential radial capillary action of ligand assay for high-throughput detection of protein-metabolite interactions. *Proc. Natl. Acad. Sci. U.S.A.* **108**, 15528–15533 (2011).
36. C. Lee *et al*., A two-domain elevator mechanism for sodium/proton antiport. *Nature* **501**, 573–577 (2013).
37. G. Karimova, J. Pidoux, A. Ullmann, D. Ladant, A bacterial two-hybrid system based on a reconstituted signal transduction pathway. *Proc. Natl. Acad. Sci. U.S.A.* **95**, 5752–5756 (1998).
38. M. Ye *et al*., DhhP, a cyclic di-AMP phosphodiesterase of *Borrelia burgdorferi*, is essential for cell growth and virulence. *Infect. Immun.* **82**, 1840–1849 (2014).
39. E. Padan, M. Venturi, Y. Gerchman, N. Dover, Na(+)/H(+) antiporters. *Biochim. Biophys. Acta* **1505**, 144–157 (2001).
40. T. A. Krulwich, G. Sachs, E. Padan, Molecular aspects of bacterial pH sensing and homeostasis. *Nat. Rev. Microbiol.* **9**, 330–343 (2011).
41. K. H. Chin *et al*., Structural insights into the distinct binding mode of cyclic di-AMP with SaCpaA_RCK. *Biochemistry* **54**, 4936–4951 (2015).
42. M. Christen, B. Christen, M. Folcher, A. Schauerte, U. Jenal, Identification and characterization of a cyclic di-GMP-specific phosphodiesterase and its allosteric control by GTP. *J. Biol. Chem.* **280**, 30829–30837 (2005).
43. S. Herbst *et al*., Transmembrane redox control and proteolysis of PdeC, a novel type of c-di-GMP phosphodiesterase. *EMBO J.* **37**, e97825 (2018).
44. C. M. Jeffries *et al*., Preparing monodisperse macromolecular samples for successful biological small-angle X-ray and neutron-scattering experiments. *Nat. Protoc.* **11**, 2122–2153 (2016).
45. C. E. Blanchet *et al*., Versatile sample environments and automation for biological solution x-ray scattering experiments at the P12 beamline (PETRA III, DESY). *J. Appl. Crystallogr.* **48**, 431–443 (2015).
46. D. Franke *et al*., *ATSAS 2.8*: A comprehensive data analysis suite for small-angle scattering from macromolecular solutions. *J. Appl. Crystallogr.* **50**, 1212–1225 (2017).
47. D. I. Svergun, C. Barberato, M. H. J. Koch, CRYSOL-A program to evaluate x-ray solution scattering of biological macromolecules from atomic coordinates. *J. Appl. Crystallogr.* **28**, 768–773 (1995).
48. N. Tschowri *et al*., Tetrameric c-di-GMP mediates effective transcription factor dimerization to control *Streptomyces* development. *Cell* **158**, 1136–1147 (2014).
49. F. Madeira *et al*., The EMBL-EBI search and sequence analysis tools APIs in 2019. *Nucleic Acids Res.* **47**, W636–W641 (2019).
50. H. Kim *et al*., Structural studies of potassium transport protein KtrA regulator of conductance of K+ (RCK) C domain in complex with cyclic diadenosine monophosphate (c-di-AMP). *J. Biol. Chem.* **290**, 16393–16402 (2015).
51. R. Rocha, C. M. Teixeira-Duarte, J. M. P. Jorge, J. H. Morais-Cabral, Characterization of the molecular properties of KtrC, a second RCK domain that regulates a Ktr channel in *Bacillus subtilis*. *J. Struct. Biol.* **205**, 34–43 (2019).

Acknowledgements

I would like to first thank PD Dr. Gregor Witte for giving me the opportunity to pursue my PhD thesis in an exciting field. I am thankful for the immense support and fruitful discussions. I learned a lot from you for which I am very thankful.

I would like to express my gratitude to Prof. Dr. Karl Peter Hopfner for the constructive and supportive research environment.

I thank the whole c-di-AMP subgroup, Dr. David Drexler, Olga Fettscher and Dr. Sandra Schuller for the great fun at work. Special thanks go to David for inspiring scientific discussions at work or on mountain peaks.

I would also like to thank the whole AG Hopfner. It has been a very special time and everyone contributed to this great experience. Special thanks to Brigitte Kessler, not only for the occasional encouragement with gummi bears but also for the help with all the little things that keep a laboratory up and running.

I am deeply thankful to my family and Lotti for all the support.